



12-2023

Development of a Portable, Tileable, Dual-Particle Radiography System

Christian Xavier Young
University of Tennessee, Knoxville, cyoung87@vols.utk.edu

Follow this and additional works at: https://trace.tennessee.edu/utk_graddiss

 Part of the [Nuclear Engineering Commons](#)

Recommended Citation

Young, Christian Xavier, "Development of a Portable, Tileable, Dual-Particle Radiography System. " PhD diss., University of Tennessee, 2023.
https://trace.tennessee.edu/utk_graddiss/9176

This Dissertation is brought to you for free and open access by the Graduate School at TRACE: Tennessee Research and Creative Exchange. It has been accepted for inclusion in Doctoral Dissertations by an authorized administrator of TRACE: Tennessee Research and Creative Exchange. For more information, please contact trace@utk.edu.

To the Graduate Council:

I am submitting herewith a dissertation written by Christian Xavier Young entitled "Development of a Portable, Tileable, Dual-Particle Radiography System." I have examined the final electronic copy of this dissertation for form and content and recommend that it be accepted in partial fulfillment of the requirements for the degree of Doctor of Philosophy, with a major in Nuclear Engineering.

Jason P. Hayward, Major Professor

We have read this dissertation and recommend its acceptance:

Michael J. Liesenfelt, Jeff R. Preston, Nicole McFarlane, Michael P. Cooper

Accepted for the Council:

Dixie L. Thompson

Vice Provost and Dean of the Graduate School

(Original signatures are on file with official student records.)

Development of a Portable, Tileable, Dual-Particle Radiography System

A Dissertation Presented for the
Doctor of Philosophy
Degree

The University of Tennessee, Knoxville

Christian Xavier Young

December 2023

© by Christian Xavier Young, 2023
All Rights Reserved.

This dissertation is dedicated to my loving wife, Katie, whose love and support over the years has helped me grow better in all aspects of my life.

Acknowledgments

The completion of this work would not have been possible without the wonderful support of my research team. I would like to thank my advisor, Dr. Jason Hayward, for his support and guidance throughout the years. His tireless mentoring has helped shape me into the researcher I am today. I would like to thank Dr. Michael Liesenfelt, who has mentored me in all areas of life, both in and out of the laboratory. Additionally, I would like to thank Dr. Nicole McFarlane, Dr. Jeff Preston, and Dr. Michael Cooper, all instrumental parts of my committee, and my team members, Sean Alcorn, Chloe Browning, and Ryan Thurber.

The Y-12 National Security Complex has allowed me to explore the things in life that I find most exciting. There are too many people to name, but I would like to thank Dr. Karen Hogue and Dr. Justin Knowles for supporting me in both of my internships at the Y-12 National Security Complex. Without them, I wouldn't be where I am today.

My amazing wife, Katie Young, has been an absolute blessing throughout my graduate career. Her patience as I worked towards the completion of my degree is unmatched, and without her I wouldn't have been able to accomplish nearly as much as I have. I want to also thank my parents, David and Mary, and my sisters, Claire and Catherine, for all of the love and support they have given me.

Finally, I would like to thank the faculty and staff of Holy Angels Parish School, Aquinas Academy, Slinger High School, Purdue University, and the University of Tennessee for inspiring my love of learning throughout my life.

Great moments are born from great opportunity.

-Herb Brooks

Abstract

A scalable, portable, multi-particle neutron radiography device has been developed using commercial-off-the-shelf-parts. The IDEAS ROSSPAD readout module was selected for use in developing the radiography panel due to its single-wire Power-over-Ethernet (PoE) connectivity and its tileable form factor. Each ROSSPAD detector is paired with an 8 by 8 array of 6-mm-pitch Sensl J-Series silicon photomultipliers (SiPMs). With both single and multi-ROSSPAD testing, a detection package consisting of a 3-mm-thick sheet of EJ-200 plastic scintillator and a 3-mm-thick sheet of acrylic light spreader was coupled to the SiPM board face. After both quality assurance of the detector packages and the calibration of the raw data from the ROSSPADs, sub-SiPM spatial resolution was achieved. For the single-ROSSPAD setup, modulation transfer functions (MTFs) showed spatial resolutions of 2.32 line pairs per centimeter at 10% MTF for gamma rays and 3.35 line pairs per centimeter at 10% MTF for neutrons. The multi-ROSSPAD setups performed similarly with gammas at 2.09 line pairs per centimeter at 10% MTF, while the neutron images lost some spatial resolution with 10% MTF values ranging from 1.30 to 1.46 line pairs per centimeter. Based on the physical characteristics of the board, the raw board spatial resolution sits at 0.833 line pairs per centimeter, meaning all of the methods developed could resolve an object at a sub-SiPM pitch spatial resolution. Additionally, changes to the cutoff values for the full-panel radiography system showed little change to the spatial resolution of the full-panel images, suggesting that the loss in spatial resolution is external to the data collection outside of the number of events recorded. Overall, this research resulted in the development of a state-of-the-art scalable neutron radiography system.

Table of Contents

1	Introduction	1
1.1	Neutron Imaging Theory	1
1.1.1	Neutron Physics	1
1.1.2	Fast Neutron Imaging Use Cases	3
1.2	Neutron Sources	3
1.2.1	Large-Scale User Facilities	5
1.2.2	Isotopic Sources	5
1.2.3	Beam-on-Target Fusion Sources	6
1.3	Acquisition Systems	7
1.3.1	Camera-and-Mirror Systems	7
1.3.2	Thin Screen Converters	8
1.3.3	Photomultiplier (PMT) Arrays	9
1.3.4	Position-Sensitive PMT Arrays	9
1.3.5	Silicon Photomultiplier Arrays	9
1.4	Original Contributions	11
2	Detector Platform	12
2.1	ROSSPAD Readout Module	13
2.1.1	Specifications	13
2.1.2	Advantages	16
2.1.3	Disadvantages	16
2.2	Full Panel Construction	17
2.3	Data Collection and Storage	20

2.3.1	Data Acquisition Process	20
2.3.2	Packet Capture (.pcap) Files	23
2.3.3	SQLite Database Structure	23
2.4	Image Generation Software	25
3	Data Calibration	31
3.1	Single ROSSPAD Data Calibration	31
3.1.1	Calibration Process	31
3.1.2	Electronic Background and Noise Removal	32
3.1.3	Gain Correction	32
3.2	Multi-ROSSPAD Data Calibration	36
3.2.1	Calibration Process	36
3.2.2	Determination of Malfunctioning ROSSPADs	38
3.2.3	Electronic Background and Noise Removal	43
3.2.4	Gain Correction	43
4	Quality Assurance of ROSSPAD Detectors	47
4.1	Failure Modes	47
4.1.1	Single High-Trigger SiPM	49
4.1.2	Single Low-Trigger SiPM	49
4.1.3	High Electronic Noise	51
4.1.4	Unstable Trigger Point	51
4.1.5	Signal Level Drift	51
5	Single-ROSSPAD Imaging	59
5.1	Weighted Average Localization	59
5.1.1	Theory	59
5.1.2	Cs-137 Images	63
5.1.3	Cf-252 Images	66
5.1.4	Comparison Between Localization Method and Bare SiPM Board	75
5.2	Two-Dimensional Gaussian Localization	79

5.2.1	Theory	79
5.2.2	Cs-137 Images	80
5.2.3	Issues With Current Method	82
6	Multi-ROSSPAD Imaging	89
6.1	Cross-ROSSPAD Triggering Effects	89
6.2	Changes to Weighted Average Localization	91
6.3	Flood Field Results	94
6.3.1	Artifact Correction	94
6.4	Spatial Resolution	97
6.4.1	Cs-137 Images	97
6.4.2	Cf-252 Images	100
6.4.3	Comparison Between Detector Packages	117
6.5	Transmission Analysis	119
7	Signal-to-Noise Ratio (SNR) Optimization	124
7.1	Parameters for Optimization	125
7.1.1	Lower Bound Signal Cutoff	125
7.1.2	Upper Bound Signal Cutoff	125
7.1.3	Noise Floor Cutoffs	127
7.1.4	Cluster Size	130
7.2	Comparison of Parameters	130
8	Conclusions & Future Work	136
8.1	Research Outcomes	136
8.2	Lessons Learned	137
8.3	Opportunities for Future Work	138
	Bibliography	141
	Appendices	150
A	Legal	151

A.1	Disclaimer	151
A.2	Copyright Notice	151
B	Supplemental Images of the Full-Panel Housing System	152
C	Supplemental Signal-to-Noise Optimization Images	156
C.1	Lower Bound Signal Cutoff	156
C.2	Upper Bound Signal Cutoff	168
C.3	Cluster Size	180
C.4	Noise Floor Cutoffs	192
Vita		201

List of Tables

1.1	Comparison of Localization Methods	4
2.1	ROSSPAD UDP Data Packet Structure	24
2.2	Raw Data Table Structures in SQLite	27
2.3	Calibration Values and Calibrated Signals Table Structures in SQLite	28
2.4	Image Generation Table Structures in SQLite	29
5.1	Comparison of Localization Methods	88
6.1	Comparison of Spatial Resolutions	118
7.1	Comparison of Lower-Bound Signal Cutoff MTF Values	132
7.2	Comparison of Upper-Bound Signal Cutoff MTF Values	133
7.3	Comparison of Noise Floor Cutoff MTF Values	134
7.4	Comparison of Cluster Size Cutoff MTF Values	135

List of Figures

1.1	Interaction cross-sections for hydrogen and tungsten.	2
1.2	A flood field using a Cs-137 source for the PSPMT array for neutron imaging. Note the distortion in the Y axis for the four groups of 3 by 3 PSPMTs [1]. .	10
2.1	A picture of the front of the ROSSPAD readout module [2].	14
2.2	A picture of the back of the ROSSPAD readout module with an Ethernet cable connected.	15
2.3	Photograph of the front of assembled full-panel housing, designed and manufactured by Chloe Browning.	18
2.4	Photograph of the back of assembled full-panel housing, designed and manufactured by Chloe Browning. Some Ethernet cables have been plugged in as a demonstration.	19
2.5	A flow chart demonstrating the process for collecting data using the IDEAS ROSSPAD.	21
2.6	Screenshot of the Testbench software developed by IDEAS. The ASIC configuration tab has been selected.	22
2.7	Screenshot of the DB Browser for SQLite software, with tables expanded to show structure.	26
3.1	A sample uncorrected signal histogram from a flood field image.	33
3.2	A histogram and map of the electronic background values for an example neutron flood field measurement.	34
3.3	A histogram and map of the electronic noise values for an example neutron flood field measurement.	35

3.4	A histogram and map of the gain values for an example neutron flood field measurement.	37
3.5	A map of electronic background values of the SiPMs on the full radiography panel.	39
3.6	A second map of electronic background values of the SiPMs on the full radiography panel, with the broken SiPM filtered out of the image.	40
3.7	A map of electronic noise values of the SiPMs on the full radiography panel.	41
3.8	Locations of the ROSSPADs selected for 4 by 3 area image.	42
3.9	A histogram and map of the electronic background values for an example neutron flood field measurement on the multi-ROSSPAD system.	44
3.10	A histogram and map of the electronic noise values for an example neutron flood field measurement on the multi-ROSSPAD system.	45
3.11	A histogram and map of the gain values for an example neutron flood field measurement on the multi-ROSSPAD system.	46
4.1	Uncorrected histograms of the 64 SiPMs on a working ROSSPAD. ($N = 1.4 \times 10^6$ counts)	48
4.2	Uncorrected histograms of the 64 SiPMs on a ROSSPAD with one SiPM's electronic background value significantly higher than the remaining SiPMs.	50
4.3	Uncorrected histograms of the 64 SiPMs on a ROSSPAD with one SiPM falling short of all of the rest of the SiPM histograms. ($N = 1.4 \times 10^6$ counts)	52
4.4	Uncorrected histograms of the 64 SiPMs on a ROSSPAD with high electronic noise. ($N = 1.4 \times 10^6$ counts)	53
4.5	Uncorrected histograms of the 64 SiPMs on a ROSSPAD with unstable triggering level. ($N = 1.4 \times 10^6$ counts)	54
4.6	Wireshark graph of the packets per second from a ROSSPAD with an unstable triggering level. The source used to produce this data provides a steady stream of gamma rays.	55
4.7	Uncorrected histograms of the 64 SiPMs on a ROSSPAD with potential signal value drift. ($N = 1.4 \times 10^6$ counts)	57

4.8	Corrected total signal histograms of a working ROSSPAD and a ROSSPAD experiencing signal value drift.	58
5.1	Experimental setup for generating a collimated Cs-137 line image.	61
5.2	Experimental setup for generating a collimated Cf-252 edge image.	62
5.3	A flood field image generated using a Cs-137 gamma source. ($N = 1.8 \times 10^6$ counts)	64
5.4	A collimated line image generated using a Cs-137 gamma source. SiPM boundaries have been overlaid onto the image. ($N = 3.2 \times 10^5$ counts)	65
5.5	Line profile of the collimated Cs-137 image.	67
5.6	Demonstration of the area evaluated for spatial resolution of the collimated Cs-137 image.	68
5.7	Modulation transfer function of the collimated Cs-137 line.	69
5.8	A flood field image generated using a Cf-252 fission neutron source. ($N = 5.5 \times 10^5$ counts)	70
5.9	Optical distortion due to the separation of the light spreader and the scintillator (circled in orange).	71
5.10	An edge image generated using a Cf-252 fission neutron source. ($N = 1.3 \times 10^6$ counts)	72
5.11	An edge image generated using a Cf-252 fission neutron source. ($N = 1.3 \times 10^6$ counts)	73
5.12	Modulation transfer function of the collimated Cf-252 edge.	74
5.13	A new edge image generated using a pixel density of 2 pixels per millimeter. ($N = 1.3 \times 10^6$ counts)	76
5.14	Edge profile of the reduced resolution image.	77
5.15	Comparison of MTF measurements using two different pixel densities.	78
5.16	Simulated two-dimensional Gaussian curve generated in Python.	81
5.17	A flood field image generated using a Cs-137 gamma source and a 2D Gaussian localization method. ($N = 1.8 \times 10^6$ counts)	83

5.18	A collimated line image generated using a Cs-137 gamma source and a 2D Gaussian localization method. ($N = 3.2 \times 10^5$ counts)	84
5.19	Line profile of the collimated Cs-137 image using the 2D Gaussian localization method.	85
5.20	Modulation transfer function of the collimated Cs-137 line using the 2D Gaussian localization method.	86
6.1	Full-panel flood field using a Cs-137 source. 35 of the 36 ROSSPADs were turned on for this experiment.	90
6.2	A single-event trigger map with the higher triggering threshold value set. The event space is shown across four ROSSPADs (cyan grid lines).	92
6.3	A single-event trigger map with the lower triggering threshold value set. The event space is shown across four ROSSPADs (cyan grid lines).	93
6.4	Full-panel flood fields using a Cs-137 gamma source weighted by a) number of counts in pixel and b) total signal from events in pixel. ($N = 1.25 \times 10^7$ counts)	95
6.5	Full-panel flood fields using a Cf-252 neutron source weighted by a) number of counts in pixel and b) total signal from events in pixel. ($N = 1.17 \times 10^7$ counts)	96
6.6	Experimental setup for generating a collimated Cs-137 line image on the full radiography panel.	98
6.7	Full-panel Cs-137 collimated line images that are a) before flood field correction and b) after flood field correction. ($N = 7.63 \times 10^6$ counts)	99
6.8	Line profile of the collimated Cs-137 image on the full radiography panel. . .	101
6.9	Modulation transfer function of the collimated Cs-137 line on the full radiography panel.	102
6.10	First experimental setup for generating a collimated Cf-252 image.	103
6.11	Full-panel Cf-252 collimated edge images that are a) before flood field correction and b) after flood field correction. ($N = 4.70 \times 10^7$ counts)	104
6.12	Line profile of the first collimated Cf-252 edge on the full radiography panel.	106

6.13	Modulation transfer function of the first collimated Cf-252 edge on the full radiography panel.	107
6.14	Second experimental setup for generating a collimated Cf-252 image.	108
6.15	Full-panel Cf-252 collimated line images that are a) before flood field correction and b) after flood field correction. ($N = 1.92 \times 10^7$ counts)	109
6.16	Profile of the collimated Cf-252 line on the full radiography panel.	111
6.17	Modulation transfer function of the collimated Cf-252 line on the full radiography panel.	112
6.18	Third experimental setup for generating a collimated Cf-252 image.	113
6.19	Second full-panel Cf-252 collimated edge images that are a) before flood field correction and b) after flood field correction. ($N = 1.23 \times 10^7$ counts)	114
6.20	Line profile of the second collimated Cf-252 edge on the full radiography panel.	115
6.21	Modulation transfer function of the second collimated Cf-252 edge on the full radiography panel.	116
6.22	A tungsten block and a plastic pipe vale in front of the radiography panel. .	121
6.23	The resultant neutron radiograph of the tungsten block and the plastic valve.	122
6.24	Mean value of the log of the ratio of the image and the flood field, circled in red. Value generated with ImageJ.	123
7.1	Comparison of MTFs for different lower bound cutoff values.	126
7.2	Comparison of MTFs for different upper bound cutoff values.	128
7.3	Comparison of MTFs for different noise floor cutoff values.	129
7.4	Comparison of MTFs for different high-signal cluster sizes.	131
1	Full-panel housing lying flat, with cooling fan ports visible.	152
2	Milling of the aluminum lid for the full-panel assembly.	153
3	Test fit of a single ROSSPAD and cooling fan in the full-panel housing. . . .	154
4	assembled housing with all fans installed.	155
5	Cf-252 flood field where all events are above 1000 total signal.	156
6	Cf-252 edge images where all events are above 1000 total signal a) before flood field correction and b) after flood field correction.	157

7	a) Line profile and b) MTF plot for a Cf-252 edge where all events are above 1000 total signal.	158
8	Cf-252 flood field where all events are above 3000 total signal.	159
9	Cf-252 edge images where all events are above 3000 total signal a) before flood field correction and b) after flood field correction.	160
10	a) Line profile and b) MTF plot for a Cf-252 edge where all events are above 3000 total signal.	161
11	Cf-252 flood field where all events are above 6000 total signal.	162
12	Cf-252 edge images where all events are above 6000 total signal a) before flood field correction and b) after flood field correction.	163
13	a) Line profile and b) MTF plot for a Cf-252 edge where all events are above 6000 total signal.	164
14	Cf-252 flood field where all events are above 9000 total signal.	165
15	Cf-252 edge images where all events are above 9000 total signal a) before flood field correction and b) after flood field correction.	166
16	a) Line profile and b) MTF plot for a Cf-252 edge where all events are above 9000 total signal.	167
17	Cf-252 flood field where all events are under 22,500 total signal.	168
18	Cf-252 edge images where all events are under 22,500 total signal a) before flood field correction and b) after flood field correction.	169
19	a) Line profile and b) MTF plot for a Cf-252 edge where all events are under 22,500 total signal.	170
20	Cf-252 flood field where all events are under 20,000 total signal.	171
21	Cf-252 edge images where all events are under 20,000 total signal a) before flood field correction and b) after flood field correction.	172
22	a) Line profile and b) MTF plot for a Cf-252 edge where all events are under 20,000 total signal.	173
23	Cf-252 flood field where all events are under 17,500 total signal.	174
24	Cf-252 edge images where all events are under 17,500 total signal a) before flood field correction and b) after flood field correction.	175

25	a) Line profile and b) MTF plot for a Cf-252 edge where all events are under 17,500 total signal.	176
26	Cf-252 flood field where all events are under 15,000 total signal.	177
27	Cf-252 edge images where all events are under 15,000 total signal a) before flood field correction and b) after flood field correction.	178
28	a) Line profile and b) MTF plot for a Cf-252 edge where all events are under 15,000 total signal.	179
29	Cf-252 flood field where the SiPMs used have signals that are above 0x the noise value of said SiPM.	180
30	Cf-252 edge images where the SiPMs used have signals that are above 0x the noise value of said SiPM a) before flood field correction and b) after flood field correction.	181
31	a) Line profile and b) MTF plot for a Cf-252 edge where the SiPMs used have signals that are above 0x the noise value of said SiPM.	182
32	Cf-252 flood field where the SiPMs used have signals that are above 1x the noise value of said SiPM.	183
33	Cf-252 edge images where the SiPMs used have signals that are above 1x the noise value of said SiPM a) before flood field correction and b) after flood field correction.	184
34	a) Line profile and b) MTF plot for a Cf-252 edge where the SiPMs used have signals that are above 1x the noise value of said SiPM.	185
35	Cf-252 flood field where the SiPMs used have signals that are above 2x the noise value of said SiPM.	186
36	Cf-252 edge images where the SiPMs used have signals that are above 2x the noise value of said SiPM a) before flood field correction and b) after flood field correction.	187
37	a) Line profile and b) MTF plot for a Cf-252 edge where the SiPMs used have signals that are above 2x the noise value of said SiPM.	188
38	Cf-252 flood field where the SiPMs used have signals that are above 4x the noise value of said SiPM.	189

39	Cf-252 edge images where the SiPMs used have signals that are above 4x the noise value of said SiPM a) before flood field correction and b) after flood field correction.	190
40	a) Line profile and b) MTF plot for a Cf-252 edge where the SiPMs used have signals that are above 4x the noise value of said SiPM.	191
41	Cf-252 flood field where no SiPMs have to have signals that are above the noise value cutoff.	192
42	Cf-252 edge images where no SiPMs have to have signals that are above the noise value cutoff a) before flood field correction and b) after flood field correction.	193
43	a) Line profile and b) MTF plot for a Cf-252 edge where no SiPMs have to have signals that are above the noise value cutoff.	194
44	Cf-252 flood field where 4 SiPMs have to have signals that are above the noise value cutoff.	195
45	Cf-252 edge images where 4 SiPMs have to have signals that are above the noise value cutoff a) before flood field correction and b) after flood field correction.	196
46	a) Line profile and b) MTF plot for a Cf-252 edge where 4 SiPMs have to have signals that are above the noise value cutoff.	197
47	Cf-252 flood field where 4 SiPMs have to have signals that are above the noise value cutoff.	198
48	Cf-252 edge images where 4 SiPMs have to have signals that are above the noise value cutoff a) before flood field correction and b) after flood field correction.	199
49	a) Line profile and b) MTF plot for a Cf-252 edge where 4 SiPMs have to have signals that are above the noise value cutoff.	200

Chapter 1

Introduction

1.1 Neutron Imaging Theory

Most state-of-the-art industrial radiographic systems rely on x-rays to generate images. Neutron radiography is maturing as another radiographic Nondestructive Evaluation (NDE) modality. Currently, most neutron radiography systems rely on thermal neutrons, which is effective but has a limit on the total penetration of the object. Beam-on-target neutron generators produce fast neutrons that are superior than both thermal neutrons and x-rays at penetrating dense, metallic objects [3].

1.1.1 Neutron Physics

Neutrons interact with the nucleus of an atom, compared to photons interacting with the electron cloud. Neutron interaction cross sections are highly dependent on the isotope the neutron is interacting with. Figure 1.1 demonstrates this difference by comparing the neutron and photon interaction cross-sections for hydrogen ($Z=1$, $A=1$) and tungsten ($Z=74$, $A=184$). The photon interaction data is provided by the NIST XCOM library[4], and the neutron data is provided by the Evaluated Nuclear Structure Data File from the National Nuclear Data Center at Brookhaven National Laboratory [5]. Hydrogen, with only a single electron, has a higher cross section for neutron interactions, while tungsten, which has 74 electrons, is dominated by photon interactions. The maximum energy transfer from a neutron

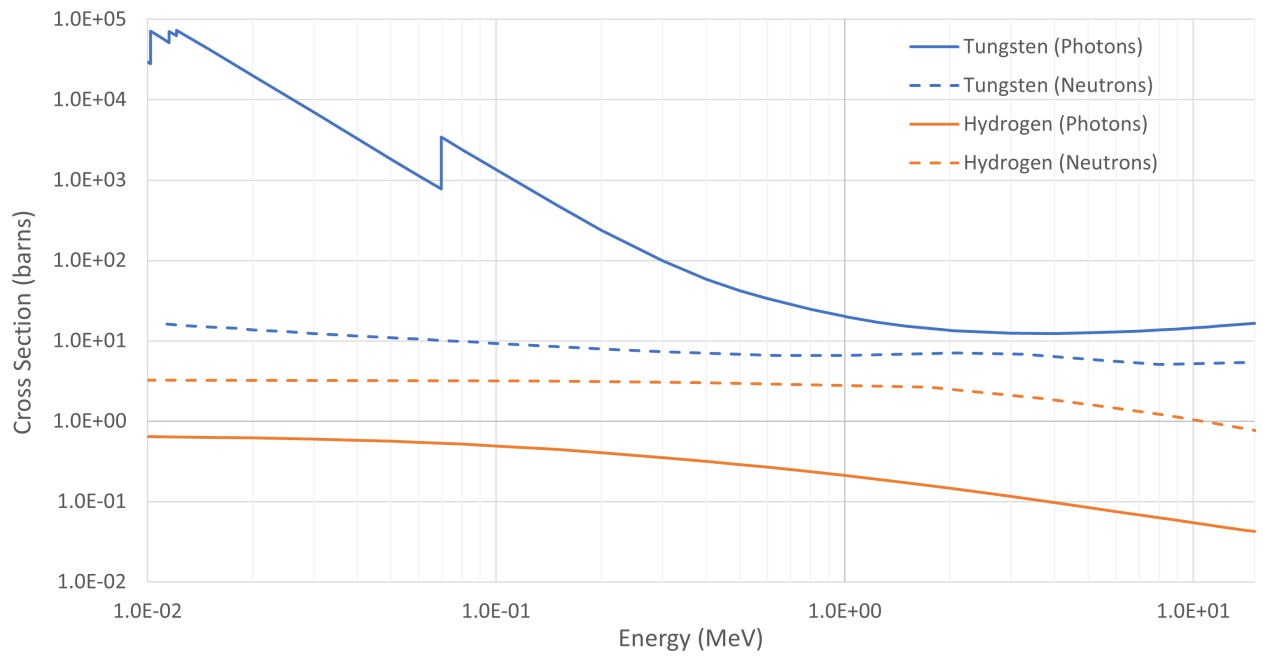


Figure 1.1: Interaction cross-sections for hydrogen and tungsten.

to a hydrogen nucleus is nearly 100%, where the maximum energy transfer from a neutron to a tungsten nucleus with an average atomic mass of 183.84 amu is approximately 3%.

Because photon interactions have a much higher cross section in high-Z materials compared to low-Z materials, nondestructive evaluation using traditional radiographic techniques prove to be difficult for dense, metallic objects. Size constraints limit the energy of portable x-ray imaging systems to below 370 keV [6]. Higher-energy x-rays can penetrate dense, metallic materials, but currently require larger, accelerator-based systems to generate the needed energies [7]. Research into more compact high-energy x-rays sources is ongoing [8]. Portable neutron radiography is a superior modality for a large number of applications.

Neutrons also add the capability of determining the isotopic compositions of interrogated materials via direct interaction with the nucleus. While photon interactions can achieve this effect using characteristic x-rays [9] or nuclear resonance fluorescence using high energy gamma rays [10], neutron interactions are easier to work with and do not require high energies to achieve.

1.1.2 Fast Neutron Imaging Use Cases

Neutron radiography has already become a standard NDE modality for several applications. For international safeguards and security, neutron radiography is used in wide ranging applications, such as neutron activation analysis [11] and neutron transmission analysis [12]. The scanning of large cargo containers, which are comprised of thick steel, allows border security personnel to more easily catch any threats entering a country via land and sea routes [13]. At Idaho National Laboratory, neutron radiography has been deployed to ensure the safe operation of several reactors on site by inspecting nuclear fuel before and after irradiation [14]. Neutron radiography has also played a role in materials science and geological research, especially when determining water content in materials [15][16].

1.2 Neutron Sources

The source of neutrons for a neutron radiography system can vary widely depending on the application needs. It is important to understand the various forms of neutron sources

Table 1.1: Comparison of Localization Methods

Source	Energy Spectrum	Can be Switched Off?	Portable?
Nuclear Reactor	Fission Spectrum. Often moderated down to thermal energies.	No	No
Spallation Source	Variable depending on incident particle. Typically moderated down to cold energies	Yes	No
Spontaneous Fission (Cf-252)	Fission spectrum	No	Yes*
(α, n) Reaction (AmBe, PuBe)	Dependent on maximum alpha energy and target isotope	No	Yes*
Deuterium-Deuterium Fusion	Monoenergetic (2.45 MeV)	Yes	Yes
Deuterium-Tritium Fusion	Monoenergetic (14.1 MeV)	Yes	Yes

* Source material is portable. Requires Shielding that may limit portability.

and their advantages and disadvantages. A table summarizing the modality, energy, and portability of each source is included as Table 1.1.

1.2.1 Large-Scale User Facilities

Research reactors are a common nuclear science tool found at many national laboratories and universities internationally. For example, the Ohio State University Research Reactor (OSURR) has beamline facilities that can be used for both teaching and fundamental research [17]. Larger and more complex nuclear reactors, like the High Flux Isotope Reactor (HFIR) at Oak Ridge National Laboratory (ORNL), may have several beamlines dedicated just to neutron imaging [18]. Nuclear reactors will often have an energy spectrum moderated both in-core and in-beamline, with many systems moderated to cold neutron energies for a wide variety of experiments. Nuclear reactors cannot be switched off due to radioactive decay products. Completely shielding the neutrons coming from the core of the reactor is the only way to stop the neutrons.

Spallation neutrons are also used at many large-scale user facilities. The most well known example of a spallation neutron source is the Spallation Neutron Source (SNS) at ORNL [19]. At SNS, a pulse of high-energy protons strike a mercury target, creating anywhere from 20-30 neutrons that are moderated to cold energies before travelling through a beamline [19]. Much like reactor systems, spallation sources are by their nature not portable. Spallation neutron sources can be turned off, unlike a nuclear reactor.

1.2.2 Isotopic Sources

Neutrons are generated using specific isotopes by spontaneous fission or $\alpha - n$ reactions. Californium-252 is a well known source of spontaneous fission neutrons, following an approximate fission energy spectrum with an average neutron energy of 2 MeV [20]. Neutrons generated from an (α, n) reaction follow a unique energy spectrum highly dependent on the maximum alpha energy and the target isotope [21]. Isotopic sources cannot be turned off, and while the source itself may be portable, the intense radiation coming from the source

may require the use of significant shielding in order to transport it. Depending on the source activity, this may render an isotopic source not readily portable.

1.2.3 Beam-on-Target Fusion Sources

Beam-on-target fusion sources use a high-energy electronic power supply to drive two lighter isotopes into one another, causing a portion of the isotopes to fuse, releasing energy and secondary particles. For the purposes of generating neutrons, there are two modalities that are commonly used: deuterium-deuterium (D-D) fusion and deuterium-tritium (D-T) fusion. D-D fusion results in a neutron of 2.45 MeV, but only in 50% of reactions [22]. D-T fusion results in a 14.1 MeV neutron that occurs in 100% of reactions [22]. Since D-T fusion releases a higher energy neutron at a higher rate than D-D fusion, it is often the standard when using fusion neutron generators for radiographic purposes. D-D fusion, however, is still used, especially if the setup requires a lower-energy neutron.

Several companies have gone on to make commercial D-D and D-T neutron generators. Phoenix, based in Fitchburg, Wisconsin, offers high-flux, stationary neutron generators that use both D-D and D-T fusion [23]. Adelphi, Starfire Industries, and ThermoFisher offer fusion neutron generators that, while lower flux than Phoenix's generators, feature a compact and portable design, making them useful for field neutron radiography [24][25][26]. There have also been some systems developed at national laboratories for use in radiography and tomography of containers holding nuclear materials [27]. The Associated Particle Neutron Imaging System (APNIS) uses a modification of a commercial-off-the-shelf neutron generator that allows the detection of the helium atom produced in the fusion reaction [27]. Tracking the location of the helium atom allows for researchers to determine the direction of the associated neutron, allowing for time-of-flight measurements not possible with a standard D-T generator [27]. ThermoFisher now offers their own commercial-off-the-shelf associated particle imaging source because of the research done at the laboratories [28].

Due to the compact nature of fusion-based neutron generators, significant consideration has been given for their use in neutron imaging systems. D-D and D-T generators can be portable, shut off at any moment, and allow for high penetration of an interrogated object.

If coupled with a portable detector system, a fusion neutron source can be used for field neutron radiography.

1.3 Acquisition Systems

Several different methods for neutron detection have been employed for use in neutron imaging systems. These systems exist at various technology readiness level (TRL) stages, and are primarily developed and used at national laboratories or research universities.

1.3.1 Camera-and-Mirror Systems

There have been several facilities that use a camera-and-mirror system to generate neutron images. In these systems, a neutron scintillator is placed in line with a neutron beam and a mirror tilted at an angle. A camera then takes a long exposure image of the scintillator through the mirror to avoid excess radiation dose, resulting in a high-resolution image.

Williams et al. generated an image by placing a 25.4-mm-thick high-density polyethylene (HDPE) imaging phantom nearly flush with the scintillator from a Neutron Optics imaging system [29]. This system uses a 2-mm-thick scintillator screen containing a mix of lithium-6 fluoride and zinc sulfide doped with copper. A 200 mm by 200 mm image was acquired using a Sony ICX694ALG CCD camera [29]. The image resolution was dependent on the position and orientation of the object due to optical distortion and blurring. A spatial resolution ranging from 0.16 line pairs per millimeter to 0.42 line pairs per millimeter was obtained at a 15% modulation transfer function (MTF) value [29].

Bishnoi et al. developed a similar system using a thick block of BC400 plastic scintillator measuring 300 mm by 300 mm by 40 mm [30]. The research group did not give a spatial resolution in line pairs per unit length, but they could resolve a hole measuring 5 mm in diameter in a block of HDPE [30]. Their scintillator choice allows for greater neutron detection efficiency, though this comes with the tradeoff of lower spatial resolution compared to other systems.

Wang et al. had a novel approach to increasing the neutron detection efficiency of a camera-and-mirror system, using a 40-mm-thick zinc sulfide scintillator bar with wavelength-shifting fibers embedded into it [31]. To generate a full image, the scintillator bar is translated relative to the object, and a complete image is formed with offset image integration [31]. Features as small as 0.5 mm in width could be resolved in the images, giving the system a high spatial resolution and high neutron detection efficiency, albeit with the added complexity of translation imaging [31].

All three of these systems share many common drawbacks. Since the scintillator material is separated from the camera, a significant amount of the scintillation light is lost without reaching the camera. This loss of photons can result in a lower spatial resolution than would be expected of a system that can detect all of the photons from an event. Scintillator screens are an integrating mode converter, which combines the events from both neutrons and gammas. The electronic noise of a CCD camera is also integrated into each acquisition frame. To counteract this issue, many of these systems are deployed at reactor beamline facilities, increasing the flux of neutrons reaching the detector. Using a beamline facility renders the system not portable. In addition to this, these systems are room-sized, making them unsuitable for field neutron radiography.

1.3.2 Thin Screen Converters

Kerr et al. developed a unique system that converts a commercial-off-the-shelf x-ray radiography panel into one that can be used for neutron radiography [32]. A polypropylene proton recoil screen is backed by a 2.4-mm-thick screen of copper-doped zinc sulfide [32]. The scintillator screen is coupled directly to a Varex Imaging XRD 1621 Thin-Film Transistor (TFT) panel [32]. This panel has an estimated spatial resolution around 2.4 mm, limited by the thickness of the converter screen, and also has high sensitivity to incident gamma rays on the detector system since it lacks the ability to perform pulse-shape discrimination (PSD) [32]. The benefit to this system, though, is the relative ease of modification and ability to use commercial-off-the-shelf image processing software to generate radiographs.

1.3.3 Photomultiplier (PMT) Arrays

McConchie et al. built a fast neutron radiography panel using a segmented plastic scintillator block attached to four Hamamatsu R9779 photomultiplier tubes [27]. The segmented scintillator block measures 10.39 cm by 10.39 cm by 5 cm, with 1-cm-pitch pixels, achieving a spatial resolution on the order of one centimeter per pixel [27]. The large PMT array makes the system not readily portable, especially when considering the large amount of electronics needed to run all of the PMTs in the system. This system has been paired with a D-T generator designed for use in associated particle imaging, but it is possible to use the neutron detection hardware for simple neutron transmission radiography.

1.3.4 Position-Sensitive PMT Arrays

Another generation of associated particle imaging detector was built by Heath et al. at Oak Ridge National Laboratory using position-sensitive PMTs (PSPMTs). The PSPMTs are read out in four-corners mode, allowing for localisation to the same 1-cm-pitch scintillator segments as the PMT-based system [1]. The PSPMTs measure approximately 5 cm by 5 cm, with each PSPMT replacing a single, regular photomultiplier tube in the previous panel [1]. This leads to the same spacial resolution of approximately 1 cm per pixel. One of the major drawbacks of the change to PSPMTs, however, can be seen in Figure 1.2 [1]. For each quadrant of PSPMTs, there is a significant amount of distortion in the Y axis of the image. Additional corrective features must be added to take into account this effect, which puts limits on how far spatial resolution can be decreased, even with changes to the scintillator package.

1.3.5 Silicon Photomultiplier Arrays

Silicon photomultipliers (SiPMs) are an alternative to the traditional vacuum tube PMTs seen in many systems. SiPMs are much more compact than traditional PMTs, operate at lower voltages, and are insensitive to strong magnetic fields [33][34]. SiPMs do have some drawbacks compared to PMTs, particularly with regards to high dark noise and high temperature dependence comparatively [33]. SiPMs are typically seen in medical

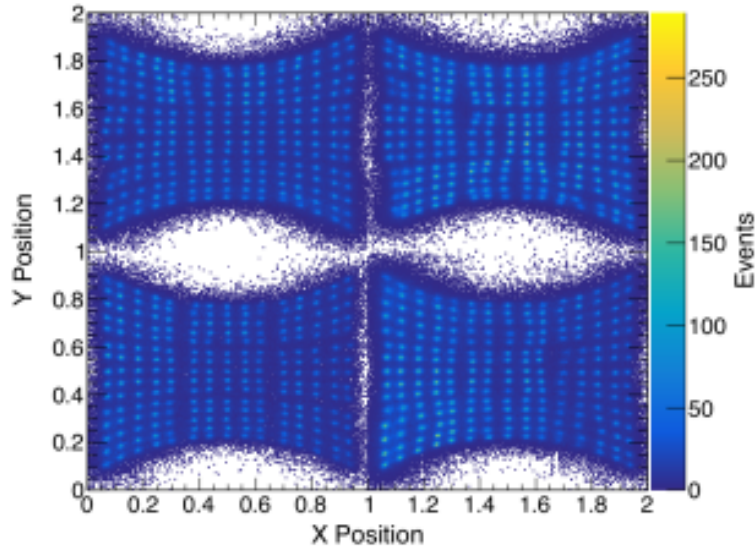


Figure 1.2: A flood field using a Cs-137 source for the PSPMT array for neutron imaging. Note the distortion in the Y axis for the four groups of 3 by 3 PSPMTs [1].

applications, particularly for positron emission tomography (PET) due to their compact size and ability to withstand the magnetic fields from nearby magnetic resonance imaging (MRI) machines [34][35]. Industrial imaging using ROSSPADs is still limited, though new research is being performed [36].

1.4 Original Contributions

The goal of this research is to develop a scalable radiography system using commercial-off-the-shelf (COTS) radiation detection equipment. The main goal is to generate neutron radiographs, but gamma radiographs will also be generated to demonstrate the ability to perform dual-particle imaging. A COTS system was selected for use in the radiography panel. After detector selection, development of methods to calibrate the detector system and generate radiographs will enable the first images to be made. A single detector module was used to quantify the spatial resolution for both imaging modalities. Additionally, a new localization method was developed and tested alongside traditional event localization on a single detector module.

After a larger system is built using multiple detector modules, spatial resolution was quantified again to study any changes between the single-detector experiment and the multi-detector experiments. Parametric studies of some of the localization parameters was performed to show how they impact the spatial resolution of images. Finally, a path forward for the radiography system was proposed, with focus on improving spatial resolution of the system.

Chapter 2

Detector Platform

The radiation detection methods discussed in Chapter 1 share many of the same limitations due to them all being integrating-type imaging systems. These detector packages cannot individually distinguish different radiation events from each other, so the electronic noise will always be integrated into the data stream. A new neutron radiography device ideally would use a counting-based method for building a radiograph. Using neutron counting reduces the electronic noise that is added into the final image, improving spatial resolution.

Many of the previously discussed systems are limited in their detection area. These systems either have no ability to tile together or are hampered by complex readout systems that put a fundamental limit on the number of detector modules that can be used. The ability to scale a radiography system in area without restriction is fundamental to building a next-generation radiography system. Not only does a detector package need to be tileable, it must also have appropriate connections for data collection that are unhampered by limits on digitizer equipment or other external factors.

A detector package built around the IDEAS ROSSPAD readout module was selected as the base of a novel compact neutron radiography system. The ROSSPAD features event mode data collection, one-wire connection for both power and data, and a tileable electronics package that makes it ideal for this research. The ROSSPAD is also a COTS product, reducing the lead time needed to develop and characterize the radiography panel.

2.1 ROSSPAD Readout Module

2.1.1 Specifications

The ROSSPAD is a compact, tileable readout module developed by Integrated Detector Electronics AS (IDEAS) from Norway [2]. The ROSSPAD module has a maximum detection rate of approximately 20,000 frames per second with a 12 bit ADC, a variable readout interval between 50 μ s and 1 s, and a programmable trigger threshold per channel [2]. The ROSSPAD also features four input charge ranges of -400 pC, -4 nC, -8 nC, and -16 nC for gain variation, as well as four shaping times of 200 ns, 400 ns, 800 ns, and 1600 ns for pulse width variation. The ROSSPAD comes with a detachable array of SiPMs installed, connected using two multipin connectors [2]. The array, measuring 8 by 8 SiPMs at a 6 mm pitch, uses the Onsemi (former SensL) MICROFJ-60035-TSV model of SiPM [37]. These SiPMs feature a breakdown voltage between 24.2 V and 24.7 V, an operating voltage between 25.2 V and 30.7 V, a spectral range between 200 nm and 900 nm, and a microcell fill factor of 75%.

The ROSSPAD measures 50.0 mm by 50.0 mm at the face and 48.5 mm deep [2]. This compact shape allows it to be tileable, meaning that ROSSPAD detectors can be tiled with little to no gap between them. This feature allows for the ROSSPAD to be used in a system than can scale infinitely in two dimensions. Additionally, the ROSSPAD uses a one-wire gigabit IEEE 802.3af Power-over-Ethernet (PoE) connection on the back of the system [2]. The PoE connection allows for the panel to scale with the addition of multiple PoE switches. Figure 2.1 shows an image of the front of the ROSSPAD module with SiPM board attached, and Figure 2.2 shows an image of the back of the ROSSPAD module.

To detect radiation, a scintillator package comprised of a 3-mm-thick sheet of EJ-200 plastic scintillator and a 3-mm-thick sheet of polycarbonate light spreader was optically coupled to the SiPM board using EJ-550 silicone grease [38][39]. The EJ-200 is sensitive to both gammas and neutrons, allowing for dual-particle radiographs to be taken with a single system. The light spreader, placed between the SiPM board and the scintillator, allows light from a scintillation event to spread across multiple SiPMs. The pattern of light distribution across multiple SiPMs enables localization of the event position. Rust-Oleum titanium dioxide white spray paint acts as a diffuse reflector for the optical package boundary

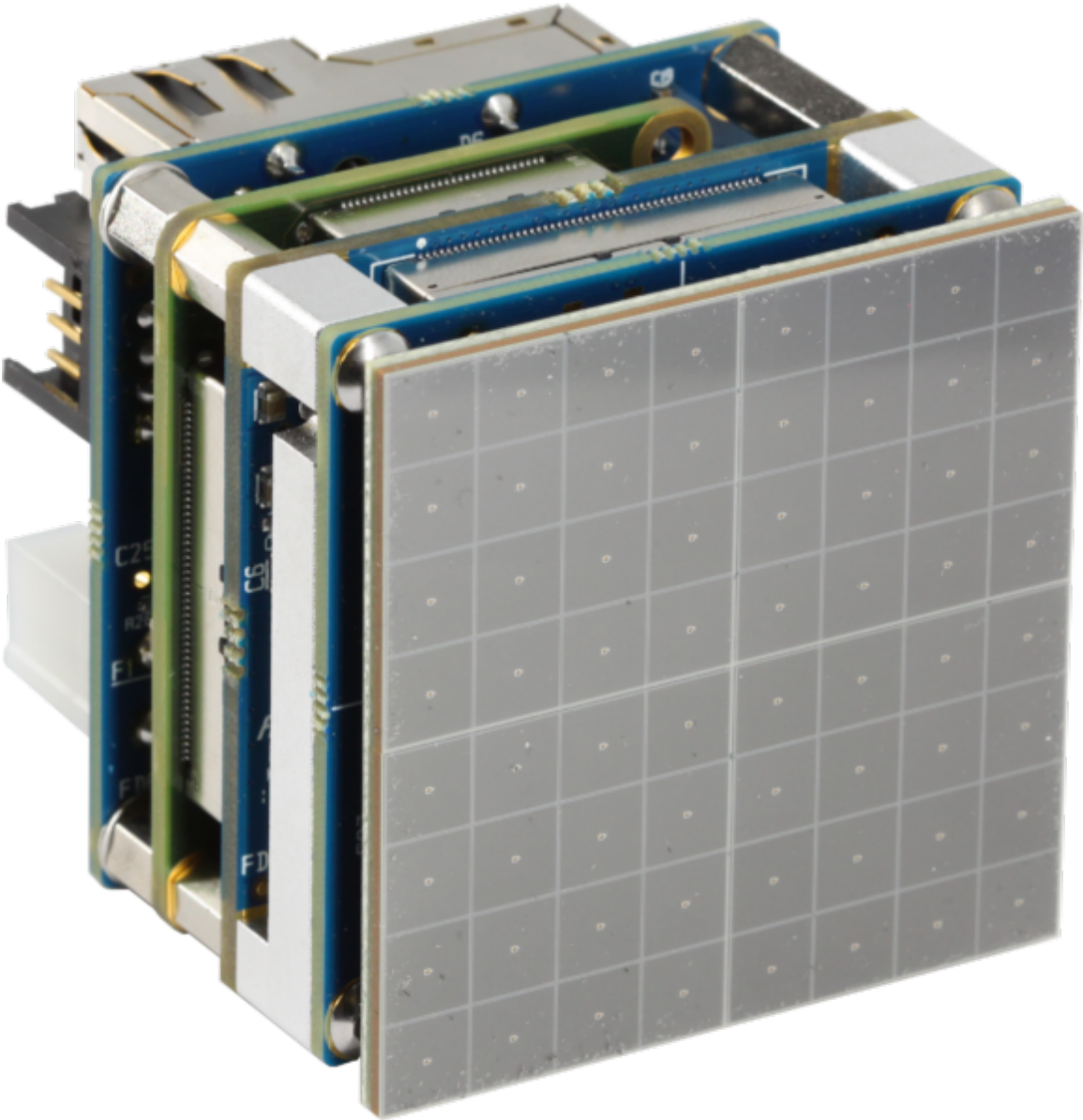


Figure 2.1: A picture of the front of the ROSSPAD readout module [2].

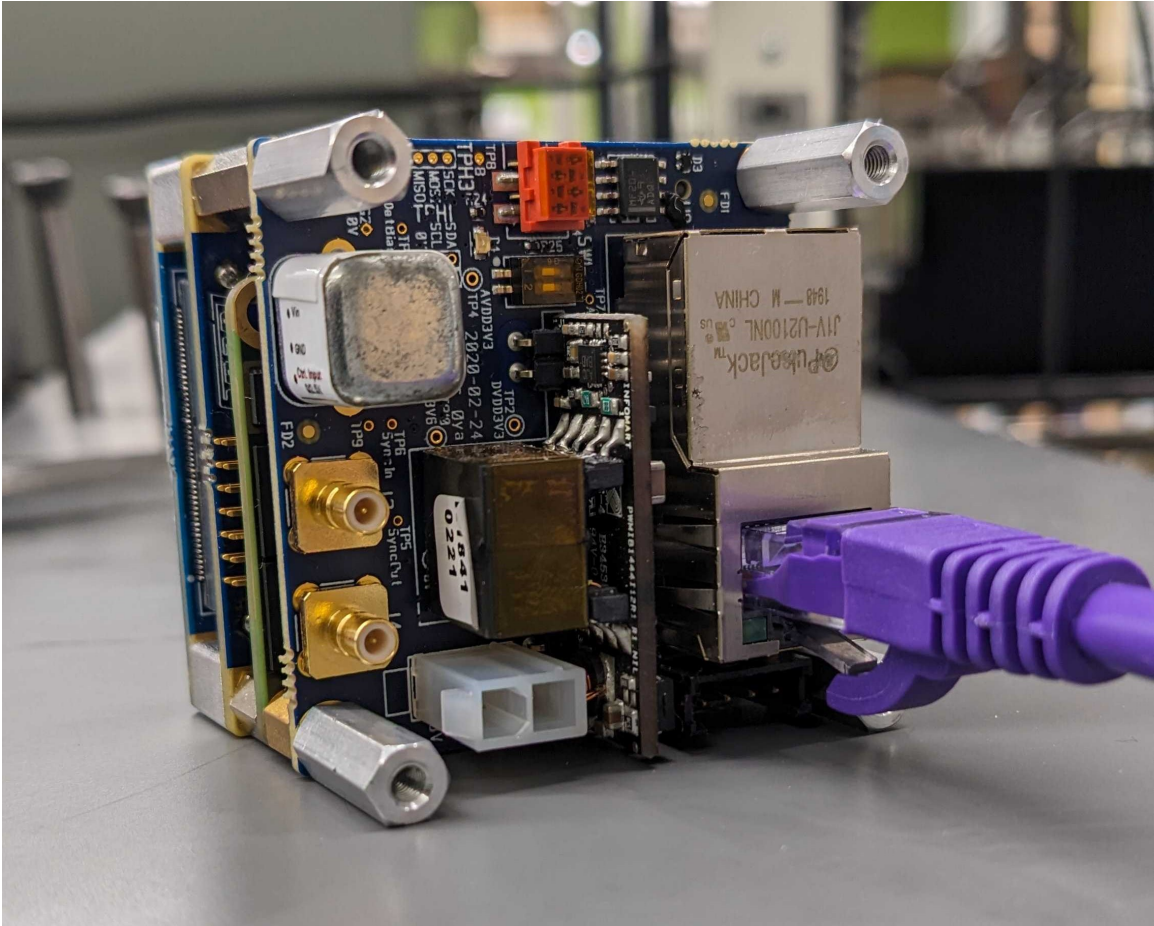


Figure 2.2: A picture of the back of the ROSSPAD readout module with an Ethernet cable connected.

[40]. This package is used for both single-ROSSPAD radiographs as well as the full-panel system.

2.1.2 Advantages

The ROSSPAD readout module’s compact and tileable nature allows for easy manufacturing of large-scale radiography systems. SiPMs are significantly thinner compared to similar systems made using PMTs or PSPMTs. The single-wire connection through PoE also facilitates easy manufacturing of large-scale radiography panels with COTS networking equipment. This feature means the only limiting factor as to the size of the radiography panel is the number of PoE ports available, which can be increased by adding more switches. Data collection with the ROSSPAD also facilitates the ability to perform particle counting imaging. While photon counting imaging has been around since the 1980’s [41], neutron counting imaging is a relatively new process that requires more advanced neutron sources [42]. Particle counting is able to separate individual events compared to integrating everything together, allowing for a reduction in the noise present in a radiograph.

2.1.3 Disadvantages

The ROSSPAD readout module has two disadvantages. SiPMs tend to have higher electronic noise and temperature sensitivity compared to their traditional PMT counterparts [43][33]. The higher electronic noise reduces the signal-to-noise ratio (SNR) of each event, which lowers localization accuracy for a neutron counting system. Quality images need more data, and thus more time, compared to images made from other systems. Careful calibration of the data, which will be discussed in Chapter 3, is necessary to generate quality images.

Manufacturer-provided software written for the ROSSPAD module was relatively new when this research was performed. The IDEAS Testbench software was bound to Windows, did not support more than one module at a time, did not perform optimally, and used a proprietary binary file format. New methods had to be developed under a partnership with Dr. Nicole McFarlane and Matthew Smalley of the Min H. Kao Department of Electrical Engineering and Computer Science. New software was written to detect all ROSSPADs

on the network and can simultaneously configure and initialize every module. While this capability was necessary in the long run, especially for the full panel system, the time and effort needed to develop the software took away from time that could have been spent better characterizing the individual ROSSPAD modules.

2.2 Full Panel Construction

For a full-panel radiography system to be portable, a housing system must be constructed so that ROSSPADs can be easily transported from location to location. The SiPM array requires housing to be light-tight so that only scintillation light from radiation interaction events are recorded. Mounting the ROSSPADs is easy because the module has four threaded mounting posts and only a single Ethernet port must be available. Additionally, the housing must allow for the ROSSPADs to be cooled. A single ROSSPAD uses approximately 4.5 watts of power, which when scaled to a full 36-ROSSPAD panel consumes approximately 160 watts. While a single ROSSPAD does not produce a significant amount of heat, a full-sized panel of 36 ROSSPADs collectively requires forced-air cooling.

An aluminum housing was built by Chloe Browning for the 36-ROSSPAD panel. The housing measures 34.4 cm high, 37.8 cm wide, and 9.1 cm deep. The front half of the housing features a solid aluminum lid that is screwed onto the face of the housing, covering the SiPM boards. To keep this section light tight, a foam gasket material is placed between the SiPM boards and the rest of the ROSSPADs, held in place between the lid and the remaining housing. Six inlet and six outlet Noctua NF-A4x20 fans flow air over all 36 ROSSPADs, with each fan capable of a maximum airflow of 9.4 cubic meters per hour [44]. Holes on the back of the panel allow access to every Ethernet port. Both the lid and the remainder of the housing have mounting points that work for both machined aluminum handles and for a large, machined aluminum base plate. Overall, the device weighs approximately 14.6 kg, making it man-portable. Figures 2.3 and 2.4 are photographs of the front and back of the housing when fully assembled, with additional photos shown in Appendix B.

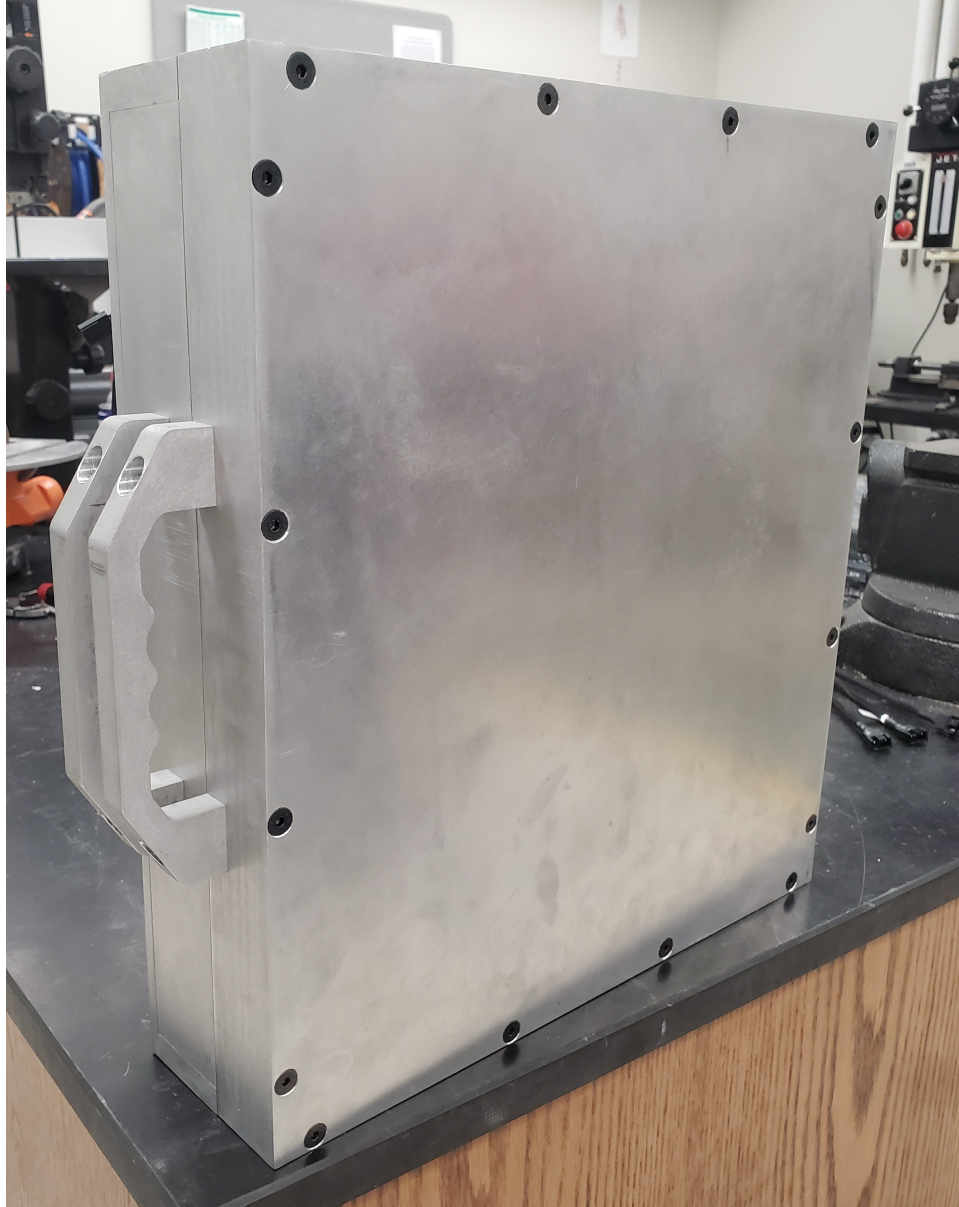


Figure 2.3: Photograph of the front of assembled full-panel housing, designed and manufactured by Chloe Browning.

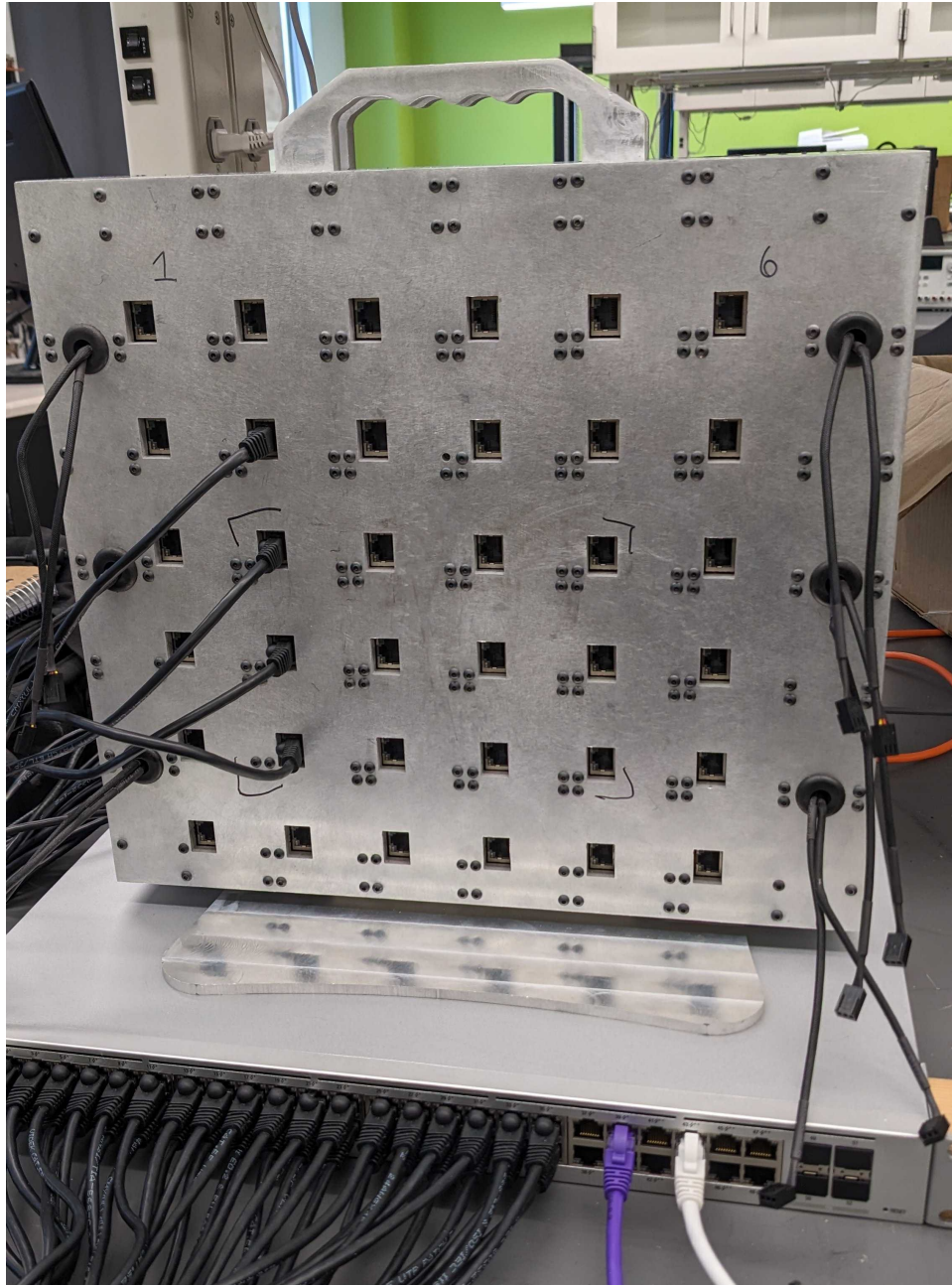


Figure 2.4: Photograph of the back of assembled full-panel housing, designed and manufactured by Chloe Browning. Some Ethernet cables have been plugged in as a demonstration.

2.3 Data Collection and Storage

2.3.1 Data Acquisition Process

Data connection can be done using a direct Ethernet connection to either a single ROSSPAD or through a PoE switch connected to a large panel of ROSSPADs. Figure 2.5 shows a flow chart of the process for collecting data. There are two different methods to start up the ROSSPAD modules. One method uses the included Testbench software suite, and the other method was written by researchers in Dr. Nicole McFarlane’s group.

IDEAS Testbench Software

The first method to setting ROSSPAD registers and voltages is to use the included IDEAS Testbench software. The software is developed as a reference platform for communicating with the ROSSPAD architecture. Testbench contains Python integration that allows the user to run pre-made or custom scripts that set registers pertaining to the ROSSPAD itself, the 4 onboard ASICs, or the 64 individual SiPMs [45]. These registers include settings such as the triggering threshold (20 arbitrary units), shaping time (1600 ns), and operating voltage (26.5 V). A table of registers is provided to the user so that they can be set individually outside of the Python scripts. Testbench produces proprietary binary files containing data sent from the connected ROSSPAD device over User Datagram Protocol (UDP). Additionally, users are able to record data outside of Testbench using Wireshark or another packet capture software. A screenshot of Testbench is shown in Figure 2.6.

Testbench is only capable of communicating with a single ROSSPAD. It is not practical to use Testbench to connect to and initialize all 36 ROSSPADs in a full radiography panel. While it can be done, the process is sequential. The process takes approximately 5 minutes for each ROSSPAD. If Testbench is used for the full panel, this process would take 3 hours in total. Additionally, this process would be entirely manual, as each ROSSPAD must be individually connected to Testbench either through plugging in the ROSSPADs one by one or changing the IP address of the ROSSPAD in the Testbench configuration file.

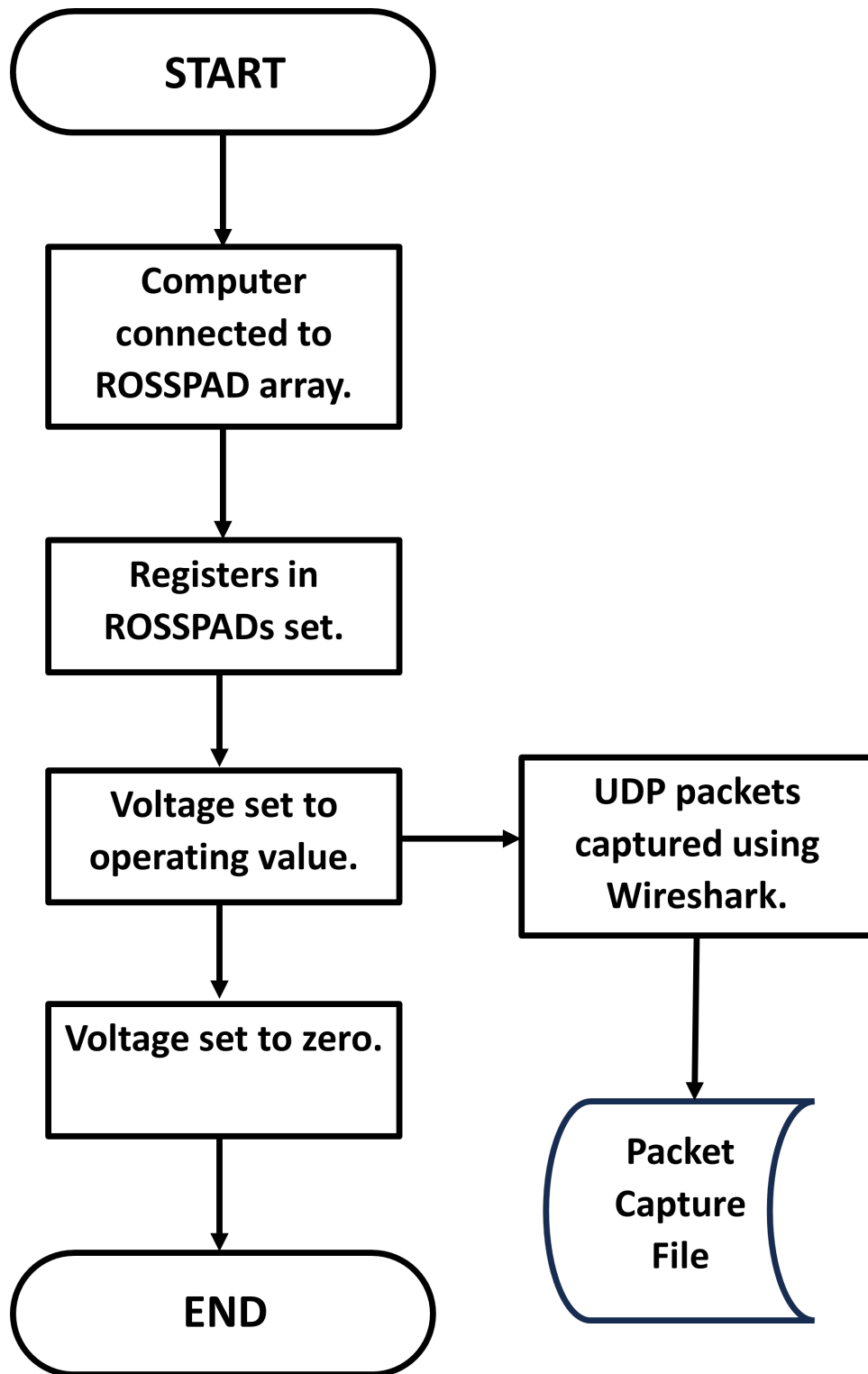


Figure 2.5: A flow chart demonstrating the process for collecting data using the IDEAS ROSSPAD.

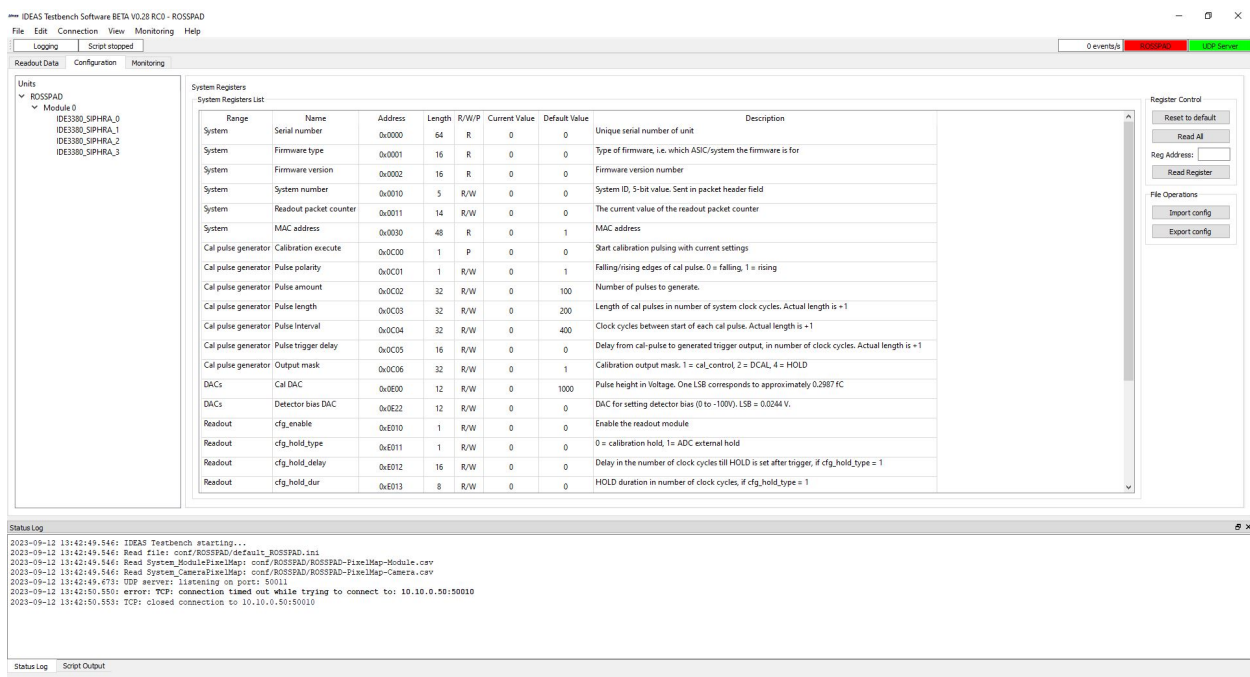


Figure 2.6: Screenshot of the Testbench software developed by IDEAS. The ASIC configuration tab has been selected.

Custom Startup Code

A custom startup script was written by Matthew Smalley under the direction of Dr. Nicole McFarlane. The script is written in JavaScript and replicates the Testbench ROSSPAD API to directly set registers over a single, bidirectional TCP connection. These scripts are executed from a command-line interface. The biggest advantage is that 36 copies of the script can be executed simultaneously. This significantly cuts down on the initialization time for the radiography panel.

2.3.2 Packet Capture (.pcap) Files

Each scintillation event is asynchronously sent to the computer in a UDP packet. These UDP packets are 200 bytes long. The first 72 bytes contain information about the packet's origin, destination, and other needed values, and the final 128 bytes contain the data from each of the 64 SiPMs on the ROSSPAD. Additionally, packet capture files save a timestamp of when each packet reached the computer's network interface that is not a part of the packet structure. These timestamps are saved and added to the collection of data. Table 2.1 shows the UDP packet structure.

UDP packets can be collected by any libpcap-compatible packet capture program [46]; for this research, Wireshark was selected as the tool for data collection [47]. Wireshark operates similarly to many command line packet capture programs, but additionally offers a graphical user interface (GUI) to make data collection easier for the user [47]. Once packets have been collected into a single .pcap file, the data stream can be replayed and reprocessed as many times as necessary. The first step in the processing routine is to extract the data from each individual UDP packet and store it into a raw data table in a SQLite database.

2.3.3 SQLite Database Structure

Data from this research is stored in different tables of a single SQLite database. SQLite is a library for C and C++ that allows for communication with a light, file-backed SQL database without the need for a fully featured SQL network server [48]. Tables within SQLite can contain a wide variety of data forms, such as integer values, floating point values, text, and

Table 2.1: ROSSPAD UDP Data Packet Structure

Byte Range	Description of Data
1-6	Destination MAC Address
7-12	Source MAC Address
13-14	Ethernet Type
15	Version and Length
16	Differentiated Services Field
17-18	Total Length
19-20	Identification
21-22	IP Flags
23	Time to Live
24	Protocol
25-26	Header Checksum
27-30	Source IP Address
31-34	Destination IP Address
35-36	Source Port
37-38	Destination Port
39-40	UDP Segment Length
41-42	Checksum
43-72	Payload Header
73-200	SiPM Signals

data blobs. SQLite is the most-used database engine in the world, is built into Python, and can be accessed with standalone programs such as DB Browser for SQLite [49]. A screenshot of a SQLite database table used in this research can be found in Figure 2.7.

2.4 Image Generation Software

Data from the raw packet capture file is extracted and stored into two raw data tables in SQLite. One table saves the data for the raw image data, and one table saves the raw data for a detector flood field used in the calibration step. The structures of the SQLite tables are shown in Table 2.2. The index of the event, the MAC address, MAC number (an integer representation of the MAC address), packet timestamp, device timestamp, payload header, and raw SiPM signals are saved for later use. Saving the raw data to the SQLite database makes reprocessing of events faster, since the .pcap files do not need to be reopened every single time a new image is generated.

After raw data has been extracted, the flood field SiPM values are used to generate the calibration values shown in Table 2.3. The raw data from the flood field is used to generate electronic background, electronic noise, and gain values for each SiPM on each ROSSPAD. This process is described in detail in Chapter 3. Events from the raw image data table are extracted, calibrated, and then saved into a new, calibrated data table.

ROSSPAD locations are read from a comma-separated values (CSV) file. The minimum and maximum x and y position along with the ROSSPAD MAC number are stored in a SQLite table shown in Table 2.4. Calibrated data is used with the relevant ROSSPAD locations to determine the x and y position of each event. Two versions of the SQLite data table have been included in Table 2.4. Older versions of the image generation software included more columns for event position calibration. Newer versions perform much of the event position generation in the same step, reducing the need for extra event position columns.

Event positions pulled from the SQLite database are used to generate two versions of the radiograph. One image is generated by adding up the total events within a given pixel of the image. The other image works similarly, but adds up the total signal values within each

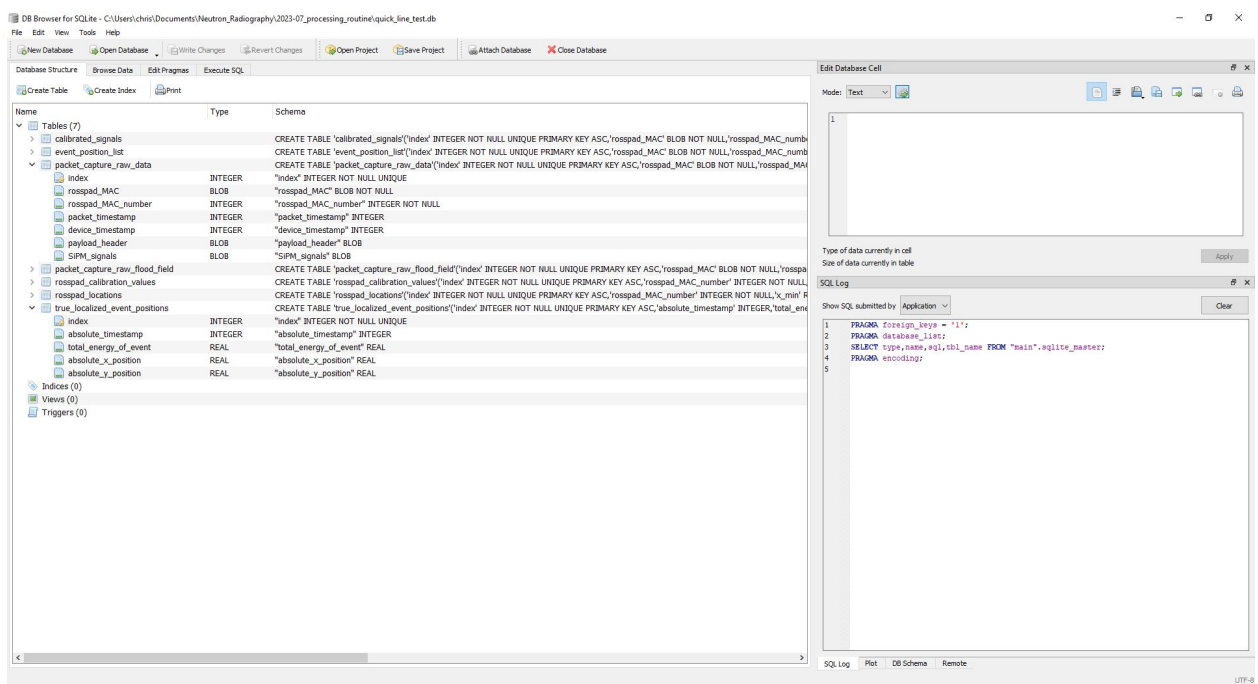


Figure 2.7: Screenshot of the DB Browser for SQLite software, with tables expanded to show structure.

Table 2.2: Raw Data Table Structures in SQLite

Data Table	Column	Type
Packet Capture Raw Data	Index	Integer
	ROSSPAD MAC Address	Blob
	ROSSPAD MAC Number	Integer
	Packet Timestamp	Integer
	Device Timestamp	Integer
	Payload Header	Blob
	SiPM Signals	Blob
Packet Capture Raw Flood Field	Index	Integer
	ROSSPAD MAC Address	Blob
	ROSSPAD MAC Number	Integer
	Packet Timestamp	Integer
	Device Timestamp	Integer
	Payload Header	Blob
	SiPM Signals	Blob

Table 2.3: Calibration Values and Calibrated Signals Table Structures in SQLite

Data Table	Column	Type
Calibration Values	Index	Integer
	ROSSPAD MAC Number	Integer
	Response Histogram	Blob
	Response CDF	Blob
	Response Histogram String	Text
	Response CDF String	Text
	Electronic Background String	Text
	Electronic Noise String	Text
	Gain Factor String	Text
	Full Device Gain	Double
	Electronic Background	Blob
	Electronic Noise	Blob
	Gain Factor	Blob
Calibrated Signals	Number of Triggers per SiPM	Blob
	Index	Integer
	ROSSPAD MAC Address	Blob
	ROSSPAD MAC Number	Integer
	Absolute Timestamp	Integer
	Calibrated SiPM Signals	Blob
	Total Signal	Real
	Noise Floor per SiPM	Blob

Table 2.4: Image Generation Table Structures in SQLite

Data Table	Column	Type
ROSSPAD Locations	Index	Integer
	ROSSPAD MAC Number	Integer
	ROSSPAD X Position Minimum	Real
	ROSSPAD X Position Maximum	Real
	ROSSPAD Y Position Minimum	Real
	ROSSPAD Y Position Maximum	Real
Event Position List (Version 1)	Index	Integer
	ROSSPAD MAC Address	Blob
	ROSSPAD MAC Number	Integer
	Absolute Timestamp	Integer
	Total Event Energy	Real
	Relative X Position	Real
	Relative Y Position	Real
	Calibrated X Position	Real
	Calibrated Y Position	Real
	Absolute X Position	Real
	Absolute Y Position	Real
Event Position List (Version 2)	Index	Integer
	Absolute Timestamp	Integer
	Total Event Energy	Real
	Absolute X Position	Real
	Absolute Y Position	Real

pixel. The images are written in continuous space, allowing them to vary in pixel density with a simple command. Once the size of the image is determined, a linear memory space is allocated and filled from localized positions. The linear memory space is then written into a text image file, which can be opened with ImageJ, an image processing software developed by the National Institutes of Health [50]. Both images with and without markings for the boundaries of SiPMs can be generated.

ImageJ can also be used to further manipulate the image to the needs of the operator [50]. Image color scheme, brightness, and contrast all provide the user with an easy method for generating the most clear image possible. Averaged profiles across the abscissa and ordinate of an image can be extracted easily, allowing for profiles of various features to be processed in other programs such as Excel or custom Python scripts. Various math functions can be applied to the image, including log scaling, normalization, and image weighting using a second, equally-sized image. Images can also be transformed, cropped, or combined, similar to the functions of many other COTS image processing programs.

Several debug images can be generated using a variety of additional helper functions developed during the process of this research. For example, one script produces images of the SiPM responses for a given packet with the predicted position overlaid with a red cross. Other scripts include generating histograms of SiPM responses, building maps of calibration values, generating full-panel SiPM response grids, and much more.

Chapter 3

Data Calibration

3.1 Single ROSSPAD Data Calibration

3.1.1 Calibration Process

A single ROSSPAD uses a unique calibration process. Since the IDEAS ROSSPAD lacks suitable connections for quantifying the noise terms throughout the electronics stack, and appears to have no method for determining dark noise, a new calibration method was developed. This method uses an even distribution of radiation events across the face of the detector to determine background, noise, and gain terms necessary to produce quality images.

First, a flood field is generated using the same particle type used for the image being processed. Next, histograms of the raw data on all 64 SiPMs are generated using the flood field data and then smoothed using a moving-average function to make finding peak values easier. An example smoothed histogram is shown in Figure 3.1. Based on this histogram, the electronic background and electronic noise are determined. The center of the Gaussian peak on the leading edge of the histogram is described as the electronic background, and the width of the peak is the electronic noise. Dark noise is a major component of the Gaussian curve, in addition to the noise terms introduced from all of the components of the electronics stack that generate the SiPM signals. Values lower than the background and noise cutoff are removed from the raw histogram. Cumulative density functions (CDFs) for each SiPM

are then generated based on this new corrected histogram. These CDFs are then used to generate gain correction values for each SiPM. Background, noise, and gain values are then saved into memory, and the code applies these values to the SiPMs when preparing the raw image data for later use.

Calibration of the ROSSPAD detectors is performed with same settings as used in single and multi-ROSSPAD image generation. For the single ROSSPAD, the shaping time was set to 1600 ns, the triggering threshold was set to 28 arbitrary units, and the bias voltage of the SiPMs was set to 16.5 V. For the mutli-ROSSPAD calibration steps, the shaping time and voltage stayed the same, but the triggering threshold was lowered from 28 to 20 arbitrary units.

3.1.2 Electronic Background and Noise Removal

Electronic background and electronic noise for each SiPM is corrected using the following equation:

$$C_n = R_n - (B_n + N_n) \quad (3.1)$$

where R_n is the raw signal from an event on SiPM n , B_n and N_n are the electronic background and electronic noise of SiPM n , and C_n is the corrected signal. The center of the Gaussian shape on the left edge of the curve is set as the electronic background for the SiPM. To find the electronic noise of the system, the distance in bin number was determined between the center of the peak and the point in the Gaussian that is n^{th} percentile of the shape on the left hand side is found. Both the electronic background and electronic noise are then subtracted from the raw data stream. If a signal falls below the zero bin, it is set to zero. Figures 3.2 and 3.3 show the electronic background and electronic noise on a single ROSSPAD for an example experiment.

3.1.3 Gain Correction

After the raw signal is electronic background and electronic noise corrected, it must be gain corrected so that the same amount of light received by two different SiPMs will be read out

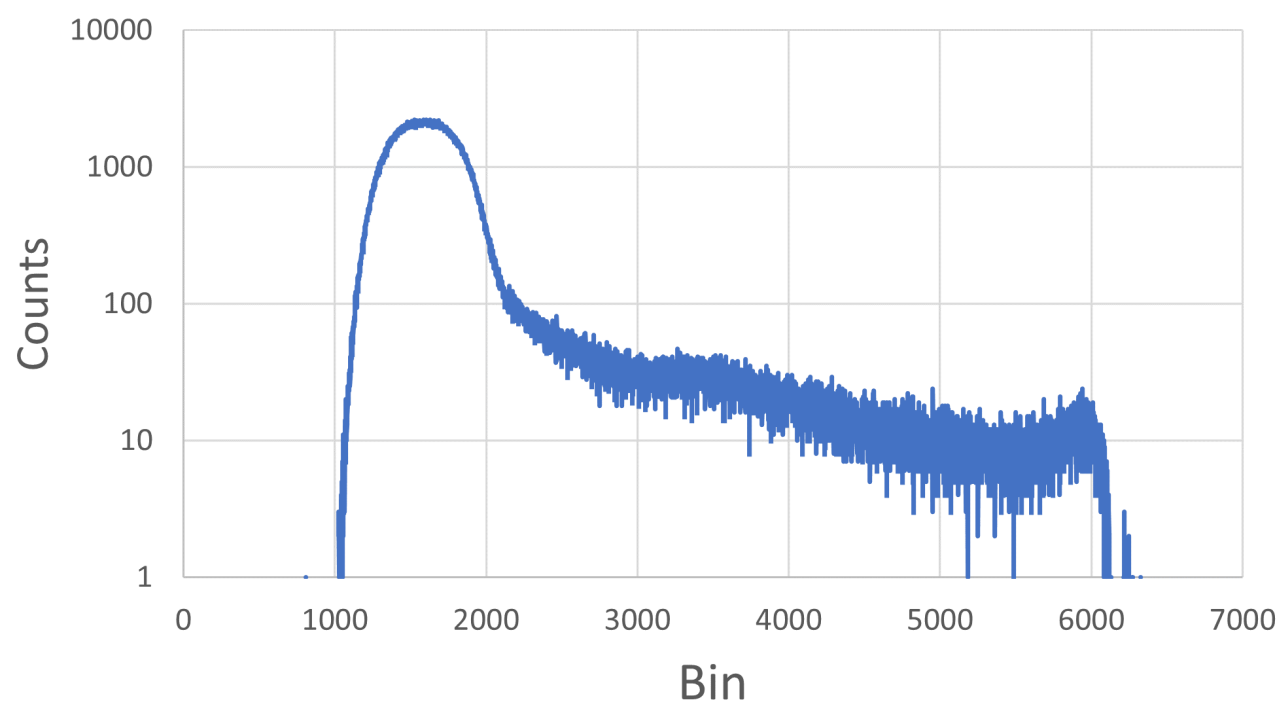


Figure 3.1: A sample uncorrected signal histogram from a flood field image.

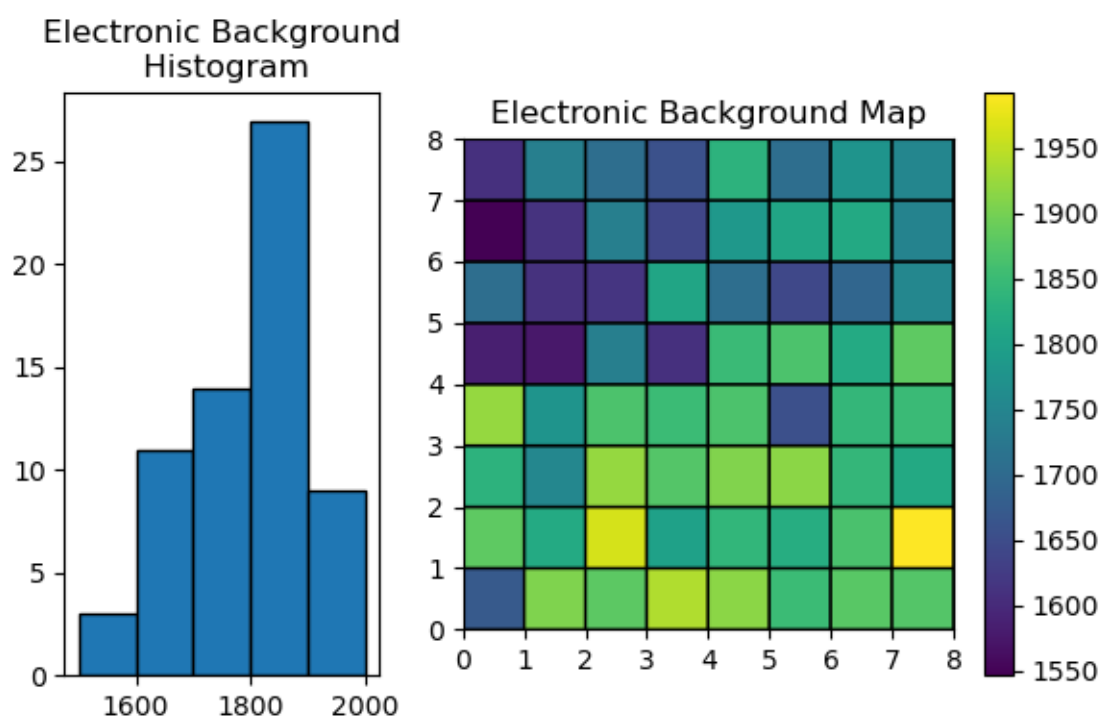


Figure 3.2: A histogram and map of the electronic background values for an example neutron flood field measurement.

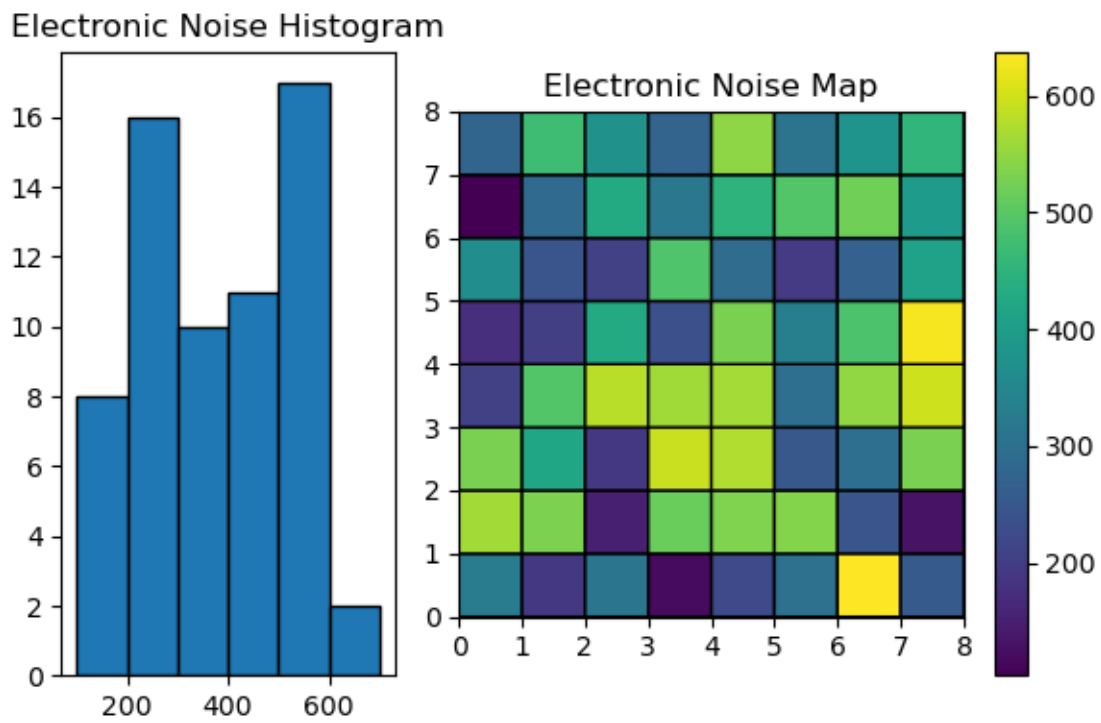


Figure 3.3: A histogram and map of the electronic noise values for an example neutron flood field measurement.

as the same signal. The equation

$$G_{avg} = \frac{\sum_{n=1}^N U_n - L_n}{N} \quad (3.2)$$

generates the average gain across the entirety of a ROSSPAD system using the cumulative distribution function (CDF) generated from each corrected SiPM. In equation 3.2, U_n and L_n are the spectral bins at the upper and lower percentiles for SiPM n and N is the number of SiPMs on the board. For the ROSSPAD, this number is 64. The lower and upper bounds can be set independently for each experiment to generate the clearest image possible. Equation 3.2 is then used to find the individual gain of each SiPM. Figure 3.4 shows the gain for each SiPM on a single ROSSPAD for an example experiment.

$$G_n = \frac{U_n - L_n}{G_{avg}}. \quad (3.3)$$

Gain, background, and electronic noise for each SiPM on each ROSSPAD are stored in their own SQLite data table, allowing for the calibration values to be reused in other sets of data if required.

Using equation 3.3 and the background and electronic noise, each individual event is calibrated on a per-SiPM basis using equation 3.4:

$$S_n = \frac{R_n - (B_n + N_n)}{G_n} \quad (3.4)$$

Once the data has been calibrated and corrected, it is stored in a SQLite table for storage and use later in the code.

3.2 Multi-ROSSPAD Data Calibration

3.2.1 Calibration Process

Muti-ROSSPAD data calibration follows nearly the exact same process as the single ROSSPAD calibration, with a few minor changes:

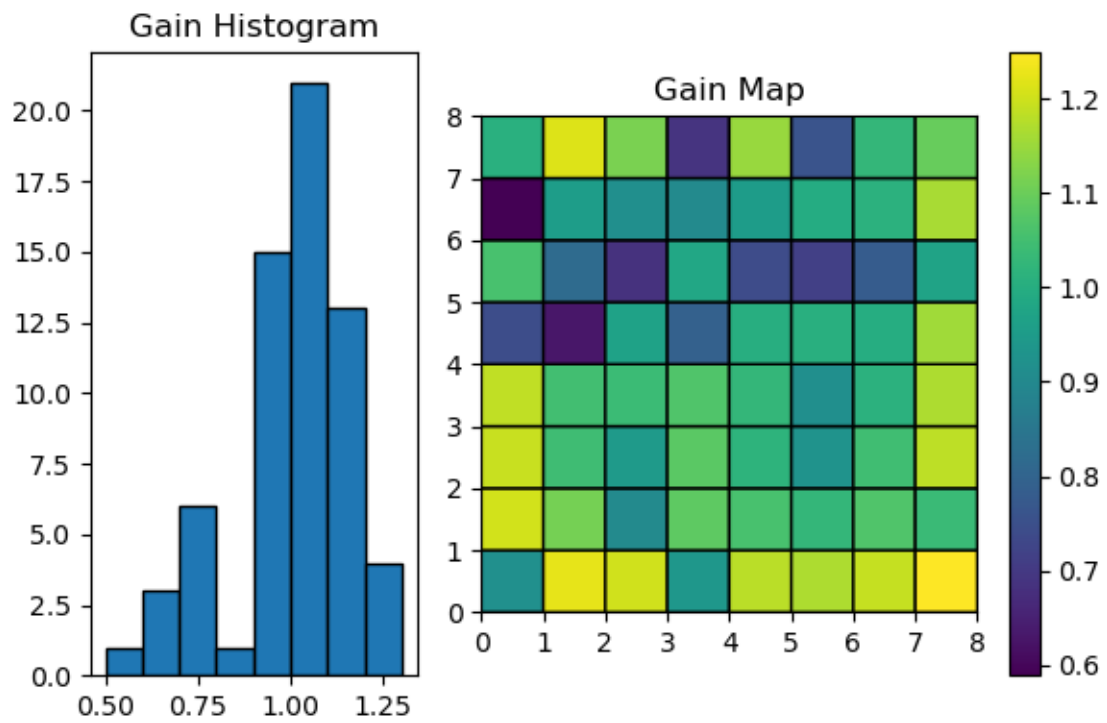


Figure 3.4: A histogram and map of the gain values for an example neutron flood field measurement.

1. ROSSPADs must be checked for defects/broken systems before calibration, as broken SiPMs or ROSSPADs will negatively impact the calibration values of working ROSSPADs.
2. Background and noise values are determined independently of the other ROSSPADs, where gain correction values are scaled by the average gain value across all SiPMs within a radiography panel

3.2.2 Determination of Malfunctioning ROSSPADs

Calibration on a multi-ROSSPAD panel requires more careful consideration to the settings and selection of detectors used. To understand the performance of all 36 detectors used in the first-of-a-kind panel, a flood field was taken with all of the ROSSPADs set to default settings. Figure 3.5 shows the electronic background values for each SiPM of the 36-ROSSPAD radiography panel. One of the SiPMs appears to have a significantly higher electronic background than the rest of the panel, similar to the one shown in Chapter 4. The same background data was plotted in Figure 3.6, but with the single high-triggering SiPM removed. More things become apparent once the scale is adjusted. First, there appear to be a few darker SiPMs indicating a significantly lower background value compared to the rest of the panel. Secondly, there are seven ROSSPADs (including the previously mentioned one) that have an average background value lower than the average of the other ROSSPADs. This is further demonstrated in the map of the noise values for the entire panel, shown in Figure 3.7, where the ROSSPADs with low background levels appear to have elevated noise values.

The large number of broken ROSSPADs (9 out of 36) means that a full-panel system will have to be smaller than initially planned for. To create a more uniform image, a smaller, 4 by 3 area has been selected for making multi-ROSSPAD radiographs. A rough example of where these ROSSPADs sit within the full panel are shown in Figure 3.8, where used ROSSPADs are shaded in green and unused ROSSPADs are shaded in red. While this area does include one broken ROSSPAD, the SiPM in question can be easily removed during image processing,

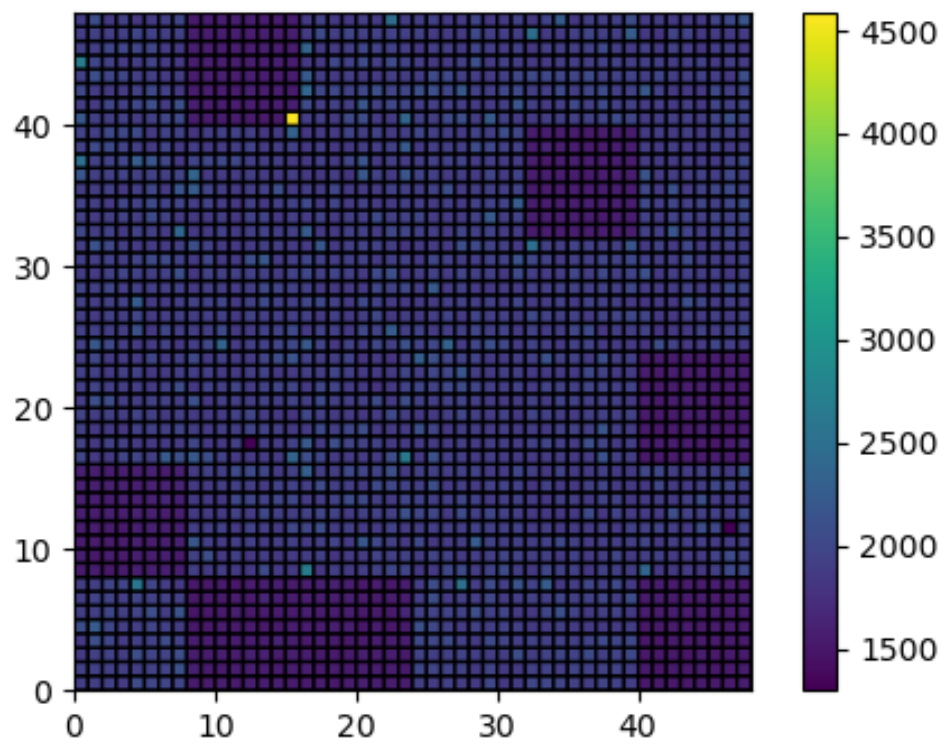


Figure 3.5: A map of electronic background values of the SiPMs on the full radiography panel.

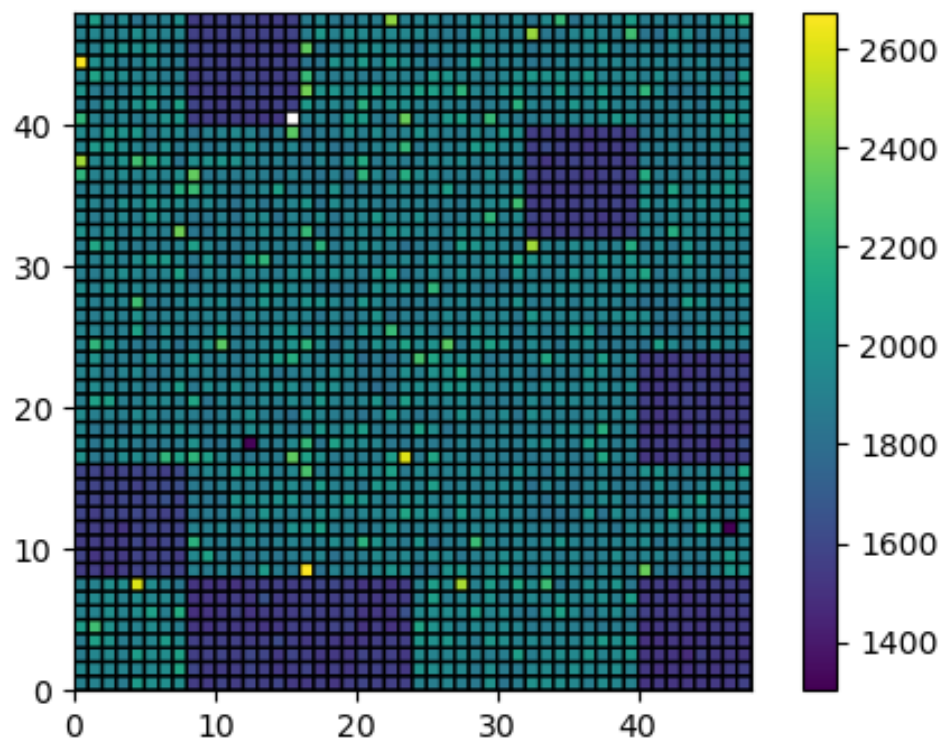


Figure 3.6: A second map of electronic background values of the SiPMs on the full radiography panel, with the broken SiPM filtered out of the image.

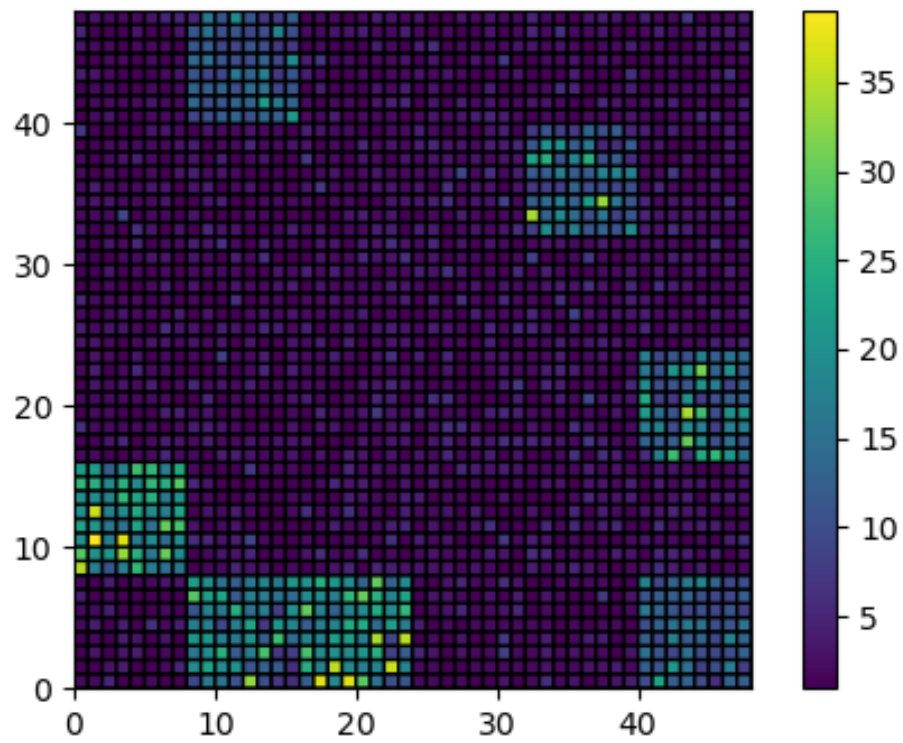


Figure 3.7: A map of electronic noise values of the SiPMs on the full radiography panel.

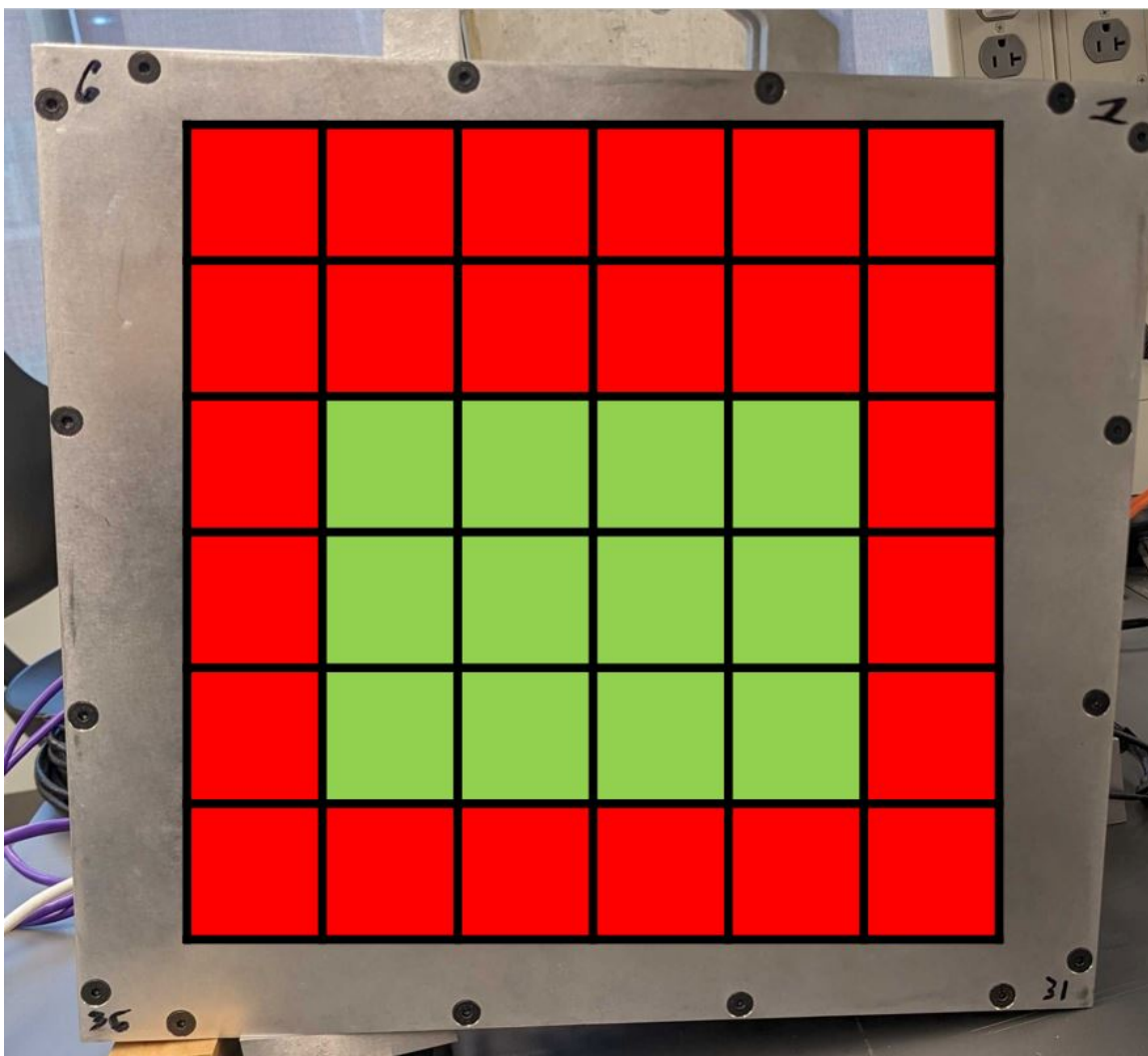


Figure 3.8: Locations of the ROSSPADs selected for 4 by 3 area image.

and it does not constantly trigger and add extra noise to the data collection. Analysis of the broken ROSSPADs both in the panel and outside of it can be found in Chapter 4.

3.2.3 Electronic Background and Noise Removal

Using the same techniques for a single ROSSPAD, background and noise maps were generated for this reduced area image using a flood field of a Cf-252 source. Figures 3.9 and 3.10 show somewhat even distribution of background and noise across the entire face of the panel.

3.2.4 Gain Correction

As previously stated, gain calibration is slightly different compared to calibration on a single ROSSPAD. Equations 3.2 and 3.3 still apply, though the average is performed across all of the SiPMs in the entire panel (768 SiPMs for a 4 by 3 ROSSPAD panel) compared to the smaller 64 SiPMs of a single ROSSPAD. Gain values for the 4 by 3 panel are shown in Figure 3.11.

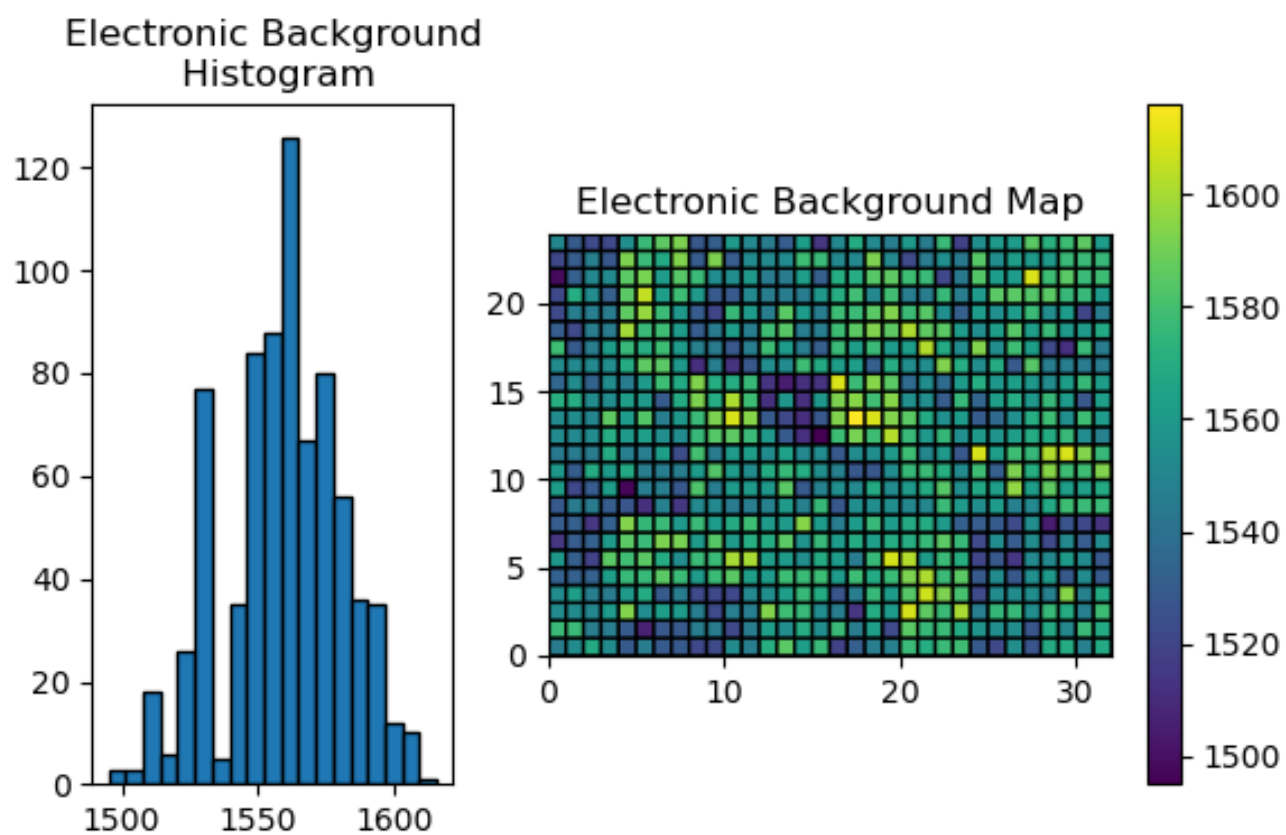


Figure 3.9: A histogram and map of the electronic background values for an example neutron flood field measurement on the multi-ROSSPAD system.

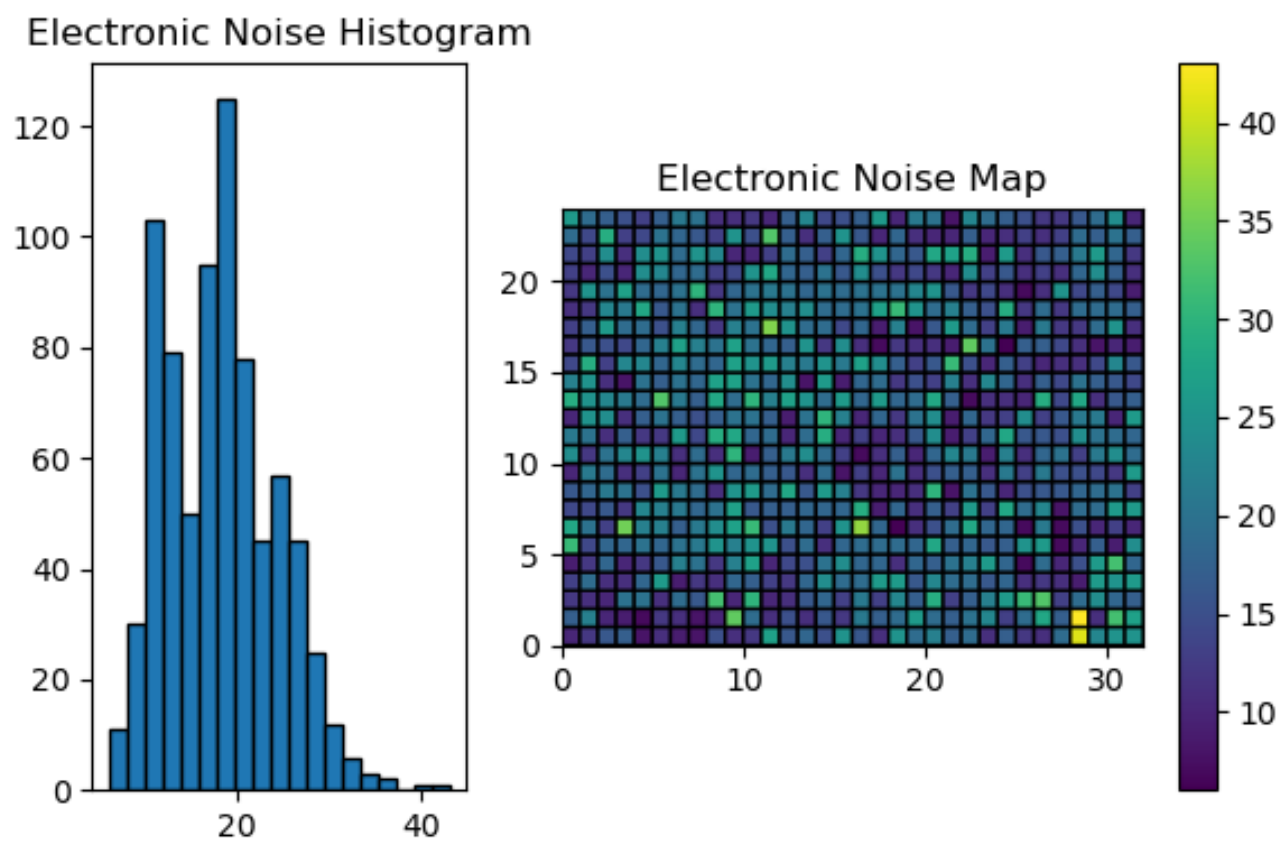


Figure 3.10: A histogram and map of the electronic noise values for an example neutron flood field measurement on the multi-ROSSPAD system.

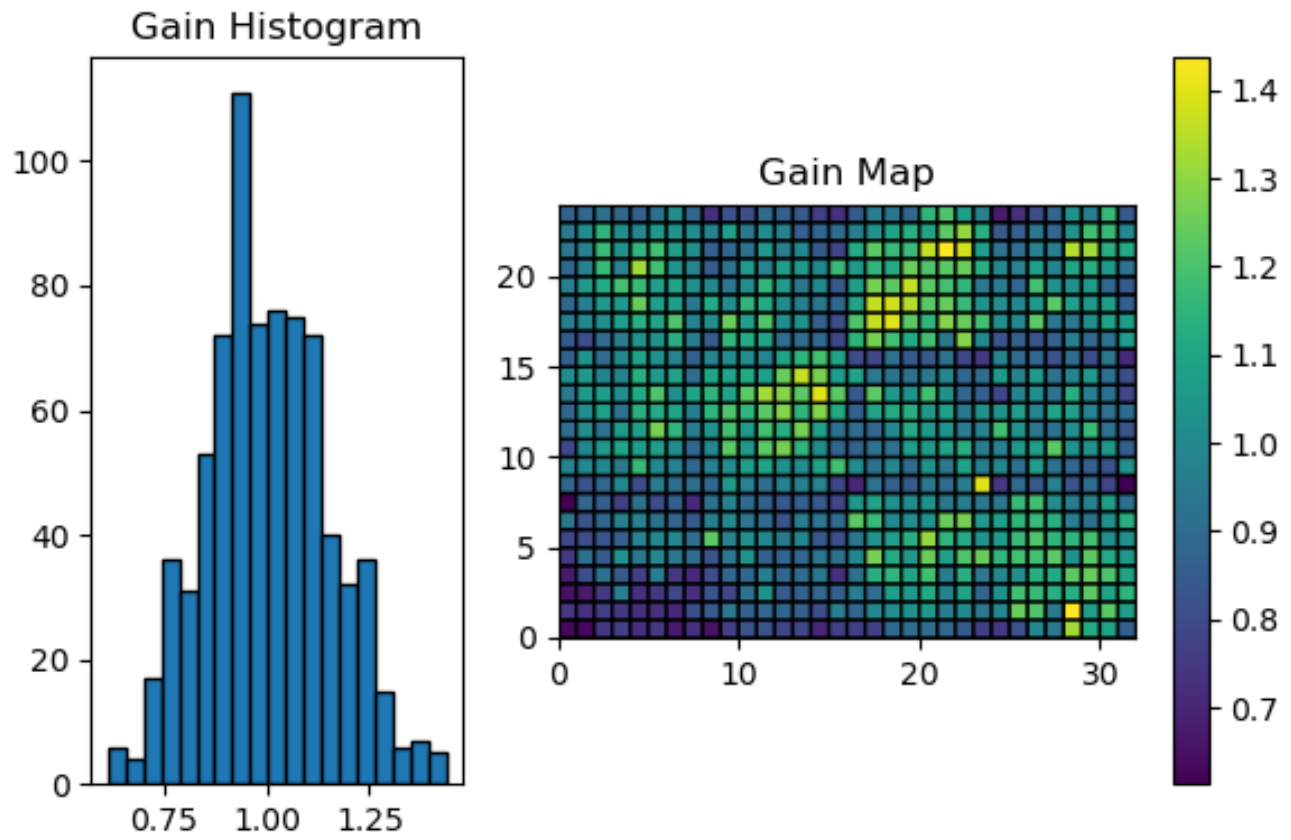


Figure 3.11: A histogram and map of the gain values for an example neutron flood field measurement on the multi-ROSSPAD system.

Chapter 4

Quality Assurance of ROSSPAD Detectors

4.1 Failure Modes

Throughout this research, several detector modules experienced some form of failure that resulted in the detectors themselves not operating normally. Out of 38 ROSSPAD detectors tested throughout the course of this project, 11 of them appeared to have some form of issue with the SiPM board or the ROSSPAD module itself. From these 11 broken detectors, 5 unique failure modes were discovered. While some failure modes can be easily accounted for (single ROSSPAD imaging was performed on a faulty detector long before it was known to be faulty), some would require the complete removal of the detector from the pool of detectors. This section seeks to demonstrate the various failure modes and how one can determine if a detector is broken in that way and how it can be resolved.

Figure [4.1](#) demonstrates the raw signal histograms for all 64 SiPMs on a working ROSSPAD. These histograms were generated from 1.4 million packets using a 0.105 mCi Cs-137 gamma source placed approximately 10 centimeters from the face of the detector. The overlaid histograms of a working ROSSPAD should have a semi-Gaussian curve at the lowest values on the curve. The curve then follows a linear trend on a semilog plot until around the 4000 ADC unit mark, where the curve bends towards the zero mark slightly

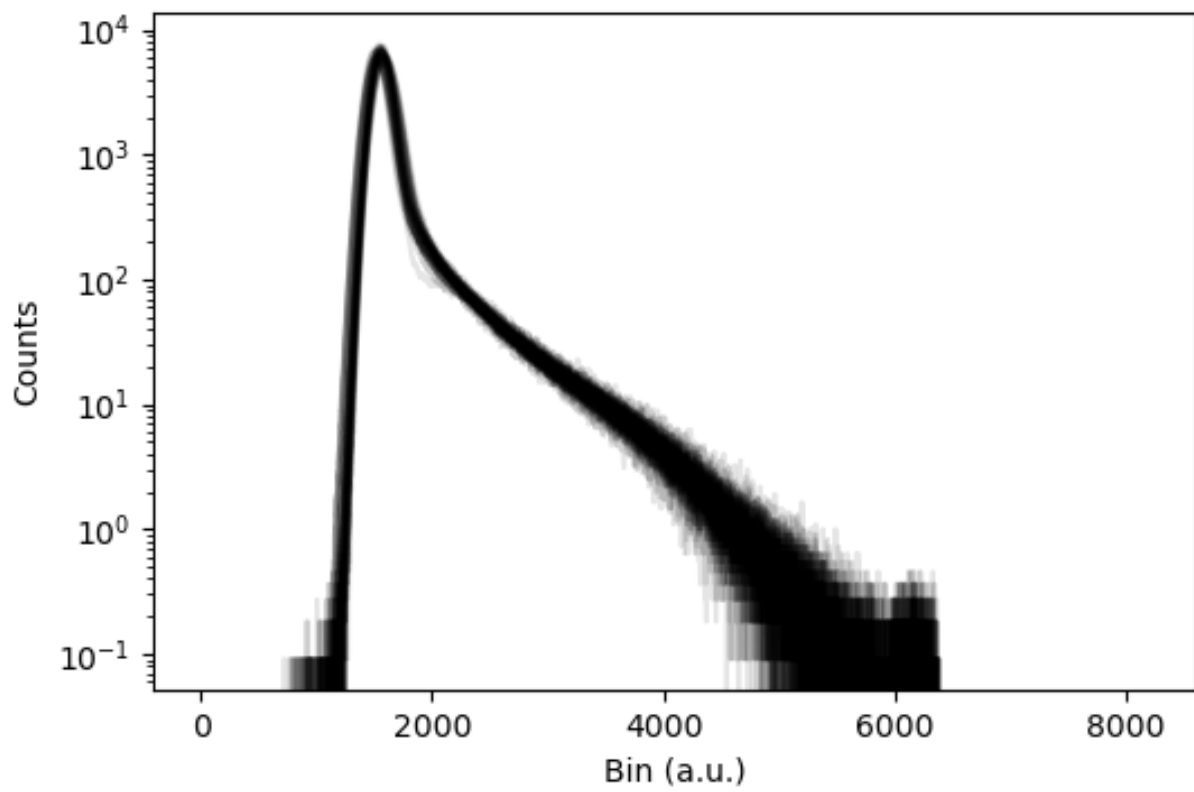


Figure 4.1: Uncorrected histograms of the 64 SiPMs on a working ROSSPAD. ($N = 1.4 \times 10^6$ counts)

above 6000 ADC units. Similar figures of each failure method have been provided so that a clear determination of the failure mode can be made.

4.1.1 Single High-Trigger SiPM

Some ROSSPAD detectors have a single SiPM out of the 64 total that tends to trigger more often than their counterparts, despite the same triggering threshold value set in the registers. Based on the raw SiPM histograms for one of these detectors, it was found that the SiPM has a high number of counts at a high signal level, as shown by the singular light grey histogram in Figure 4.2. Because this SiPM tends to dominate any event that is recorded by the ROSSPAD, and the ROSSPAD does not allow for individual SiPMs to be switched off, this ROSSPAD has to be removed entirely from the pool of detectors until a fix can be made.

It may be possible to fix this ROSSPAD by just replacing the SiPM board itself. However, this ROSSPAD was installed into the larger panel before quality assurance testing was performed, and was therefore unable to be removed at the time. Further testing may prove that replacing the SiPM board will fix the issue completely, reducing the cost of replacement significantly.

4.1.2 Single Low-Trigger SiPM

Similarly to the high-triggering ROSSPAD, some ROSSPADs have SiPMs that tend to trigger lower than the remaining bunch, as shown in Figure 4.3. In this case, the low-triggering SiPM follows the same trend as the rest of the SiPMs at lower signal values, but falls short of where the rest of them end on the graph. Changing detector gain settings within the ROSSPAD registers may fix the issue if the gain could be changed on a SiPM-by-SiPM basis. However, the gain registers are an ASIC-level register; if the gain register is changed to fix the one broken SiPM, the 15 other SiPMs on the same ASIC will be shifted upward. The calibration code in Chapter 3 will fix the disproportionate signal. The SiPM does also have fewer triggers than the rest, which could lead to defects within generated imaged. As stated before, this ROSSPAD may be fixed by changing the SiPM board, though this wasn't able to be tested

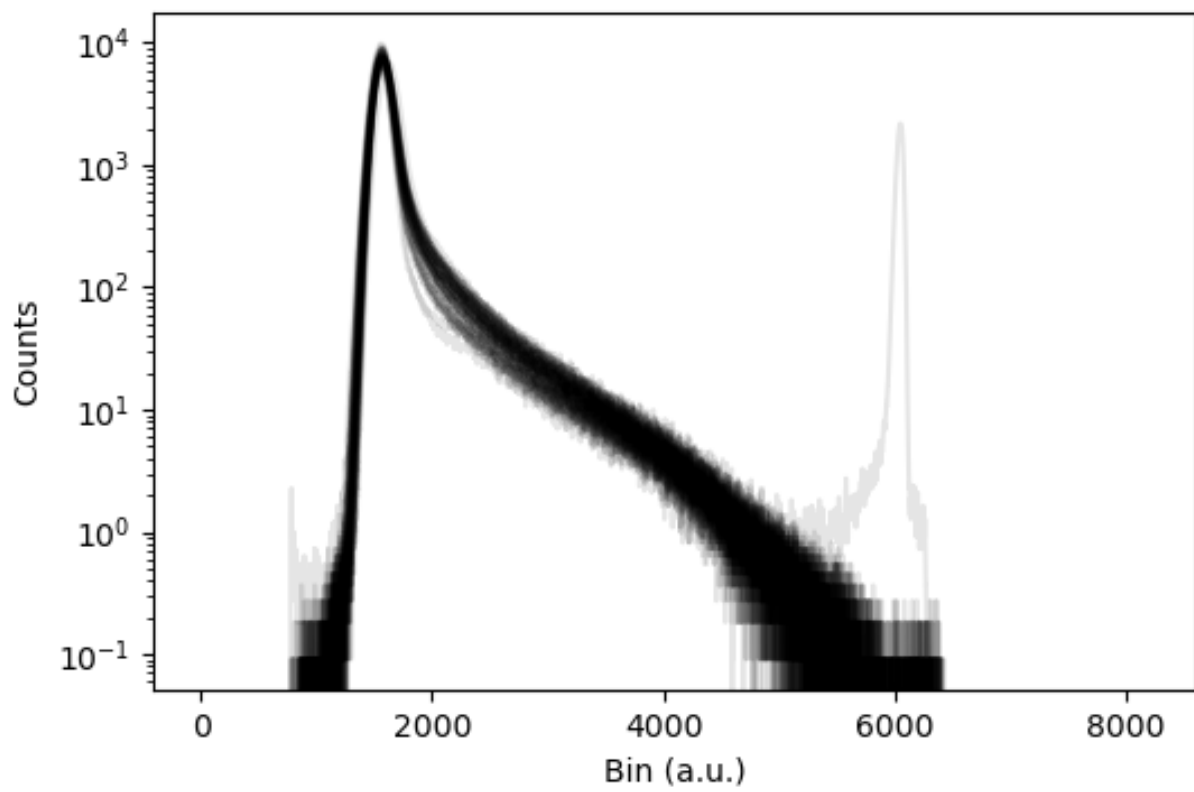


Figure 4.2: Uncorrected histograms of the 64 SiPMs on a ROSSPAD with one SiPM's electronic background value significantly higher than the remaining SiPMs.

as it was added into the panel. Since this SiPM isn't dominating the events the ROSSPAD records, this ROSSPAD can be kept within a radiography panel, though there will appear to be a lack of events in the vicinity of the SiPM.

4.1.3 High Electronic Noise

The third failure mode features a ROSSPAD in which the electronic background peak appears to be an order of magnitude larger than the start of the linear section of the graph compared to a correct histogram, shown in Figure 4.4. The high triggering rate and large electronic noise mean that these ROSSPADs need to be removed from the pool, as they will not be able to contribute to a clean image. Since this defect is uniform across all 64 SiPMs, it is unclear if changing the SiPM board will have a positive impact or not.

4.1.4 Unstable Trigger Point

Some ROSSPADs may fail by not having a stable triggering point. While the SiPMs in a ROSSPAD can read any light level, the ROSSPAD will not send out a data packet unless one of the SiPMs has reached a set triggering threshold. If this threshold is not stable, not only will there be instability in the raw data histograms, there will also be instability in the count rate. Figure 4.5 shows the raw signal histograms for a ROSSPAD found to have an unstable triggering point. The histograms themselves do not necessarily prove that the triggering point is unstable. Figure 4.6, however, shows that for an unchanging gamma source, the ROSSPAD with the unstable trigger will have points where it suddenly records more events per second than normal. This could be the result of many issues, including faulty electrical connections at any point within the ROSSPAD electronics stack.

4.1.5 Signal Level Drift

SiPMs, if not properly cooled, may encounter signal drift. Initial testing on a single ROSSPAD generated SiPM histograms that appear to look different than a nominal SiPM histogram from the full panel. Initially, it was assumed that this histogram was the correct response a ROSSPAD should have for a given gamma source, especially since the data

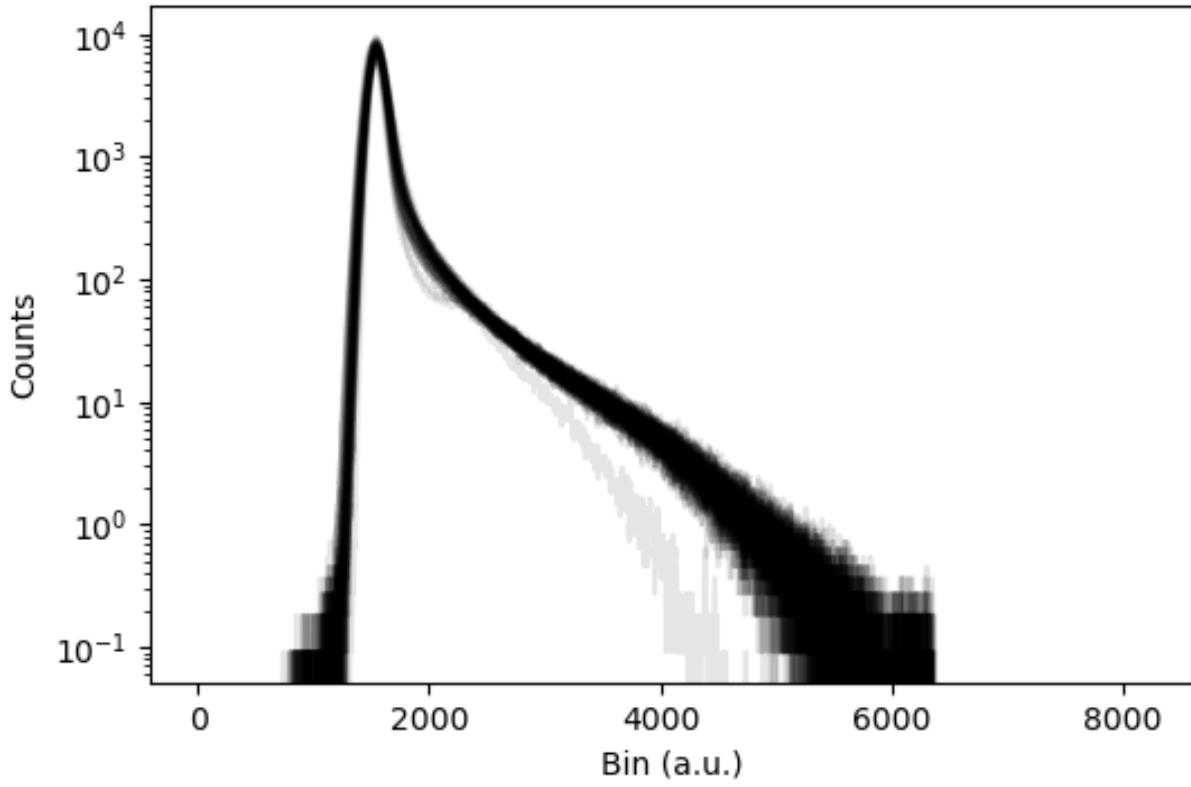


Figure 4.3: Uncorrected histograms of the 64 SiPMs on a ROSSPAD with one SiPM falling short of all of the rest of the SiPM histograms. ($N = 1.4 \times 10^6$ counts)

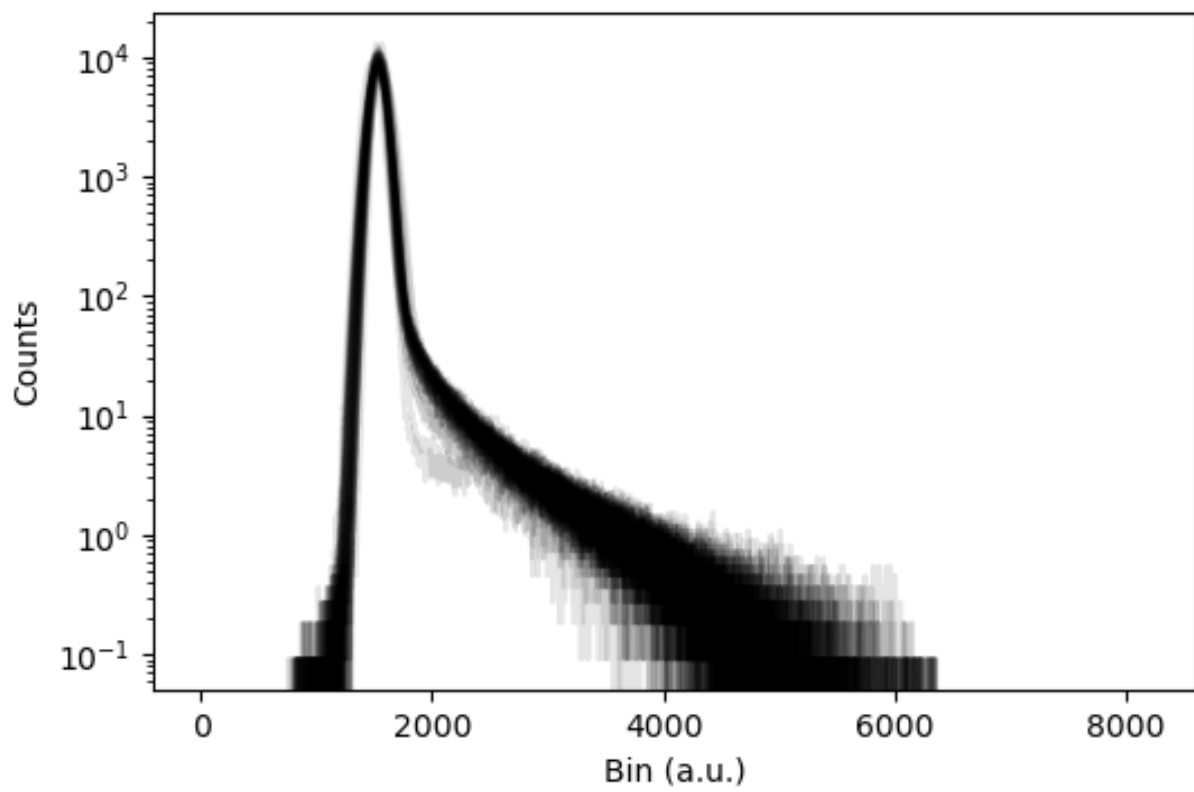


Figure 4.4: Uncorrected histograms of the 64 SiPMs on a ROSSPAD with high electronic noise. ($N = 1.4 \times 10^6$ counts)

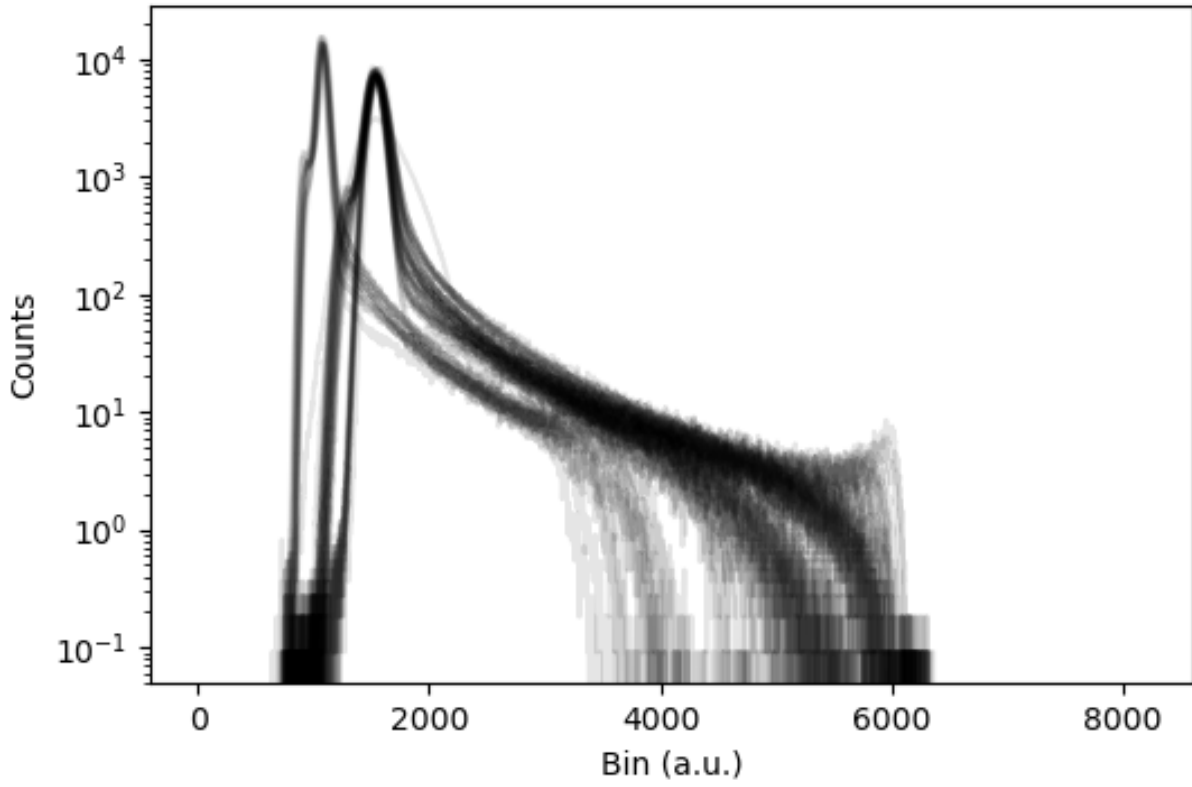


Figure 4.5: Uncorrected histograms of the 64 SiPMs on a ROSSPAD with unstable triggering level. ($N = 1.4 \times 10^6$ counts)

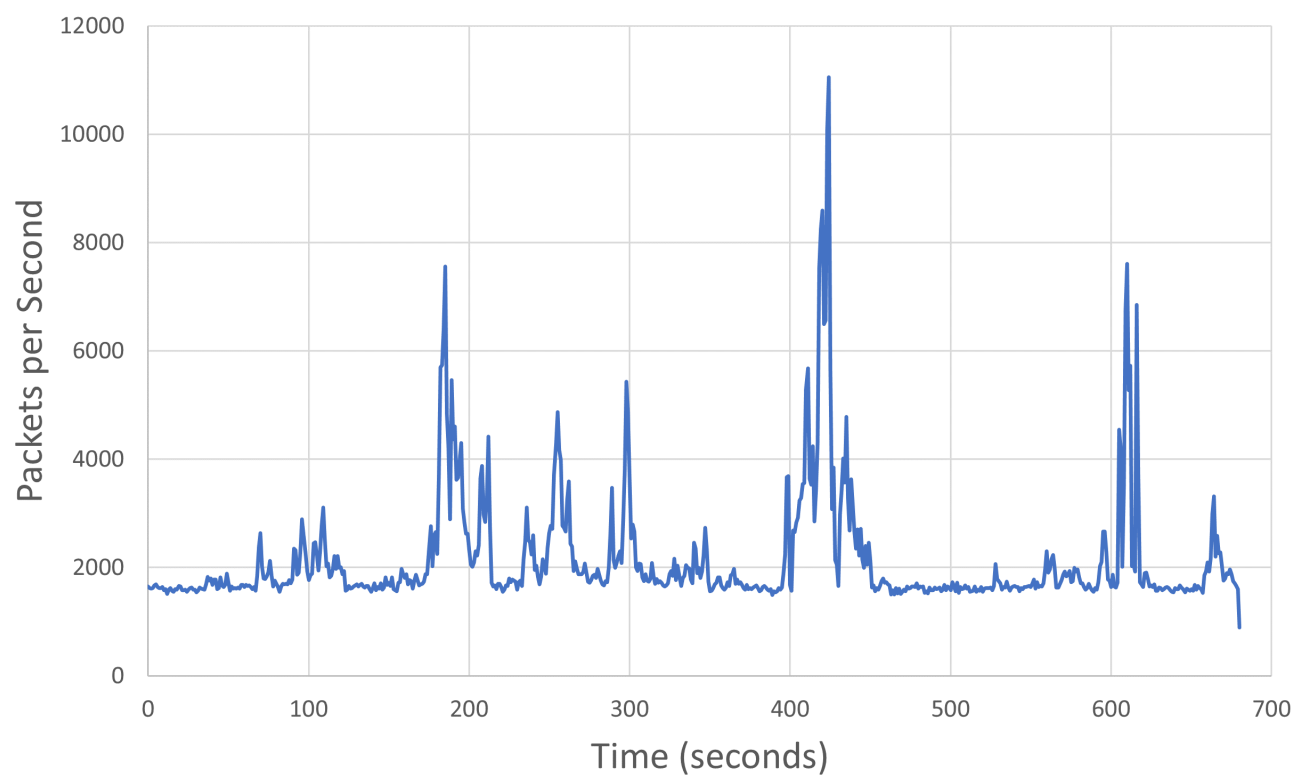


Figure 4.6: Wireshark graph of the packets per second from a ROSSPAD with an unstable triggering level. The source used to produce this data provides a steady stream of gamma rays.

from this test generated usable radiographs (see Chapter 5). However, the raw data histograms and the calibrated total signal histograms shown in Figure 4.8 demonstrate that this ROSSPAD is experiencing some form of signal drift. Since the initial testing was done without active cooling, it is assumed that this phenomenon is temperature dependent. Further testing is needed to demonstrate if this is true or not.

This ROSSPAD was able to generate images with good spatial resolution on its own. However, if surrounding ROSSPADs do not have the same response profile, they will not be able to work together in a full panel. Adjacent ROSSPADs must respond similarly so that cross-ROSSPAD localization can occur.

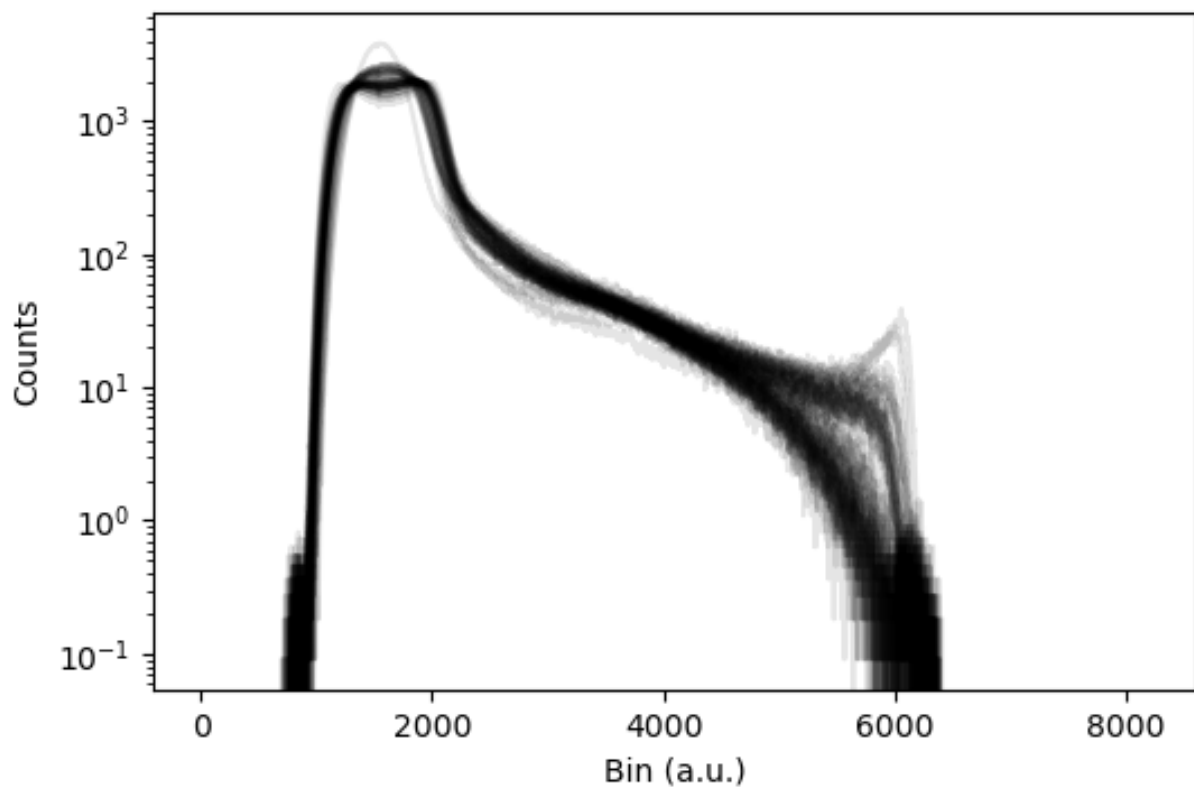


Figure 4.7: Uncorrected histograms of the 64 SiPMs on a ROSSPAD with potential signal value drift. ($N = 1.4 \times 10^6$ counts)

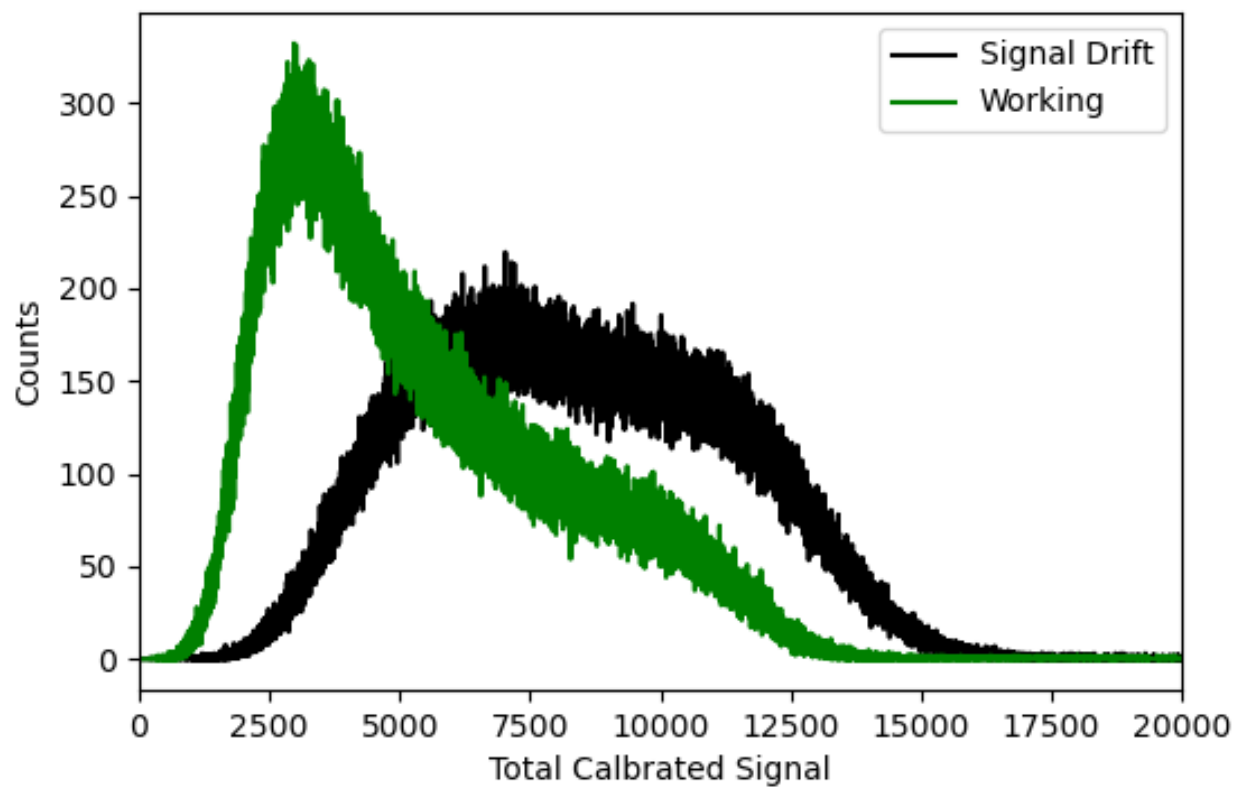


Figure 4.8: Corrected total signal histograms of a working ROSSPAD and a ROSSPAD experiencing signal value drift.

Chapter 5

Single-ROSSPAD Imaging

Sections of this chapter have been taken from *Scalable Detector Design for a High-Resolution Fast-Neutron Radiography Panel* [51].

5.1 Weighted Average Localization

5.1.1 Theory

The weighted-average method sums up the rows and columns together into one row and one column, both containing the entire set of data from one event. A weighted mean position is calculated in the summed row and column, giving a final position in x and y. The localized event position is stored into a data table within the same SQLite database file used for storage of raw and calibrated event data. Both the relative x- and y-position of the event on a ROSSPAD system as well as the true x- and y-position across the scope of the entire system are available, along with the sum of all of the SiPM signals, the event timestamp, and the identification of the ROSSPAD that produced that event.

Four reference images were generated. Each image is used to demonstrate the performance of one or more specific aspects of the localization method. Two images were generated using a 0.105 mCi Cs-137 gamma source placed 15 cm away from the face of the detector. A flood field image was generated with nothing between the source and the face of the detector, and a collimated line was generated with two 3.8 ± 0.1 cm thick tungsten

blocks (equivalent to approximately 7 mean free paths for a 662 keV gamma ray [4]) placed 0.083 ± 0.003 cm apart to create the collimated line. The detector was placed on a 15° angle block relative to the plane of the table so that the line would cross a larger amount of SiPMs. Given the distance to the detector face and the distribution of the cesium source, it is assumed that the collimated line will be even across the face of the detector. The collimated line setup is shown in figure 5.1.

Spatial resolution values based on the collimated Cs-137 image and the Cf-252 edge were generated using a modulation transfer function (MTF) [52]. By taking the real component of a fast Fourier transform (FFT) of the collimated Cs-137 line or the derivative of the Cf-252 edge, it is possible to understand how the spatial frequency of the object being imaged is transferred to the radiograph [52]. MTF measurements are a common method of determining image quality and spatial resolution in many forms of images.

The other two images were generated using a 0.109 mCi Cf-252 fission neutron source. A flood field image was taken with the source placed approximately 10 cm away from the face of the detector. An edge image was taken with the source placed approximately 40 cm away from the face of the detector. A block of high-density polyethylene (HDPE) measuring 15.25 ± 0.1 cm thick (equivalent to approximately 5 mean free paths assuming an average fission neutron energy of 2.105 MeV [53]) was placed approximately 12 cm from the face of the detector, in between the source and the detector. For both setups, a 0.2 ± 0.0025 cm thick sheet (equivalent to approximately 2 mean free paths for Cf-252's highest energy gamma ray at 0.207 MeV [4]) of lead was placed in front of the detector face, attenuating 87.5% of the gammas that come from the direct decay of Cf-252. Since the ROSSPAD module does not have the ability to distinguish neutron events from photon events via pulse-shape discrimination (PSD), this is the best method for reducing the number of gamma events when taking a neutron radiograph. The edge setup is shown in figure 5.2. While a line profile similar to the one created using cesium would be preferred, difficulties with the experimental setup made it easier to use an edge for the neutron-based image characterization.

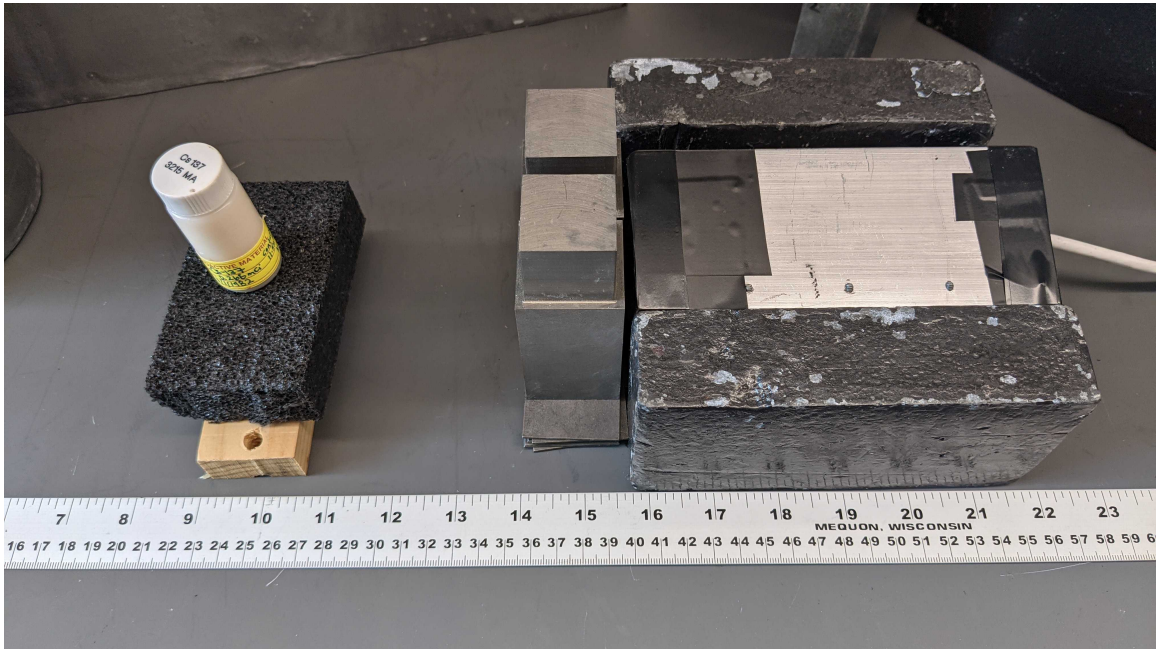


Figure 5.1: Experimental setup for generating a collimated Cs-137 line image.

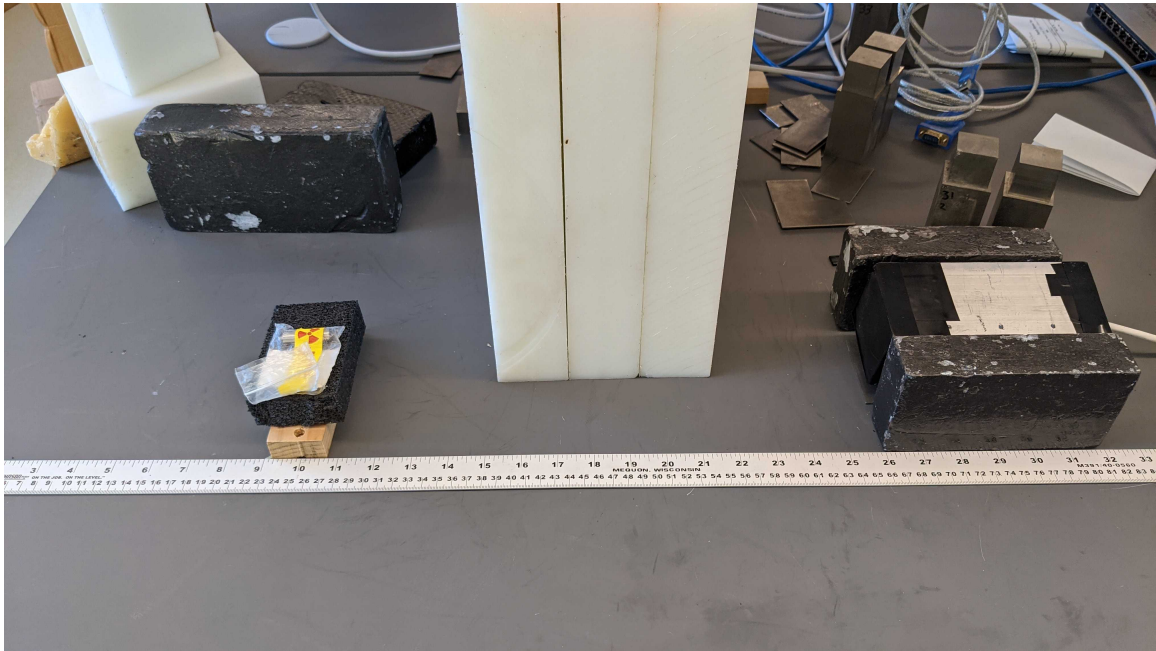


Figure 5.2: Experimental setup for generating a collimated Cf-252 edge image.

5.1.2 Cs-137 Images

A flood field image is shown in figure 5.3. This image shows an even spread of points across the center of the face of the detector, with an elevated number of events at the edges and the corners of the image. In addition, the flood field does not have any localized events within a half-SiPM border at the edge of the detector. These edge effects are due to a combination of the localization method employed and the housing of one ROSSPAD reflecting light towards the center of the system if there is a scintillation event at the edge.

Figure 5.4 shows the result of a line generated with 3.2×10^5 total events. The line has the same increased light collection at the edges seen in the flood field image. Even across the boundaries of SiPMs, the line continues straight with little deviation. At the top and bottom of the line, we see an increase of events that appears brighter than the rest of the line. This is likely due to the localization method performing poorly at the edge of the ROSSPAD module due to the optical engineering with respect to light collection. It is expected that by extending the light spreader across multiple ROSSPAD modules, this systematic error in event position estimation will go away.

Figure 5.5 shows the profile of the normalized intensities across the collimated line source image. This profile was generated by taking an average of the intensities along the line using ImageJ. The average of the intensities along the line excludes the increase in counts at both ends of the line. The image generated uses pixels that correspond to a pitch of 0.25 millimeters on the face of the detector. This pixel density was chose to highlight any artifacts that may appear in the image. These artifacts are cause by issues such as light refraction from air pockets in the scintillator package or event buildup as the result of issues with the localization algorithm. Each pixel corresponds to a point in space in order to make generating an MTF value easier. For the profile displayed in Figure 5.5, the position in space is relative to the start of the data. A demonstration of this process is shown in Figure 5.6. Since the profile of the line can be closely approximated with a Gaussian curve, a true Gaussian curve was fit to the data, and from this fit a modulation transfer function (MTF) was generated. The image likely does not fit a perfect Gaussian curve due to geometric unsharpness [54] with regards to the placement of the source, object, and detector. Typically, a collimator is used

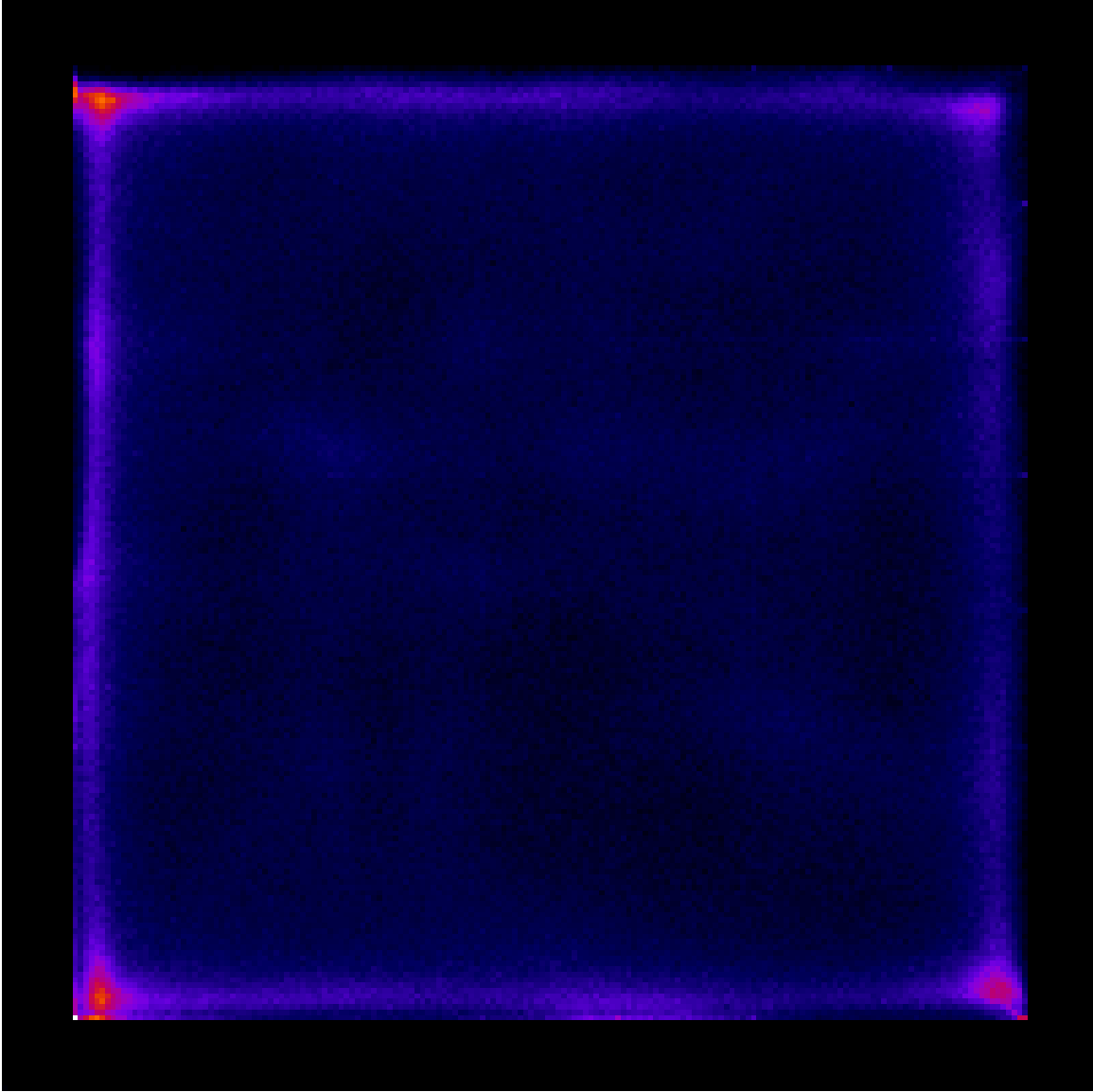


Figure 5.3: A flood field image generated using a Cs-137 gamma source. ($N = 1.8 \times 10^6$ counts)

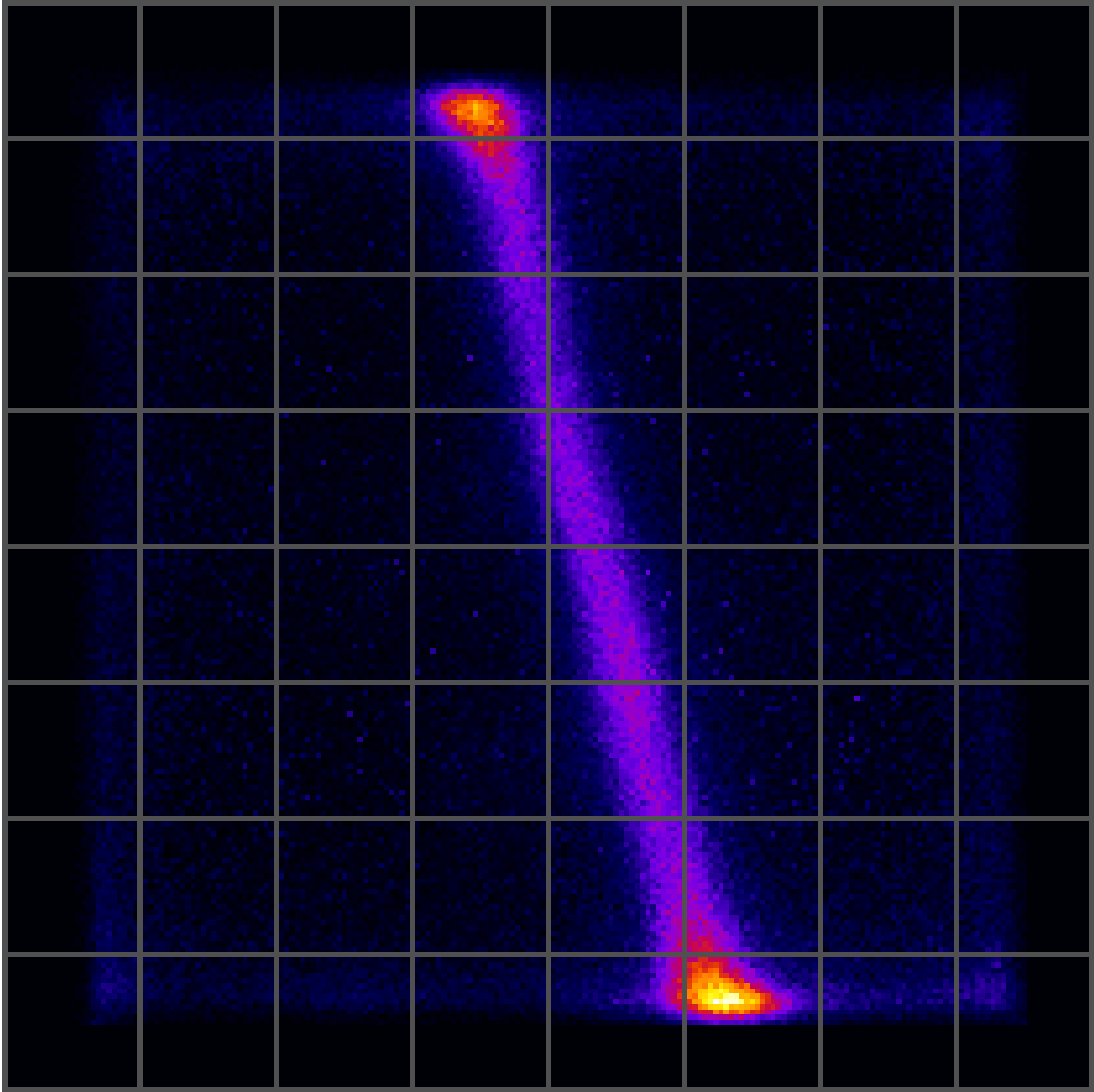


Figure 5.4: A collimated line image generated using a Cs-137 gamma source. SiPM boundaries have been overlaid onto the image. ($N = 3.2 \times 10^5$ counts)

to improve the spatial resolution of a radiograph by improving the geometric unsharpness factor [55]. Since the source in this configuration is only collimated by the object itself, unsharpness from the distribution of the source material within the container is introduced. Figure 5.7 shows a 90% spatial resolution of approximately 0.47 line pairs per centimeter and a 10% spatial resolution of approximately 2.32 line pairs per centimeter.

5.1.3 Cf-252 Images

Similar to the flood field from the gamma source, Figure 5.8 shows the same even spread in the center of the image and similar edge effects. This image was generated using 5.5×10^5 total events. Though it is likely that the majority of these events come from neutron interactions within the data, the lack of PSD capability means that photon events cannot be fully removed from the image. The Cf-252 flood field shows that the upper right corner is pulled in slightly to the center compared to the Cs-137 flood field. It is possible that separation of the light spreader and SiPM board or light spreader and scintillator diffracts light and causes the image to pull towards the center. An example of this separation is shown in Figure 5.9.

Figure 5.10 shows the result of an edge generated with 1.3×10^6 total counts. Note that the corners appear significantly brighter due to contrast adjustments needed to make the edge clearly visible. In addition, SiPM boundary lines have not been included to improve image clarity.

Figure 5.11 shows an error function fit to the normalized intensity profile of the edge, generated using the same technique used for the collimated Cs-137 line. The derivative of the function is used to generate a Gaussian curve, which was then used to generate the MTF show in Figure 5.12. The MTF shows a 90% spatial resolution of approximately 0.70 line pairs per centimeter and a 10% spatial resolution of approximately 3.35 line pairs per centimeter.

The collimated edge using neutrons is not as clear as the collimated line using gammas. There are many possibilities for this, including the inability to discriminate photon interactions from neutron ones and the increased geometric unsharpness caused by a volumetric Cf-252 source and increased distance between the object and the face of the

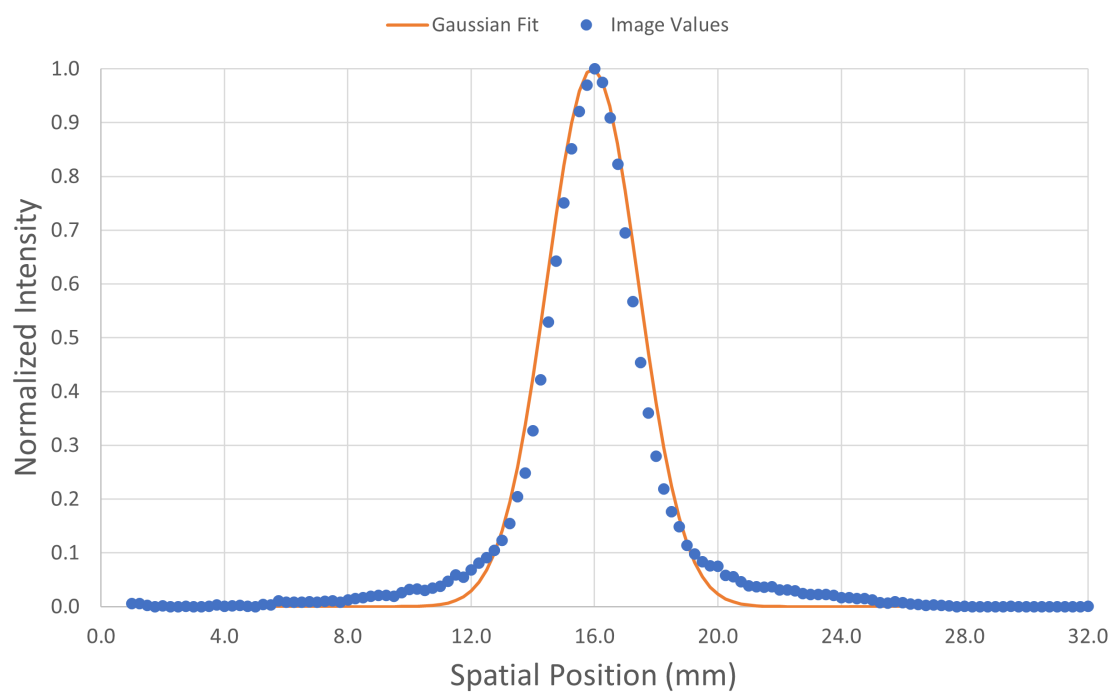


Figure 5.5: Line profile of the collimated Cs-137 image.

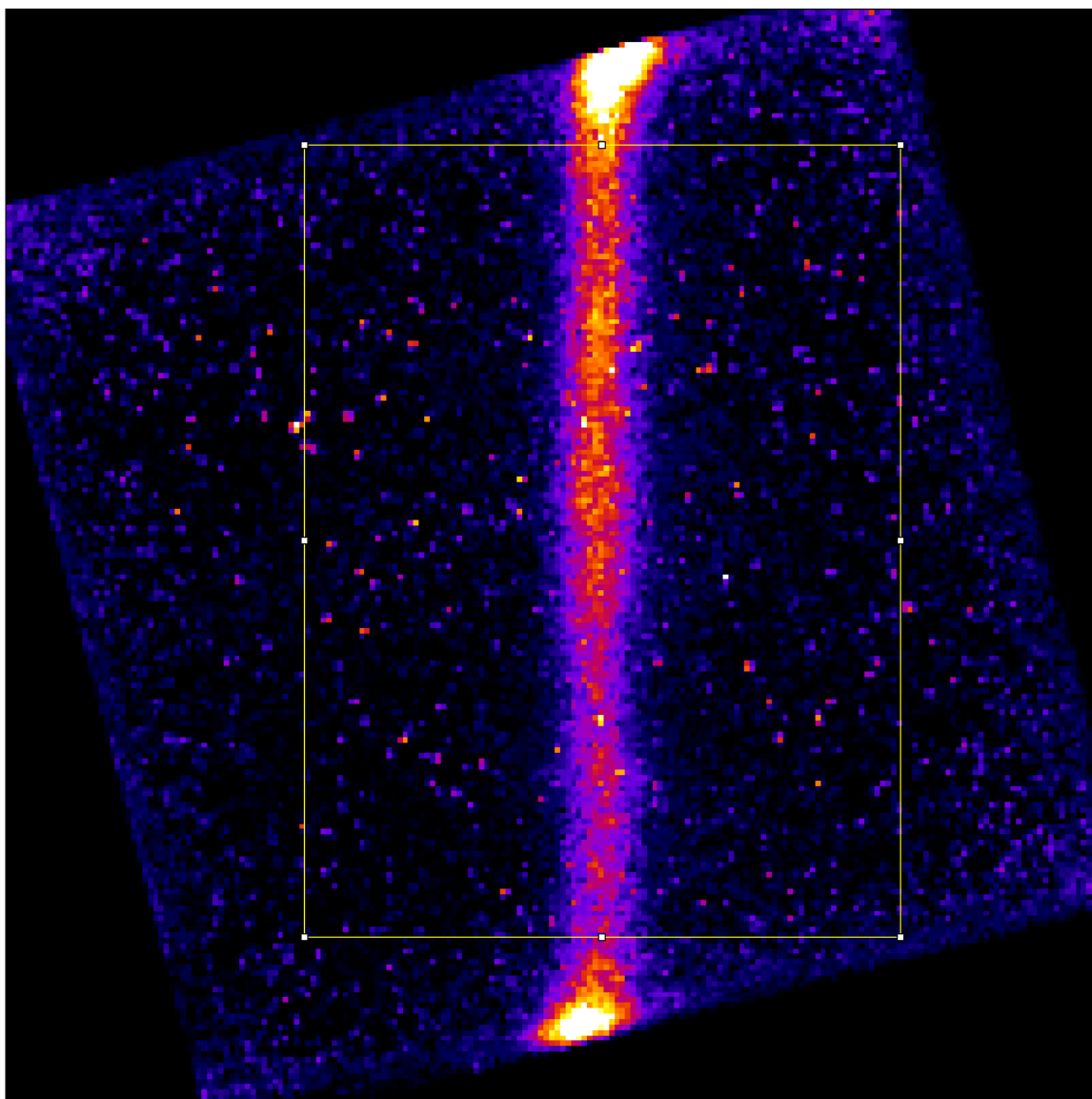


Figure 5.6: Demonstration of the area evaluated for spatial resolution of the collimated Cs-137 image.

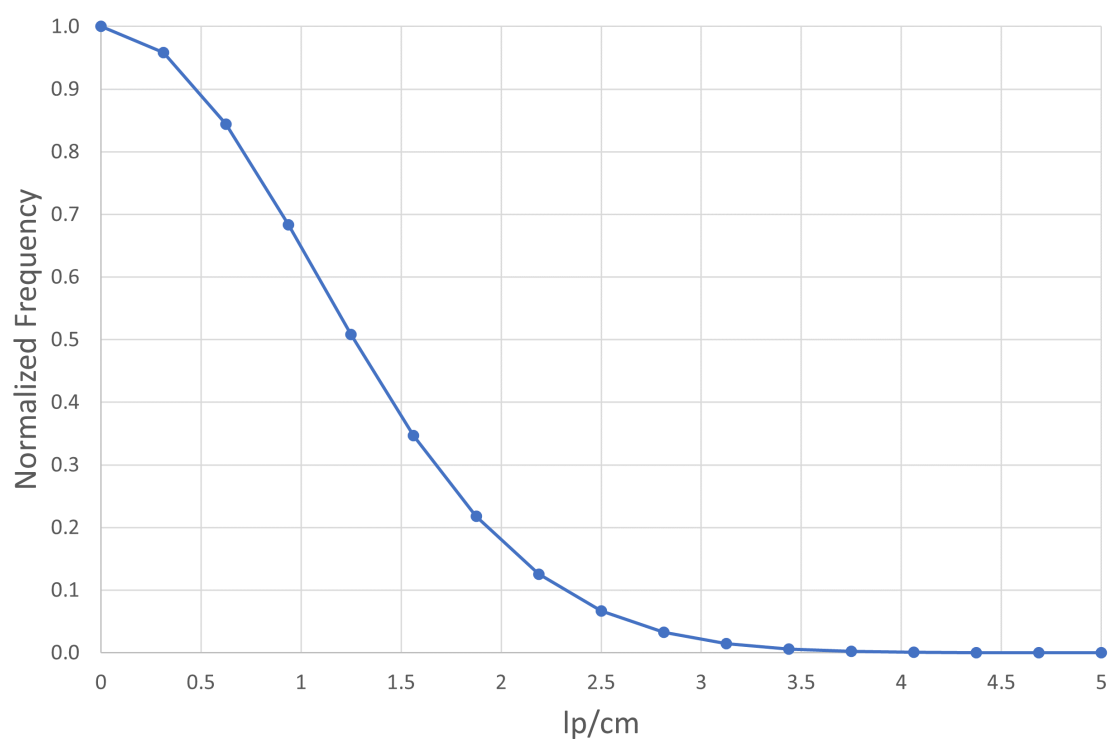


Figure 5.7: Modulation transfer function of the collimated Cs-137 line.

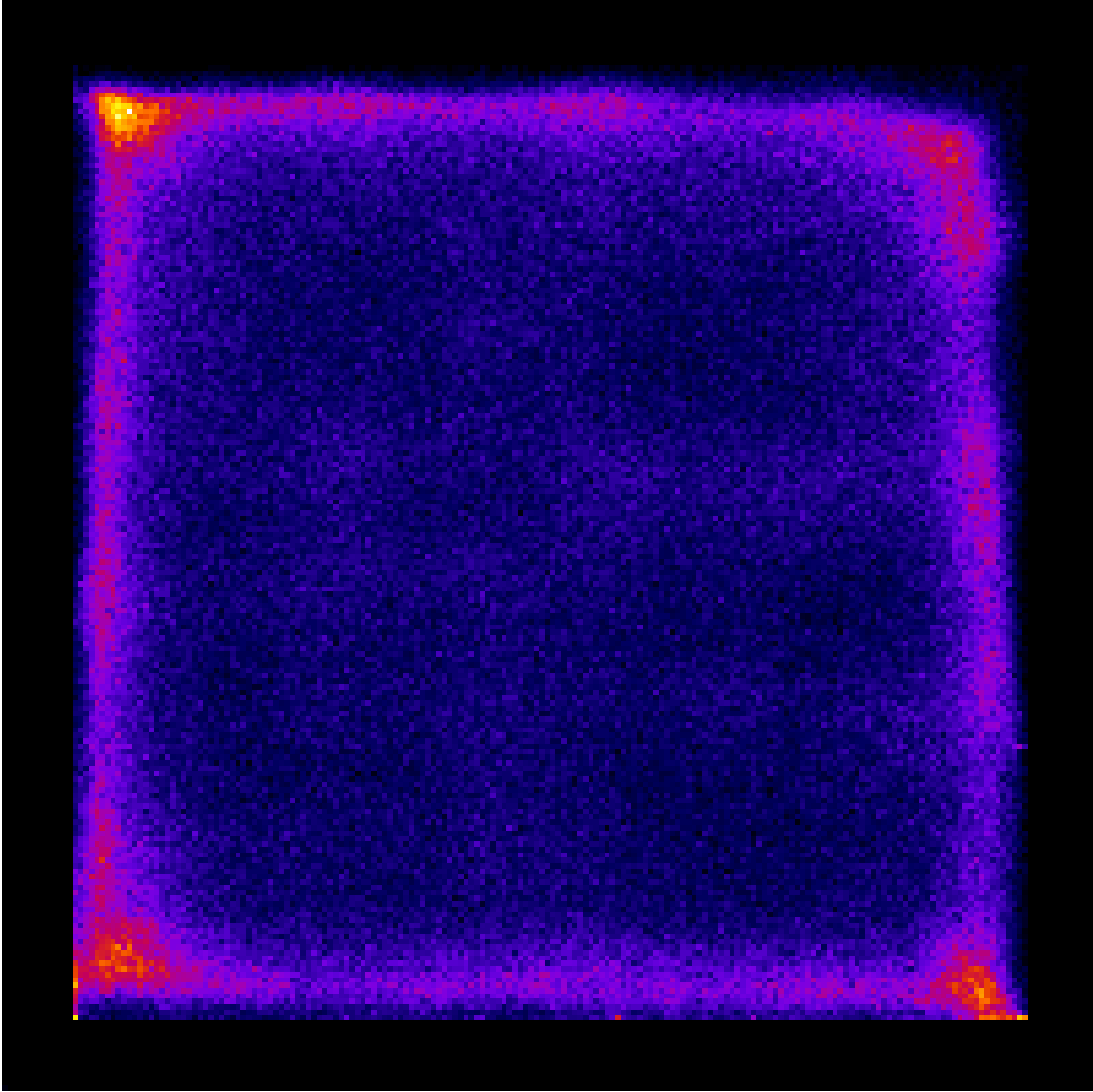


Figure 5.8: A flood field image generated using a Cf-252 fission neutron source. ($N = 5.5 \times 10^5$ counts)



Figure 5.9: Optical distortion due to the separation of the light spreader and the scintillator (circled in orange).

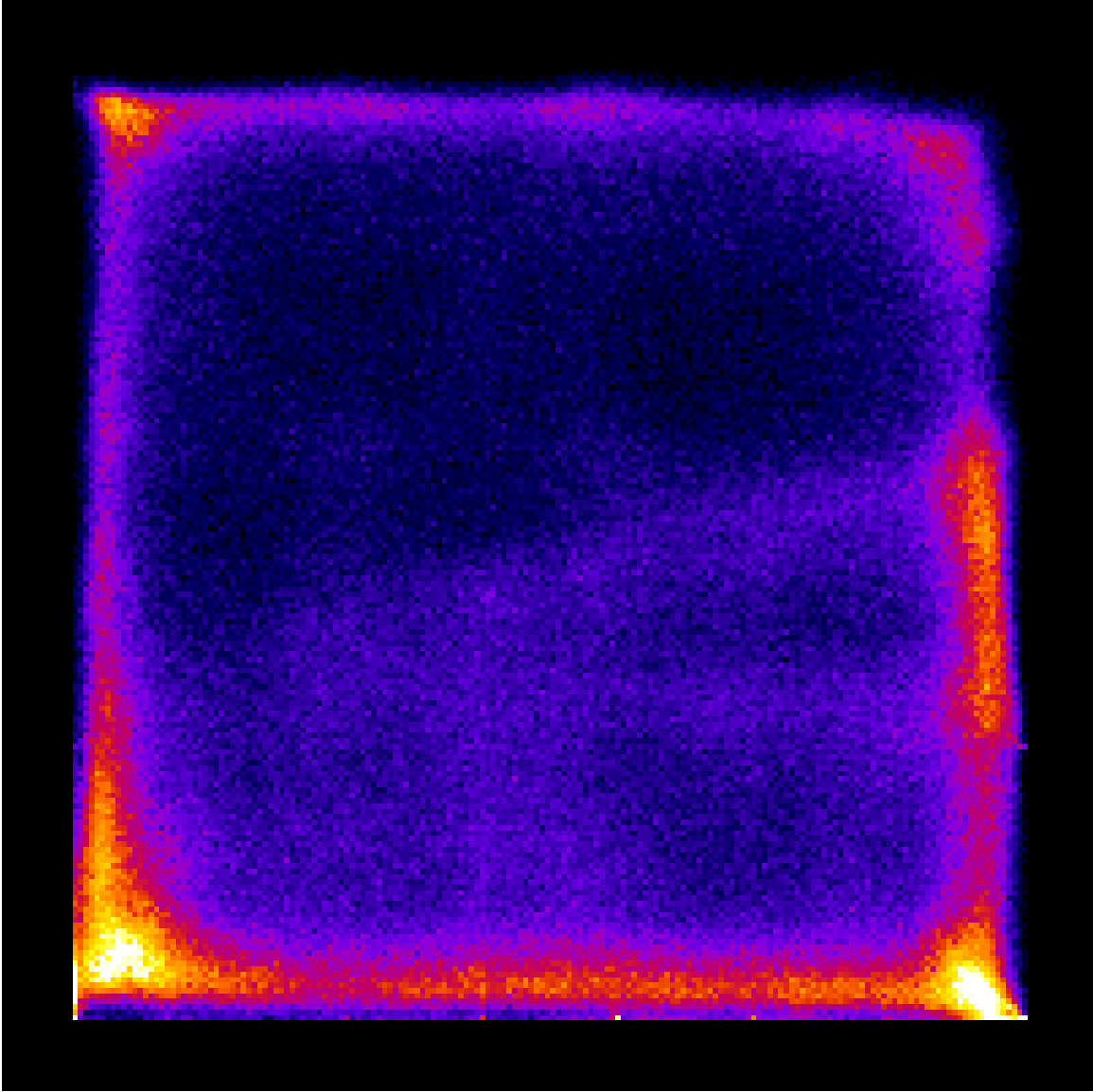


Figure 5.10: An edge image generated using a Cf-252 fission neutron source. ($N = 1.3 \times 10^6$ counts)

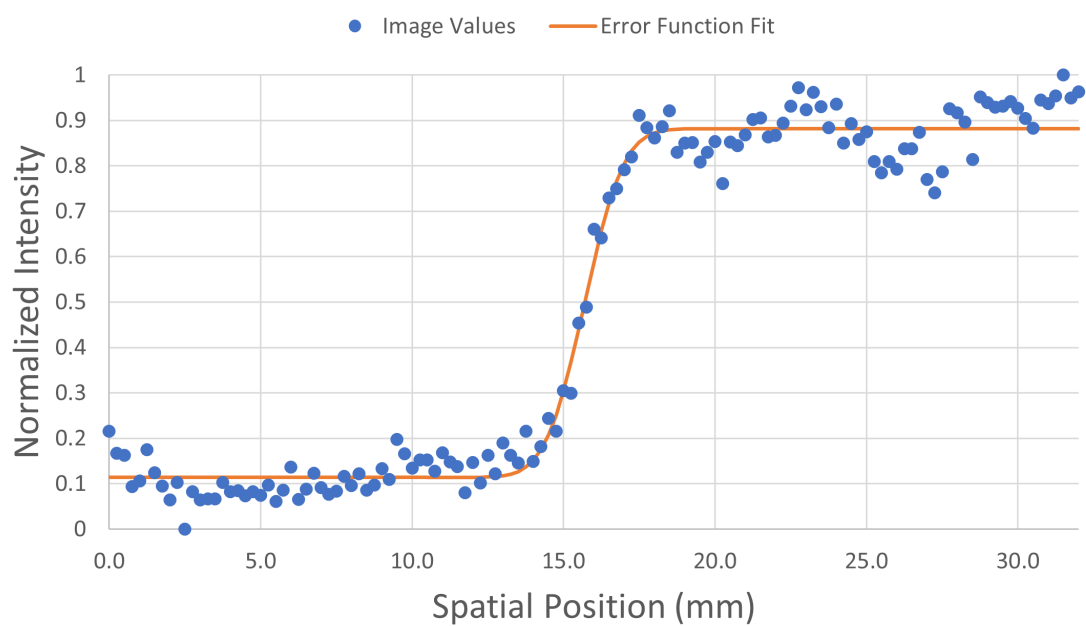


Figure 5.11: An edge image generated using a Cf-252 fission neutron source. ($N = 1.3 \times 10^6$ counts)

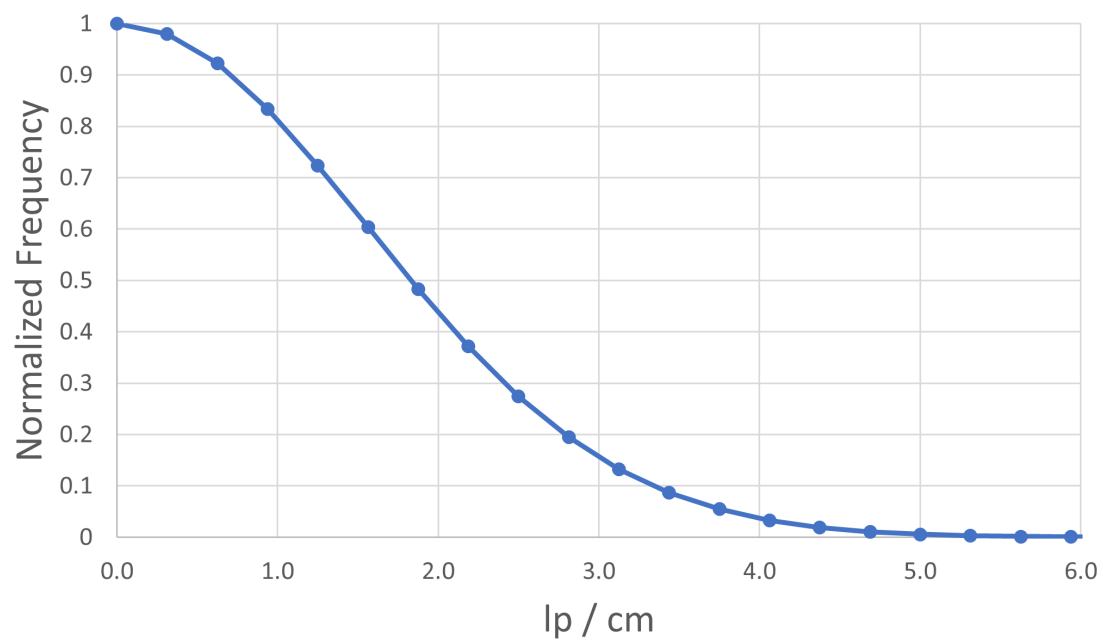


Figure 5.12: Modulation transfer function of the collimated Cf-252 edge.

detector [55]. Despite having more events in the image than the collimated gamma line, the neutron edge has increased variation in the intensities of the pixels in the image.

To verify the integrity of the Cf-252 MTF measurement, a second image was generated at a lower resolution. While the original image was generated with a density of 4 pixels per millimeter (40,000 total pixels), the second image was generated with a density of 2 pixels per millimeter (10,000 total pixels). With 1.3 million events in each image, this brings the number of events per pixel from 32.5 to 130. Figures 5.13 and 5.14 display the image and the edge profile for this new pixel density.

Figure 5.15 shows the difference in MTF value for the two different pixel densities. While the original image had a 90% spatial resolution of approximately 0.65 line pairs per centimeter and a 10% spatial resolution of approximately 3.30 line pairs per centimeter, this new image has a 90% spatial resolution of approximately 0.79 line pairs per centimeter and a 10% spatial resolution of approximately 3.75 line pairs per centimeter. Variation from the edge profile did not improve significantly between the two pixel densities, so the improved MTF values are likely not as representative of the image as it appears. The MTF values are, however, close between the two images, indicating that the method for generating the MTF values has some consistency despite the variation in pixel intensity.

5.1.4 Comparison Between Localization Method and Bare SiPM Board

Due to the relative size of the SiPMs compared to light collection electronics used in other neutron radiography panels, a system could be built using the size of the SiPMs as the size of the pixels in an image. Doing this puts a hard cap on the spatial resolution of a radiograph that is only derived from the size of the SiPMs. Localization methods are used to bring the spatial resolution lower than the pitch of the SiPM board. As such, it is important to compare the bare SiPM board spatial resolution to that of the localization methods used.

From the pitch of the SiPMs on the board, a reference spatial resolution can be derived with the following equation:

$$R = \frac{1}{2 * P} \quad (5.1)$$

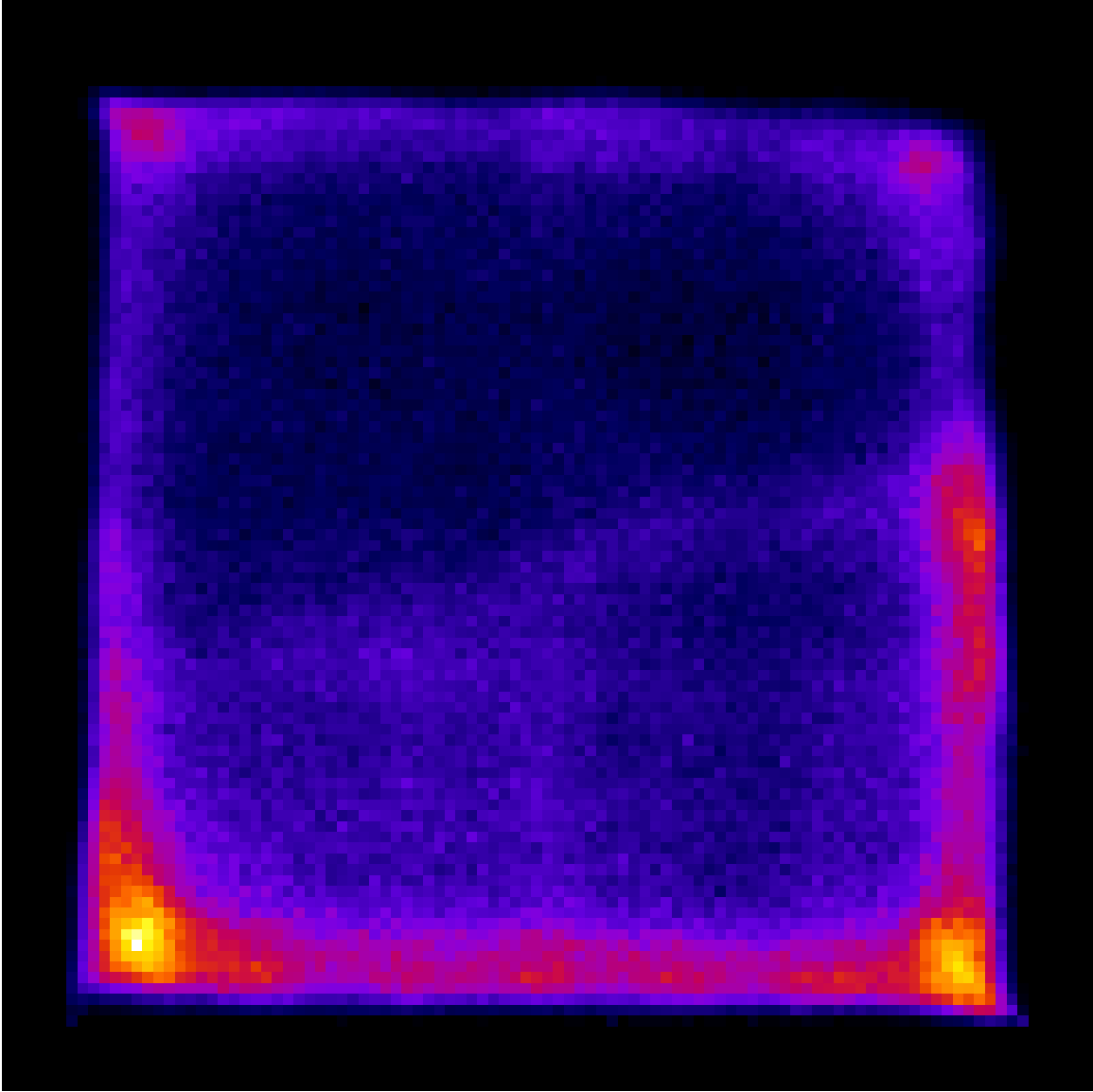


Figure 5.13: A new edge image generated using a pixel density of 2 pixels per millimeter.
($N = 1.3 \times 10^6$ counts)

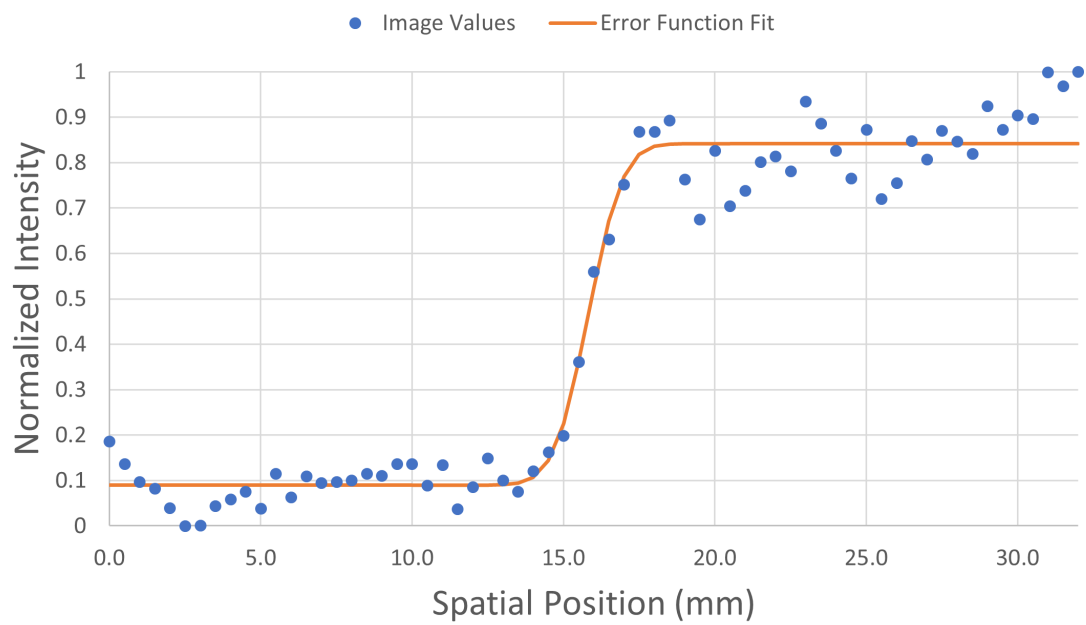


Figure 5.14: Edge profile of the reduced resolution image.

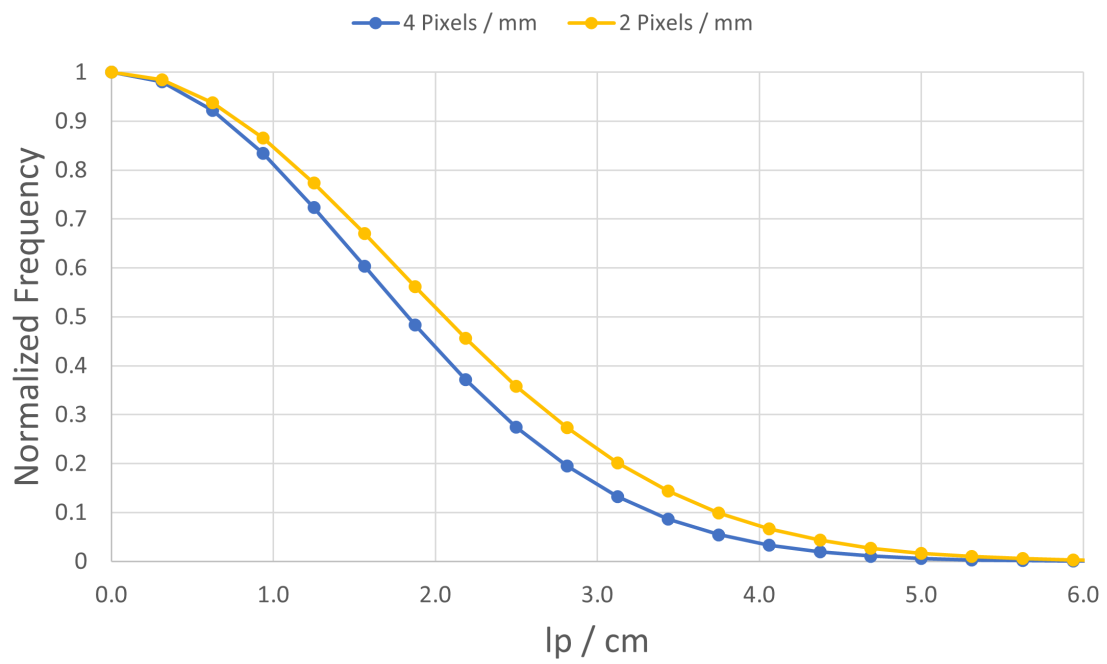


Figure 5.15: Comparison of MTF measurements using two different pixel densities.

where R is the spatial resolution of a bare SiPM board and P is the pitch of the SiPMs on the board in centimeters. Since the pitch of the SiPMs on the board is 0.6 cm, the board itself, with no localization, can generate images with a spatial resolution of 0.833 line pairs per cm.

The weighted average localization method is able to generate images with a 10% spatial resolution of 2.32 line pairs per centimeter for photons and 3.35 line pairs per centimeter for neutrons. These results demonstrate the ability to perform sub-SiPM event localization on the ROSSPAD readout module using the weighted average method.

5.2 Two-Dimensional Gaussian Localization

5.2.1 Theory

While weighted-average localization performs well for both photons and neutrons, the method has limitations that impact its ability to perform in large-scale radiography panels. The weighted-average method works well when the SiPMs in a panel are in a perfect grid, even across ROSSPAD modules. Deviations in the array or gaps between ROSSPADs make it difficult for the method to localize accurately where these issues arise. Additionally, a dead or broken SiPM (demonstrated in Chapter 3) would significantly impact the method beyond the boundary of the dead SiPM itself. As such, a new method has been proposed to potentially mitigate these issues.

A new method was proposed that utilized the area under a 2D Gaussian curve. Based on results from the Master's thesis of Sean Alcorn, simulated light distribution across the face of the ROSSPAD appears to follow a Gaussian profile, with the center of the Gaussian approximating the origin of the scintillation light [56]. By predicting where the scintillation event occurred, simulating the expected SiPM response by integrating the expected Gaussian over the area of each SiPM, and comparing it to the true SiPM responses, a given event can be localized using the Gaussian that least deviates from a given event.

A normalized two-dimensional Gaussian curve follows the equation:

$$f(x, y) = \frac{1}{2\pi\sigma_x\sigma_y} \exp\left(-\left(\frac{(x-x_0)^2}{2\sigma_x^2} + \frac{(y-y_0)^2}{2\sigma_y^2}\right)\right) \quad (5.2)$$

where x_0 and y_0 are the center of the Gaussian curve, and σ_x and σ_y are the standard deviations in the x and y dimensions. A simplified version of the integral of a two dimensional Gaussian curve can be calculated by taking the integral in each dimension separately and then multiplying them together:

$$V(x, y) = \frac{1}{2\pi\sigma_x\sigma_y} \int_{x_1}^{x_2} \exp\left(-\frac{(x-x_0)^2}{2\sigma_x^2}\right) dx \int_{y_1}^{y_2} \exp\left(-\frac{(y-y_0)^2}{2\sigma_y^2}\right) dy \quad (5.3)$$

which simplifies down to:

$$V(x, y) = \frac{1}{4} \left[\operatorname{erf}\left(-\frac{x-x_0}{\sqrt{2\sigma_x^2}}\right) \right] \Big|_{x_1}^{x_2} \left[\operatorname{erf}\left(-\frac{y-y_0}{\sqrt{2\sigma_y^2}}\right) \right] \Big|_{y_1}^{y_2} \quad (5.4)$$

Though equation 5.4 does not represent the exact area under a two-dimensional Gaussian curve, it is a computationally affordable method for determining the area. An example of a normalized 2D Gaussian curve can be found in Figure 5.16.

The same sets of data that were used to generate images for the weighted average localization method were used to test the 2D Gaussian localization method. This allows for direct comparisons of both the spatial resolution and the acquisition time for both methods. The results will allow for one method to be selected when moving on to multi-ROSSPAD imaging.

5.2.2 Cs-137 Images

A flood field image is shown in figure 5.17. The 2D Gaussian localization method was found to take longer to process than the weighted-average method, so the initial flood field image was generated at a lower pixel density (1 pixel per mm) compared to the same flood field for weighted-average method (4 pixels per mm). This flood field does not appear to be as even across the face of the detector as the flood field generated using the previous method, and

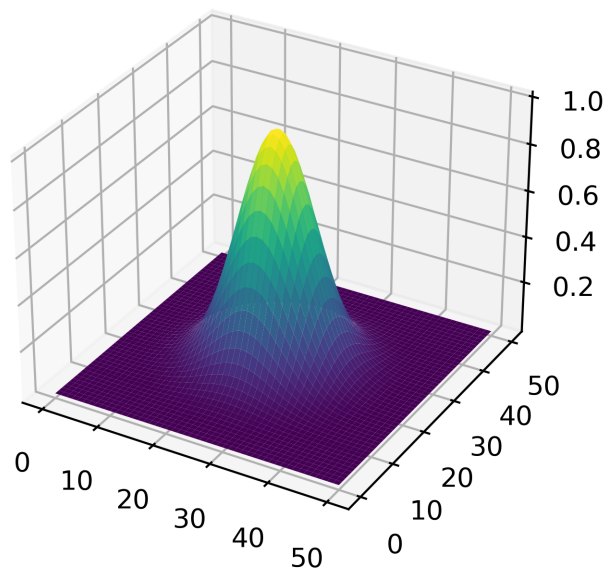


Figure 5.16: Simulated two-dimensional Gaussian curve generated in Python.

deviations in the flood field potentially caused by air bubbles or gaps within the scintillator package become more apparent. Like previous methods, the events appear to concentrate at the edges of the image, but again do not extend all the way to the true edge of the face of the detector; this is likely the result of light reflection at the edges.

Figure 5.18 shows the result of a line generated with 3.2×10^5 counts. This 2D Gaussian line appears to be slightly straighter than the weighted-average line, though it also appears to have variation at the edges of the line. Additionally, there is a discontinuous point towards the upper end of the line. Since the 2D Gaussian flood field appeared to be less even than the weighted-average one, this could be the result of either air pockets being exaggerated with the new localizer or issues with the localizer’s performance in general.

Despite the potential issues with the quality of the 2D Gaussian line, a profile was generated using ImageJ. Figure 5.19 shows the profile of the normalized intensities across the collimated line source image and the Gaussian fit generated using the data. Like the previous collimated line, this line doesn’t exactly match the fitted Gaussian curve, likely as the result of geometric unsharpness. Figure 5.20 shows a 90% spatial resolution of approximately 0.5 line pairs per centimeter and a 10% spatial resolution of approximately 2.5 line pairs per centimeter.

5.2.3 Issues With Current Method

After Cs-137 results were generated, both localization methods were compared to determine which should be prioritized for multi-ROSSPAD imaging. While generating Cf-252 results would normally be considered, the Cs-137 measurements showed that the 2D Gaussian localization method does not appear to be worthwhile at this point. Currently, the weighted-average method is performed entirely on a single thread of a processor, whereas the 2D Gaussian localization method had to be made parallel and run across all threads to make processing manageable.

Data processing for both localizers was performed on an AMD Ryzen 9 5900HX processor. This processor contains eight cores and sixteen threads operating at a base clock speed of 3.3 GHz and a boost clock speed of 4.6 GHz [57]. To determine make comparisons between the weighted average localization method (single-core) and the two-dimensional Gaussian

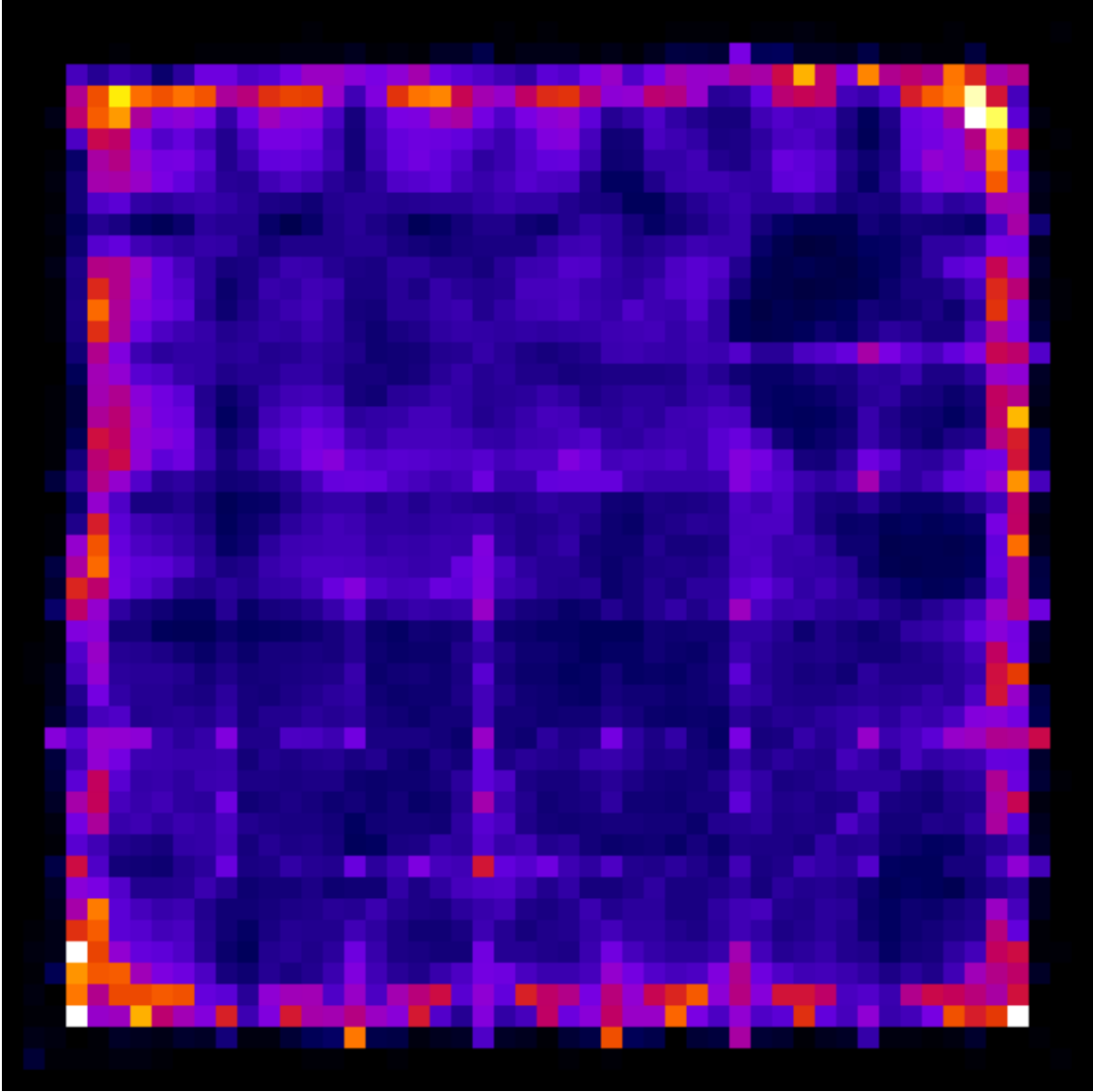


Figure 5.17: A flood field image generated using a Cs-137 gamma source and a 2D Gaussian localization method. ($N = 1.8 \times 10^6$ counts)

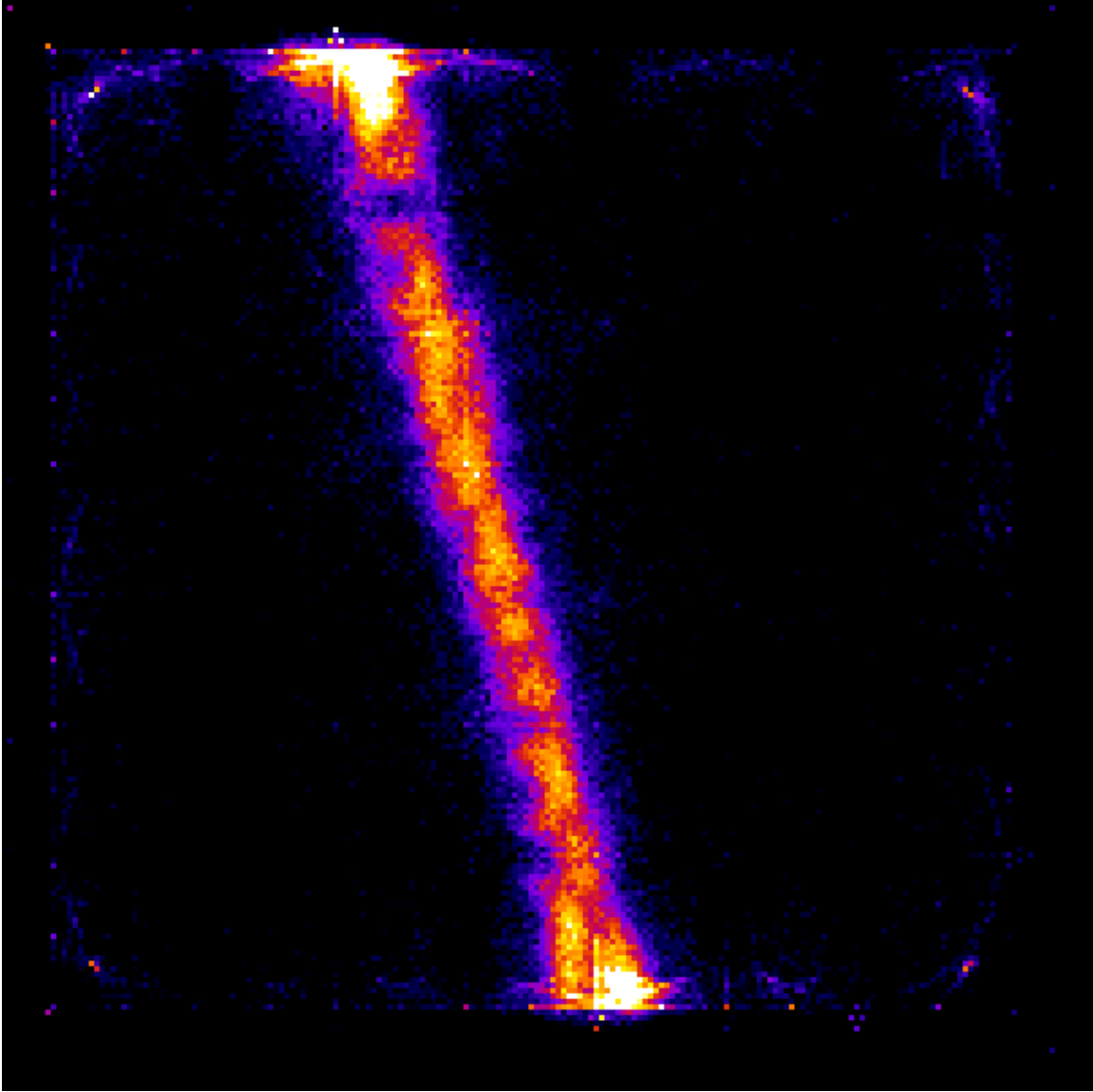


Figure 5.18: A collimated line image generated using a Cs-137 gamma source and a 2D Gaussian localization method. ($N = 3.2 \times 10^5$ counts)

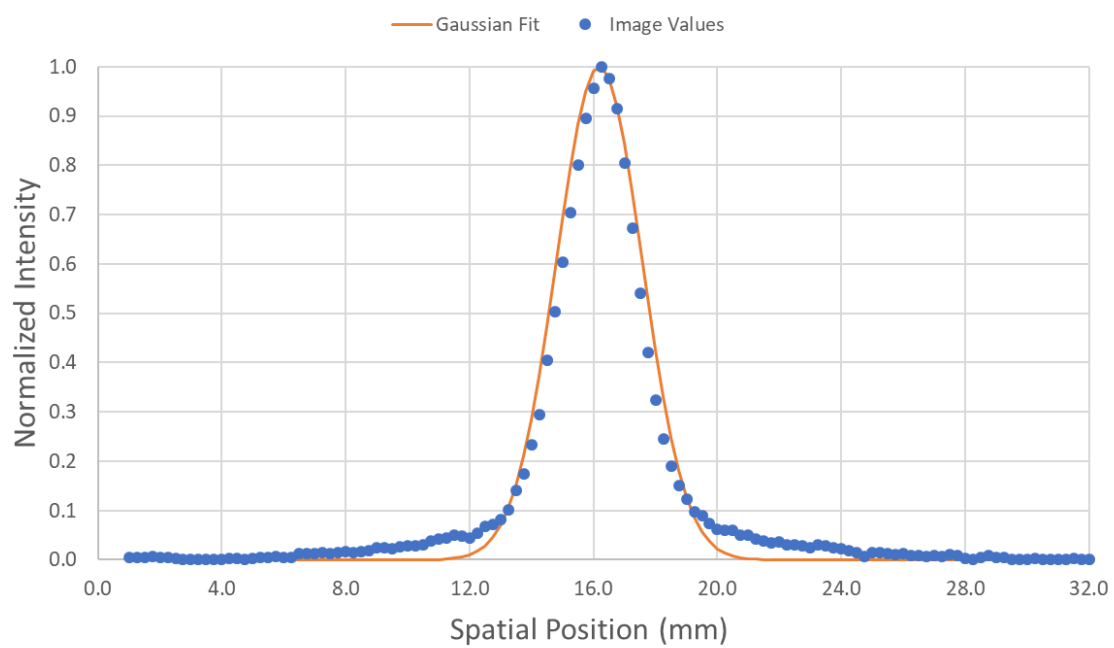


Figure 5.19: Line profile of the collimated Cs-137 image using the 2D Gaussian localization method.

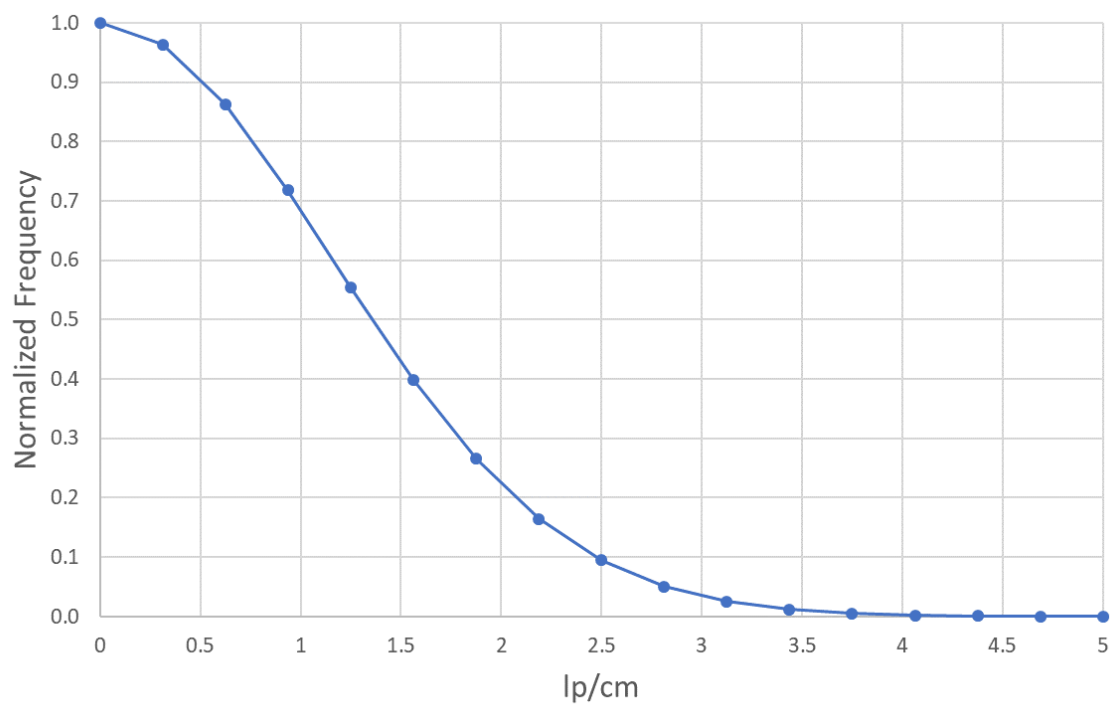


Figure 5.20: Modulation transfer function of the collimated Cs-137 line using the 2D Gaussian localization method.

localization method (multi-core), a figure of merit (FOM) was defined using the following formula:

$$FOM = \frac{t}{MTF_{10\%}} \quad (5.5)$$

where t is the time to generate an image in minutes and $MTF_{10\%}$ is the 10% modulation transfer function value of the image generated. For this FOM, a smaller number represents better performance. FOM results can be found in Table 5.1.

The FOM for the 2D Gaussian localizer is roughly 18 times larger than the FOM for the weighted-average localization method. Although the 2D Gaussian localizer performs $\approx 7.8\%$ better than the weighted-average method, the time it takes to generate is significantly longer, despite the fact that it has been optimized to run in parallel. While the 2D Gaussian localizer will perform better with more cores, optimization of the weighted-average method would widen the FOM gap between the two methods further. While the 2D Gaussian localization method may be promising for future projects, priority for this project was given to the weighted average method.

Table 5.1: Comparison of Localization Methods

Localization Method	10% MTF (lp/cm)	Time to Generate (Minutes)	FOM
Weighted Average	2.32	1.27	0.55
2D Gaussian	2.5	24.85	9.94

Chapter 6

Multi-ROSSPAD Imaging

6.1 Cross-ROSSPAD Triggering Effects

One of the biggest challenges when moving from a single ROSSPAD module to a panel of multiple ROSSPADs is how to account for events at the edges. On a single ROSSPAD, the localization method can only localize an event out to the middle of the edge SiPMs, meaning that a small portion of the detection area is lost. By using a continuous light spreader and scintillator, this can be fixed for most of the detector panel. A single event can trigger multiple ROSSPADs, and using the data from both allows for events to be localized closer to the edges of the ROSSPAD. This will work for the boundaries between ROSSPADs, but won't fix the very outer edges of the panel. Despite this, cross-ROSSPAD localization will allow for a much larger usable radiography area, especially as more detectors are added.

An initial flood field using a 0.105 mCi Cs-137 gamma source was generated as an initial test on 35 of the 36 ROSSPADs. This was done before testing was performed to determine all of the methods of failure with the ROSSPAD detectors. Figure 6.1 shows a somewhat even distribution of counts across the centers of each ROSSPAD. However, between ROSSPAD detectors there is a clear band, with the edge of the band appearing darker than the center of the band. The corner intersection of four ROSSPADs additionally shows significantly lower counts than the rest of the flood field. Looking at the data from the SQLite data tables, it appears that the issue may relate to the triggering threshold of the ROSSPAD detectors.

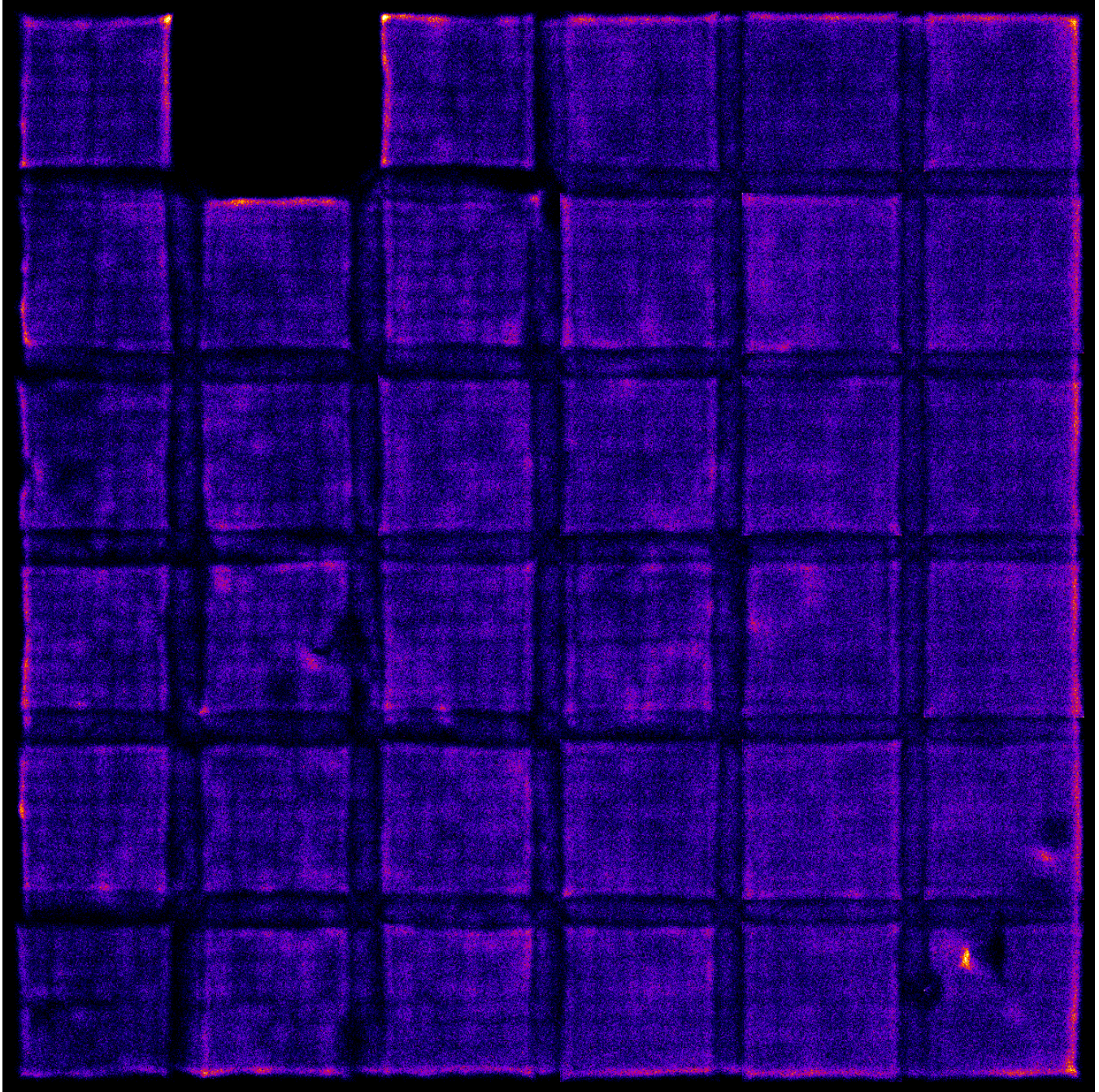


Figure 6.1: Full-panel flood field using a Cs-137 source. 35 of the 36 ROSSPADs were turned on for this experiment.

At the default triggering threshold of 28 arbitrary units, a large amount of light reaching a ROSSPAD is needed to trigger the detector so an event can be recorded. When an event triggers on a SiPM at the edge of a ROSSPAD, however, the residual light that makes it to a neighboring ROSSPAD might not be enough to trigger it. This means that many events that require a neighboring ROSSPAD to trigger do not receive sufficient light to trigger at default settings. Figure 6.2 shows an event that occurs at the corner of four ROSSPADs. Despite this, only one of the four ROSSPADs triggers, resulting in the event position being skewed away from the corner where the ROSSPADs meet. The triggering threshold was lowered to 20 arbitrary units across all of the detectors in the panel to compensate for the lower light spread onto neighboring SiPMs. An example of a now-corrected triggering map is shown in Figure 6.3.

6.2 Changes to Weighted Average Localization

Full-panel image generation requires slight modification of the weighted average localization method discussed in Chapter 5. Instead of performing localization on the signals from the SiPMs on one ROSSPAD, a scratchpad of the entire panel is made, and all events occurring within the same timestamp are added to the scratchpad. The highest-signal value SiPM is chosen as the triggering SiPM of the scratchpad, and weighted average localization is performed on a seven by seven section of SiPMs with the triggering SiPM in the center.

Two additional parameters were added to reduce the noise present in the scratchpad-based event localization. The localizer checks to make sure that for a SiPM to be added to the weighted average it must be above a set noise threshold. The noise threshold is based on a given multiple of the electronic noise for a given SiPM found during the calibration process discussed in Chapter 3. For the test images generated, the SiPMs considered needed to have a signal value three times greater than the electronic noise value of the SiPM. The other parameter checks to make sure enough SiPMs in the weighted average process were above the electronic noise. For the test images generated, nine of the forty-nine SiPMs had to have a signal value above the noise threshold. If there were less than nine SiPMs above

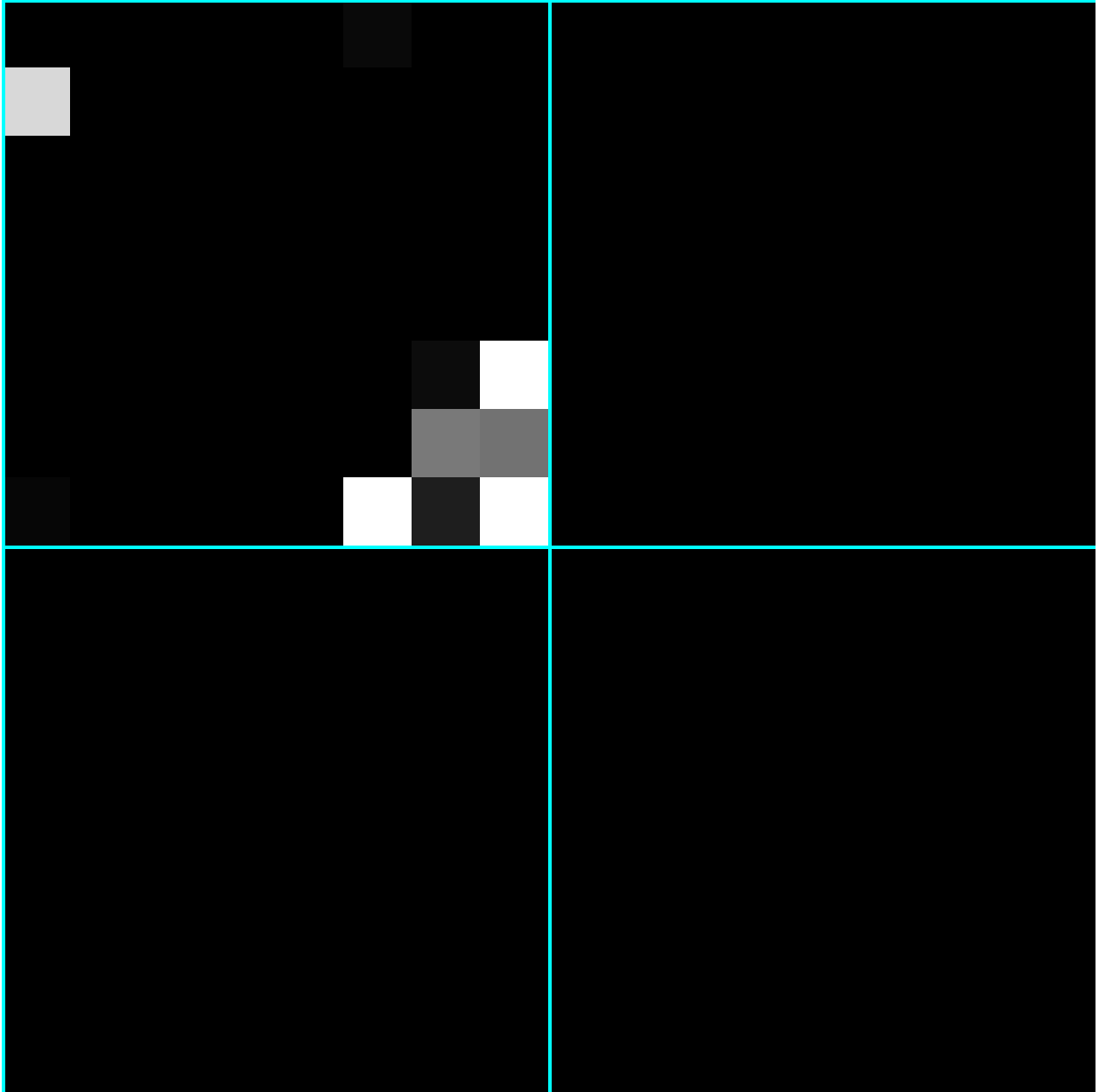


Figure 6.2: A single-event trigger map with the higher triggering threshold value set. The event space is shown across four ROSSPADs (cyan grid lines).

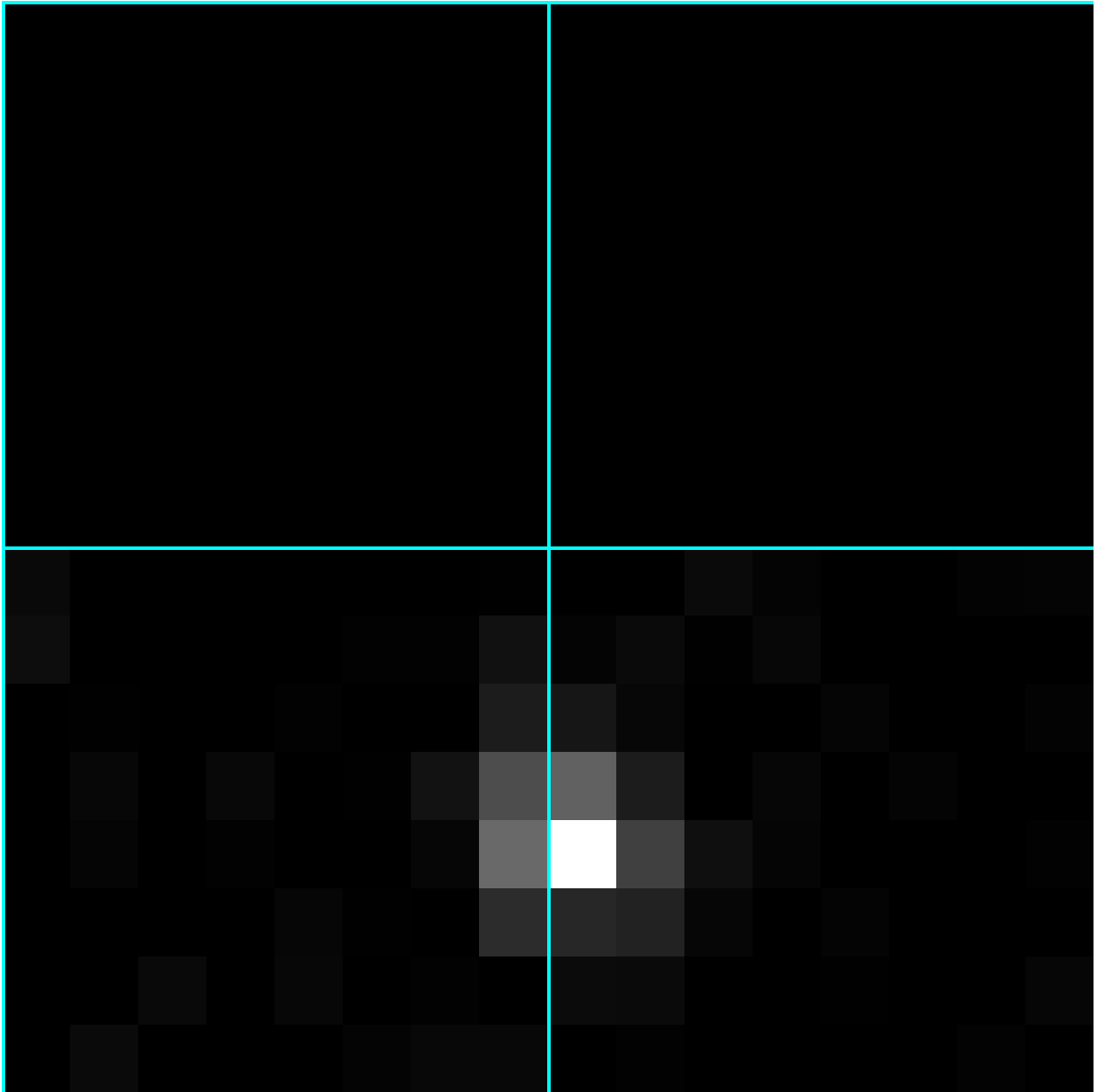


Figure 6.3: A single-event trigger map with the lower triggering threshold value set. The event space is shown across four ROSSPADs (cyan grid lines).

the noise threshold, the event would be thrown out, and the next event in the data stream would be loaded in.

Further analysis of the impact of these two parameters, as well as other parameters considered when building images, is discussed in Chapter 7.

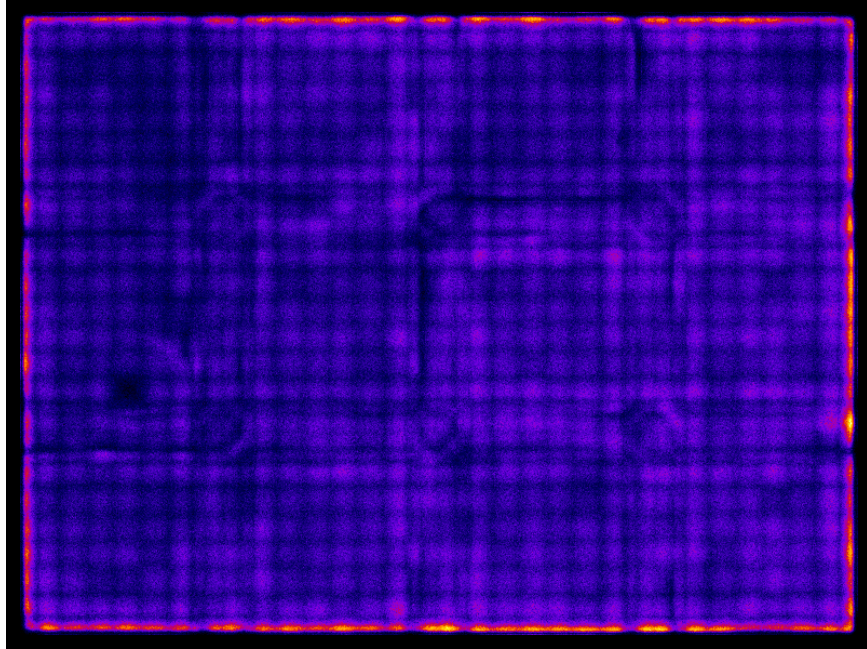
6.3 Flood Field Results

After removing broken ROSSPADs from the image and adjusting the triggering threshold to better perform cross-ROSSPAD localization, two flood fields were generated using a 0.105 mCi Cs-137 gamma source for the first flood field and a 0.090 mCi Cf-252 neutron source for the second. When generating the actual flood field images for each, both images weighted by number of counts in the pixel and weighted by total signal deposited into the pixel were made. Figure 6.4 demonstrates that events can now be localized to the edges of ROSSPADs with a Cs-137 source. However, both of these images appear to have significantly more artifacting than the flood fields generated on the single ROSSPAD detector. In the single-ROSSPAD images, the individual SiPMs cannot be easily seen, but on the full panel the SiPMs appear to almost pull events closer to their centers.

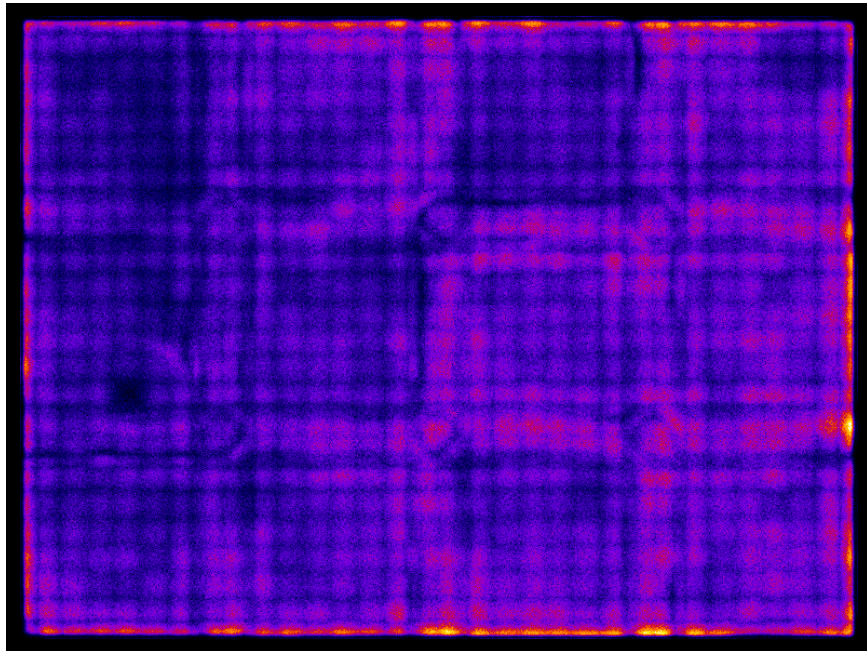
Similarly, Figure 6.5 shows the count-weighted and signal-weighted flood fields using a Cf-252 neutron source. Figure 6.5a appears to have more issues at the edges of ROSSPADs compared to Figure 6.4a. However, Figure 6.5b appears to be much more continuous across the face of the panel compared to Figure 6.4b. These differences are likely the result of differences in the light production within the EJ-200 scintillator between gamma interactions and neutron interactions. For both source types, the artifacting introduced when the full-panel radiography system was developed will lead to poor image quality when taking actual radiographs of objects.

6.3.1 Artifact Correction

Correcting radiographs for both radiation types requires a method for scaling the image based on the response of a flood field. A similar technique is already used for commercial-off-the-shelf x-ray radiography devices [58]. For a typical x-ray radiography panel, several flood

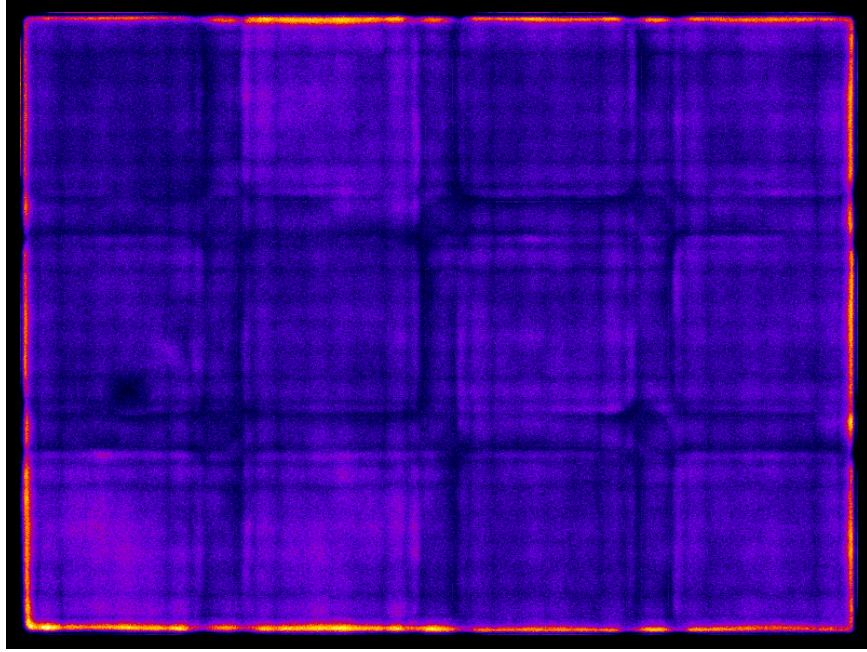


(a) Counts

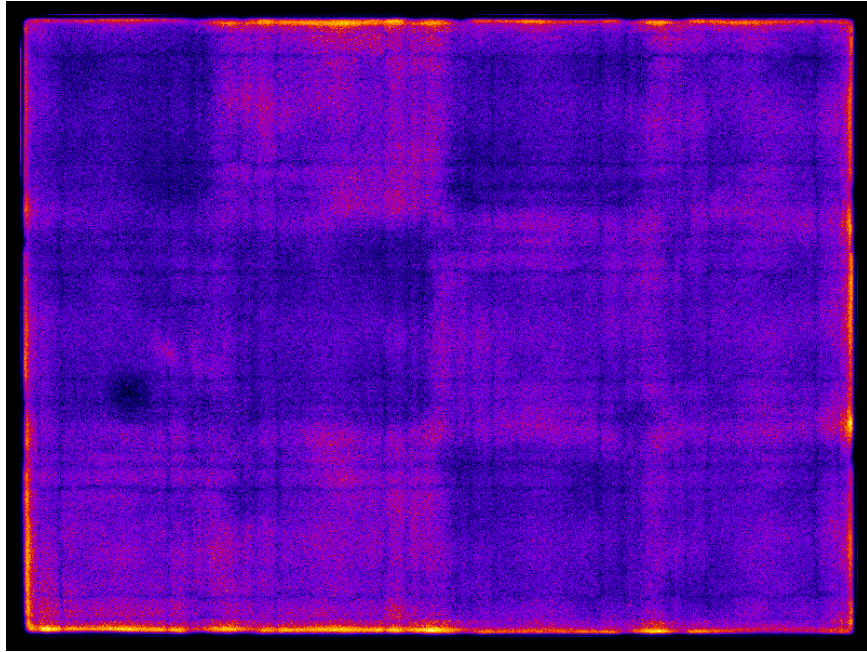


(b) Signal

Figure 6.4: Full-panel flood fields using a Cs-137 gamma source weighted by a) number of counts in pixel and b) total signal from events in pixel. ($N = 1.25 \times 10^7$ counts)



(a) Counts



(b) Signal

Figure 6.5: Full-panel flood fields using a Cf-252 neutron source weighted by a) number of counts in pixel and b) total signal from events in pixel. ($N = 1.17 \times 10^7$ counts)

fields at various source energy levels not only allow artifacts to be removed from the x-ray panel images, but also allow for nonlinear energy calibration for each individual photodiode [58].

Since the radiography panel works in a particle-counting mode, the lowest flood field level is assumed to be a value of zero in every pixel. Additionally, it is assumed that the response from the radiography panel would be linear, since it only has to add up events individually. Thus, a flood field correction formula can be simplified to:

$$P_{(x,y)} = \frac{R_{(x,y)}}{F_{(x,y)}} \quad (6.1)$$

where $P_{(x,y)}$ is the value of the (x, y) pixel in the post-correction image, $R_{(x,y)}$ is the value of the (x, y) pixel in the raw, uncorrected image, and $F_{(x,y)}$ is the value of the (x, y) pixel in a flood field using the same source of radiation. Equation 6.1 can be applied to any image easily with ImageJ, allowing for the process of artifact correction to be done quickly by the operator [50].

6.4 Spatial Resolution

6.4.1 Cs-137 Images

A collimated Cs-137 line was imaged across the face of the full-panel detector. Figure 6.6 shows two stacks of 3.8 ± 0.1 cm thick tungsten blocks (equivalent to approximately 7 mean free paths for a 662 keV gamma ray [4]) placed on top of each other, with a 0.2 ± 0.0025 cm thick gap separating the two stacks apart. The radiography panel was placed at a 10° angle so that the line can fall over multiple ROSSPAD boundaries in both x and y, and the 0.105 mCi Cs-137 gamma source was placed approximately 25.4 ± 0.1 cm away from the faces of the tungsten blocks. Figure 6.7 shows the uncorrected and corrected count-weighted line images. While the line still appears to have some artifacting present, particularly in areas where dual-ROSSPAD imaging is needed to localize near the edges of two detectors, the line still appears straight and well collimated, much like the results from the single-ROSSPAD imaging in Chapter 5.

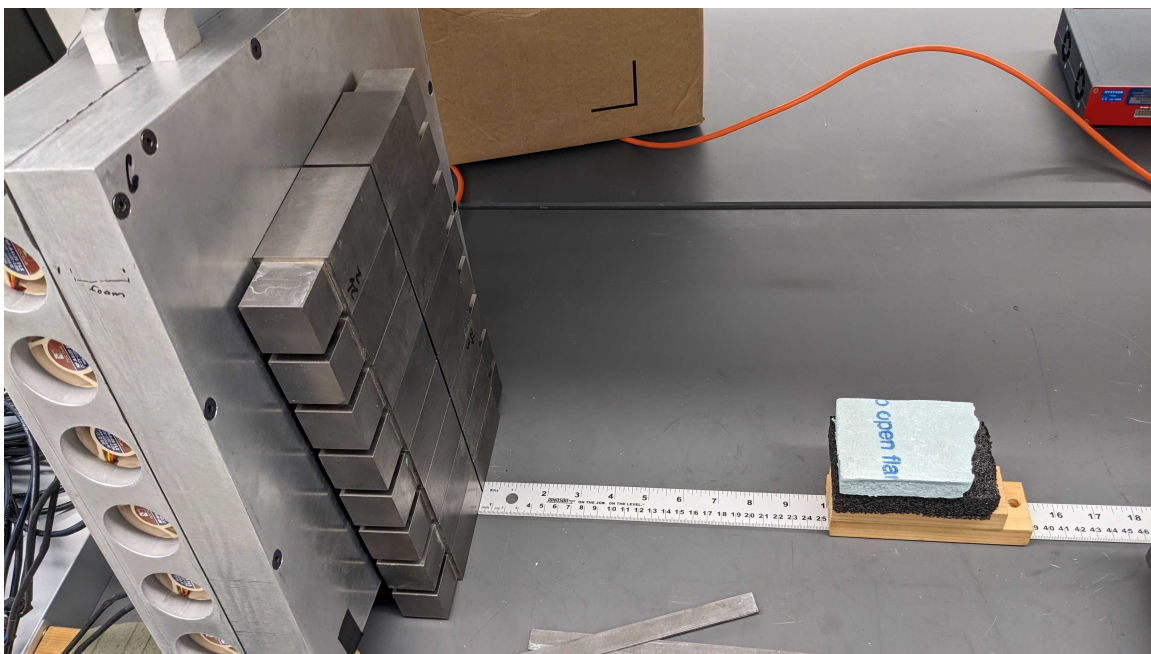
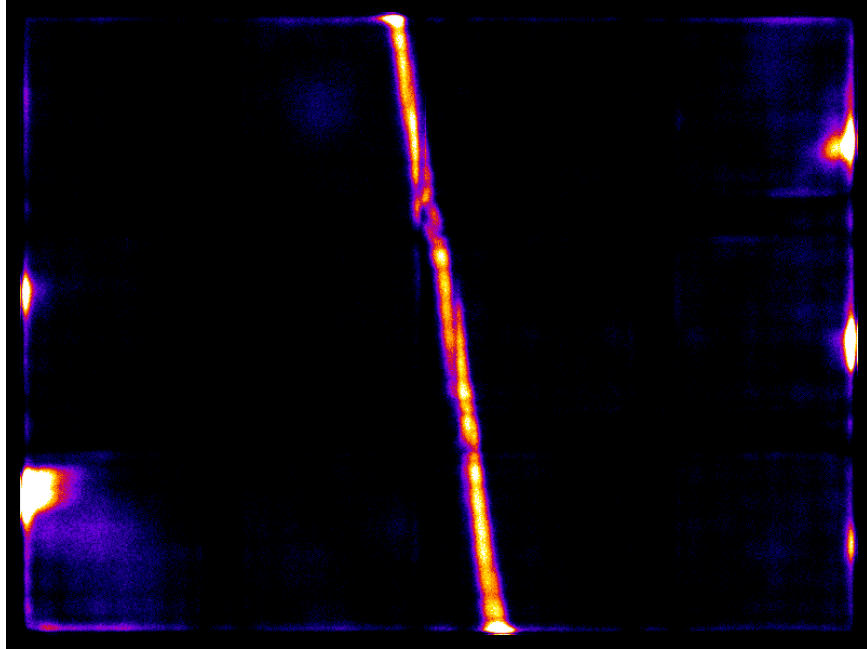
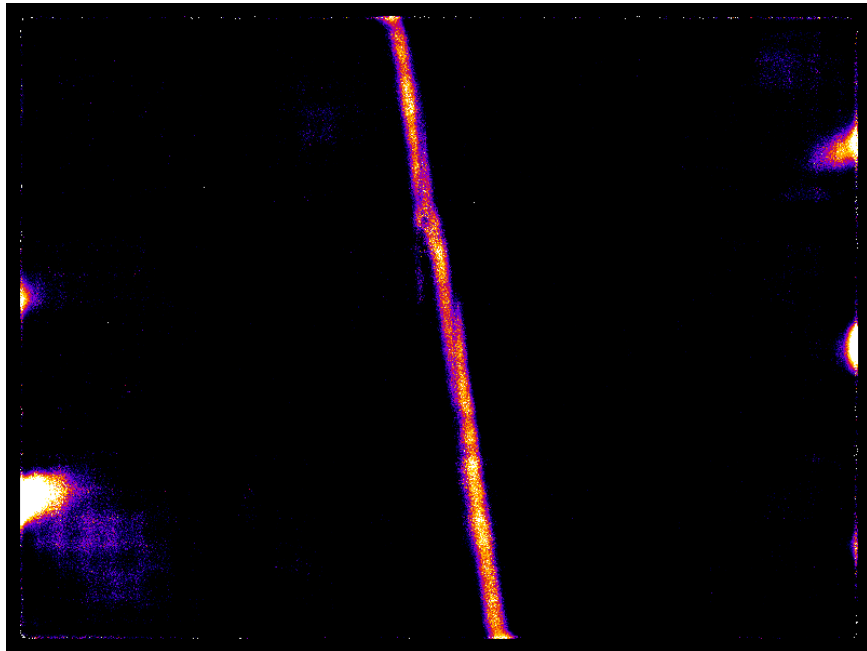


Figure 6.6: Experimental setup for generating a collimated Cs-137 line image on the full radiography panel.



(a) Uncorrected



(b) Corrected

Figure 6.7: Full-panel Cs-137 collimated line images that are a) before flood field correction and b) after flood field correction. ($N = 7.63 \times 10^6$ counts)

The line was rotated 10° in ImageJ, and an average profile of the line was generated and exported to Excel. Both the averaged line values from ImageJ and a fitted Gaussian curve to the values are shown in Figure 6.8. On the full panel, the Gaussian fit appeared to fit the profile from ImageJ better than the fit on the single ROSSPAD, though there is still some deviation on the left side of the profile. Figure 6.9 shows a 90% spatial resolution of approximately 0.42 line pairs per centimeter and a 10% spatial resolution of approximately 2.09 line pairs per centimeter. Both of these values are slightly less than the same values for the Cs-137 MTF in Chapter 5. This may be the result of geometric unsharpness [55]. The gap between the face of the scintillator and the tungsten blocks for the single ROSSPAD was only the width of a few pieces of tape, where the larger radiography panel has several millimeters of foam and aluminum separating the tungsten blocks and the scintillator package.

6.4.2 Cf-252 Images

A collimated Cf-252 edge was imaged across the face of the full-panel detector. Figure 6.10 shows a stack of high-density polyethylene (HDPE) measuring 15.25 ± 0.1 cm thick (equivalent to approximately 5 mean free paths assuming an average fission neutron energy of 2.105 MeV [53]) placed at the face of the panel. The radiography panel was again placed at a 10° angle. The 0.090 mCi Cf-252 neutron source was placed approximately 14.0 ± 0.1 cm away from the face of the HDPE blocks. The source was placed on a lead shelf-like object that allowed for approximately 2.5 ± 0.1 cm of lead to shield the detector from the gamma rays coming off of the daughter products of the source. Figure 6.11 shows the uncorrected and corrected signal-weighted edge images. The edge in the uncorrected image is almost impossible to see, but the corrected image does make the edge significantly more clear, highlighting the importance of correcting the radiographs using a flood field. Some slight artifacting at the boundaries of ROSSPADs can still be seen in the corrected image; overall, the radiograph is clear enough to use for an MTF measurement.

The edge was rotated 10° in ImageJ, and an average profile of the line was generated and exported to Excel. Both the averaged line values from ImageJ and a fitted ERF function to the values are shown in Figure 6.12. Since significantly more counts were used to generate this profile compared to the profile on the single ROSSPAD in Chapter 5, there is significantly

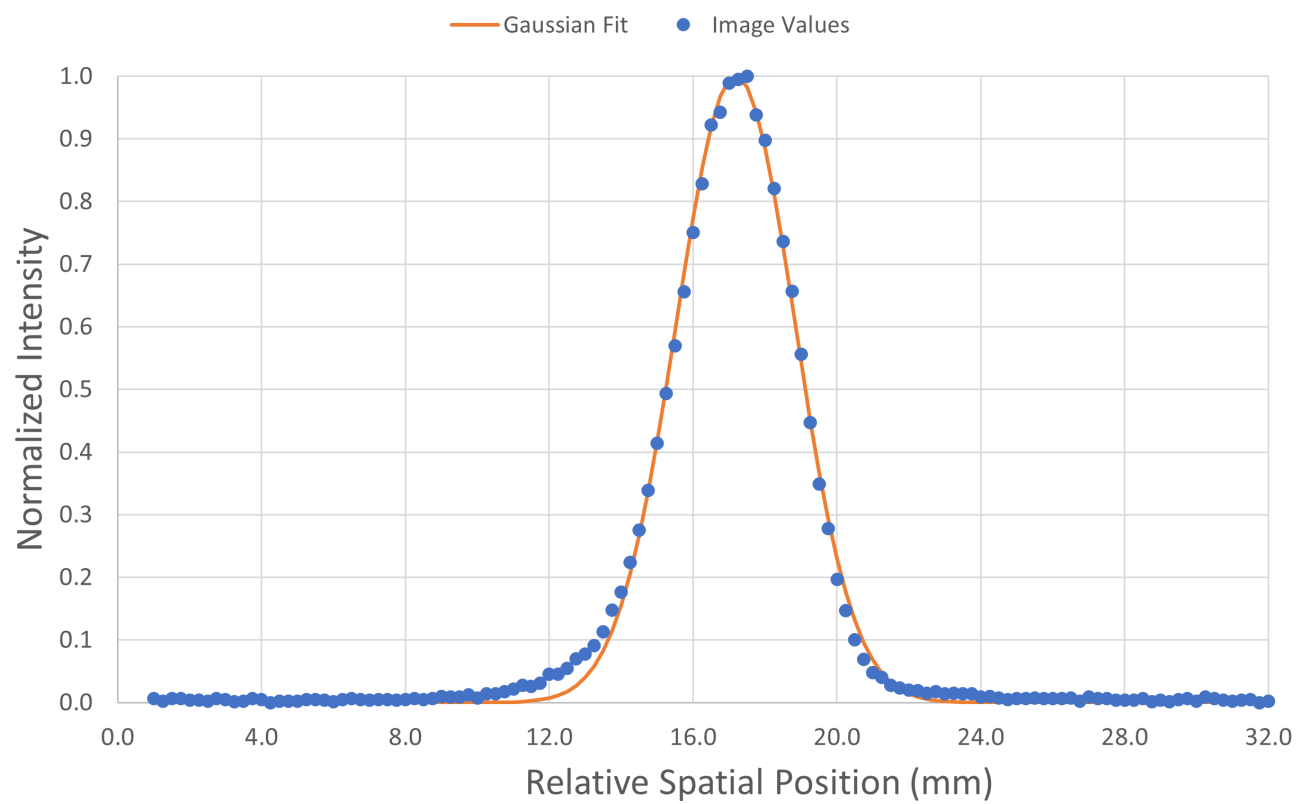


Figure 6.8: Line profile of the collimated Cs-137 image on the full radiography panel.

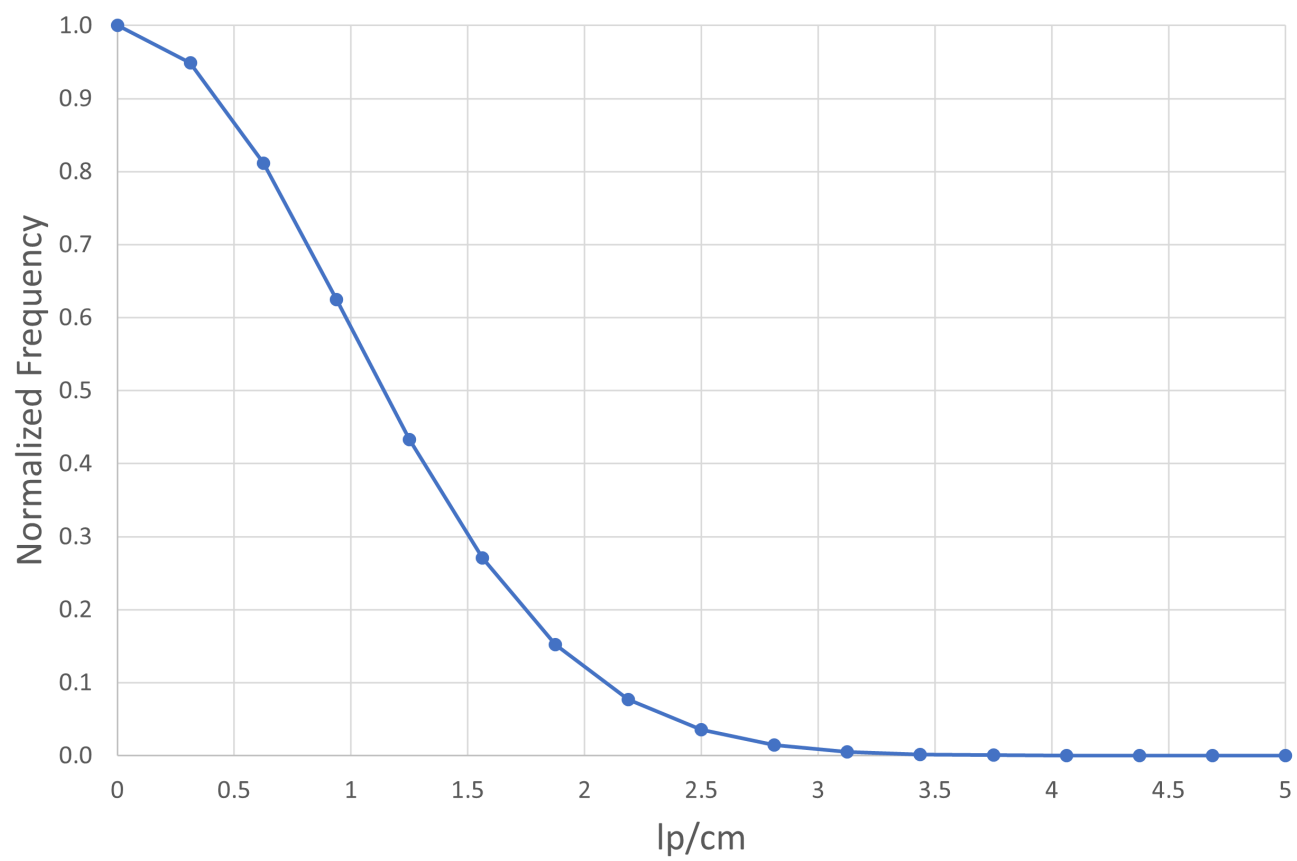


Figure 6.9: Modulation transfer function of the collimated Cs-137 line on the full radiography panel.

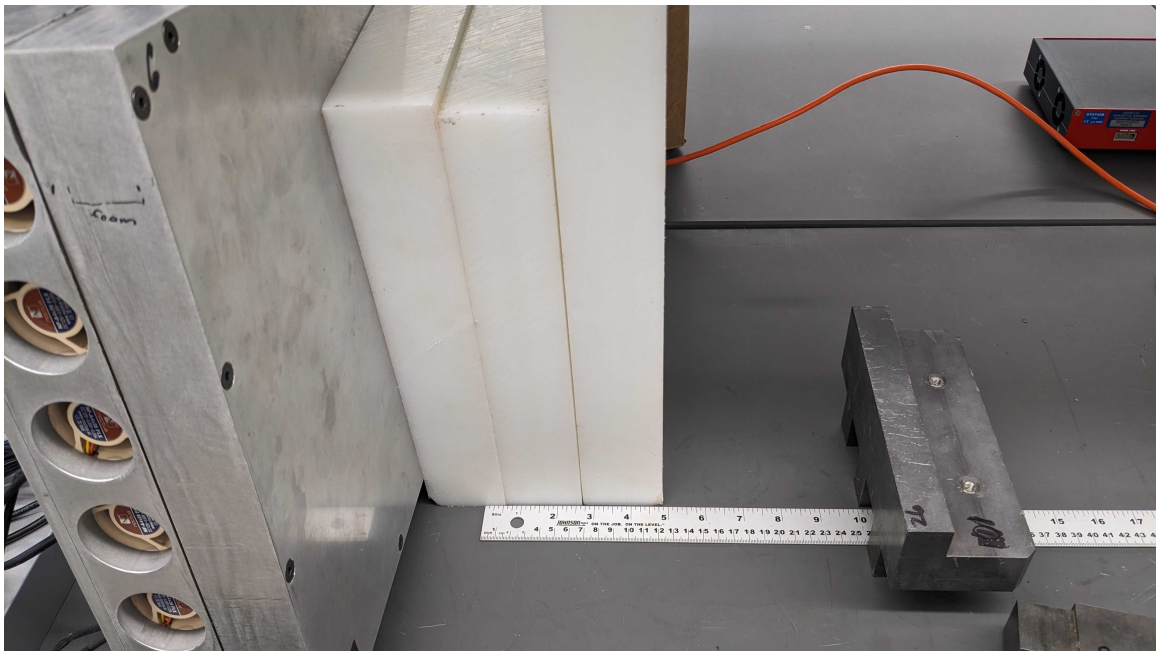
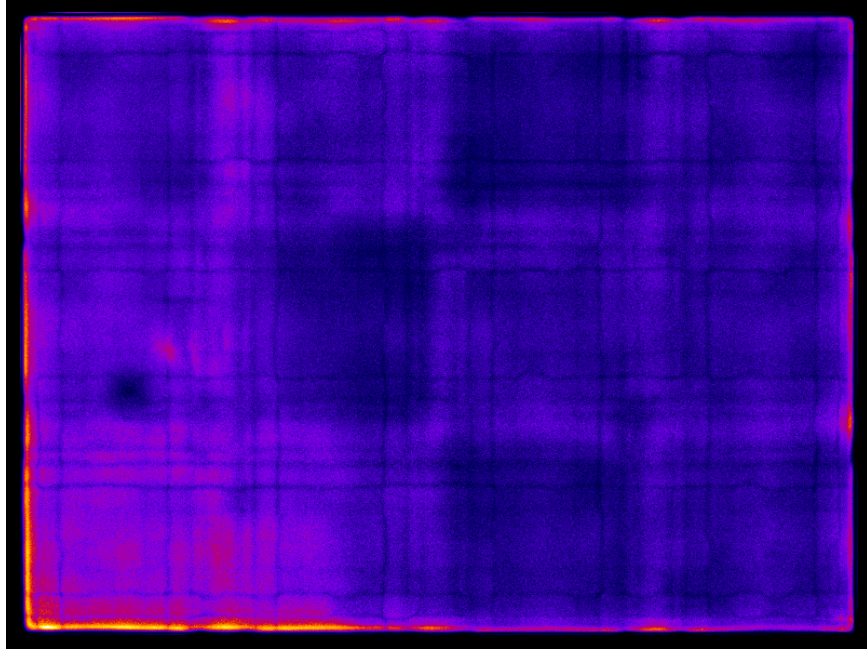
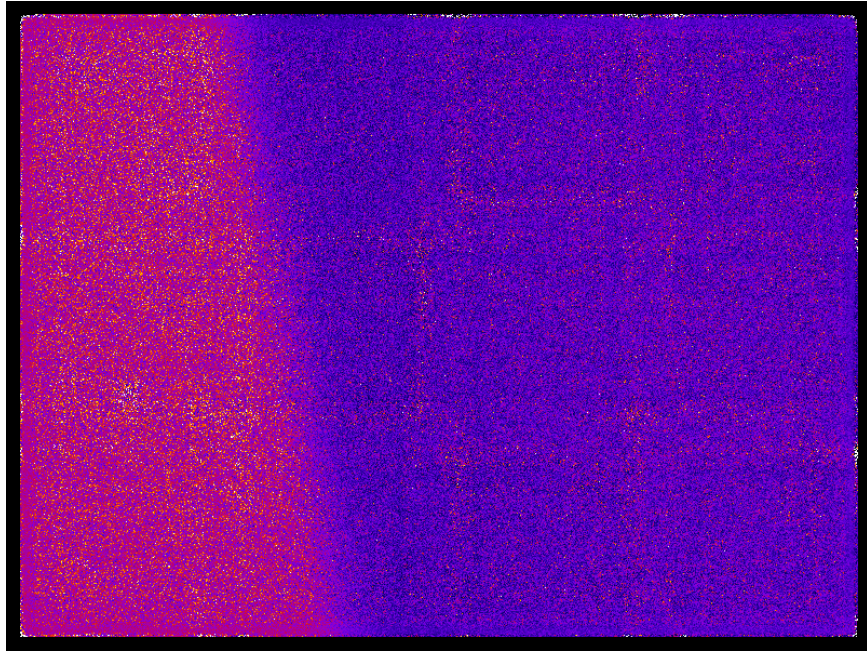


Figure 6.10: First experimental setup for generating a collimated Cf-252 image.



(a) Uncorrected



(b) Corrected

Figure 6.11: Full-panel Cf-252 collimated edge images that are a) before flood field correction and b) after flood field correction. ($N = 4.70 \times 10^7$ counts)

less variation, allowing for the function fit to approximate the experimental data much more closely. Figure 6.13 shows a 90% spatial resolution of approximately 0.24 line pairs per centimeter and a 10% spatial resolution of approximately 1.30 line pairs per centimeter. Both of these values are significantly less than the same values for the Cf-252 MTF in Chapter 5. While some loss of spatial resolution was expected due to the geometric unsharpness added from the design of the radiography panel, the amount loss does not correlate to the same amount of loss seen with the Cs-137 MTF.

A second Cf-252 experiment, shown in Figure 6.14, was performed in an attempt to reduce the geometric unsharpness created by the setup and potentially improve spatial resolution. Instead of an edge, a collimated line was generated using two 5.1 ± 0.1 cm HDPE blocks placed 0.2 ± 0.0025 cm apart, similar to the experiment performed with the Cs-137 gamma source. The source configuration was kept unchanged between this and the last setup, with the 0.090 mCi Cf-252 neutron source placed approximately 14.0 ± 0.1 cm away from the face of the HDPE blocks. The same lead object that allowed for approximately 2.5 ± 0.1 cm of lead to shield gamma rays from the Cf-252 source. Figure 6.15 shows the uncorrected and corrected signal-weighted line images. The thinner HDPE blocks used to generate the line decrease the contrast of the line compared to the rest of the image significantly. Because of this, the line is nearly impossible to see in the uncorrected image and just barely visible in the corrected one. Additionally, the lower number of counts cause by a decrease in acquisition time makes the data significantly more noisy, further complicating the MTF measurement.

The line was rotated 10° in ImageJ, and an average profile of the line was generated and exported to Excel. Both the averaged line values from ImageJ and a fitted Gaussian function to the values are shown in Figure 6.16. The extremely high amount of noise in the image and the lack of a true zero value where the HDPE blocks covered the panel meant that a Gaussian curve did not fit well to the experimental data. Though the results of an MTF measurement performed on this Gaussian curve may not be high-quality, it was still generated in case it offered any insight into the radiography panel; if the MTF showed promise, a second line measurement could be taken. Figure 6.17 shows a 90% spatial resolution of approximately 0.30 line pairs per centimeter and a 10% spatial resolution of approximately 1.46 line pairs per centimeter. While these values are a slightly better than the collimated edge results,

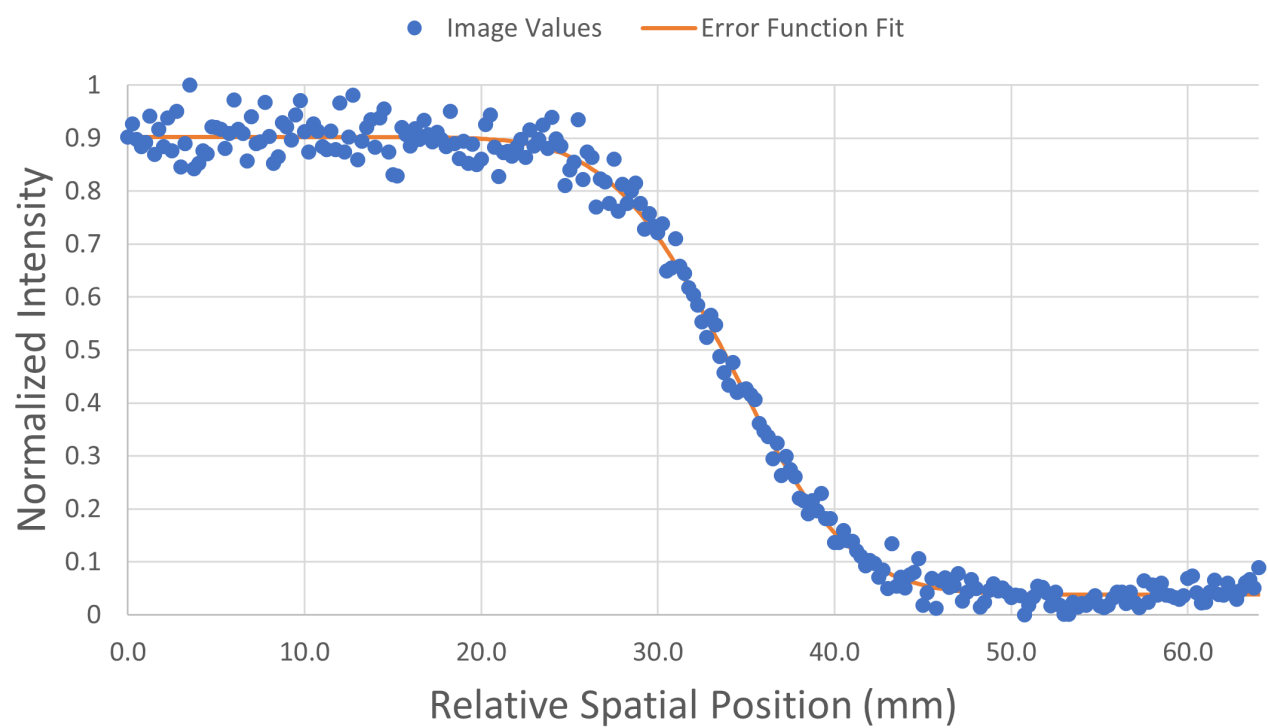


Figure 6.12: Line profile of the first collimated Cf-252 edge on the full radiography panel.

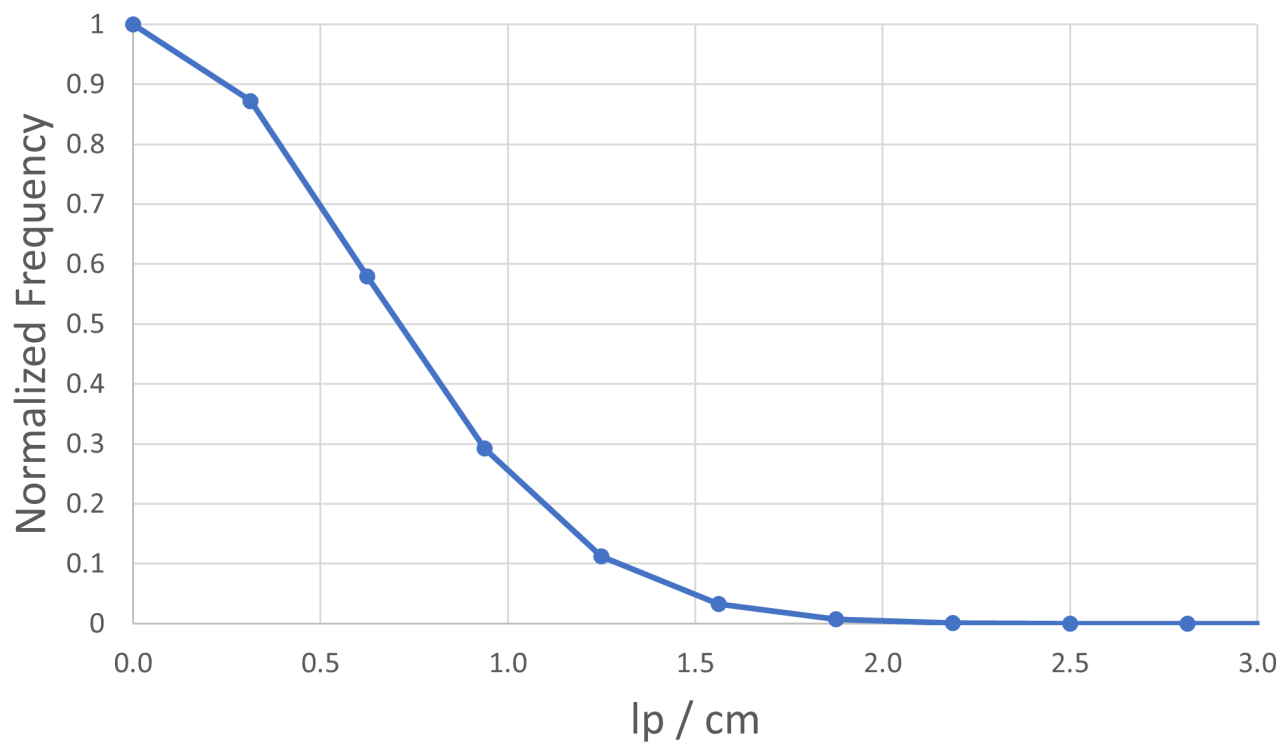


Figure 6.13: Modulation transfer function of the first collimated Cf-252 edge on the full radiography panel.

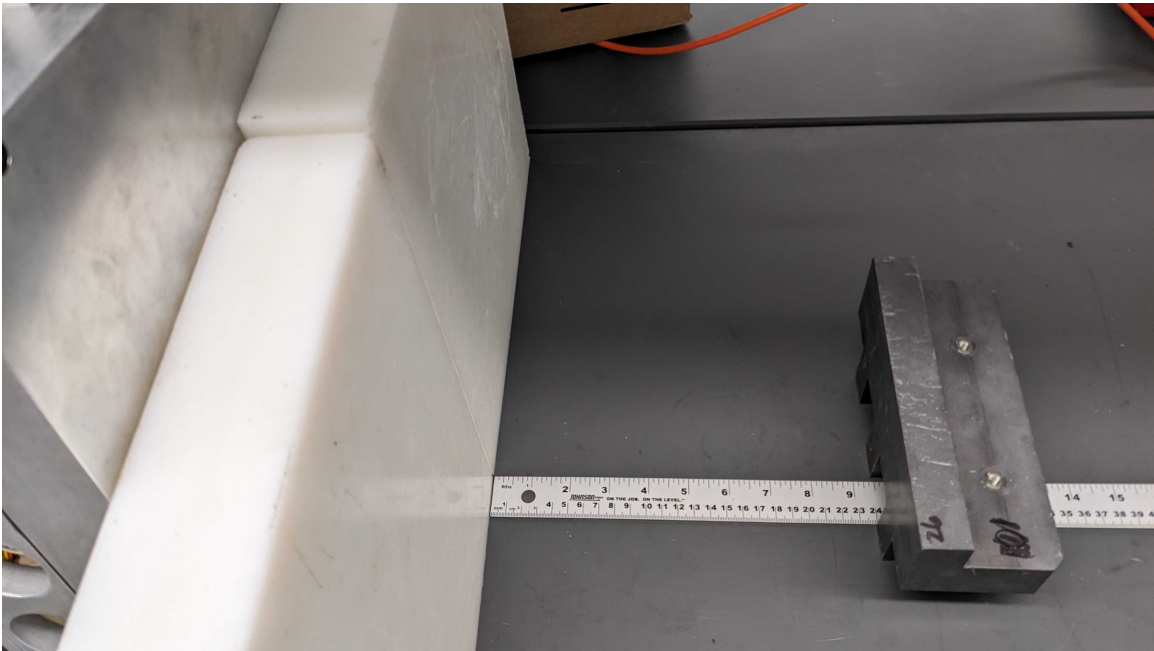
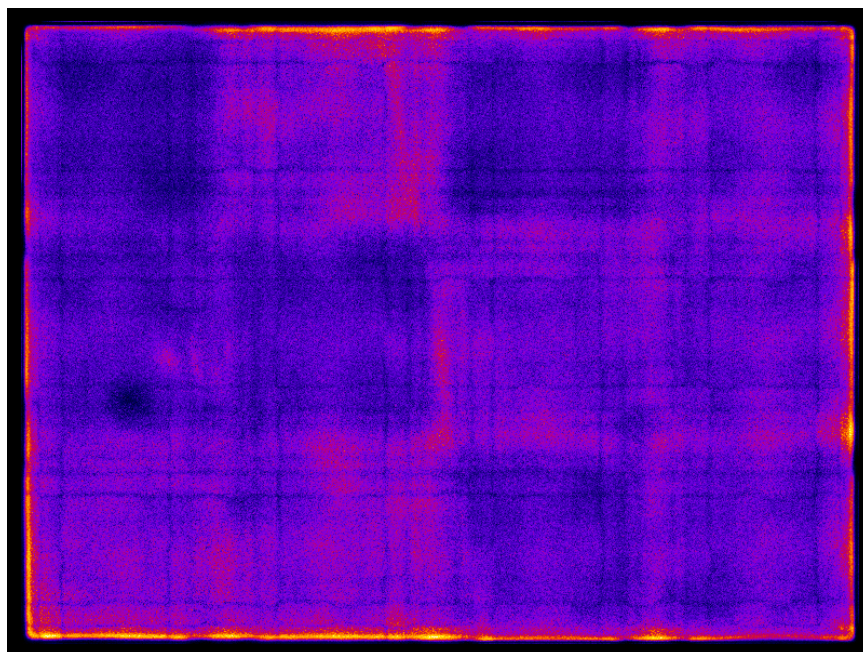
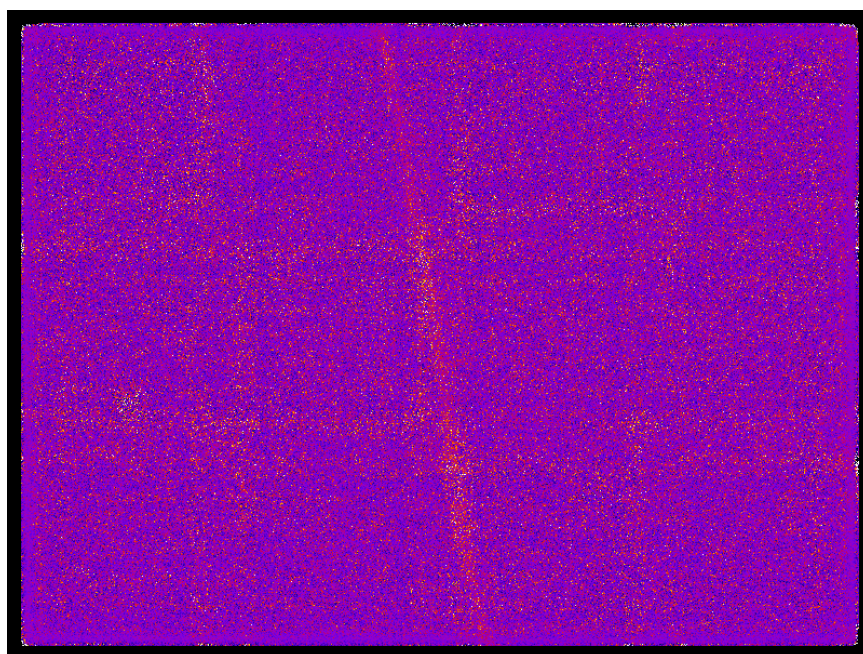


Figure 6.14: Second experimental setup for generating a collimated Cf-252 image.



(a) Uncorrected



(b) Corrected

Figure 6.15: Full-panel Cf-252 collimated line images that are a) before flood field correction and b) after flood field correction. ($N = 1.92 \times 10^7$ counts)

the high variance and poor Gaussian fit means that these values cannot be trusted as a true improvement in spatial resolution. Additionally, they are still far off from the Cf-252 MTF values in Chapter 5.

A third and final measurement was taken to quantify the spatial resolution of neutrons on the full-panel radiography system. The previous two experiments had different configurations compared to the experiment in Chapter 5. To account for possible changes in the spatial resolution based on the setup, the third measurement was set up to be similar to the first, where a gap separates the HDPE blocks from the face of the detector and the source from the HDPE blocks. Figure 6.18 shows a stack of high-density polyethylene (HDPE) measuring 15.25 ± 0.1 cm thick (equivalent to approximately 5 mean free paths assuming an average fission neutron energy of 2.105 MeV [53]) placed approximately 22.9 ± 0.1 cm from the face of the panel. A 0.090 mCi Cf-252 neutron source was placed approximately 40.6 ± 0.1 cm away from the face of the HDPE blocks. A sheet of lead 0.2 ± 0.0025 cm thick was placed in front of the Cf-252 source to block out some of the gamma rays Figure 6.19 shows the uncorrected and corrected signal-weighted line images. Much like the first edge image, the corrected radiograph is much more clear than the uncorrected radiograph, allowing for an accurate MTF measurement to be taken.

The edge was rotated 10° in ImageJ, and an average profile of the line was generated and exported to Excel. Both the averaged line values from ImageJ and a fitted ERF function to the values are shown in Figure 6.20. While there are fewer counts in this image compared to the first collimated edge, the variation is still lower than the variation the edge profile from Chapter 5. Figure 6.21 shows a 90% spatial resolution of approximately 0.27 line pairs per centimeter and a 10% spatial resolution of approximately 1.40 line pairs per centimeter. Both values are slight improvements compared to the first edge measurement. However, this and the other two full-panel MTF measurements are similarly far off from the measurement in Chapter 5, indicating that the loss in spatial resolution is not the result of a change in experimental setup but rather a change somewhere in the detector configuration or image generation process.

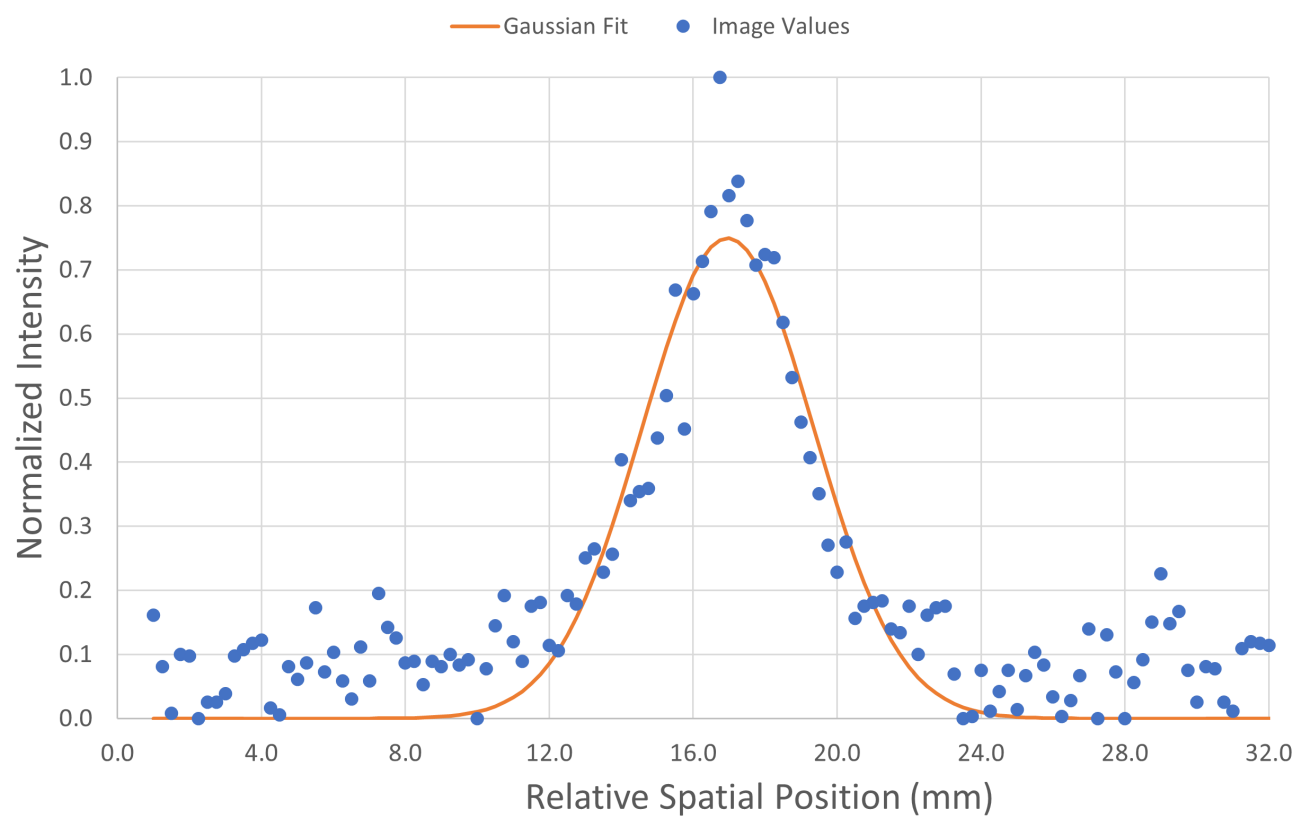


Figure 6.16: Profile of the collimated Cf-252 line on the full radiography panel.

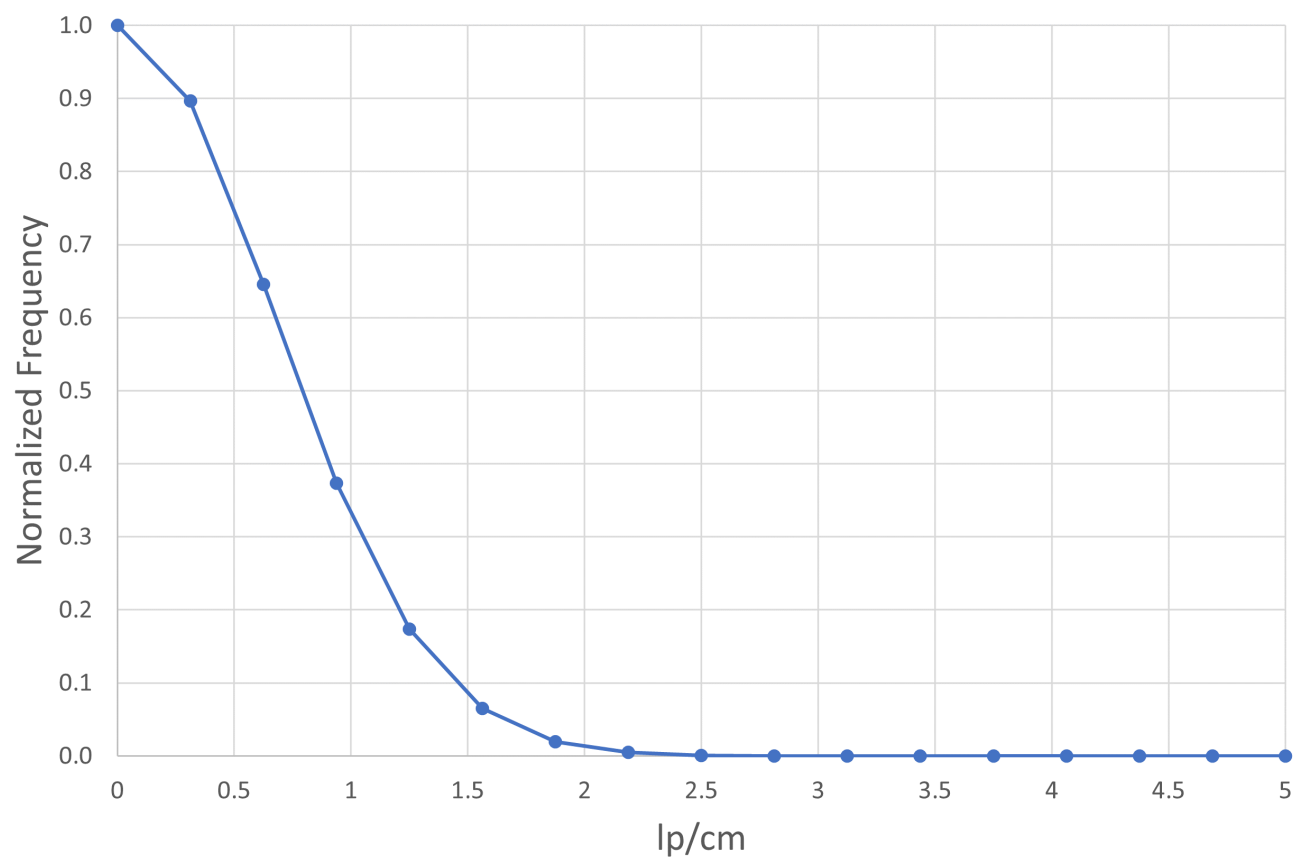


Figure 6.17: Modulation transfer function of the collimated Cf-252 line on the full radiography panel.

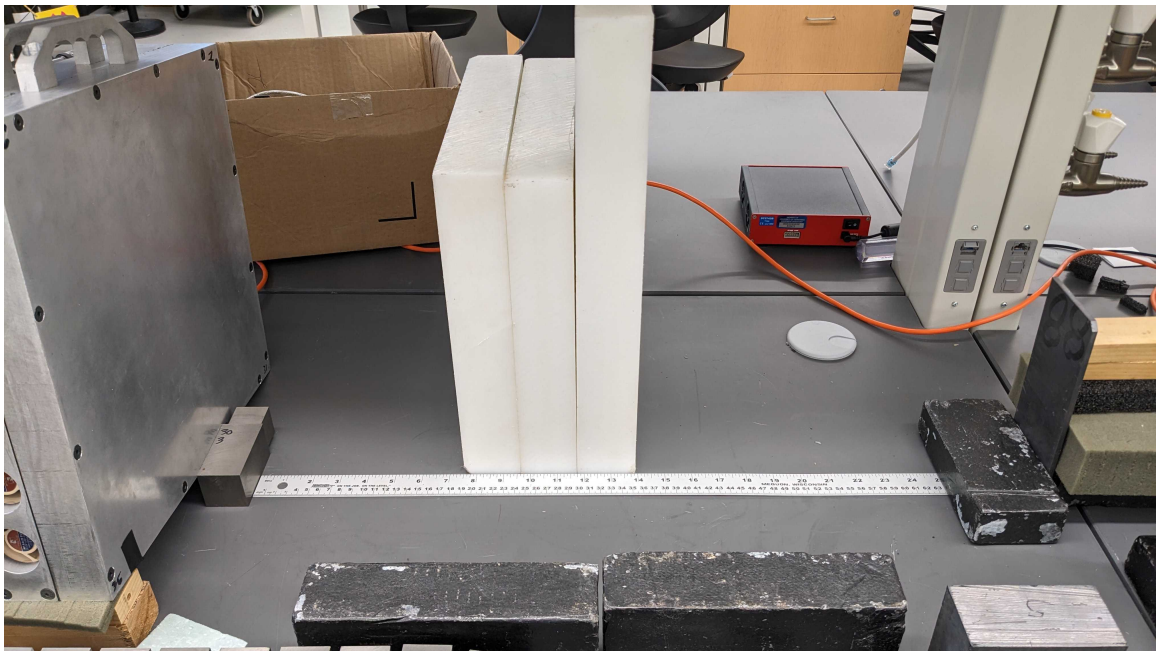
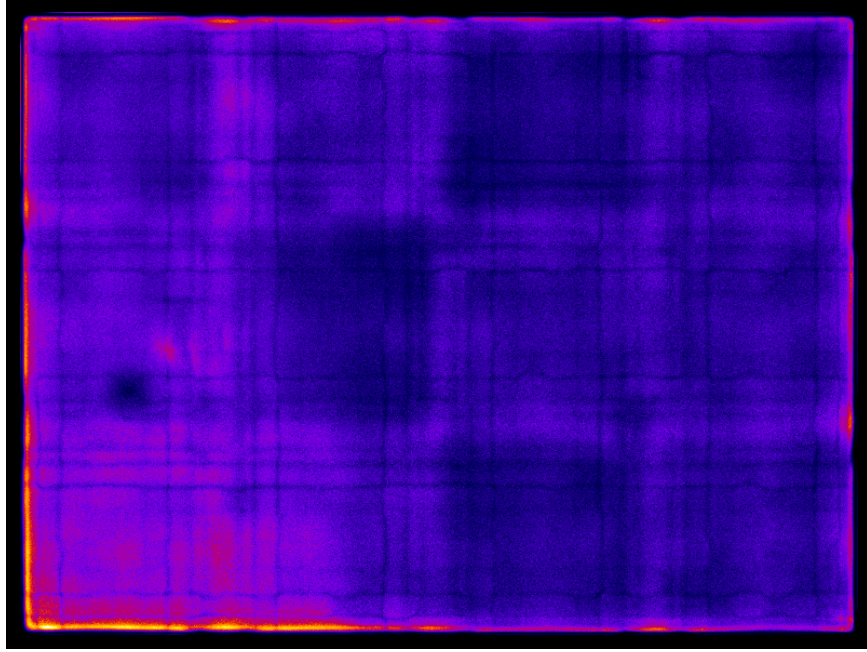
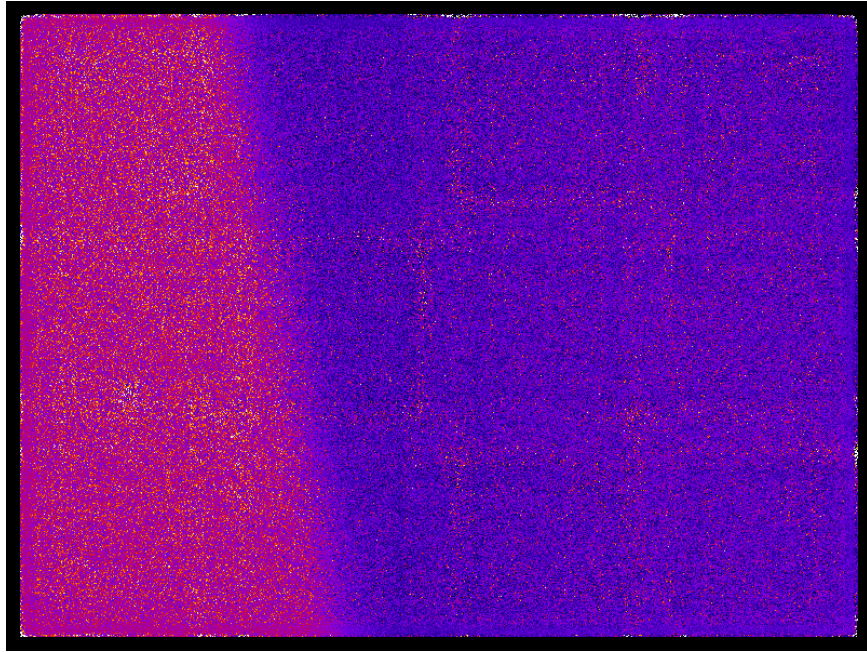


Figure 6.18: Third experimental setup for generating a collimated Cf-252 image.



(a) Uncorrected



(b) Corrected

Figure 6.19: Second full-panel Cf-252 collimated edge images that are a) before flood field correction and b) after flood field correction. ($N = 1.23 \times 10^7$ counts)

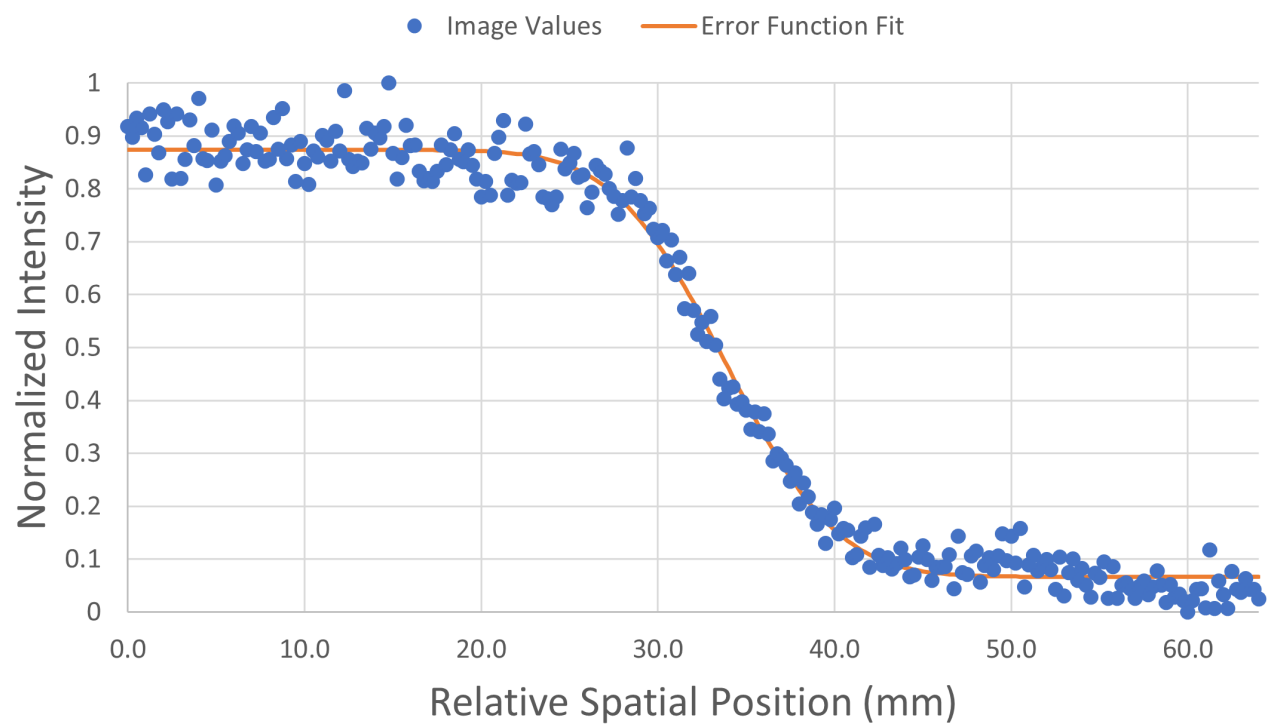


Figure 6.20: Line profile of the second collimated Cf-252 edge on the full radiography panel.

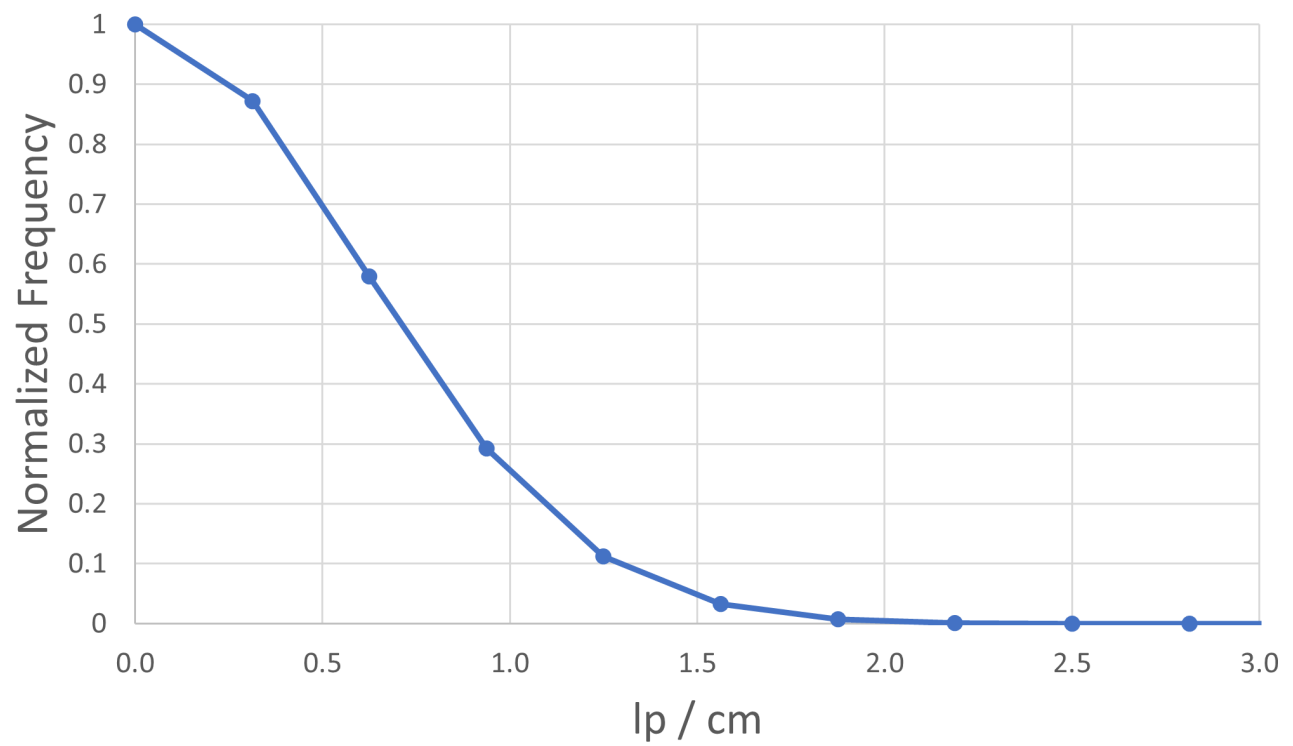


Figure 6.21: Modulation transfer function of the second collimated Cf-252 edge on the full radiography panel.

6.4.3 Comparison Between Detector Packages

Table 6.1 compares the spatial resolution of the different radiography systems for both gamma rays and neutrons. For gamma rays, the differences between the single-ROSSPAD system and the multi-ROSSPAD system are relatively minor. The 90% MTF was reduced by 10.6% and the 10% MTF reduced by 9.9%. The decrease in spatial resolution is likely the result in the change of the geometry of the setup for the experiment. With the single ROSSPAD detector, the tungsten blocks could be placed against the face of the scintillator with only tape between them. The full panel, however, has a gap between the scintillator face and the outside of the housing. Increasing the distance between the object and the detector panel is known to decrease spatial resolution, making detector configuration changes the most-likely culprit for resolution changes [55].

When moving to neutron radiographs, the changes between setups were much more drastic. The three experiments saw decreases in spatial resolution at 90% MTF of 65.7%, 57.1%, and 61.4% respectively. The 90% MTF values saw decreases of 61.2%, 56.4%, and 58.2%. These reductions are significantly higher than the reductions between the Cs-137 MTFs, despite the detector geometry being consistent between the Cs-137 images and the Cf-252 images. Additionally, changes to the experimental setup across the three Cf-252 full-panel MTF measurements demonstrate that the large decrease compared to Cs-137 images is likely connected to the type of radiation used (neutrons vs. gamma rays).

The most likely explanation behind the sudden decrease in spatial resolution is the introduction of more material in front of the ROSSPAD. The full-panel system has a aluminum lid that is a quarter of an inch thick, and compressible foam was added between the lid and the scintillator package to help keep the scintillator in place. The introduction of these materials likely leads to increased scattering for both gammas and neutrons. Gamma rays, after scattering, are more likely to be absorbed at their decreased energies within the aluminum or foam compared to fission spectrum neutrons. The difference between the energies of the two particles (0.662 MeV gammas vs. 2.105 MeV (average) neutrons) and the differences in interaction mechanisms means that the neutron images will be more blurry due to scattering than gamma images will be. Further testing on small-area, multi-ROSSPAD

Table 6.1: Comparison of Spatial Resolutions

Measurement Setup	90% MTF (lp/cm)	10% MTF (lp/cm)
Cs-137 Line (Single ROSSPAD)	0.47	2.32
Cs-137 Line (Multi-ROSSPAD)	0.42	2.09
Cf-252 Edge (Single ROSSPAD)	0.70	3.35
Cf-252 Edge #1 (Multi-ROSSPAD)	0.24	1.30
Cf-252 Line (Multi-ROSSPAD)	0.30	1.46
Cf-252 Edge #2 (Multi-ROSSPAD)	0.27	1.40

panels with and without the aluminum and foam are needed to further determine if this is the main cause of the decrease in spatial resolution.

6.5 Transmission Analysis

Since a Cf-252 fission neutron source was used to generate neutron images, it is important to demonstrate that radiographs with the source are actually comprised of neutrons and not mostly comprised of gamma rays from daughter products of the Cf-252 isotope. Normally, pulse-shape discrimination (PSD) would help in eliminating many of the gamma rays from the Cf-252 source. However, since the ROSSPAD detectors cannot perform PSD, a new method was developed as a quick test to determine if neutrons are present.

The ratio of the gamma rays that can transmit through an object is governed by the equation:

$$\frac{I}{I_0} = \exp\left(-\frac{\mu}{\rho} * \rho * x\right) \quad (6.2)$$

where $\frac{I}{I_0}$ is the fraction of the gammas that do not interact with the object, $\frac{\mu}{\rho}$ is the attenuation coefficient of the material, ρ is the density of the object, and x is the thickness of the object. Correction using the flood field gives an approximation of $\frac{I}{I_0}$, and by rearranging Equation 6.2 into:

$$\frac{\mu}{\rho} = -\frac{\ln \frac{I}{I_0}}{\rho * x} \quad (6.3)$$

the approximate transmission coefficient for the incident particles in the material can be derived and compared to NIST XCOM [4].

Figure 6.22 shows a simple test of the neutron radiography capabilities for the full-panel radiography system. The resultant radiograph generated using a Cf-252 source is shown in Figure 6.23. Using ImageJ, the log of the ratio of the image to the flood field is calculated for a large portion of the tungsten block, shown in Figure 6.24 [50]. By plugging the mean value from ImageJ into Equation 6.3, as well as the density of tungsten ($19.28 \frac{g}{cm^3}$) and the thickness of the tungsten block ($3.81cm$), an approximate value for the attenuation coefficient of the particles through the tungsten is found to be $1.572 \times 10^{-2} \frac{cm^2}{g}$. In comparison, XCOM lists the total attenuation coefficient of 0.662 MeV gamma rays (from Cs-137) through tungsten

to be $9.793 \times 10^{-2} \frac{cm^2}{g}$. These numbers indicate that the particles from the Cf-252 neutron source are approximately 6.2 times more penetrating than the gammas from a Cs-137 source, an indication that the majority of the events in the image come from neutrons and not from gamma rays.

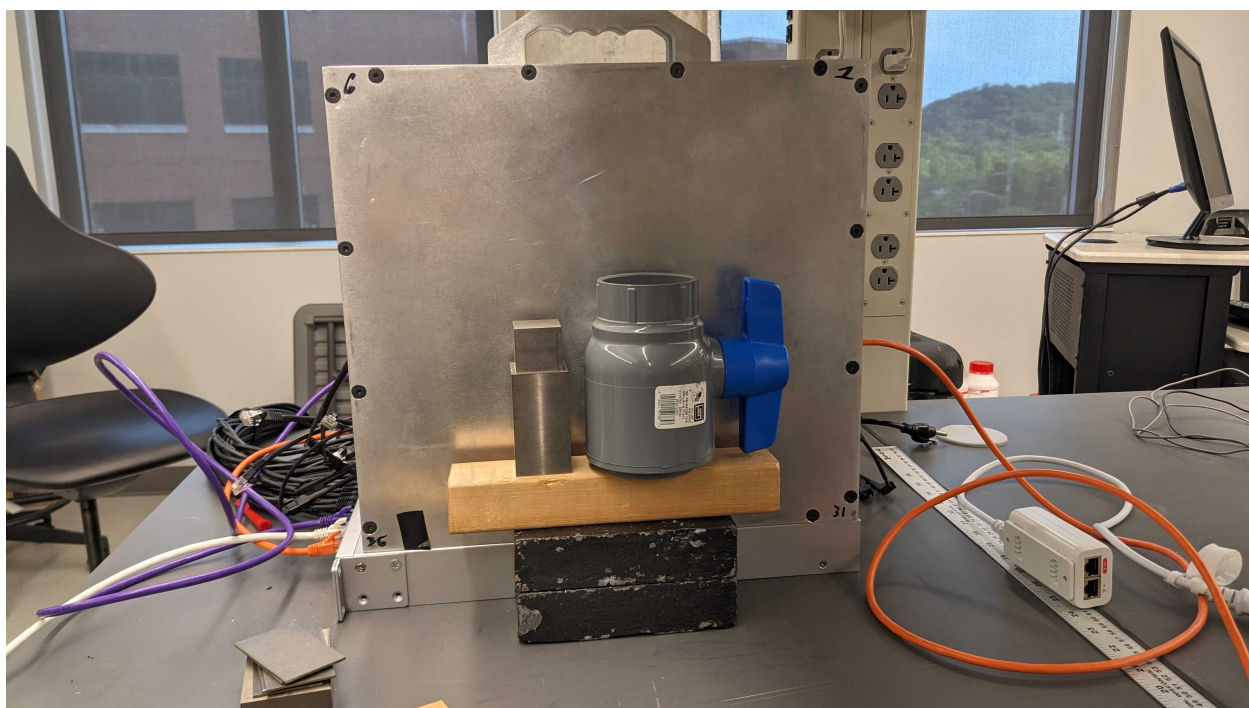


Figure 6.22: A tungsten block and a plastic pipe vale in front of the radiography panel.

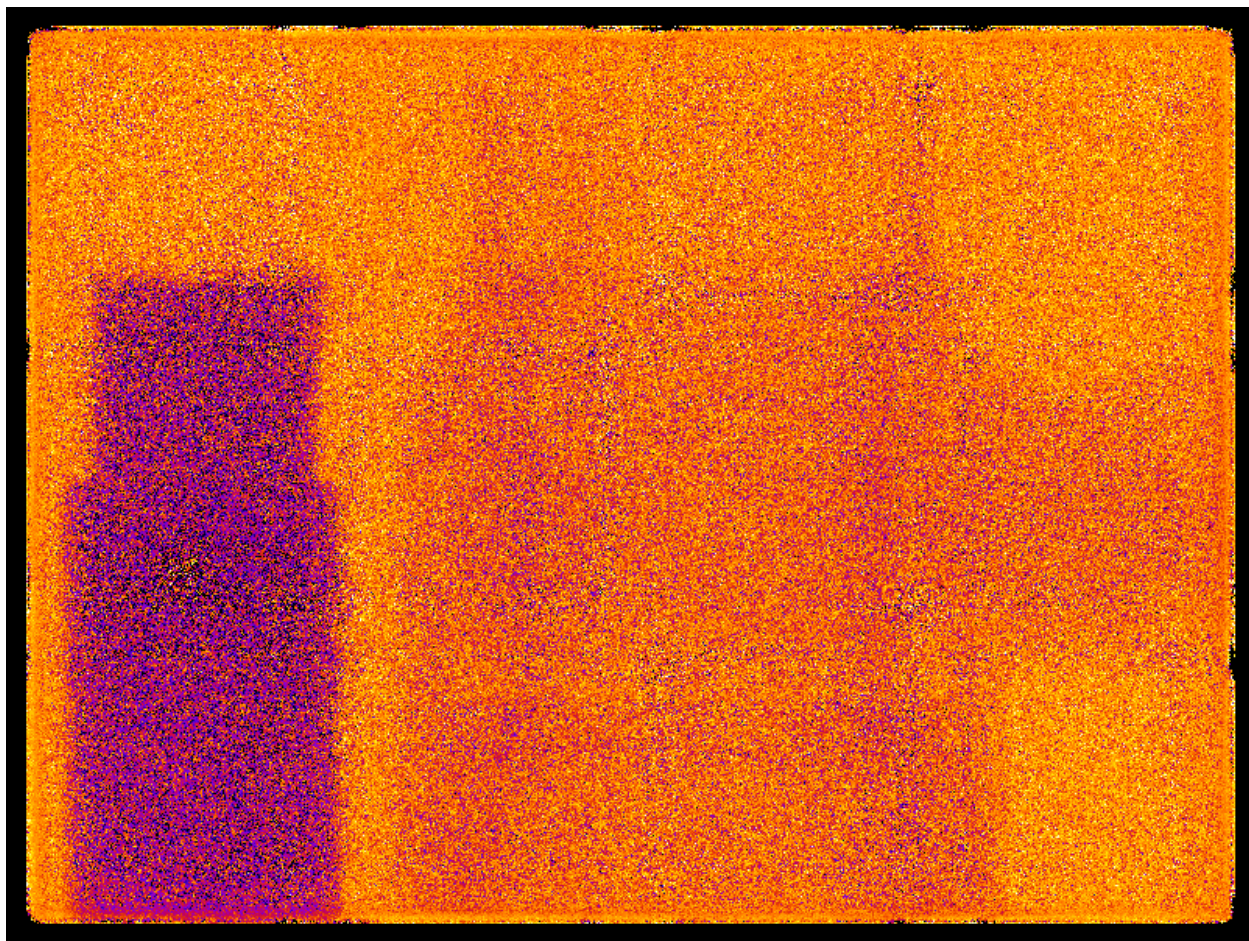


Figure 6.23: The resultant neutron radiograph of the tungsten block and the plastic valve.

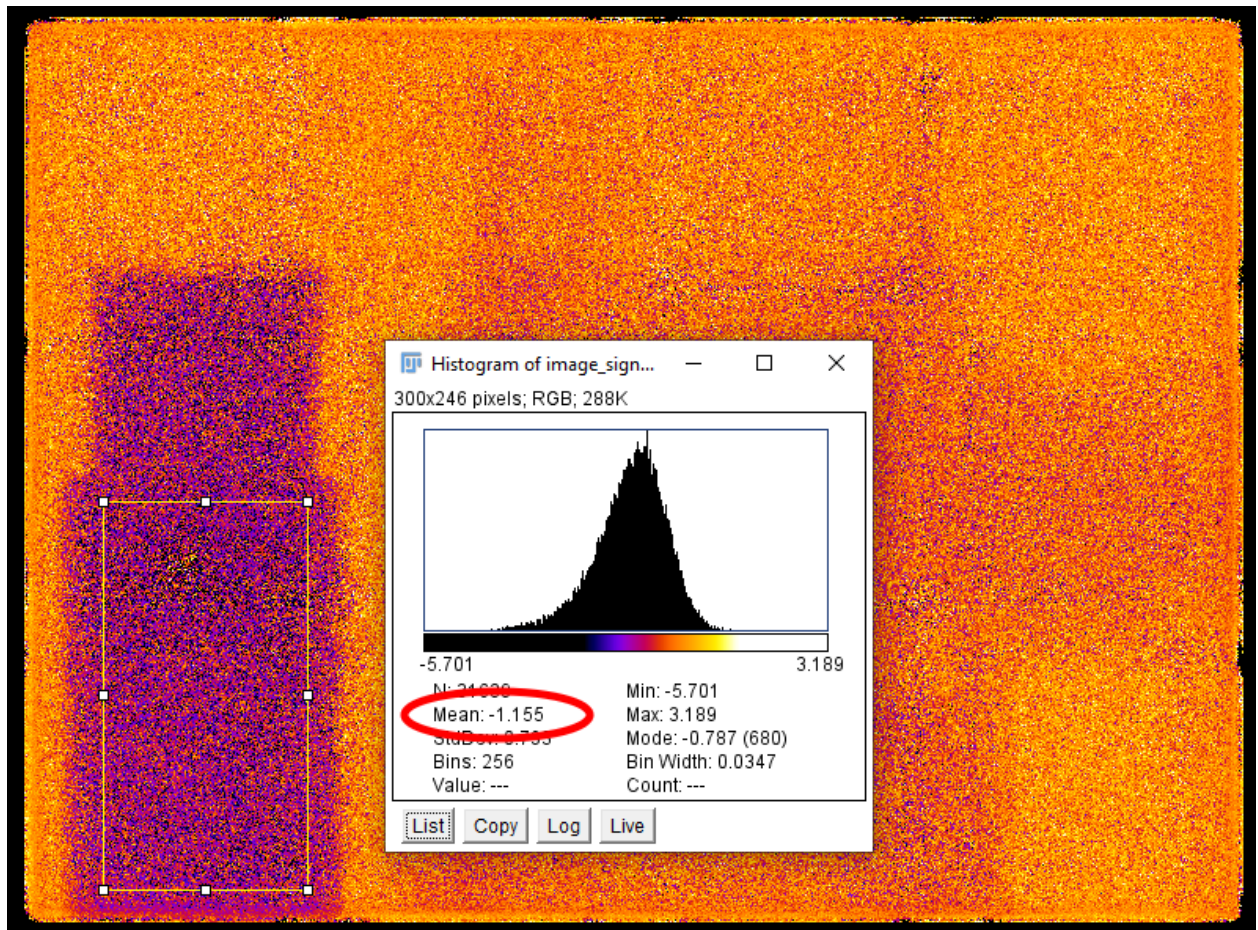


Figure 6.24: Mean value of the log of the ratio of the image and the flood field, circled in red. Value generated with ImageJ.

Chapter 7

Signal-to-Noise Ratio (SNR)

Optimization

Improving the spatial resolution of the neutron radiographs generated from the full-panel detector system requires optimization of several parameters within the image generation code. The lack of pulse-shape discrimination (PSD) and overall difficulty tuning the ROSSPAD detectors means that images generated on the full-panel system have a low signal-to-noise ratio (SNR). Low SNR introduces statistical variation into the images and this decreases spatial resolution. In an effort to increase SNR within the panel, four parameters that impact the generation of images were studied. For each of the four parameters, A flood field and a flood field corrected edge image are generated. An MTF measurement on the edge is generated for each change in parameter, with all of the MTF curves plotted together on one final graph. Additional images for each parameter can be found in [Appendix C](#).

Previous MTF measurements in [Chapter 6](#) were generated at what are considered "default" values for each parameter. When one parameter is changed in this chapter, the remaining three will be kept at default level in order to determine the impact of the lone parameter being studied. Default values are indicated in each of the four comparison plots, and an explanation for why it was set as the default are included in each subsection.

7.1 Parameters for Optimization

7.1.1 Lower Bound Signal Cutoff

A lower-bound cutoff prevents events that fall below a specific signal value to not be included in the final image. Low-signal events could potentially be the result of low-energy neutrons that have scattered multiple times or x-rays produced from incident particle interactions on the housing of the full panel. Theoretically, filtering these low-energy events will allow for more of the data to come from the source itself and not from secondary particles. However, since single-ROSSPAD results from Chapter 5 did not include a signal cutoff, a signal cutoff was not included by default for the full-panel images.

Figure 7.1 shows the MTF graphs for several lower-bound signal cutoff values. While the cutoff values of 1000 and 3000 appeared to have MTF graphs nearly the same, overall there was a trend of decreasing spatial resolution with increasing signal cutoff threshold. While it may be possible that low-energy secondary particles are being filtered out, the lower cutoff values could be removing true events from the image, worsening the spatial resolution. As the cutoff value increases, the number of events that make up the image decreases, which generally leads to more uncertainty and thus lower spatial resolution.

7.1.2 Upper Bound Signal Cutoff

An upper-bound cutoff acts similarly to the lower-bound cutoff. This time, events that fall above a certain signal threshold value are excluded. High-signal events may be the result of cosmic rays that interact with the detector. Muons, though hard to detect, have a high amount of energy. If they scatter within the plastic scintillator, they will produce a significant amount of light and will not contribute to the overall image. Removing them may improve image quality and spatial resolution. Again, an upper-bound signal cutoff was not included in Chapter 5, and was thus not included by default.

Figure 7.2 shows the MTF graphs for several upper-bound signal cutoff values. While the change in spatial resolution was less drastic compared to the change in MTF shown in Figure 7.1, adding an upper-bound signal cutoff decreased the spatial resolution of the

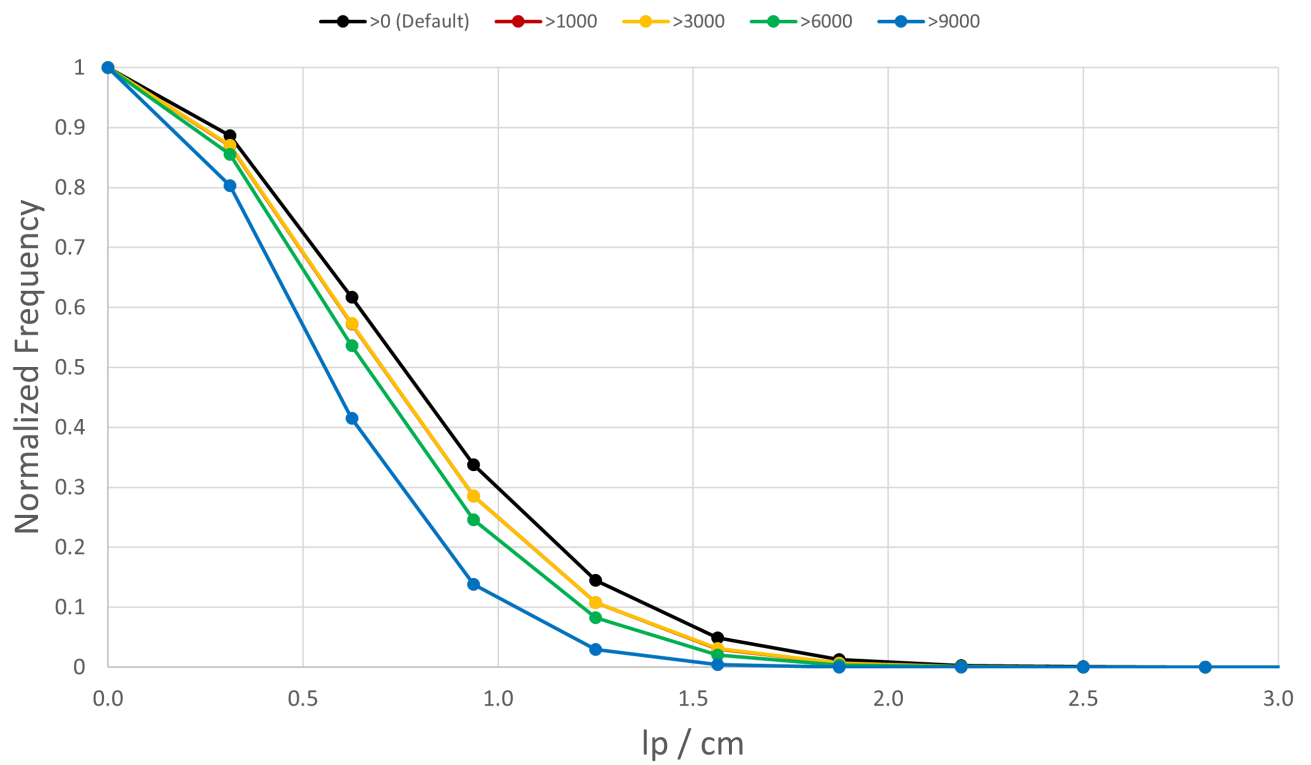


Figure 7.1: Comparison of MTFs for different lower bound cutoff values.

system. While removing high-signal events may help, the low spectral range of the ROSSPAD detectors may pile up some higher-energy neutron interactions with high-energy cosmic ray interactions. By setting an upper-level cutoff, some legitimate data may still be removed, though it is clear that this cutoff has less of an impact overall.

7.1.3 Noise Floor Cutoffs

When initially looking to generate images on the full-panel system, a common issue seen was the introduction of "greedy SiPM" artifacts, where there would be slightly increased counts at the centers of SiPMs compared to their edges. The prevailing theory was that lower-energy events would only set off a small number of SiPMs on a given ROSSPAD. The center triggering SiPM will have a larger signal value compared to the surrounding SiPMs. If there are too few SiPMs that have signal values significantly above the noise floor, the center of the event will be disproportionately influenced by the location of the triggering SiPM. To compensate for this, a method was added to take the SiPM electronic noise values and compare them to the signals of the SiPMs for a given event. If not enough SiPMs were above some multiple of the noise floor, the event would be rejected. By default, the threshold value was set to 3 times the electronic noise of a given SiPM. This value, at the time, produced uncorrected images that looked the cleanest of any of the other values; after flood field correction methods were introduced, this was rendered partially obsolete, though it was assumed that it may still aid in producing high-resolution images.

Figure 7.3 shows the MTF graphs for several multipliers of the noise floor used as a signal cutoff. Similar to the other cutoff values used, setting the floor to 0 (essentially using no filtering) leads to the best spatial resolution. With other noise floor values set, they appear to decrease the spatial resolution of the images, though there is no clear trend, and they all coalesce near each other. This indicates that while adding a noise floor cutoff does impact spatial resolution, it does not have a clear relationship depending on the level selected. Simply removing data of any form from the image itself is what appears to have the most impact on the spatial resolution of the image. Other optimization settings used in conjunction with noise floor cutoffs may help determine a trend. No matter the trend, however, the best method is to not have a noise floor cutoff at all.

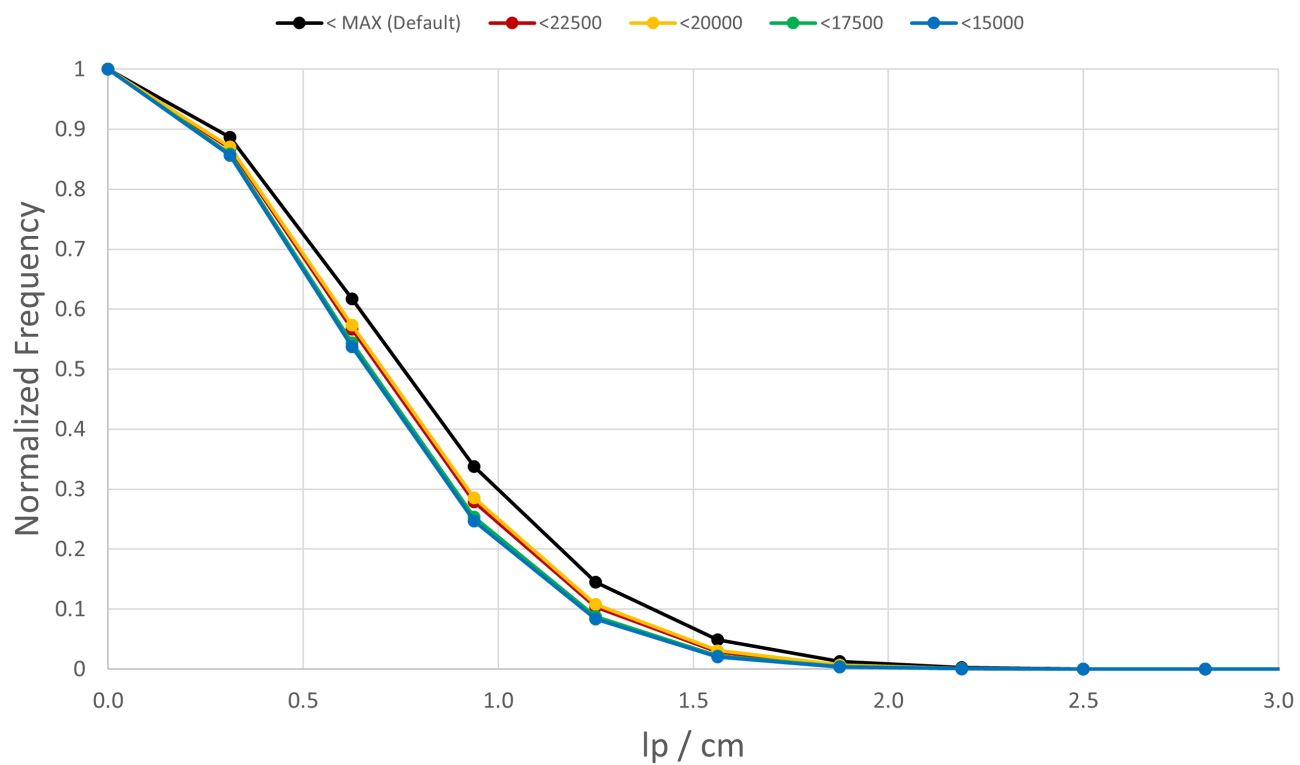


Figure 7.2: Comparison of MTFs for different upper bound cutoff values.

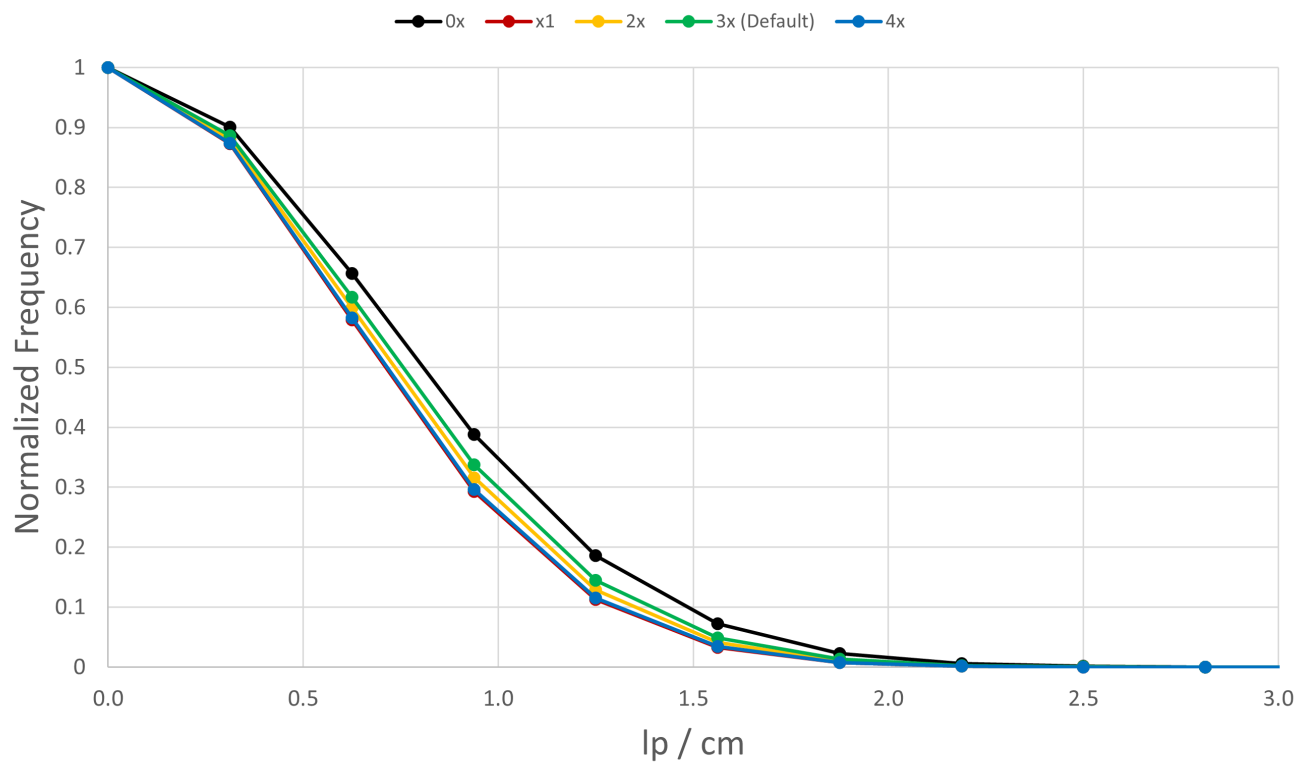


Figure 7.3: Comparison of MTFs for different noise floor cutoff values.

7.1.4 Cluster Size

The other parameter created in order to improve the quality of uncorrected images is referred to as "cluster size." When an event is being localized, a tally is made of how many SiPMs have signals above the noise floor cutoff. For the event to be counted, this tally must reach a certain threshold. This was initially set to 9 SiPMs above the noise floor (a cluster size of 9), as it produced the best uncorrected images and did not remove too much of the raw data. Though the artifacts seen in the images in Appendix C are a lot more extreme as this cluster size is reduced, this was again fixed using the flood field correction method. It should be noted that the noise floor cutoff is still in effect; signals that are not above the noise floor are just not used in the localization process, even if the event in general is kept.

Figure 7.4 shows the MTF graphs for several different cluster size cutoffs. Interestingly, this was the only parameter of the four checked where there was little to no change in the MTFs depending on the cluster size cutoff used. This is despite the fact that as the cluster size cutoff is increased, the amount of events that make it into the image decreased. Figures 7.3 and 7.4 show that the noise floor cutoff had more of an impact on the actual spatial resolution of the system, where the cluster size only had an impact on how the raw image looked.

7.2 Comparison of Parameters

Tables 7.1, 7.2, 7.3, and 7.4 show the 90% and 10% MTF values for each parameter tested. Removing the noise floor cutoff entirely from the localization process had the largest positive impact, bringing the 90% MTF from 0.27 line pairs per centimeter to 0.31 line pairs per centimeter and the 10% MTF from 1.40 line pairs per centimeter to 1.49 line pairs per centimeter. The parameters generally had a negative impact on the spatial resolution of the images. The parameters tested were unable to return the spatial resolution of the full-panel images seen in Chapter 6 to the spatial resolution values seen in Chapter 5. Removal of these parameters from the image generation process completely will produce the best images.

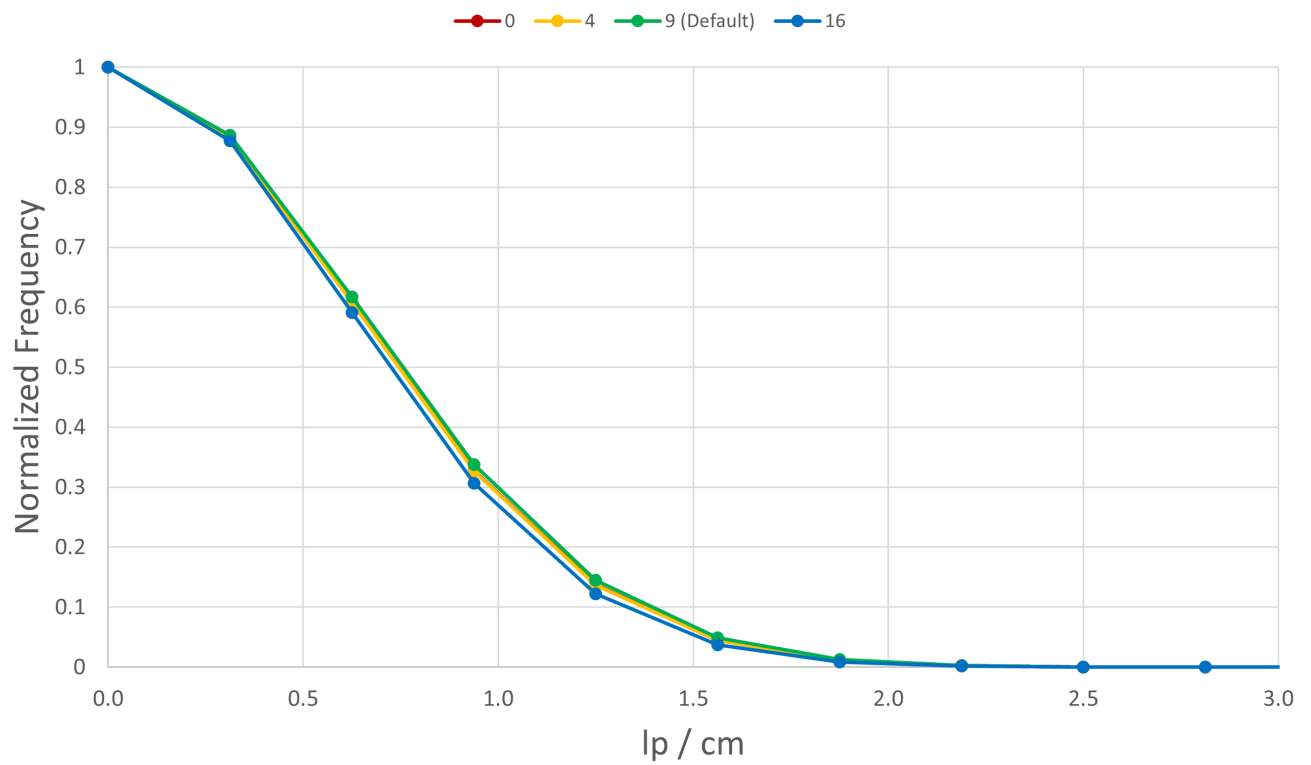


Figure 7.4: Comparison of MTFs for different high-signal cluster sizes.

Table 7.1: Comparison of Lower-Bound Signal Cutoff MTF Values

Lower-Bound Signal Cutoff	90% MTF	10% MTF
0 (Default)	0.27	1.40
1000	0.24	1.28
3000	0.24	1.28
6000	0.22	1.21
9000	0.16	1.05

Table 7.2: Comparison of Upper-Bound Signal Cutoff MTF Values

Upper-Bound Signal Cutoff	90% MTF	10% MTF
MAX (Default)	0.27	1.40
22,500	0.24	1.26
20,000	0.24	1.28
17,500	0.22	1.23
15,000	0.22	1.22

Table 7.3: Comparison of Noise Floor Cutoff MTF Values

Noise Floor Cutoff	90% MTF	10% MTF
0x	0.31	1.49
1x	0.24	1.30
2x	0.26	1.35
3x (Default)	0.27	1.40
4x	0.25	1.31

Table 7.4: Comparison of Cluster Size Cutoff MTF Values

Cluster Size Cutoff	90% MTF	10% MTF
0	0.27	1.38
4	0.27	1.37
9 (Default)	0.27	1.40
16	0.25	1.33

Chapter 8

Conclusions & Future Work

8.1 Research Outcomes

This research sought to demonstrate a first-of-a-kind scalable radiography system based on the IDEAS ROSSPAD readout module. While the initial research was for the system to be a fast-neutron specific radiography panel, analysis of the system with both photons and neutrons demonstrated its ability to perform radiography with both modalities. For imaging with a single ROSSPAD module, Figures 5.7 and 5.12 demonstrate the ability to generate radiographs with 10% MTF spatial resolutions better than the spatial resolution of the bare, 6-mm-pitch SiPM board, as discussed in Section 5.1.4. The MTF values in Figures 6.9, 6.13, 6.17, and 6.21 show that spatial resolution remained similar for gamma rays, but neutron radiographs lost significant spatial resolution.

As demonstrated in Chapter 5, weighted-average localization appears to be the most promising method. A novel 2D Gaussian localization method was proposed as an alternative to weighted-average localization. The 2D Gaussian method was developed with the goal of mitigating some of the artifacting issues present within the single-ROSSPAD radiographs generated with the weighted average method. However, the high computational cost of the 2D Gaussian localization method has proven it ineffective at this stage for use in a full-panel radiography device. Table 5.1 shows that only a 7.8% improvement requires over 19 times as long to compute. The multi-ROSSPAD panels generate significantly more events that need

to be localized, meaning that image generation times can balloon to the order of days to complete.

There is no surefire way to improve the spatial resolution of the full-panel system. Despite changing four different parameters of the system - lower bound cutoff, upper bound cutoff, noise floor cutoff, and cluster size cutoff - spatial resolution values from data presented in Chapter 6 could not be improved to the same levels seen in Chapter 5. Optimization of these parameters demonstrated the need to take a large amount of data, which guides further research into the best practices for setting up an experiment. It also indicates that other factors outside of data collection and processing are the reason for the drop in spatial resolution of the full-panel system.

Portable fast-neutron radiography is a nondestructive evaluation modality that is still relatively in its infancy. This first-of-a-kind full-panel system demonstrates that the capability to perform field neutron radiography can be developed to a point where it can actually be deployed in a user facility. The system is the first ROSSPAD-based neutron imaging system to be published at the time of writing. Further developments can bring this research to a higher technology readiness level, allowing for more widespread use of this modality in a wide variety of industries.

8.2 Lessons Learned

A large portion of this research went into the development of new methods to take data from the IDEAS ROSSPAD module and store it in a way that was easily readable for anyone who may need to use the system later. While the off-the-shelf Testbench software was useful for a wide range of use cases, developing methods that completely bypass Testbench mean that data acquisition was faster and more stable. Developing these tools also allowed for a chance to learn about wired networking, parallel computing, and handling of big data sets.

Chapter 4 demonstrated that, with any detector system, it is important to understand what is considered "optimal" operation and what is considered "faulty" operation. Every system out there has the potential to break at any point in the research process. Much was learned about how specifically the ROSSPADs operate and how they can be characterized

in order to determine which ones are working and which are not. However, the lessons from this can be applied to any system; developing diagnostic tools is an important step for any fundamental research, especially if the systems used are not developed in house and thus not intimately known by those performing the work. This also stressed the importance of understanding the systems being used before they are deployed in a larger setup. Since characterization of the ROSSPAD modules was not properly done before they were installed in the larger radiography array, a large section of the panel could not be used in the research. This could have been avoided with good characterization and testing at the very beginning of the project.

Developing the skills to quantitatively analyze a fast-neutron radiography device has allowed for a better understand of what is needed within the NDE community. At the 2023 Workshop On Radiographic Imaging and Applications (WORIA) at Oak Ridge National Laboratory, one of the key points stressed was the need for a standard way to compare spatial resolution between the vast array of neutron radiography systems [59]. Although the methods used in this research are not the only method for determining spatial resolution, the research has demonstrated that it is a viable path forward for the industry, especially given that MTF measurements have already seen widespread use in other industries [60].

8.3 Opportunities for Future Work

One of the most significant drawbacks of the current setup is the use of a 3-mm-thick continuous sheet of EJ-200 light spreader. The continuous scintillator package limits the spatial resolution of the radiographs produced, and the thin sheet of scintillator will decrease the chance of a neutron recoil compared to thicker scintillator blocks seen in previous research. A thicker, continuous scintillator block would allow for more neutrons to be detected, but it would spread the light of the event out further, reducing spatial resolution in the process. Initially, this research was intended to have segmented scintillator blocks comprised of 1-mm-pitch pixels that were 20 mm thick. Issues with the delivery of these blocks meant that the research had to be pivoted to a much scintillator package that had some inherent drawbacks. While this research did prove that a continuous neutron scattering

scintillator package could be used in a flat-panel radiography device, further work will allow for the device to have both decreased acquisition time and increased spatial resolution, both important for its use in a non-laboratory environment.

The scope of this research had to be performed without an actual D-T neutron generator. A Cf-252 fission source was an adequate replacement for the time being, but did limit the tests that could be performed. First, the Cf-252 source used outputs significantly fewer neutrons than a typical D-T generator operating at nominal settings. This means that image acquisition times are significantly longer for the Cf-252 images than they would be for D-T images. Additionally, the neutrons from a Cf-252 spectrum are of a lower energy than that of D-T neutrons, meaning that lead shielding used to reduce the gammas from the Cf-252 source are more likely to scatter the Cf-252 neutrons. A thinner sheet of lead can be used with the D-T generator to block off the lower-energy x-rays given off by the fusion reaction. Finally, the lack of D-T neutrons in this research means that there has not been an demonstration of the final use case of the system yet. While this research does prove that the system works, there is no way to tell if there are issues that will arise when a D-T generator is finally used on the panel.

The ROSSPAD modules were a great start for developing a scalable, compact fast-neutron radiography system. At the time of writing, there are few SiPM-based tileable systems available on the commercial market. However, the ROSSPAD does have some drawbacks that make it worthwhile to explore other COTS systems or the development of a brand new readout module. The initial plan for this research was to use EJ-276, a plastic scintillator that was developed for use in systems that can take advantage of pulse shape discrimination (PSD). While PSD does not mean that a system can tell the difference between a photon and a neutron 100% of the time, it still allows for significant noise reduction, as many background gamma rays can be eliminated from the data stream. As of now, the IDEAS ROSSPAD cannot perform PSD, meaning that there is no way of determining what event was a photon and what event was a neutron. The ROSSPADs also does not have well-developed control software; for this research, everything from data collection to data processing had to be made from scratch. Future development of these data processing programs is not only

important for future work with this radiography panel, but also important for anyone else who may want to use the ROSSPAD for their research.

Bibliography

- [1] M. Heath, B. Canion, L. Fabris, I. Garishvili, A. Glenn, J. Hausladen, P. Hausladen, D. Lee, S. McConchie, L. Nakae, J. Newby, and R. Wurtz, “Development of a portable pixelated fast-neutron imaging panel,” vol. 69, no. 6, 6 2022. [Online]. Available: <https://www.osti.gov/biblio/1884004> [xii](#), [9](#), [10](#)
- [2] “Rosspad: Sipm readout module for x-ray and gamma-ray spectroscopy and imaging.” [Online]. Available: <https://ideas.no/products/rospad/#> [xii](#), [13](#), [14](#)
- [3] J. S. Brzosko, B. V. Robouch, L. Ingrosso, A. Bortolotti, and V. Nardi, “Advantages and limits of 14-mev neutron radiography,” *Nuclear instruments & methods in physics research. Section B, Beam interactions with materials and atoms*, vol. 72, no. 1, pp. 119–131, 1992. [1](#)
- [4] M. J. Berger and J. H. Hubbell, “Xcom: Photon cross sections on a personal computer,” *OSTI*, 7 1987. [1](#), [60](#), [97](#), [119](#)
- [5] D. Brown, M. Chadwick, R. Capote, A. Kahler, A. Trkov, M. Herman, A. Sonzogni, Y. Danon, A. Carlson, M. Dunn, D. Smith, G. Hale, G. Arbanas, R. Arcilla, C. Bates, B. Beck, B. Becker, F. Brown, R. Casperson, J. Conlin, D. Cullen, M.-A. Descalle, R. Firestone, T. Gaines, K. Guber, A. Hawari, J. Holmes, T. Johnson, T. Kawano, B. Kiedrowski, A. Koning, S. Kopecky, L. Leal, J. Lestone, C. Lubitz, J. Márquez Damián, C. Mattoon, E. McCutchan, S. Mughabghab, P. Navratil, D. Neudecker, G. Nobre, G. Noguere, M. Paris, M. Pigni, A. Plompen, B. Pritychenko, V. Pronyaev, D. Roubtsov, D. Rochman, P. Romano, P. Schillebeeckx, S. Simakov, M. Sin, I. Sirakov, B. Sleaford, V. Sobes, E. Soukhovitskii, I. Stetcu, P. Talou,

- I. Thompson, S. van der Marck, L. Welser-Sherrill, D. Wiarda, M. White, J. Wormald, R. Wright, M. Zerkle, G. Žerovnik, and Y. Zhu, “Endf/b-viii.0: The 8th major release of the nuclear reaction data library with cielo-project cross sections, new standards and thermal scattering data,” *Nuclear Data Sheets*, vol. 148, pp. 1–142, 2018, special Issue on Nuclear Reaction Data. [Online]. Available: <https://www.sciencedirect.com/science/article/pii/S0090375218300206> 1
- [6] “Xrs4 - Golden Engineering,” Jul 2022. [Online]. Available: <https://www.goldenengineering.com/products/xrs4/> 3
- [7] “Linear accelerators archives.” [Online]. Available: https://www.vareximaging.com/solution_cat/linear-accelerators-heavy-metal-castings/ 3
- [8] D. R. Rusby, P. M. King, A. Pak, N. Lemos, S. Kerr, G. Cochran, I. Pagano, A. Hannasch, H. Quevedo, M. Spinks, M. Donovan, A. Link, A. Kemp, S. C. Wilks, G. J. Williams, M. J.-E. Manuel, Z. Gavin, A. Haid, F. Albert, M. Aufderheide, H. Chen, C. W. Siders, A. Macphee, and A. Mackinnon, “Enhancements in laser-generated hot-electron production via focusing cone targets at short pulse and high contrast,” *Phys. Rev. E*, vol. 103, p. 053207, May 2021. [Online]. Available: <https://link.aps.org/doi/10.1103/PhysRevE.103.053207> 3
- [9] N. Kardjilov, I. Manke, A. Hilger, M. Strobl, and J. Banhart, “Neutron imaging in materials science,” *Materials Today*, vol. 14, no. 6, pp. 248–256, 2011. [Online]. Available: <https://www.sciencedirect.com/science/article/pii/S1369702111701390> 3
- [10] B. A. Ludewigt, B. J. Quiter, and S. D. Ambers, “Nuclear resonance fluorescence for safeguards applications,” *Materials Protection, Accounting and Control for Transmutation (MPACT)*, 2 2011. [Online]. Available: <https://www.osti.gov/biblio/1022713> 3
- [11] K. A. Schmidt, “Karin and katrin: A new technology for high power 14 mev d-t fusion neutron generator tubes for radiotherapy, fast neutron activation analysis, safeguards, neutron radiography and laboratory applications,” in *Neutron Radiography*, J. P. Barton,

- G. Farny, J.-L. Person, and H. Röttger, Eds. Dordrecht: Springer Netherlands, 1987, pp. 239–252. [3](#)
- [12] E. A. Klein, F. Naqvi, J. E. Bickus, H. Y. Lee, A. Danagoulian, and R. J. Goldston, “Neutron-resonance transmission analysis with a compact deuterium-tritium neutron generator,” *Phys. Rev. Appl.*, vol. 15, p. 054026, May 2021. [Online]. Available: <https://link.aps.org/doi/10.1103/PhysRevApplied.15.054026> [3](#)
- [13] B. Sowerby and J. Tickner, “Recent advances in fast neutron radiography for cargo inspection,” *Nuclear Instruments and Methods in Physics Research Section A: Accelerators, Spectrometers, Detectors and Associated Equipment*, vol. 580, no. 1, pp. 799–802, 2007, proceedings of the 10 th International Symposium on Radiation Physics. [Online]. Available: <https://www.sciencedirect.com/science/article/pii/S0168900207010868> [3](#)
- [14] A. E. Craft, D. M. Wachs, M. A. Okuniewski, D. L. Chichester, W. J. Williams, G. C. Papaioannou, and A. T. Smolinski, “Neutron radiography of irradiated nuclear fuel at idaho national laboratory,” *Physics Procedia*, vol. 69, pp. 483–490, 2015, proceedings of the 10th World Conference on Neutron Radiography (WCNR-10) Grindelwald, Switzerland October 5–10, 2014. [Online]. Available: <https://www.sciencedirect.com/science/article/pii/S1875389215006781> [3](#)
- [15] D. Snoeck, P. Van den Heede, T. Van Mullem, and N. De Belie, “Water penetration through cracks in self-healing cementitious materials with superabsorbent polymers studied by neutron radiography,” *Cement and Concrete Research*, vol. 113, pp. 86–98, 2018. [Online]. Available: <https://www.sciencedirect.com/science/article/pii/S0008884617312279> [3](#)
- [16] V. Cnudde, M. Dierick, J. Vlassenbroeck, B. Masschaele, E. Lehmann, P. Jacobs, and L. Van Hoorebeke, “High-speed neutron radiography for monitoring the water absorption by capillarity in porous materials,” *Nuclear Instruments and Methods in Physics Research Section B: Beam Interactions with Materials*

- and Atoms*, vol. 266, no. 1, pp. 155–163, 2008. [Online]. Available: <https://www.sciencedirect.com/science/article/pii/S0168583X07015996> 3
- [17] D. J. Turkoglu, “Design, construction and characterization of an external neutron beam facility at the ohio state university nuclear reactor laboratory,” Ph.D. dissertation, The Ohio State University, 2011. [Online]. Available: http://rave.ohiolink.edu/etdc/view?acc_num=osu1325228897 5
- [18] L. Santodonato, H. Bilheux, B. Bailey, J. Bilheux, P. Nguyen, A. Tremsin, D. Selby, and L. Walker, “The cg-1d neutron imaging beamline at the oak ridge national laboratory high flux isotope reactor,” *Physics Procedia*, vol. 69, pp. 104–108, 2015, proceedings of the 10th World Conference on Neutron Radiography (WCNR-10) Grindelwald, Switzerland October 5–10, 2014. [Online]. Available: <https://www.sciencedirect.com/science/article/pii/S1875389215006252> 5
- [19] T. Mason, D. Abernathy, I. Anderson, J. Ankner, T. Egami, G. Ehlers, A. Ekkebus, G. Granroth, M. Hagen, K. Herwig, J. Hodges, C. Hoffmann, C. Horak, L. Horton, F. Klose, J. Larese, A. Mesecar, D. Myles, J. Neuefeind, M. Ohl, C. Tulk, X.-L. Wang, and J. Zhao, “The spallation neutron source in oak ridge: A powerful tool for materials research,” *Physica B: Condensed Matter*, vol. 385-386, pp. 955–960, 2006. [Online]. Available: <https://www.sciencedirect.com/science/article/pii/S092145260601177X> 5
- [20] “0751 - H122 - Basic Health Physics - 25 - Neutron Sources,” Oct 2010. [Online]. Available: <https://www.nrc.gov/docs/ML1122/ML11229A704.pdf> 5
- [21] D. J. Mitchell, G. G. Thoreson, and L. T. Harding, “Summary of alpha-neutron sources in gadras.” *OSTI*, 5 2012. [Online]. Available: <https://www.osti.gov/biblio/1044955> 5
- [22] *Fusion Physics*, ser. Non-serial Publications. Vienna: INTERNATIONAL ATOMIC ENERGY AGENCY, 2012. [Online]. Available: <https://www.iaea.org/publications/8879/fusion-physics> 6
- [23] “Transforming nuclear technology since 2005,” Dec 2021. [Online]. Available: <https://phoenixwi.com/> 6

- [24] “Neutron sources.” [Online]. Available: <https://adelphitech.com/> 6
- [25] “Ngen™ neutron generators.” [Online]. Available: <https://www.starfireindustries.com/ngen.html> 6
- [26] “P 383 neutron generator.” [Online]. Available: <https://www.thermofisher.com/order/catalog/product/153993-G1?SID=srch-srp-153993-G1> 6
- [27] S. McConchie, D. Archer, J. Mihalcz, B. Palles, and M. Wright, “Transportable, low-dose active fast-neutron imaging,” Oak Ridge National Laboratory, Tech. Rep., 07 2017. 6, 9
- [28] “Api 120 neutron generator.” [Online]. Available: <https://www.thermofisher.com/order/catalog/product/151762A?SID=srch-hj-151762A> 6
- [29] D. L. Williams, C. M. Brown, D. Tong, A. Sulyman, and C. K. Gary, “A fast neutron radiography system using a high yield portable dt neutron source,” *Journal of imaging*, vol. 6, no. 12, pp. 128–, 2020. 7
- [30] S. Bishnoi, P. S. Sarkar, R. G. Thomas, T. Patel, M. Pal, P. S. Adhikari, A. Sinha, A. Saxena, and S. C. Gadkari, “Preliminary experimentation of fast neutron radiography with d-t neutron generator at barc,” *Journal of nondestructive evaluation*, vol. 38, no. 1, pp. 1–9, 2018. 7
- [31] S. Wang, C. Cao, W. Yin, Y. Wu, H. Huo, Y. Sun, B. Liu, X. Yang, R. Li, S. Zhu, C. Wu, H. Li, and B. Tang, “A novel ndt scanning system based on line array fast neutron detector and d-t neutron source,” *Materials*, vol. 15, no. 14, 2022. [Online]. Available: <https://www.mdpi.com/1996-1944/15/14/4946> 8
- [32] P. L. Kerr, N. Cherepy, J. Church, G. Guethlein, J. Hall, C. McNamee, S. O’Neal, K. Champley, A. Townsend, M. Sasagawa, and A. Hardy, “Neutron transmission imaging with a portable d-t neutron generator,” 8 2021. [Online]. Available: <https://www.osti.gov/biblio/1814672> 8

- [33] M. Grodzicka-Kobylka, M. Moszyński, and T. Szcześniak, “Silicon photomultipliers in gamma spectroscopy with scintillators,” *Nuclear Instruments and Methods in Physics Research Section A: Accelerators, Spectrometers, Detectors and Associated Equipment*, vol. 926, pp. 129–147, 2019, silicon Photomultipliers: Technology, Characterisation and Applications. [Online]. Available: <https://www.sciencedirect.com/science/article/pii/S0168900218313792> 9, 16
- [34] S. España, L. Fraile, J. Herraiz, J. Udías, M. Desco, and J. Vaquero, “Performance evaluation of sipm photodetectors for pet imaging in the presence of magnetic fields,” *Nuclear Instruments and Methods in Physics Research Section A: Accelerators, Spectrometers, Detectors and Associated Equipment*, vol. 613, no. 2, pp. 308–316, 2010. [Online]. Available: <https://www.sciencedirect.com/science/article/pii/S0168900209022815> 9, 11
- [35] K. Shimazoe, M. Yoshino, Y. Ohshima, M. Uenomachi, K. Oogane, T. Orita, H. Takahashi, K. Kamada, A. Yoshikawa, and M. Takahashi, “Development of simultaneous pet and compton imaging using gagg-sipm based pixel detectors,” *Nuclear Instruments and Methods in Physics Research Section A: Accelerators, Spectrometers, Detectors and Associated Equipment*, vol. 954, p. 161499, 2020, symposium on Radiation Measurements and Applications XVII. [Online]. Available: <https://www.sciencedirect.com/science/article/pii/S0168900218314918> 11
- [36] T. Nesjø, “Development and verification of a high-resolution x-ray spectroscopy line scanner,” Master’s thesis, University of Oslo, Oslo, Norway, September 2023, available at <https://www.duo.uio.no/handle/10852/104380?show=full>. 11
- [37] “J-Series SiPM Sensors Data Sheet,” Aug 2021. 13
- [38] “General purpose plastic scintillator ej-200, ej-204, ej-208, ej-212.” 13
- [39] “Silicone grease ej-550, ej-552.” 13
- [40] “Rust-oleum enamel spray paint: White, flat, 12 oz.” [Online]. Available: <https://www.mscdirect.com/product/details/46975983> 16

- [41] Y. Tsuchiya, E. Inuzuka, T. Kuroono, and M. Hosoda, “Photon-counting imaging and its application,” in *Photo-Electronic Image Devices*, ser. Advances in Electronics and Electron Physics, B. Morgan, Ed. Academic Press, 1986, vol. 64, pp. 21–31. [Online]. Available: <https://www.sciencedirect.com/science/article/pii/S0065253908616005> 16
- [42] A. Tremsin, J. McPhate, J. Vallergera, O. Siegmund, W. Feller, E. Lehmann, and M. Dawson, “Improved efficiency of high resolution thermal and cold neutron imaging,” *Nuclear Instruments and Methods in Physics Research Section A: Accelerators, Spectrometers, Detectors and Associated Equipment*, vol. 628, no. 1, pp. 415–418, 2011, vCI 2010. [Online]. Available: <https://www.sciencedirect.com/science/article/pii/S0168900210015561> 16
- [43] S. M. Decker, M. Pizzichemi, A. Polesel, M. Paganoni, E. Auffray, and S. Gundacker, “The digital-analog sipm approach: a story of electronic and excess noise,” in *2019 IEEE Nuclear Science Symposium and Medical Imaging Conference (NSS/MIC)*, 2019, pp. 1–5. 16
- [44] “Noctua.at - premium cooling components designed in austria.” [Online]. Available: <https://noctua.at/en/nf-a4x20-pwm/specification> 17
- [45] “Ide3380 ds-1r11 2019,” Jun 2019. 20
- [46] “Home | tcpdump & libpcap.” [Online]. Available: <https://www.tcpdump.org/index.html> 23
- [47] “Wireshark - go deep.” [Online]. Available: <https://www.wireshark.org/> 23
- [48] “SQLite home page.” [Online]. Available: <https://www.sqlite.org/index.html> 23
- [49] “Db browser for sqlite,” May 2023. [Online]. Available: <https://sqlitebrowser.org/> 25
- [50] “Imagej: Image processing and analysis in java.” [Online]. Available: <https://imagej.net/ij/index.html> 30, 97, 119
- [51] C. X. Young, C. A. Browning, R. J. Thurber, M. R. Smalley, M. J. Liesenfelt, J. P. Hayward, N. McFarlane, M. P. Cooper, and J. R. Preston, “Scalable

- detector design for a high-resolution fast-neutron radiography panel,” *Journal of Nondestructive Evaluation*, vol. 42, no. 4, Sep. 2023. [Online]. Available: <https://doi.org/10.1007/s10921-023-00999-x> 59
- [52] S. N. Ahmed, “7 - position-sensitive detection and imaging,” in *Physics and Engineering of Radiation Detection (Second Edition)*, 2nd ed., S. N. Ahmed, Ed. Elsevier, 2015, pp. 435–475. [Online]. Available: <https://www.sciencedirect.com/science/article/pii/B9780128013632000073> 60
- [53] D. Nikezic, M. Beni, D. Krstic, and P. Yu, “Characteristics of protons exiting from a polyethylene converter irradiated by neutrons with energies between 1 kev and 10 mev,” *PLOS ONE*, vol. 11, p. e0157627, 06 2016. 60, 100, 110
- [54] “Nondestructive evaluation physics: X-ray - geometric unsharpness.” [Online]. Available: <https://www.nde-ed.org/Physics/X-Ray/GeometricUnsharp.xhtml> 63
- [55] R. YASUDA, T. NOJIMA, H. IIKURA, T. SAKAI, and M. MATSUBAYASHI, “Development of a small-aperture slit system for a high collimator ratio at the thermal neutron radiography facility in jrr-3,” *Journal of Nuclear Science and Technology*, vol. 48, no. 7, pp. 1094–1101, 2011. [Online]. Available: <https://www.tandfonline.com/doi/abs/10.1080/18811248.2011.9711794> 66, 75, 100, 117
- [56] S. Alcorn, “Advanced radiation and optical characterization of a novel fast neutron imaging array,” Master’s Thesis, The University of Tennessee, Knoxville, July 2022. 79
- [57] “Amd ryzen 9 5900hx mobile processor.” [Online]. Available: <https://www.amd.com/en/products/apu/amd-ryzen-9-5900hx> 82
- [58] A. L. C. Kwan, J. A. Seibert, and J. M. Boone, “An improved method for flat-field correction of flat panel x-ray detector,” *Medical Physics*, vol. 33, no. 2, pp. 391–393, 2006. [Online]. Available: <https://aapm.onlinelibrary.wiley.com/doi/abs/10.1118/1.2163388> 94, 97
- [59] B. Quiter and E. Miller, “Session 8: Algorithm development & data fusion,” Workshop On Radiographic Imaging and Applications (WORIA), Feb 2023. 138

- [60] S. N. Ahmed, “7 - position-sensitive detection and imaging,” in *Physics and Engineering of Radiation Detection (Second Edition)*, 2nd ed., S. N. Ahmed, Ed. Elsevier, 2015, pp. 435–475. [Online]. Available: <https://www.sciencedirect.com/science/article/pii/B9780128013632000073> 138

Appendices

A Legal

A.1 Disclaimer

This work of authorship and those incorporated herein were prepared by Consolidated Nuclear Security, LLC (CNS) as accounts of work sponsored by an agency of the United States Government under Contract DE-NA0001942. Neither the United States Government nor any agency thereof, nor CNS, nor any of their employees, makes any warranty, express or implied, or assumes any legal liability or responsibility to any non-governmental recipient hereof for the accuracy, completeness, use made, or usefulness of any information, apparatus, product, or process disclosed, or represents that its use would not infringe privately owned rights. Reference herein to any specific commercial product, process, or service by trade name, trademark, manufacturer, or otherwise, does not necessarily constitute or imply its endorsement, recommendation, or favoring by the United States Government or any agency or contractor thereof. The views and opinions of authors expressed herein do not necessarily state or reflect those of the United States Government or any agency or contractor (other than the authors) thereof.

A.2 Copyright Notice

This document has been authored by Consolidated Nuclear Security, LLC, a contractor of the U.S. Government under contract DE-NA0001942, or a subcontractor thereof. Accordingly, the U.S. Government retains a paid-up, nonexclusive, irrevocable, worldwide license to publish or reproduce the published form of this contribution, prepare derivative works, distribute copies to the public, and perform publicly and display publicly, or allow others to do so, for U. S. Government purposes.

B Supplemental Images of the Full-Panel Housing System



Figure 1: Full-panel housing lying flat, with cooling fan ports visible.

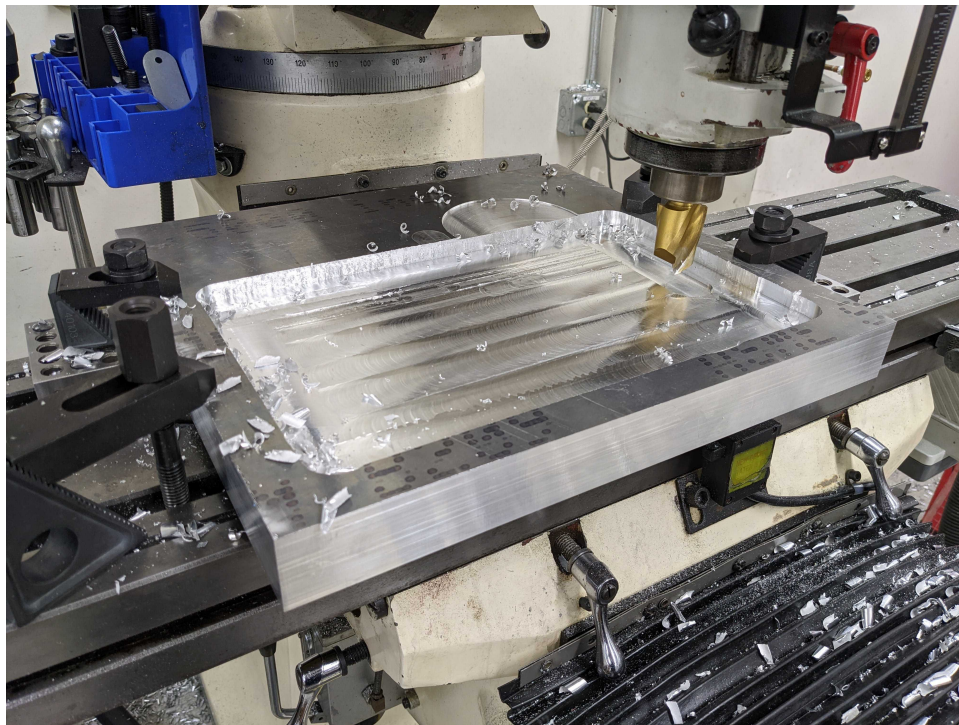


Figure 2: Milling of the aluminum lid for the full-panel assembly.

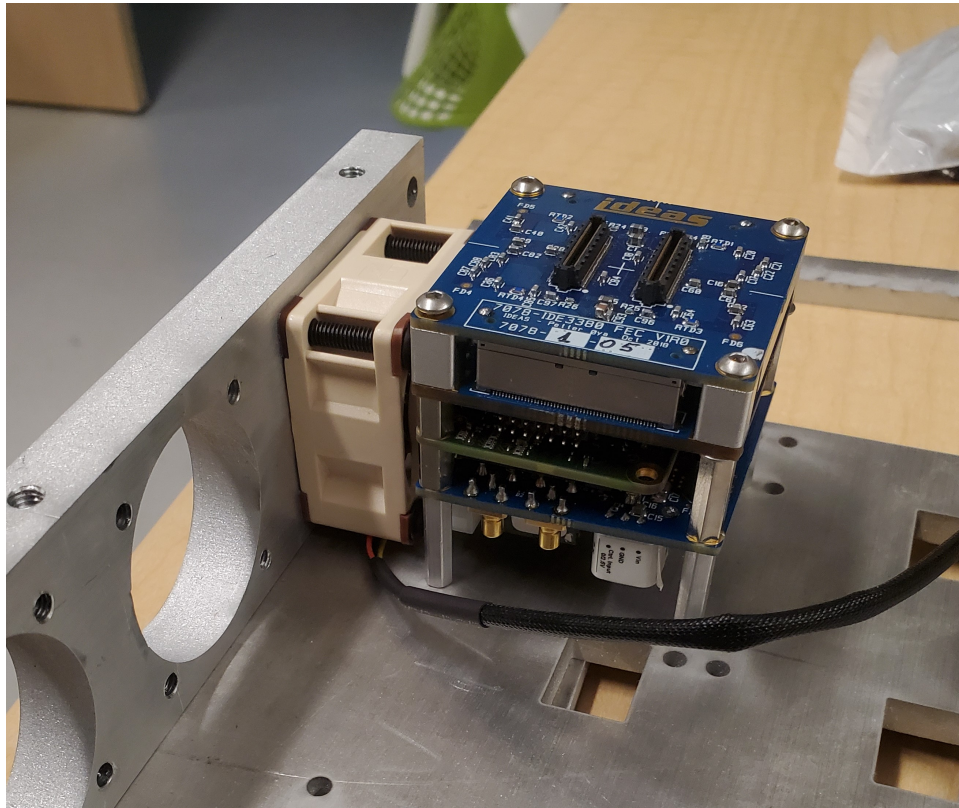


Figure 3: Test fit of a single ROSSPAD and cooling fan in the full-panel housing.

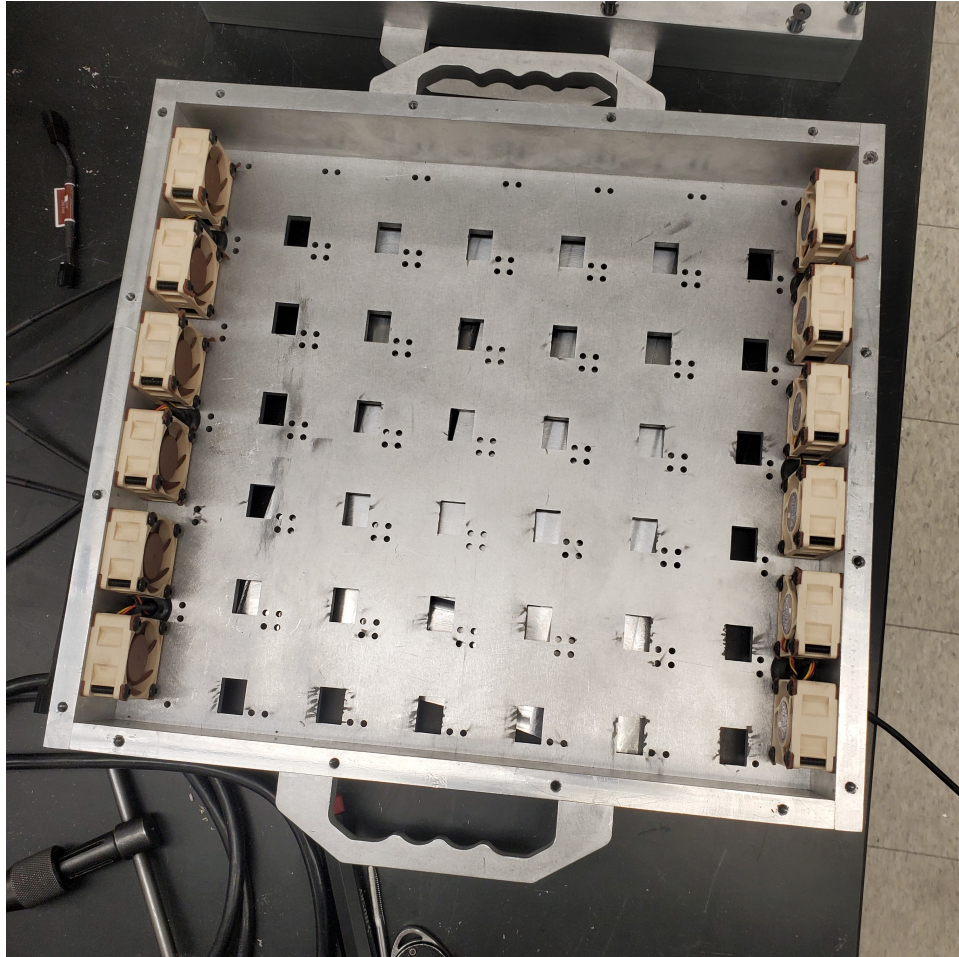


Figure 4: assembled housing with all fans installed.

C Supplemental Signal-to-Noise Optimization Images

C.1 Lower Bound Signal Cutoff

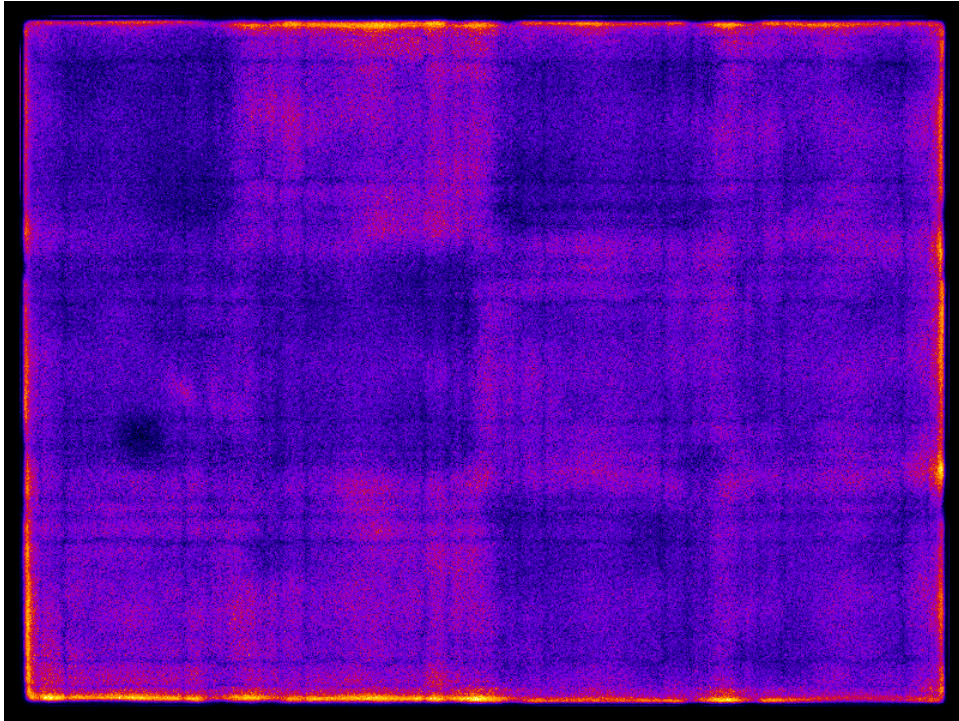
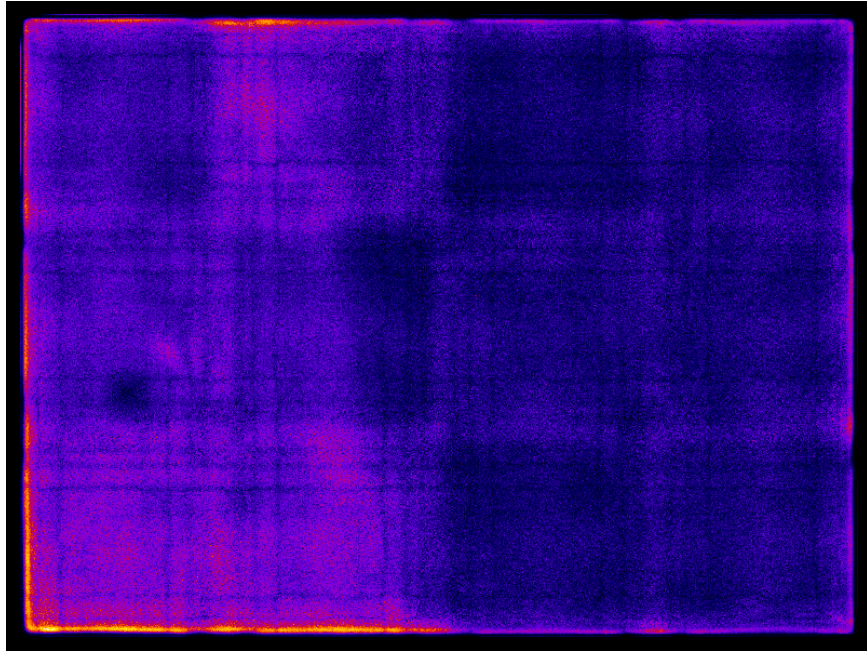
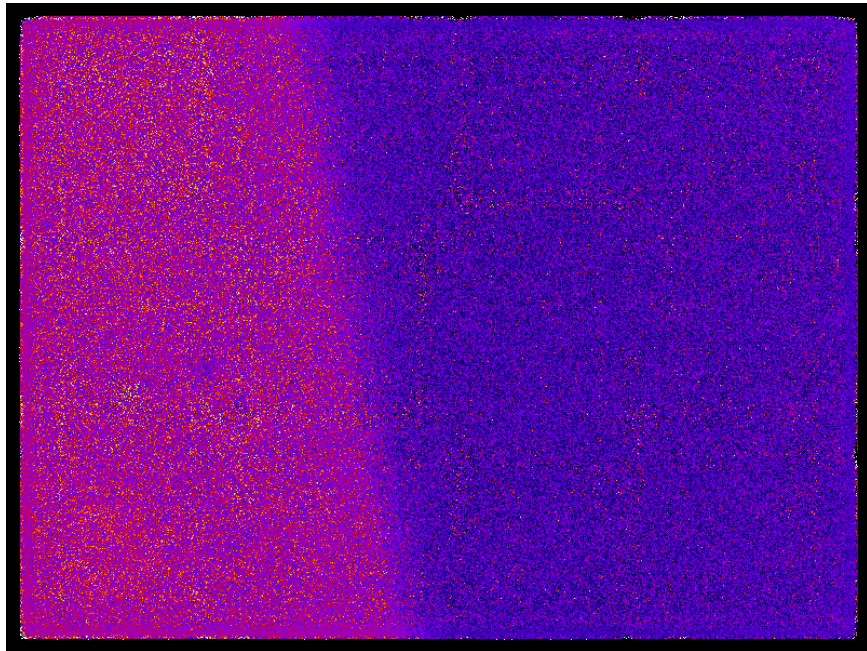


Figure 5: Cf-252 flood field where all events are above 1000 total signal.

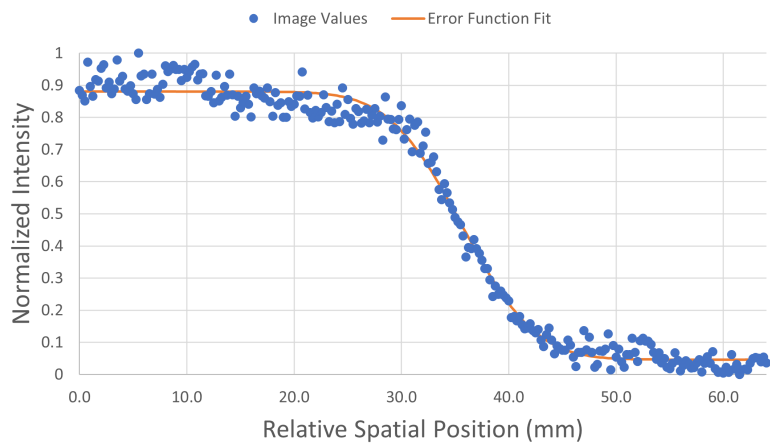


(a) Uncorrected

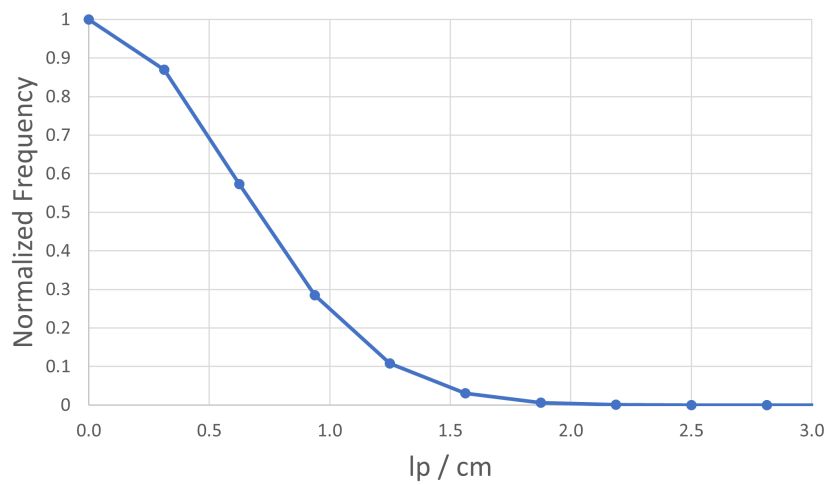


(b) Corrected

Figure 6: Cf-252 edge images where all events are above 1000 total signal a) before flood field correction and b) after flood field correction.



(a) Profile



(b) MTF

Figure 7: a) Line profile and b) MTF plot for a Cf-252 edge where all events are above 1000 total signal.

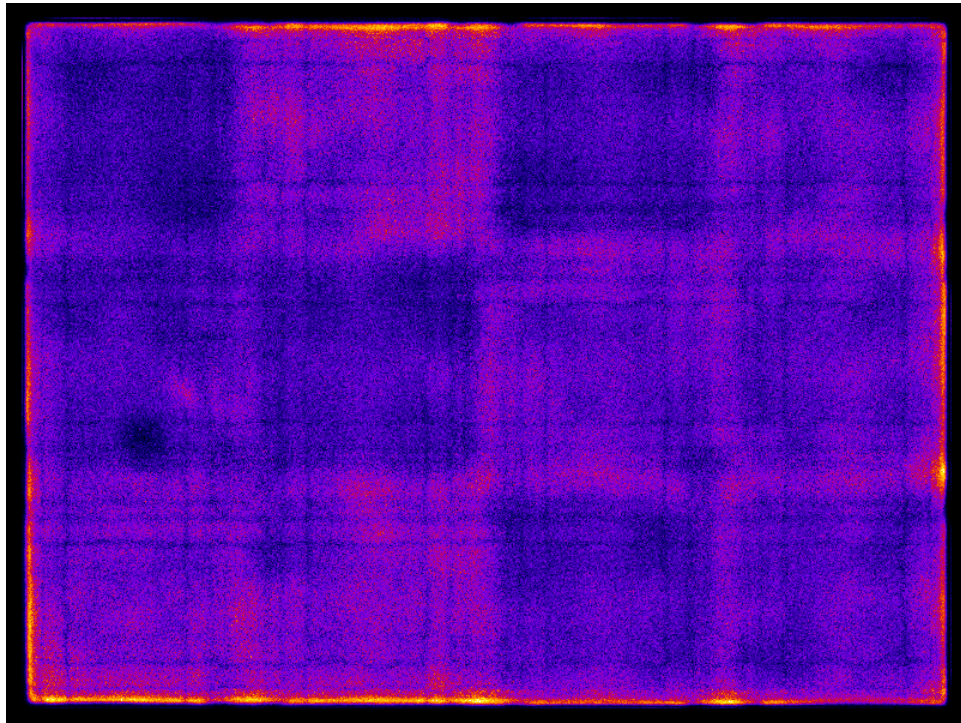
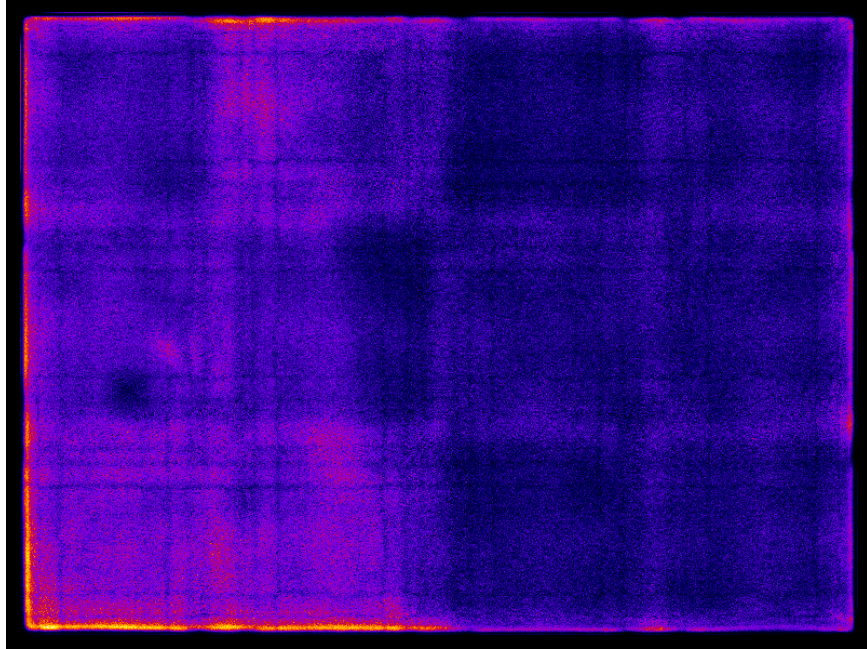
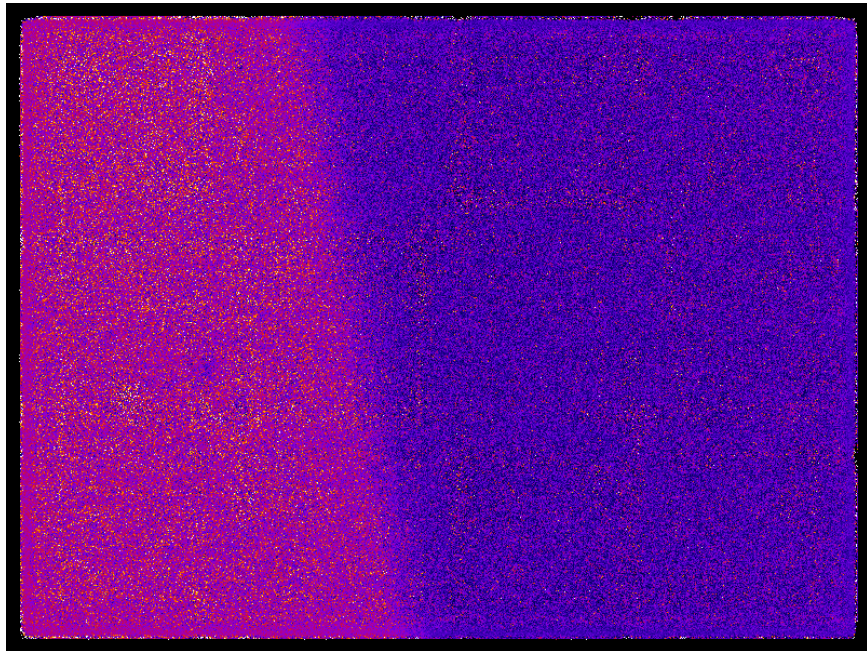


Figure 8: Cf-252 flood field where all events are above 3000 total signal.

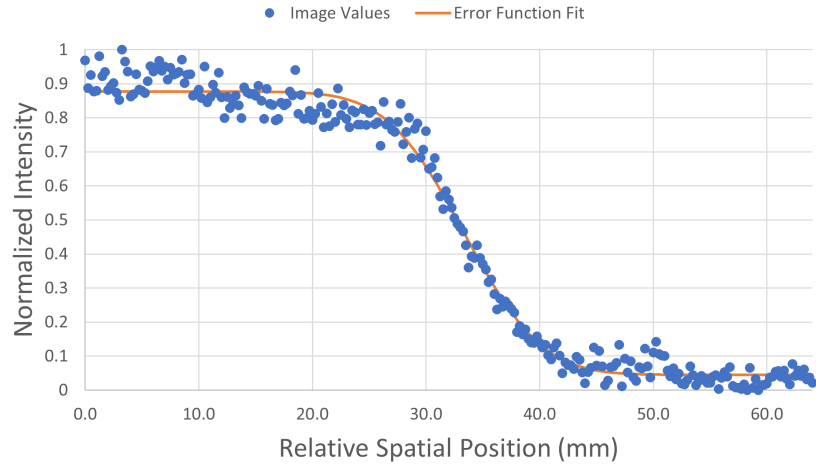


(a) Uncorrected

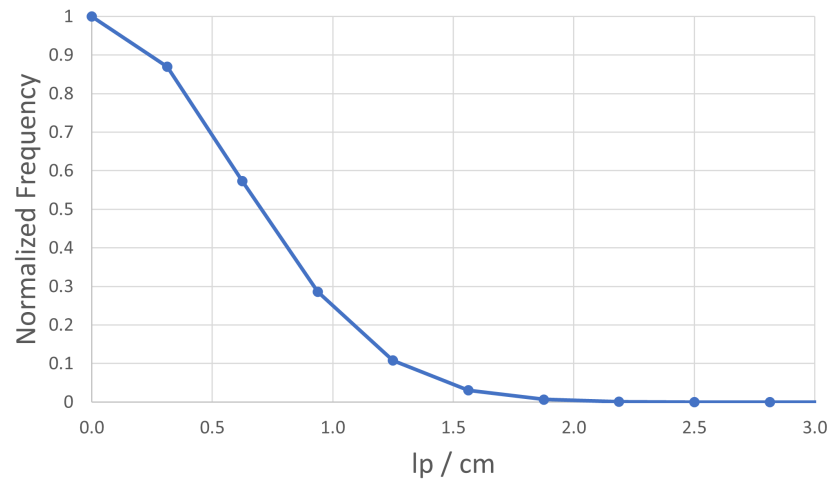


(b) Corrected

Figure 9: Cf-252 edge images where all events are above 3000 total signal a) before flood field correction and b) after flood field correction.



(a) Profile



(b) MTF

Figure 10: a) Line profile and b) MTF plot for a Cf-252 edge where all events are above 3000 total signal.

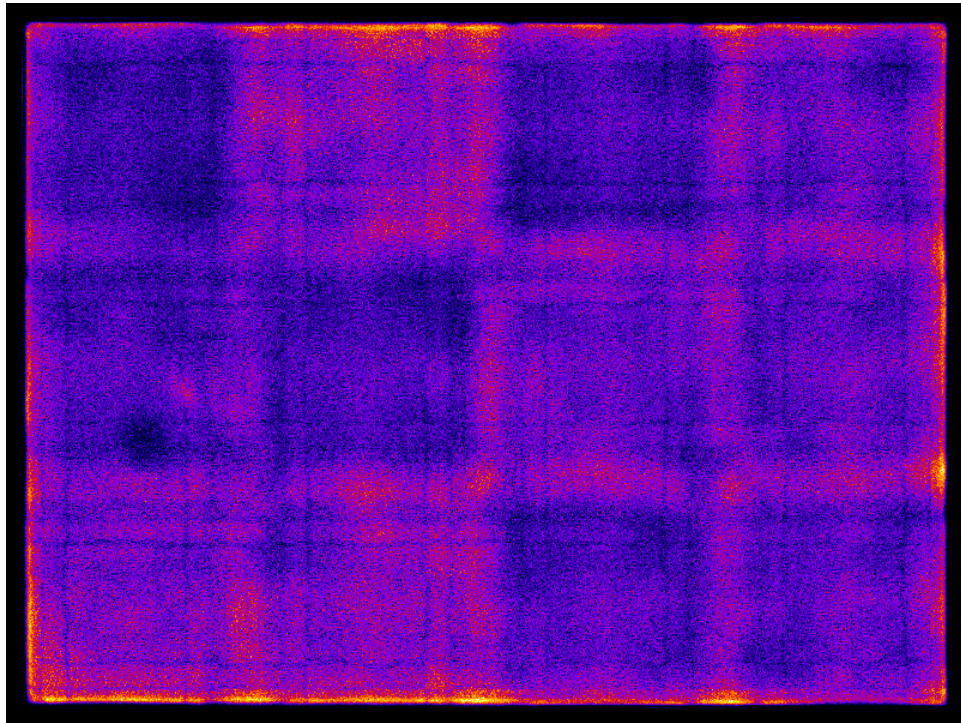
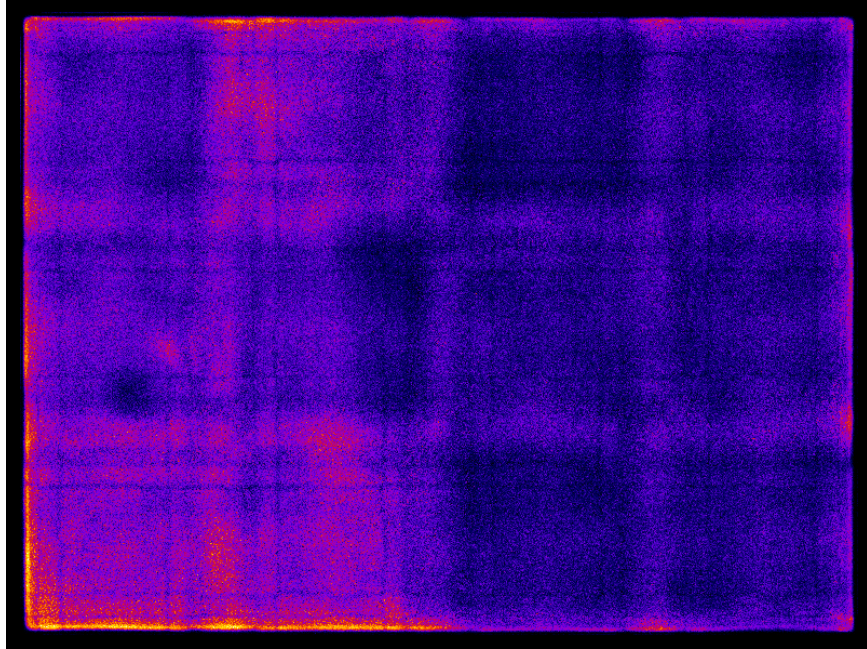
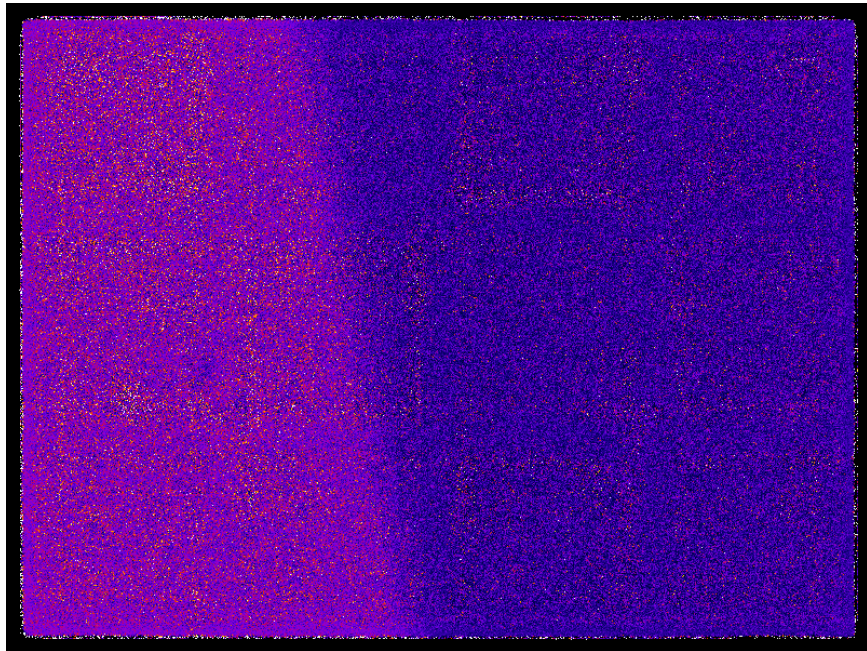


Figure 11: Cf-252 flood field where all events are above 6000 total signal.

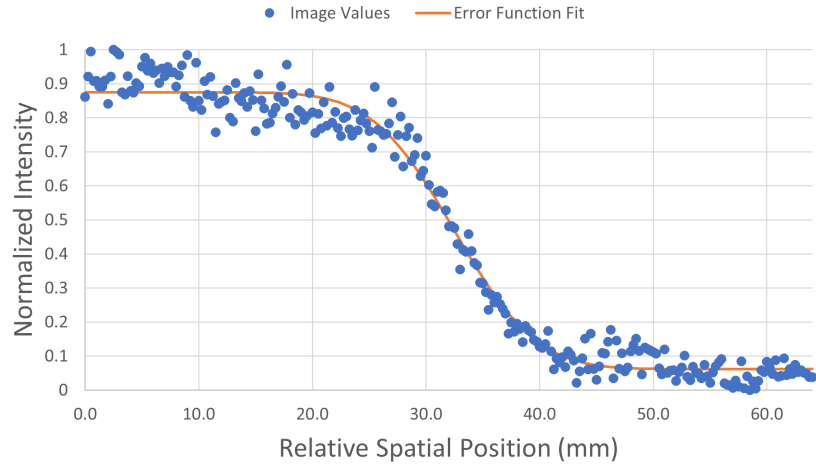


(a) Uncorrected

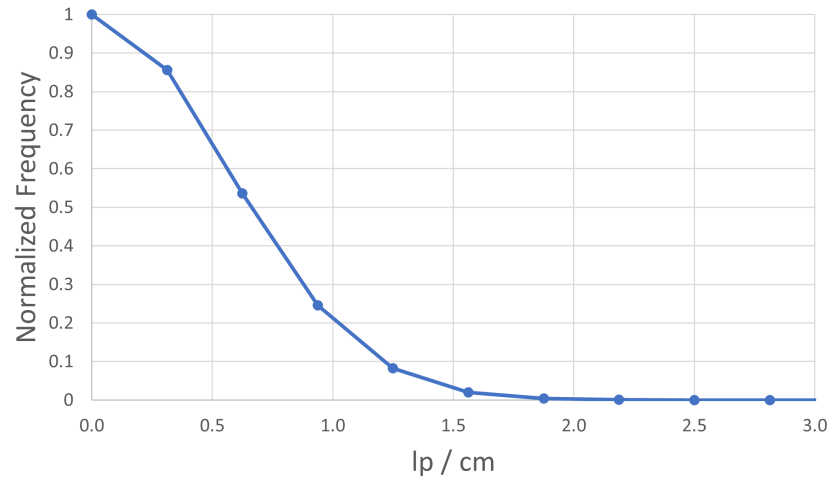


(b) Corrected

Figure 12: Cf-252 edge images where all events are above 6000 total signal a) before flood field correction and b) after flood field correction.



(a) Profile



(b) MTF

Figure 13: a) Line profile and b) MTF plot for a Cf-252 edge where all events are above 6000 total signal.

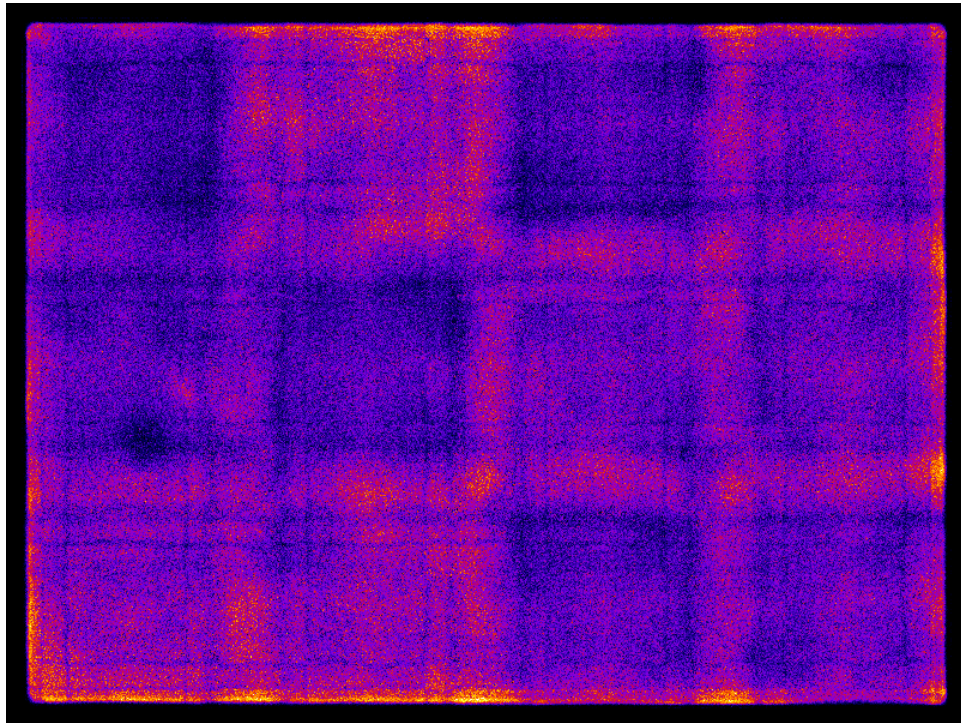
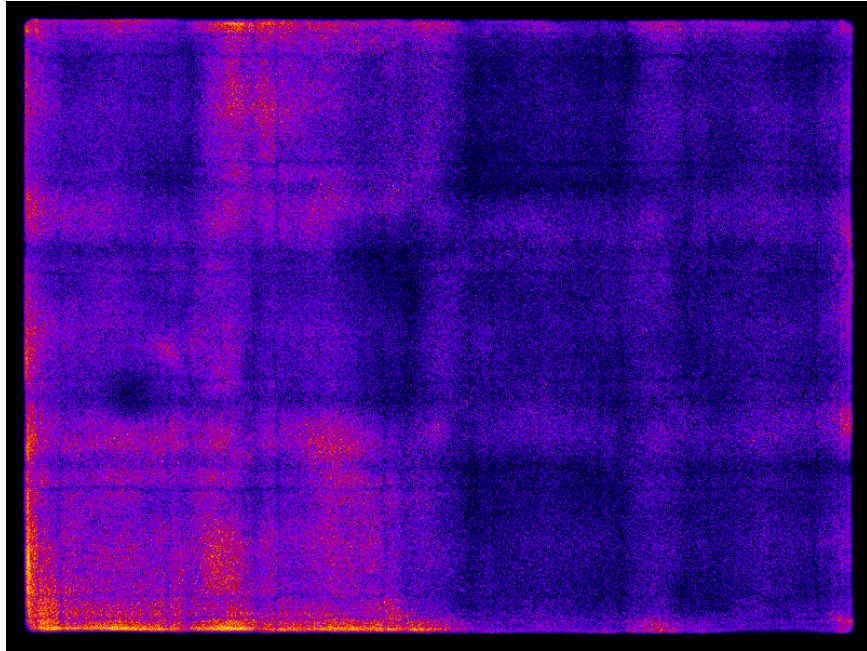
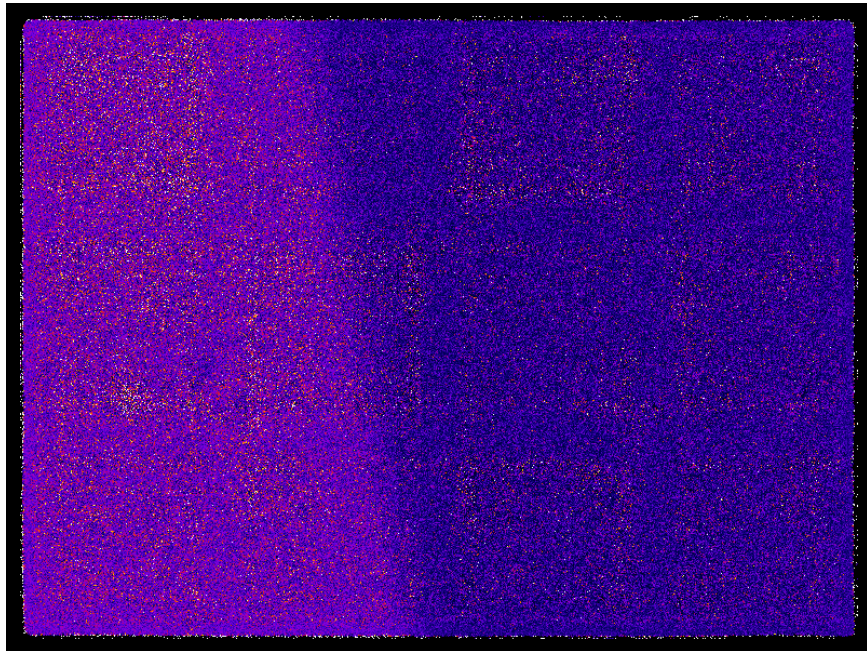


Figure 14: Cf-252 flood field where all events are above 9000 total signal.

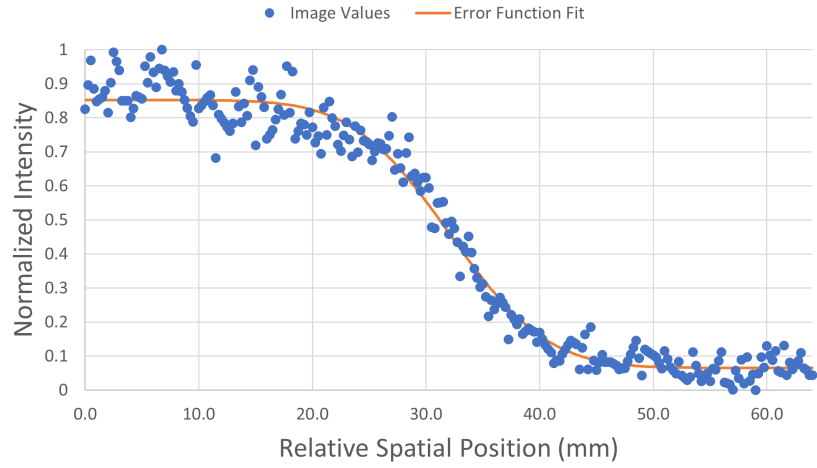


(a) Uncorrected

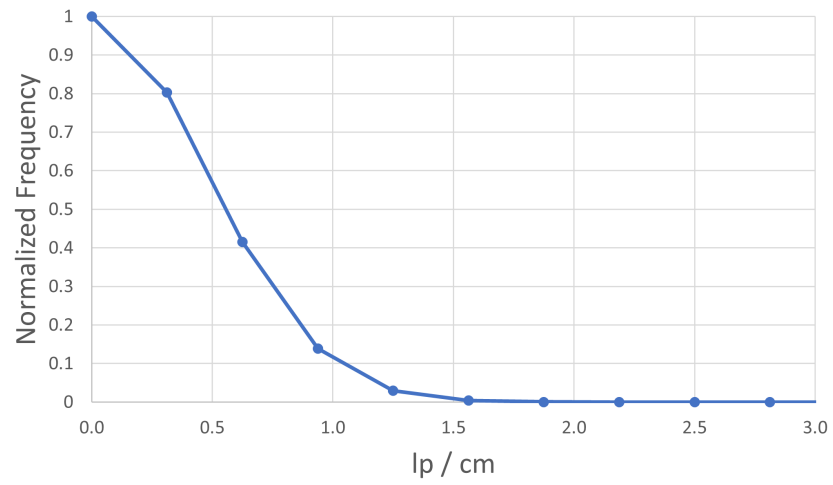


(b) Corrected

Figure 15: Cf-252 edge images where all events are above 9000 total signal a) before flood field correction and b) after flood field correction.



(a) Profile



(b) MTF

Figure 16: a) Line profile and b) MTF plot for a Cf-252 edge where all events are above 9000 total signal.

C.2 Upper Bound Signal Cutoff

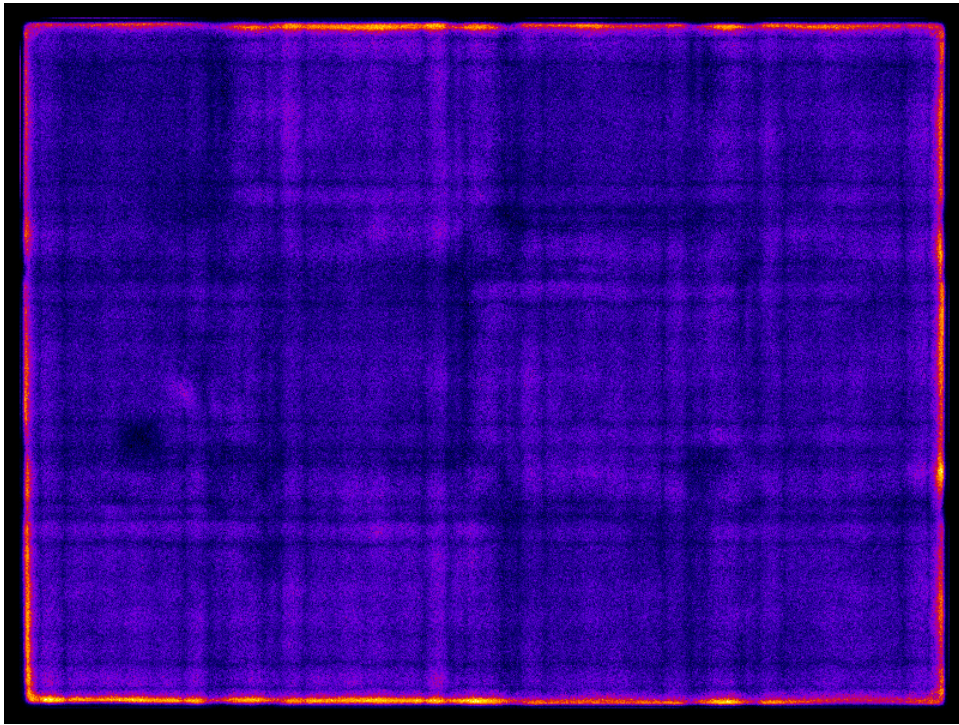
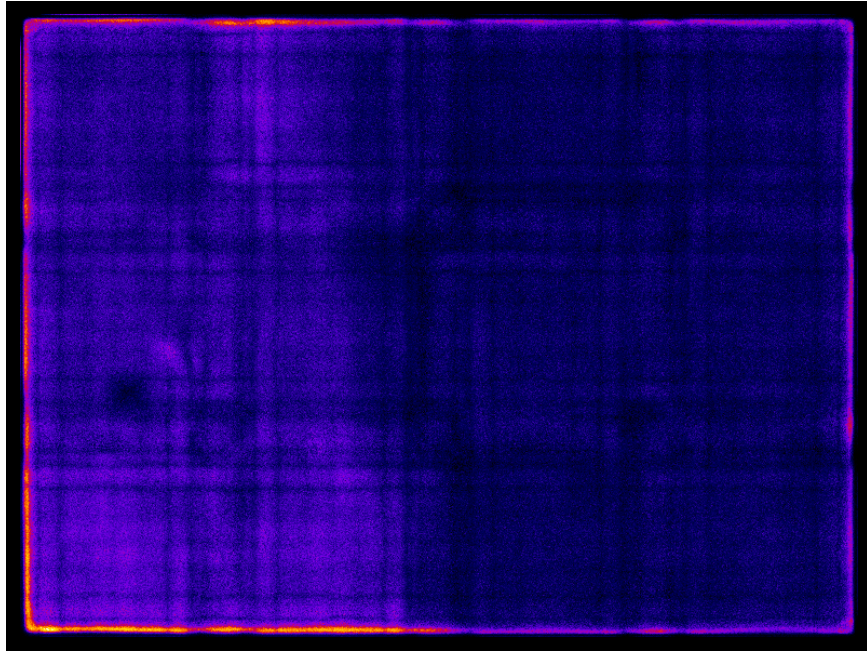
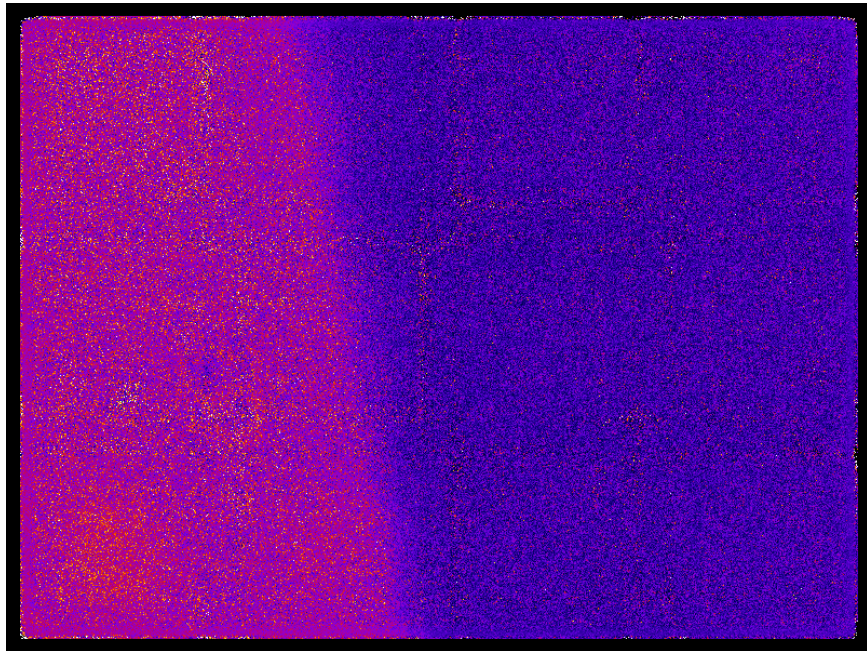


Figure 17: Cf-252 flood field where all events are under 22,500 total signal.

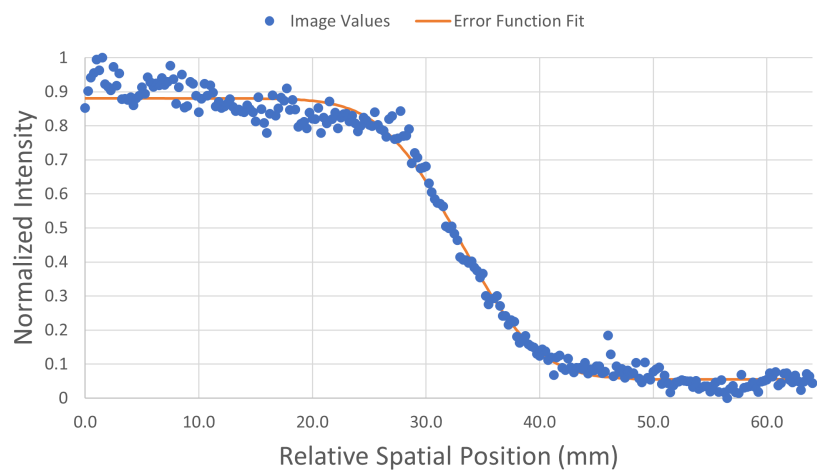


(a) Uncorrected

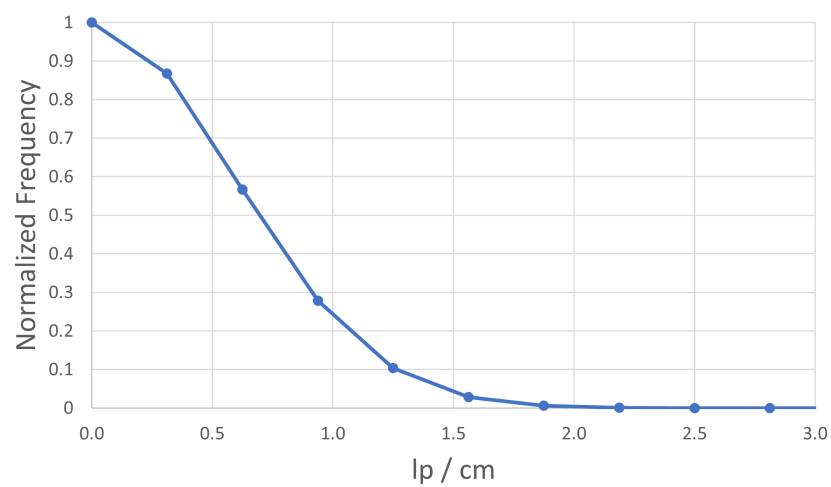


(b) Corrected

Figure 18: Cf-252 edge images where all events are under 22,500 total signal a) before flood field correction and b) after flood field correction.



(a) Profile



(b) MTF

Figure 19: a) Line profile and b) MTF plot for a Cf-252 edge where all events are under 22,500 total signal.

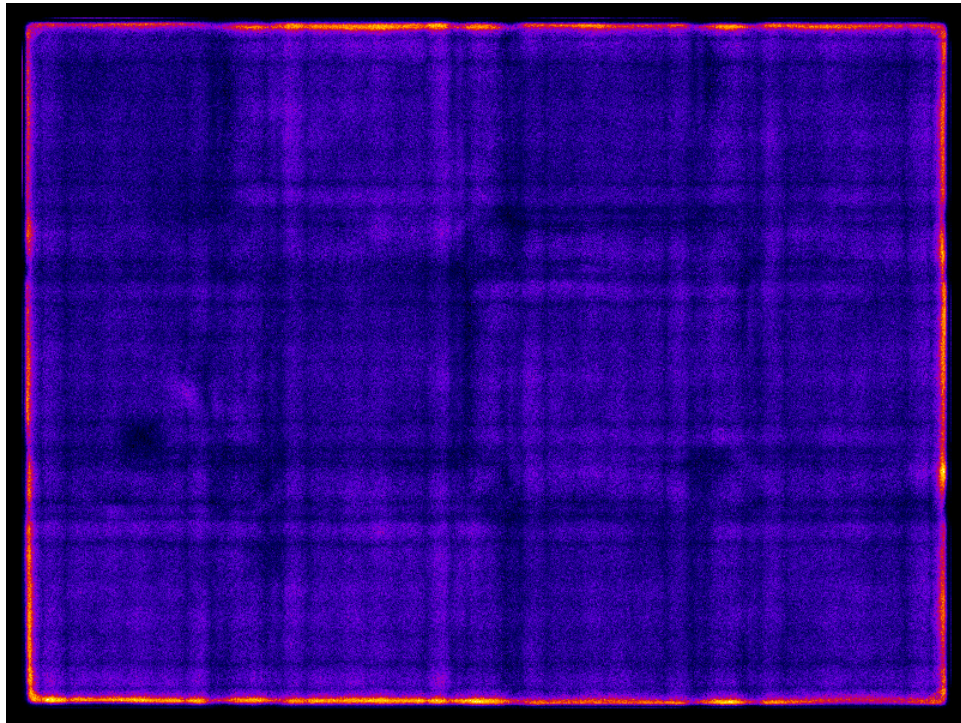
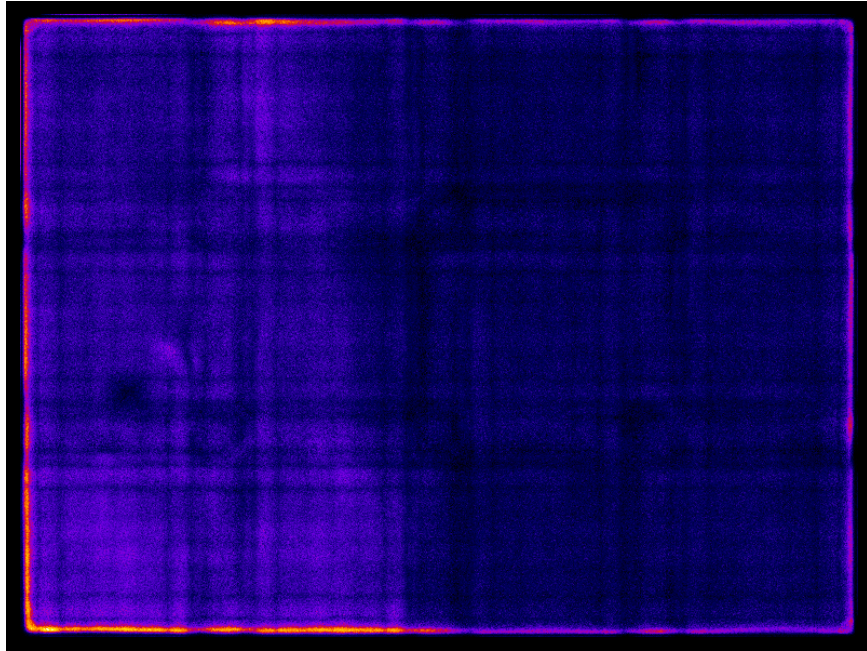
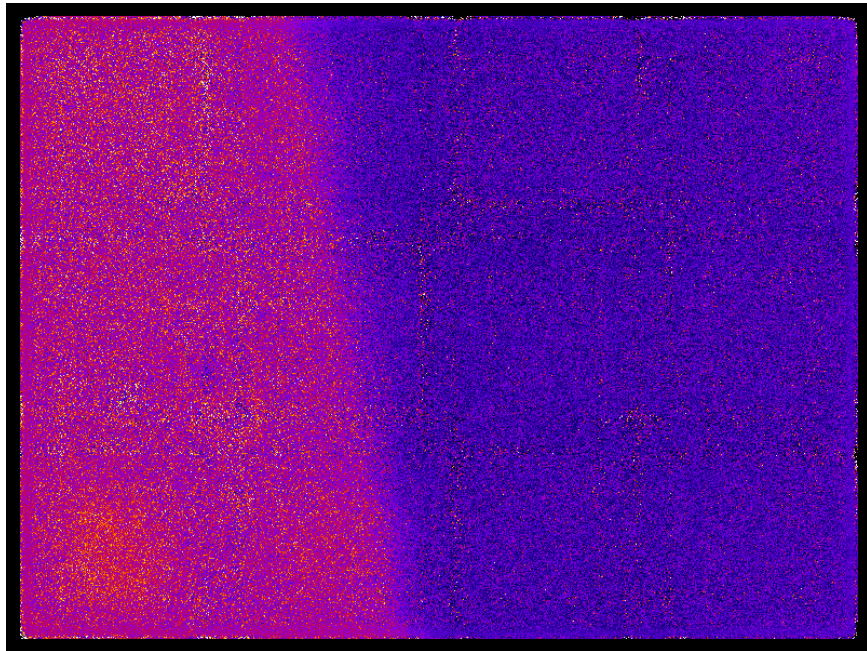


Figure 20: Cf-252 flood field where all events are under 20,000 total signal.

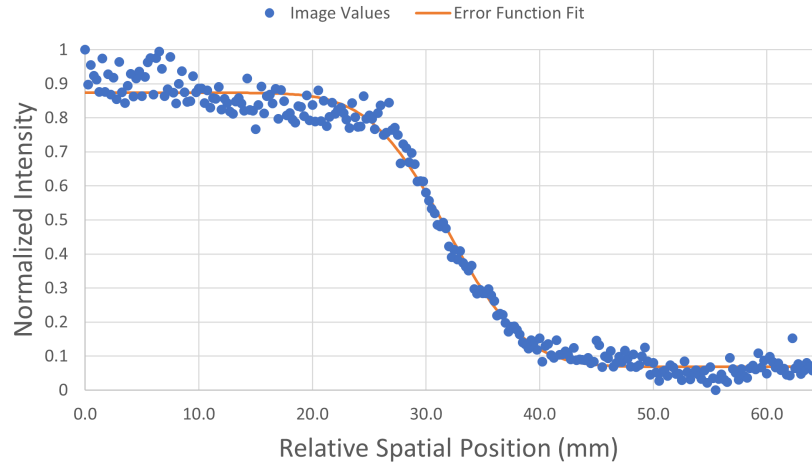


(a) Uncorrected

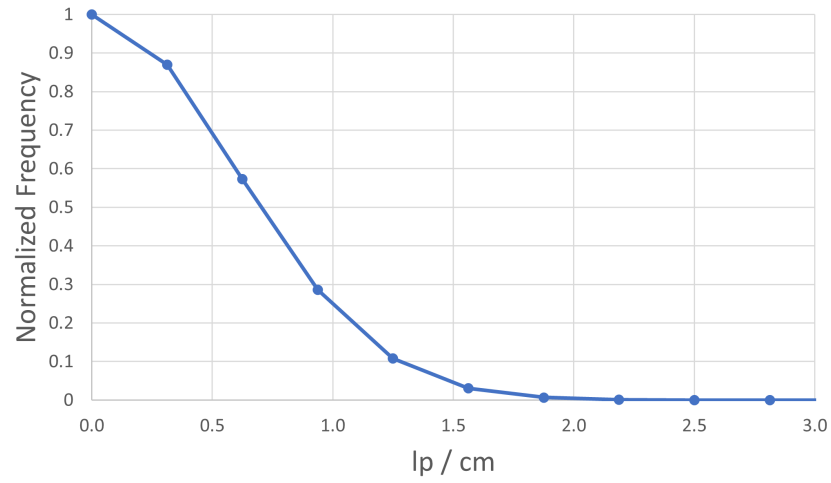


(b) Corrected

Figure 21: Cf-252 edge images where all events are under 20,000 total signal a) before flood field correction and b) after flood field correction.



(a) Profile



(b) MTF

Figure 22: a) Line profile and b) MTF plot for a Cf-252 edge where all events are under 20,000 total signal.

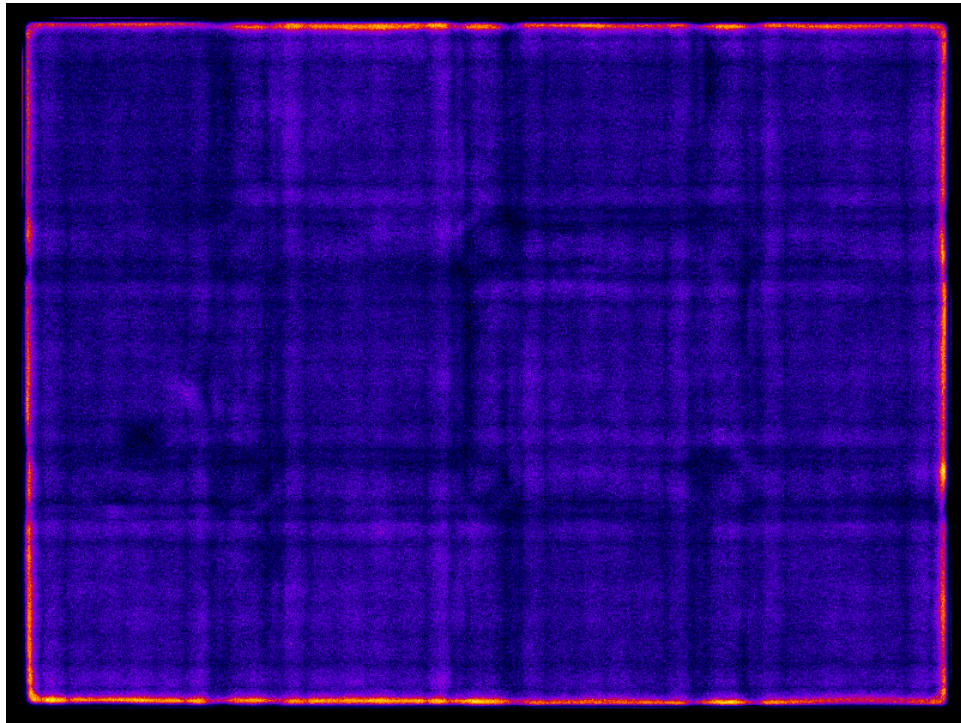
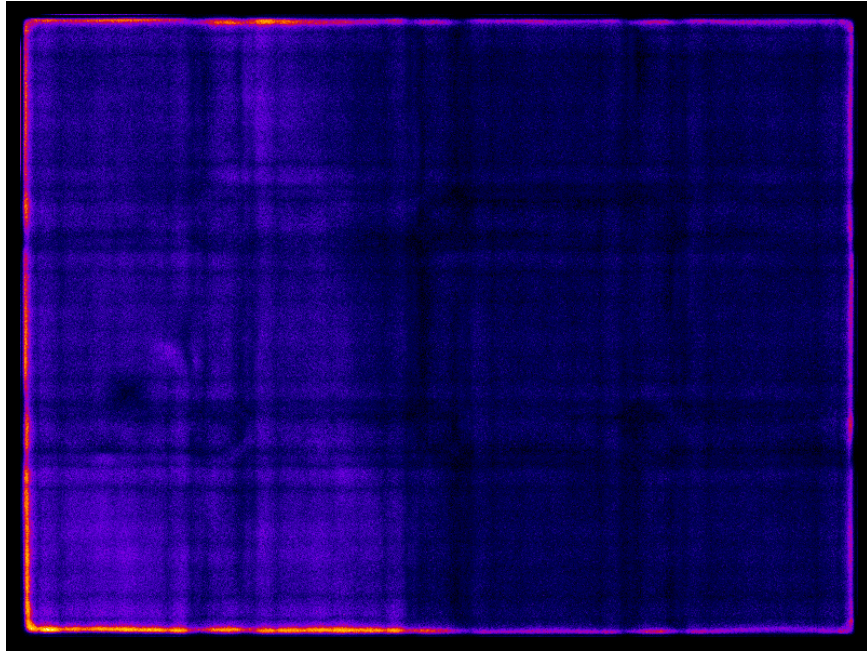
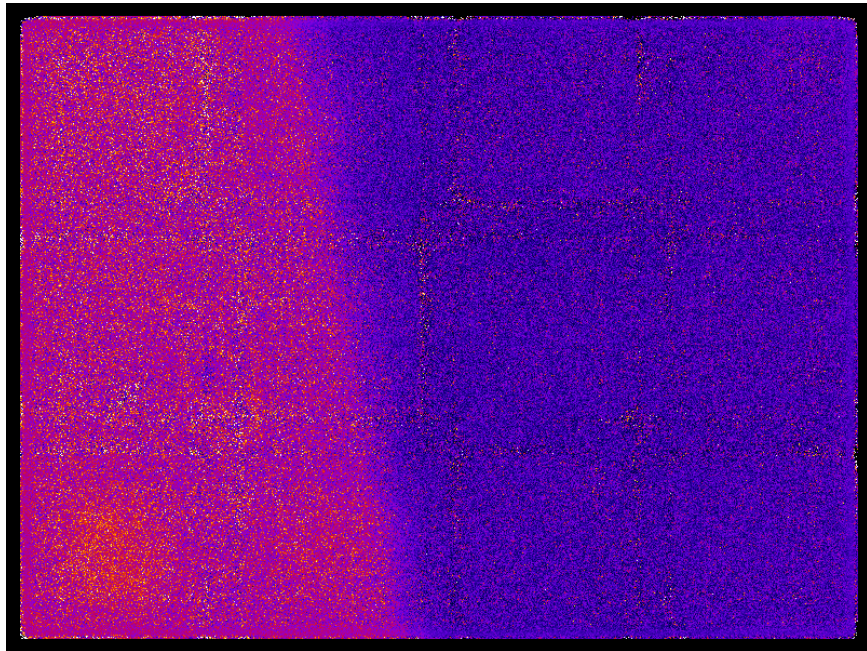


Figure 23: Cf-252 flood field where all events are under 17,500 total signal.

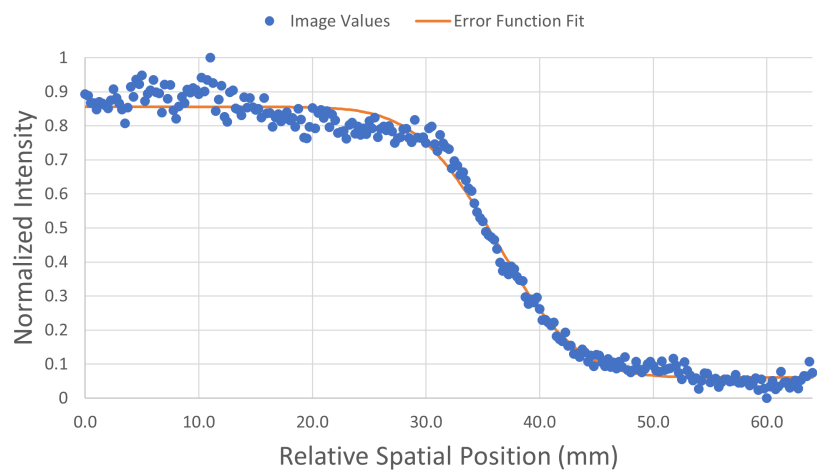


(a) Uncorrected

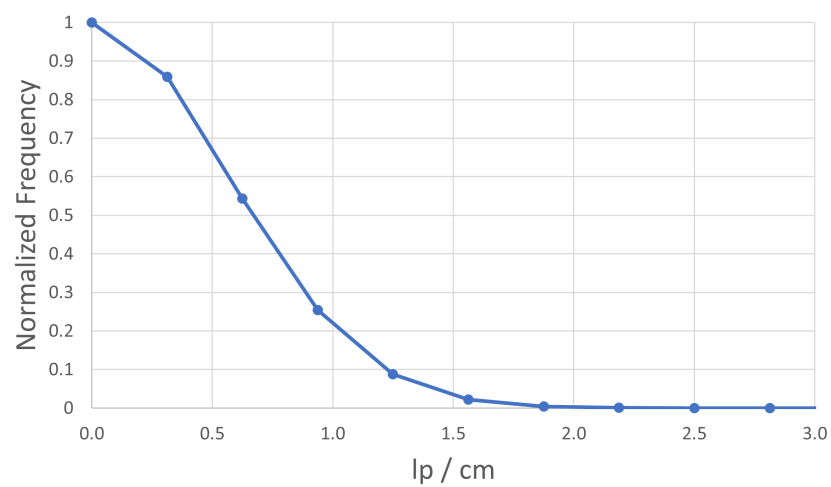


(b) Corrected

Figure 24: Cf-252 edge images where all events are under 17,500 total signal a) before flood field correction and b) after flood field correction.



(a) Profile



(b) MTF

Figure 25: a) Line profile and b) MTF plot for a Cf-252 edge where all events are under 17,500 total signal.

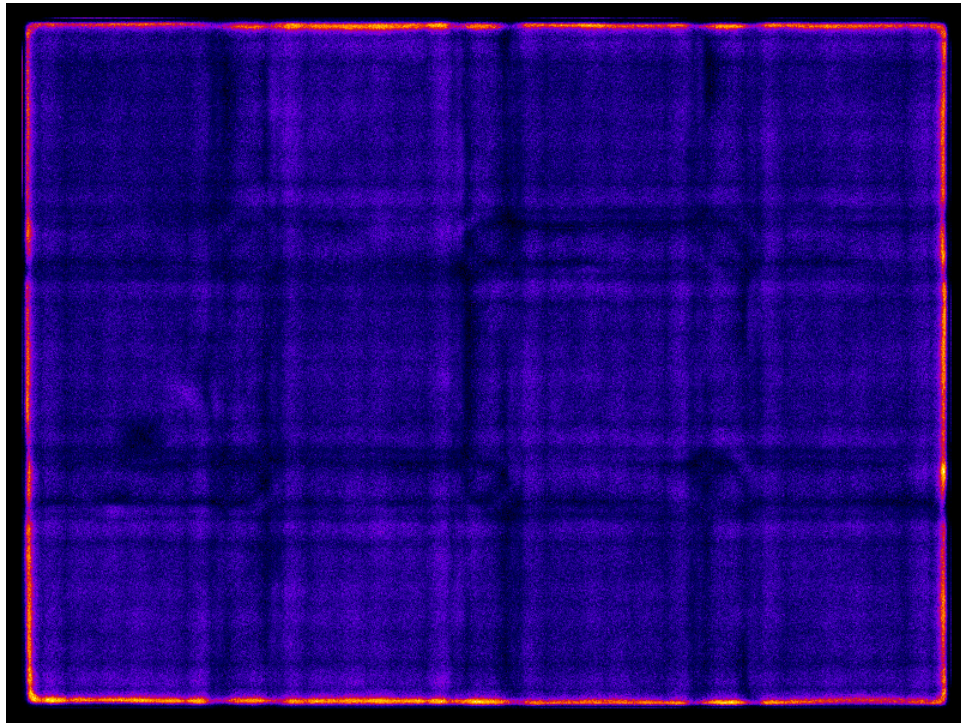
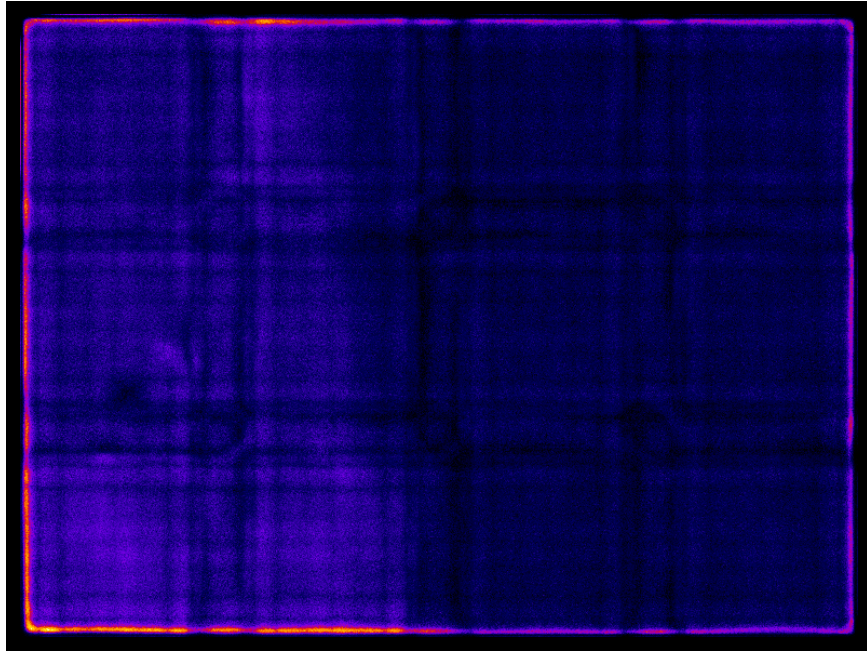
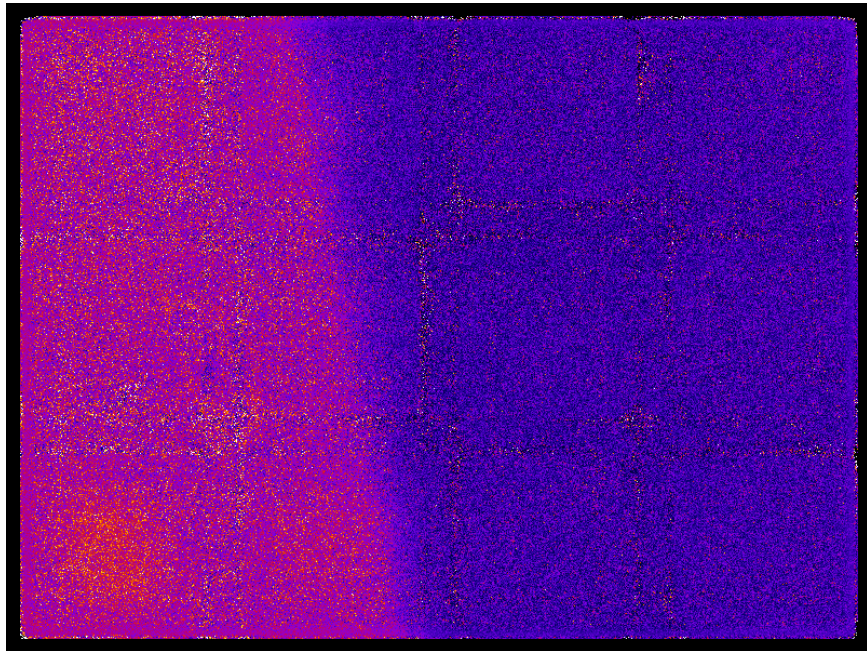


Figure 26: Cf-252 flood field where all events are under 15,000 total signal.

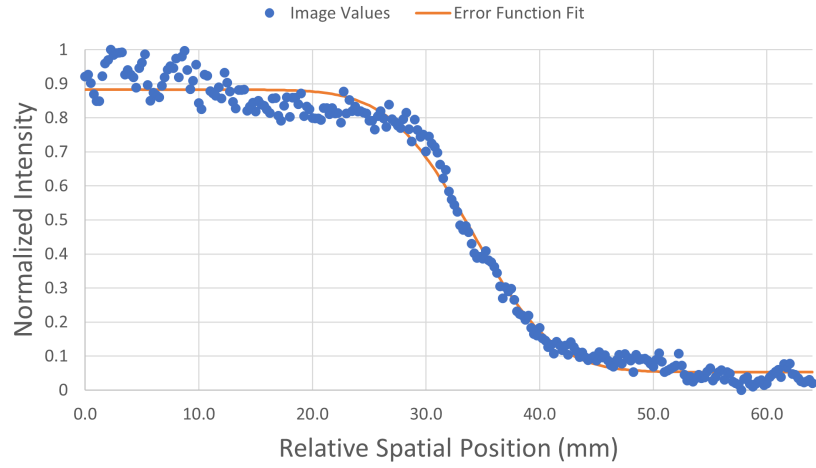


(a) Uncorrected

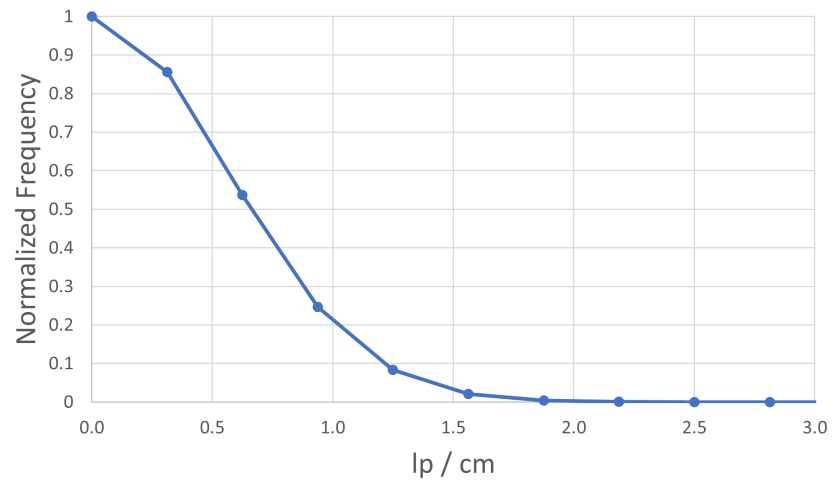


(b) Corrected

Figure 27: Cf-252 edge images where all events are under 15,000 total signal a) before flood field correction and b) after flood field correction.



(a) Profile



(b) MTF

Figure 28: a) Line profile and b) MTF plot for a Cf-252 edge where all events are under 15,000 total signal.

C.3 Cluster Size

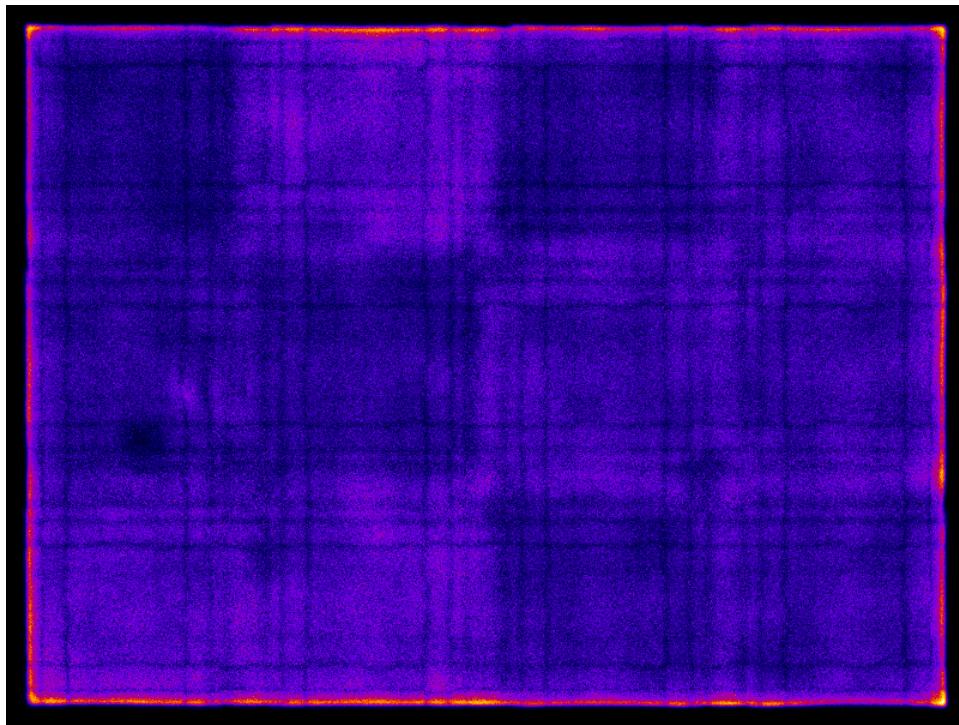
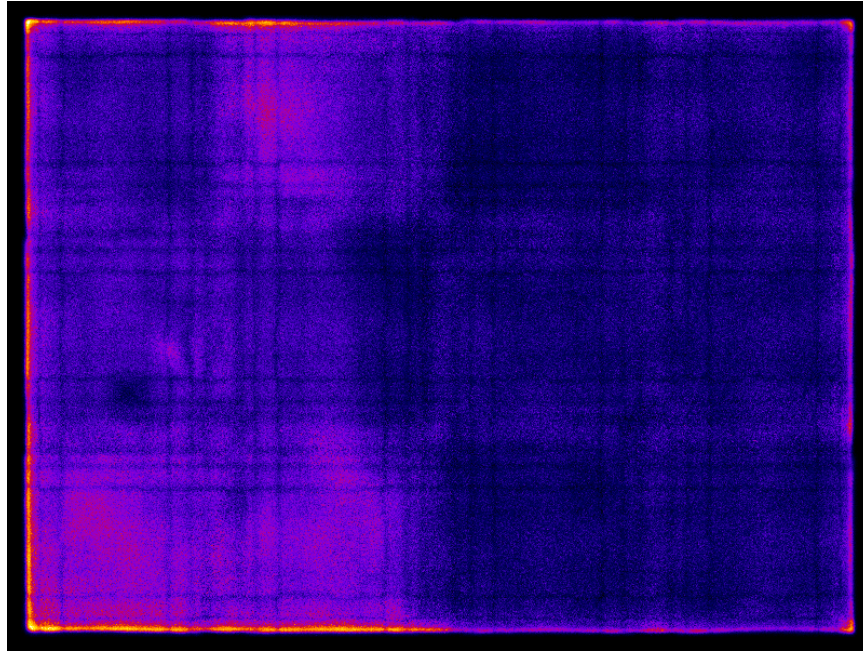
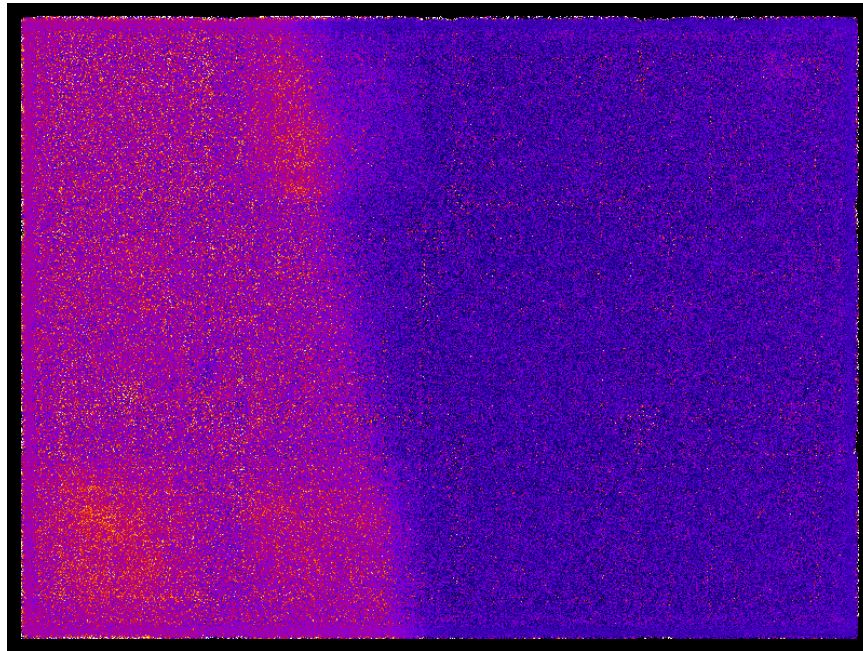


Figure 29: Cf-252 flood field where the SiPMs used have signals that are above 0x the noise value of said SiPM.

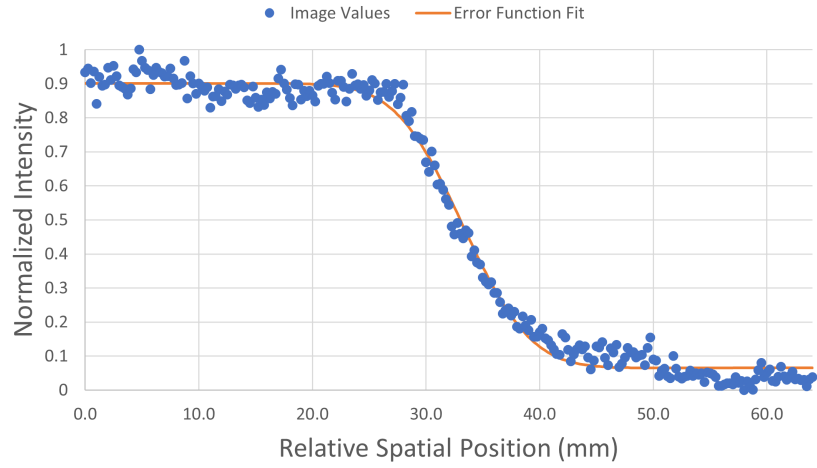


(a) Uncorrected

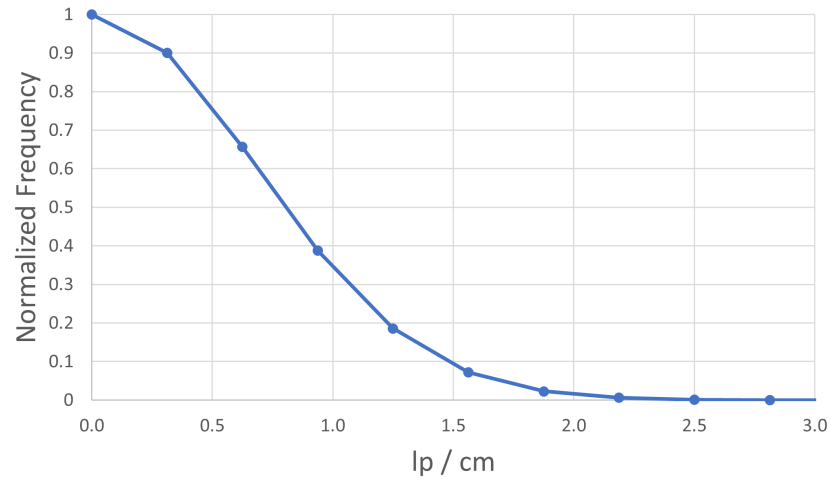


(b) Corrected

Figure 30: Cf-252 edge images where the SiPMs used have signals that are above 0x the noise value of said SiPM a) before flood field correction and b) after flood field correction.



(a) Profile



(b) MTF

Figure 31: a) Line profile and b) MTF plot for a Cf-252 edge where the SiPMs used have signals that are above 0x the noise value of said SiPM.

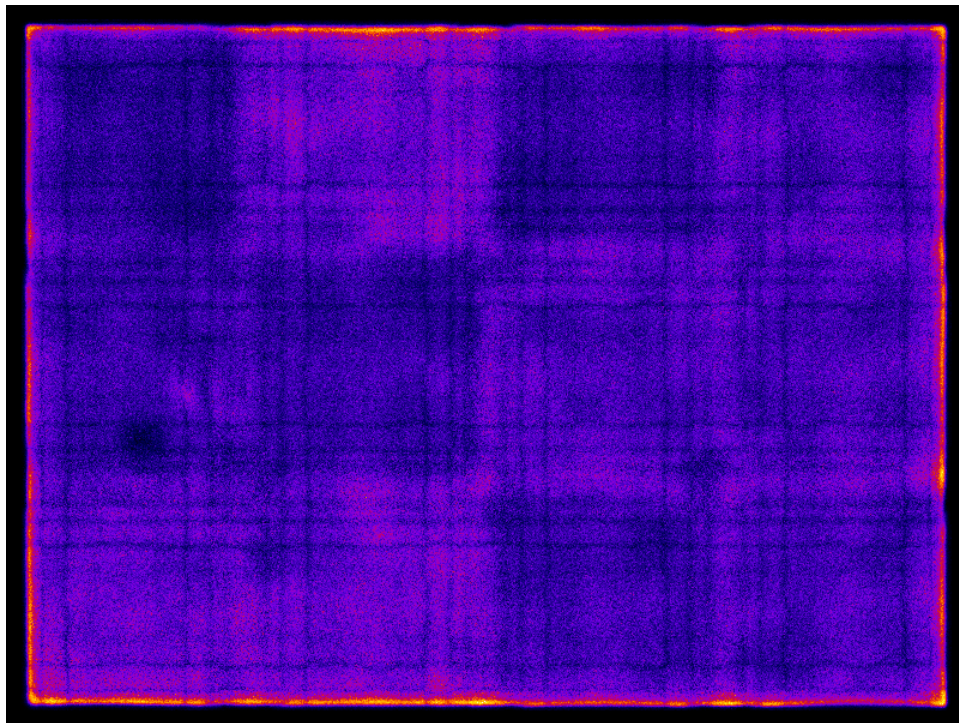
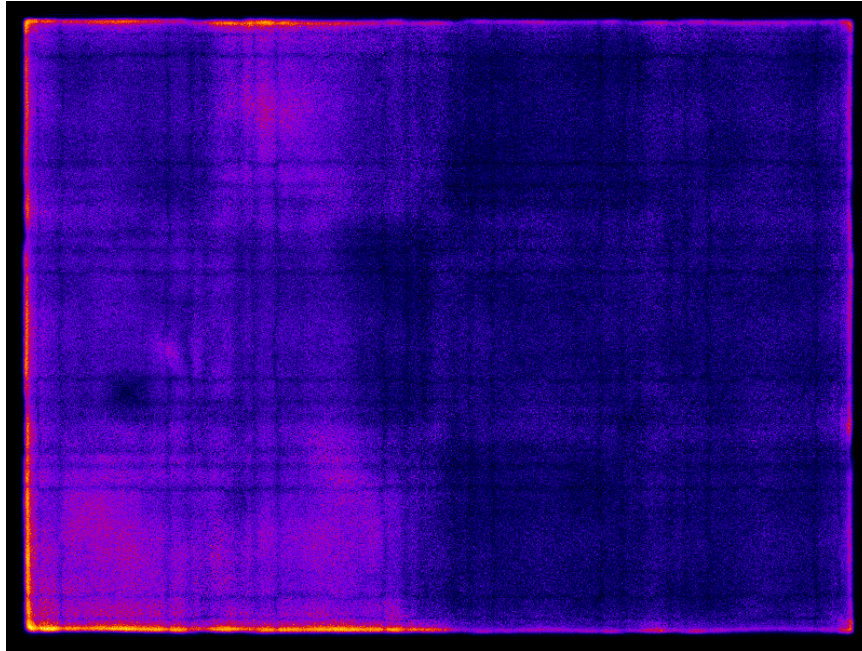
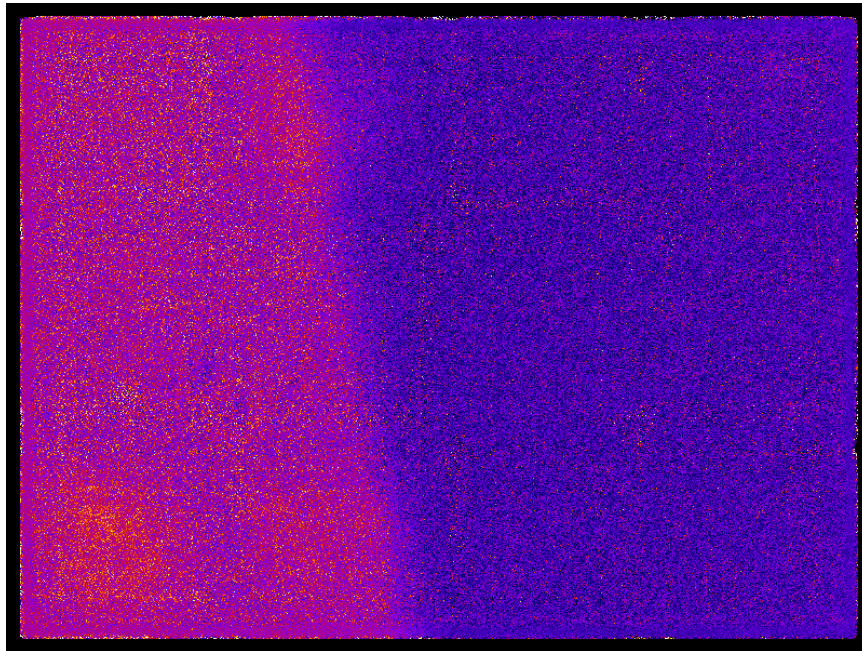


Figure 32: Cf-252 flood field where the SiPMs used have signals that are above 1x the noise value of said SiPM.

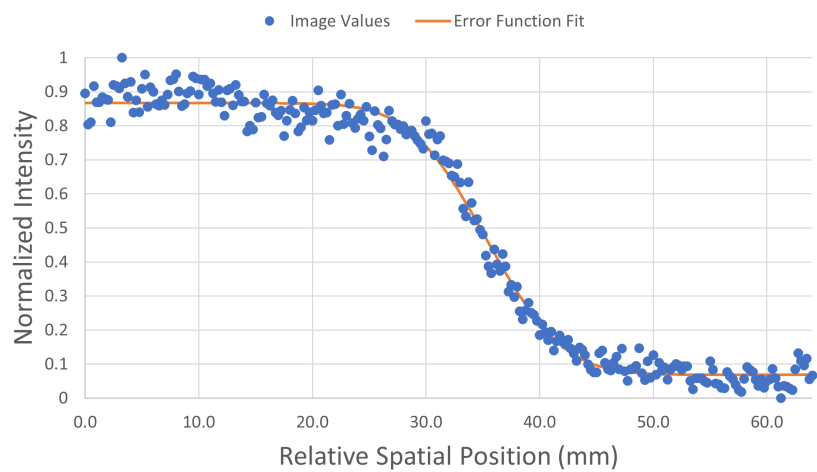


(a) Uncorrected

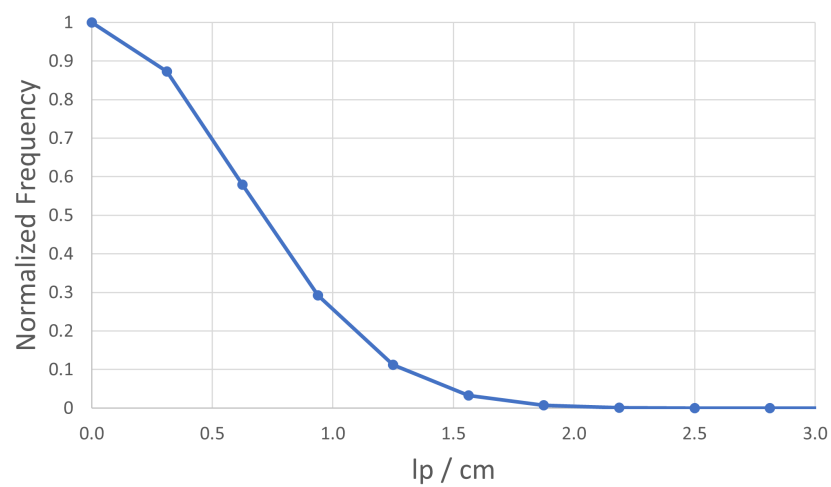


(b) Corrected

Figure 33: Cf-252 edge images where the SiPMs used have signals that are above 1x the noise value of said SiPM a) before flood field correction and b) after flood field correction.



(a) Profile



(b) MTF

Figure 34: a) Line profile and b) MTF plot for a Cf-252 edge where the SiPMs used have signals that are above 1x the noise value of said SiPM.

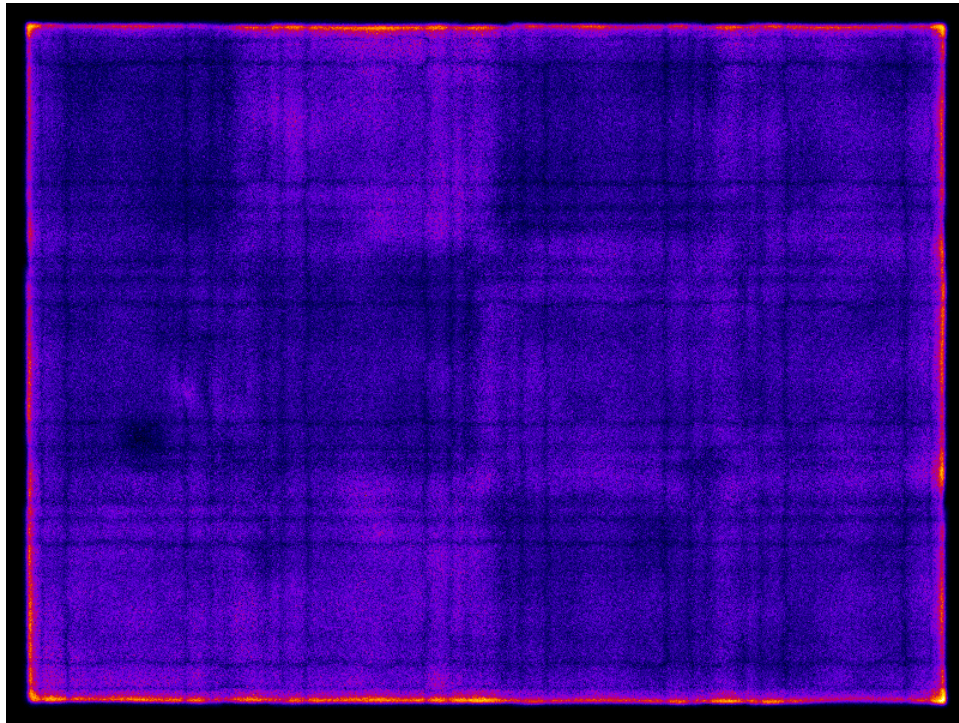
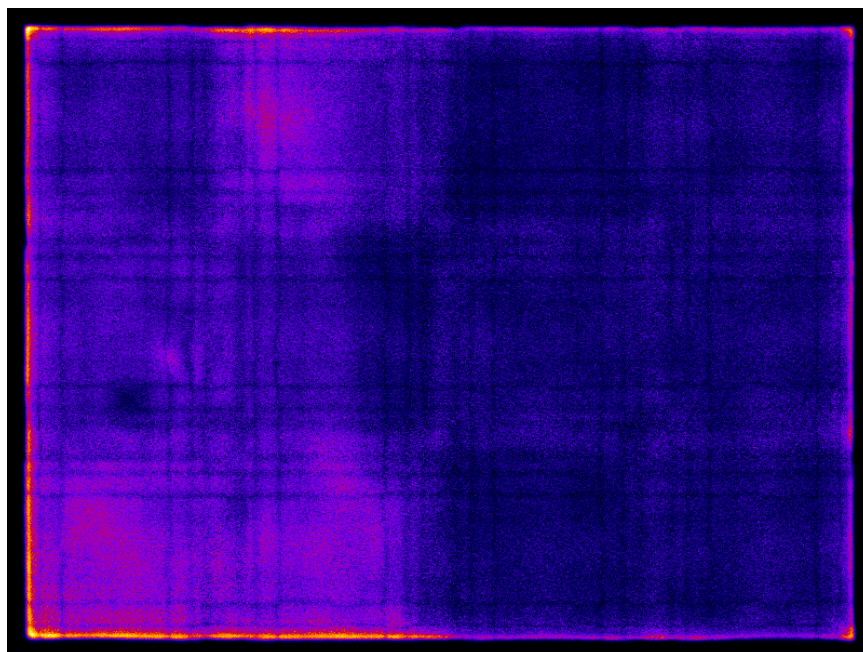
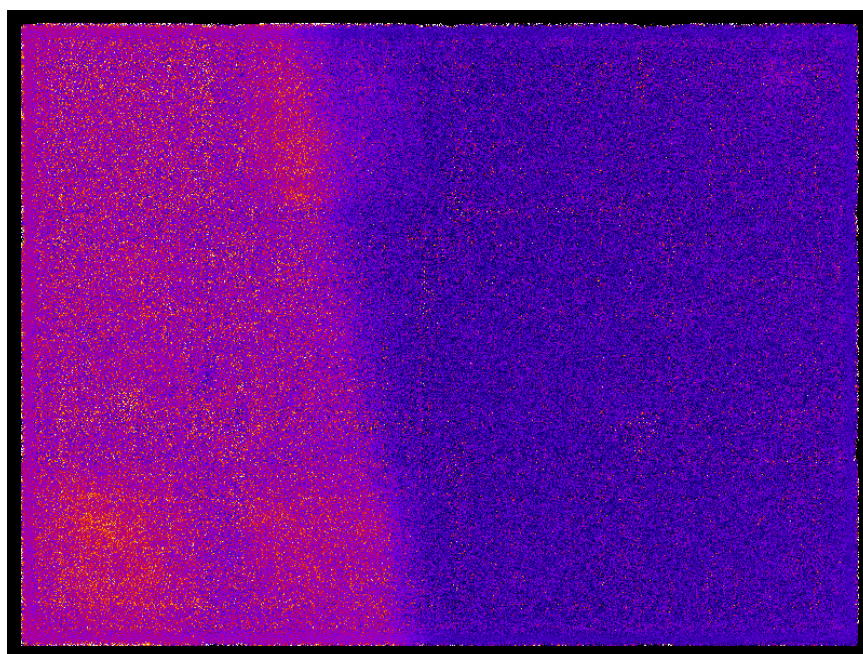


Figure 35: Cf-252 flood field where the SiPMs used have signals that are above 2x the noise value of said SiPM.

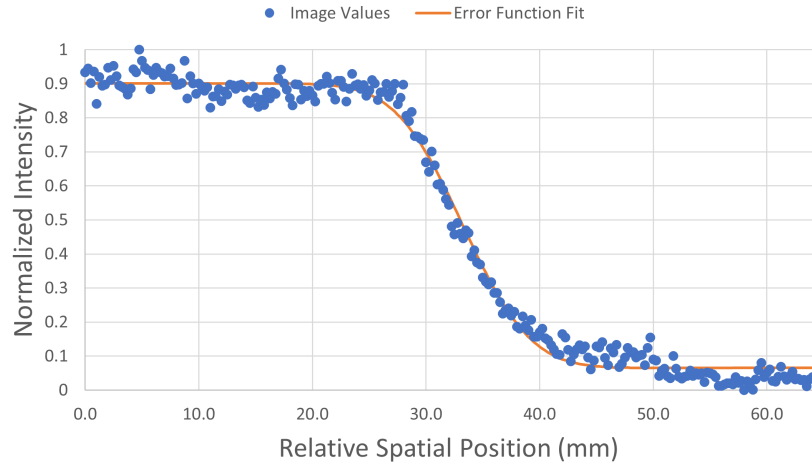


(a) Uncorrected

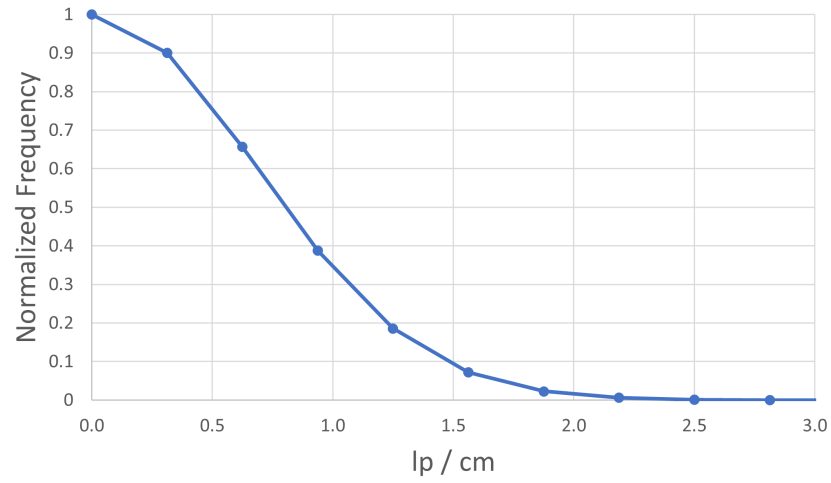


(b) Corrected

Figure 36: Cf-252 edge images where the SiPMs used have signals that are above 2x the noise value of said SiPM a) before flood field correction and b) after flood field correction.



(a) Profile



(b) MTF

Figure 37: a) Line profile and b) MTF plot for a Cf-252 edge where the SiPMs used have signals that are above 2x the noise value of said SiPM.

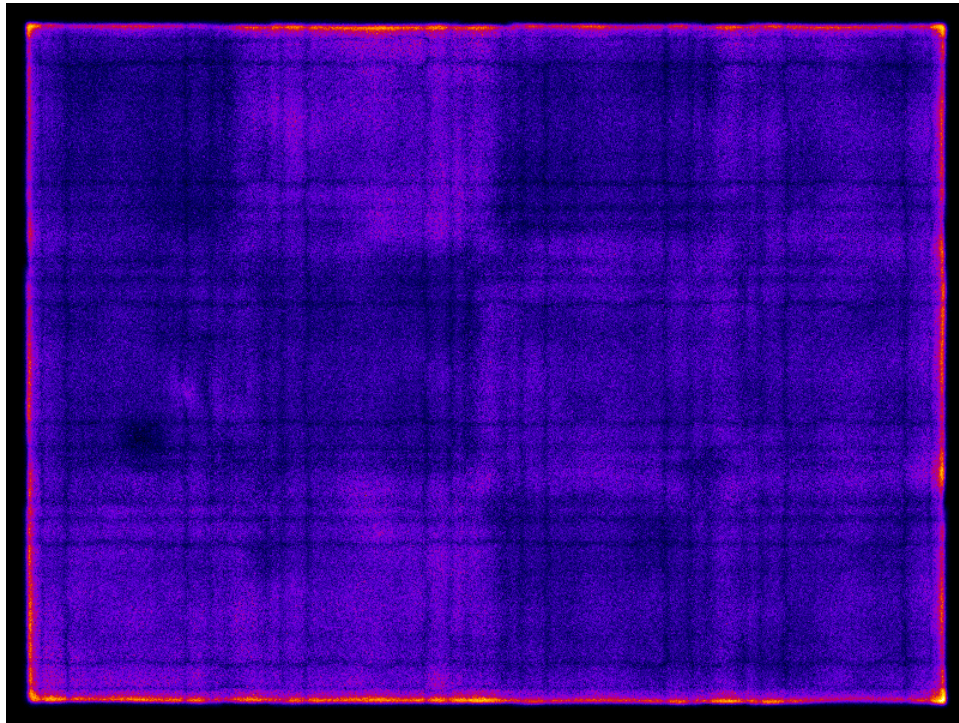
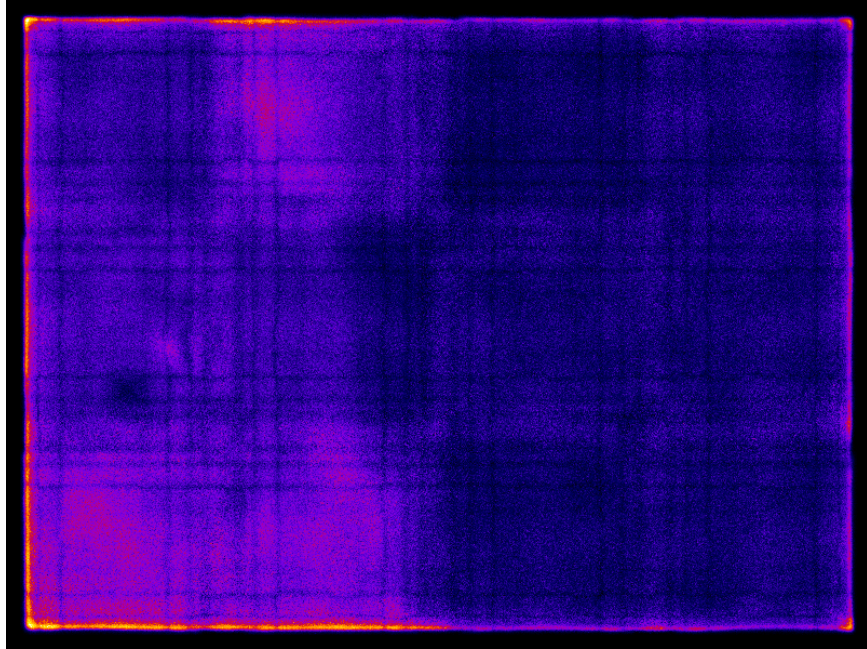
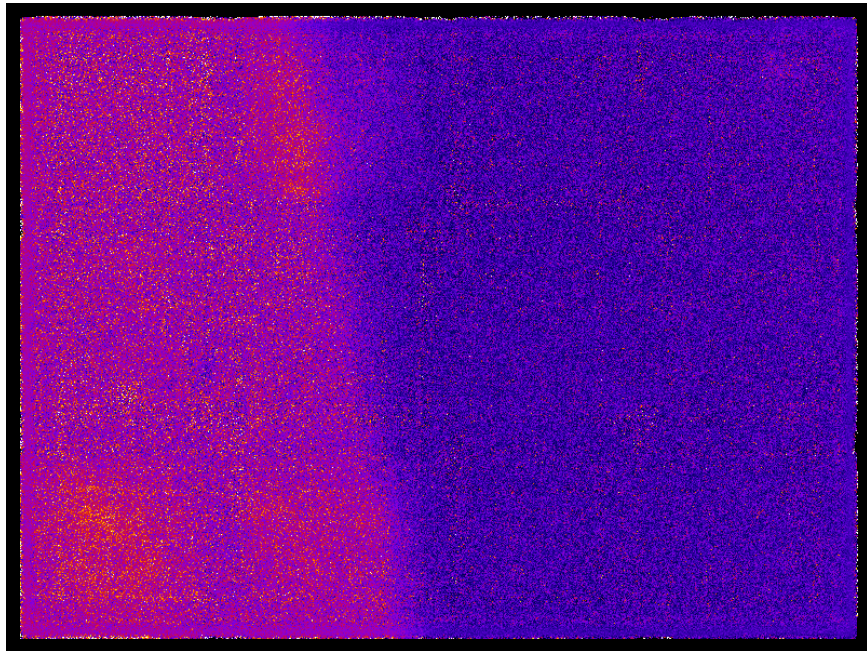


Figure 38: Cf-252 flood field where the SiPMs used have signals that are above 4x the noise value of said SiPM.

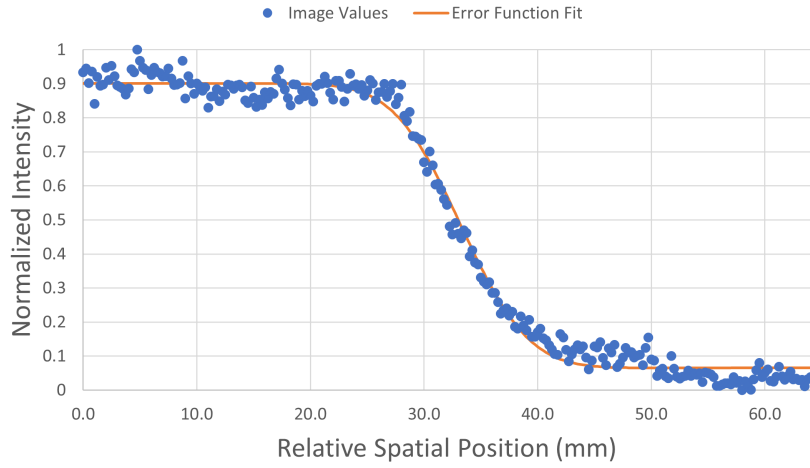


(a) Uncorrected

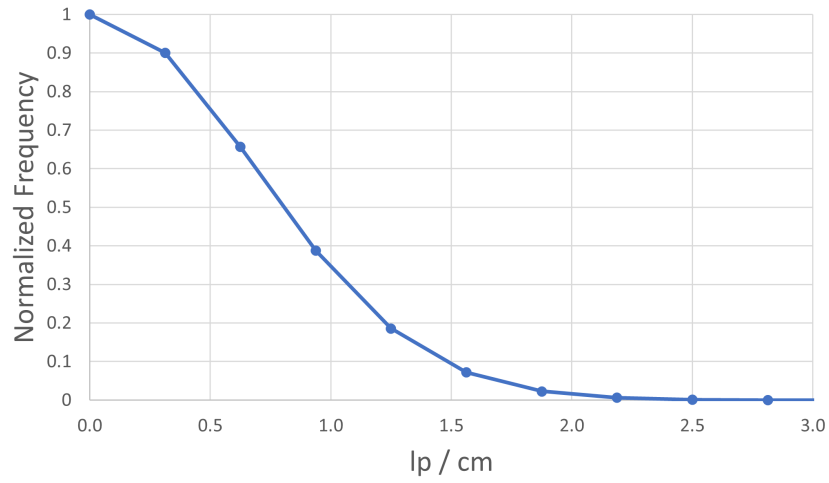


(b) Corrected

Figure 39: Cf-252 edge images where the SiPMs used have signals that are above 4x the noise value of said SiPM a) before flood field correction and b) after flood field correction.



(a) Profile



(b) MTF

Figure 40: a) Line profile and b) MTF plot for a Cf-252 edge where the SiPMs used have signals that are above 4x the noise value of said SiPM.

C.4 Noise Floor Cutoffs

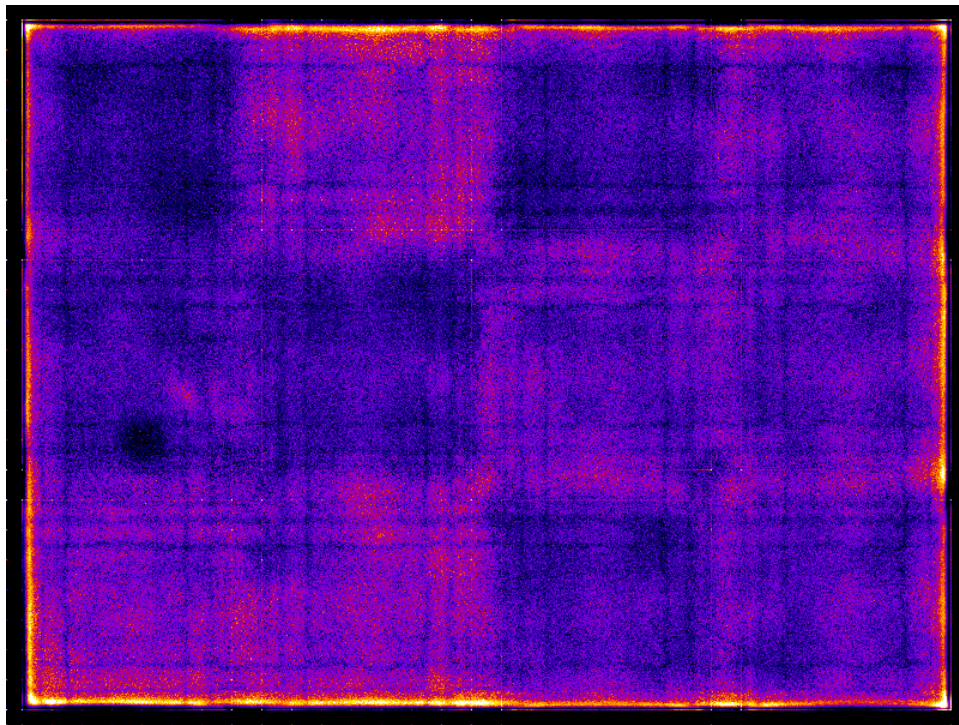
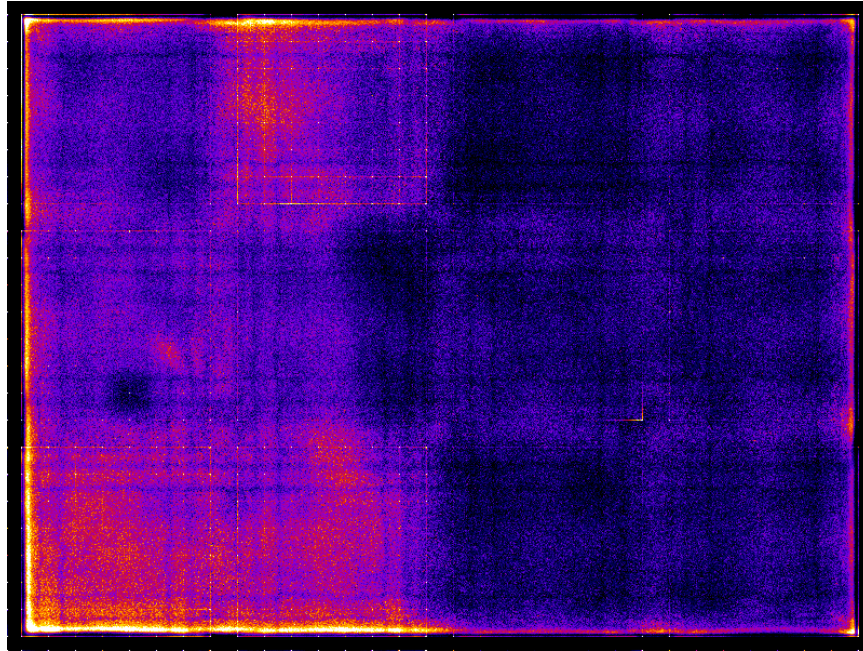
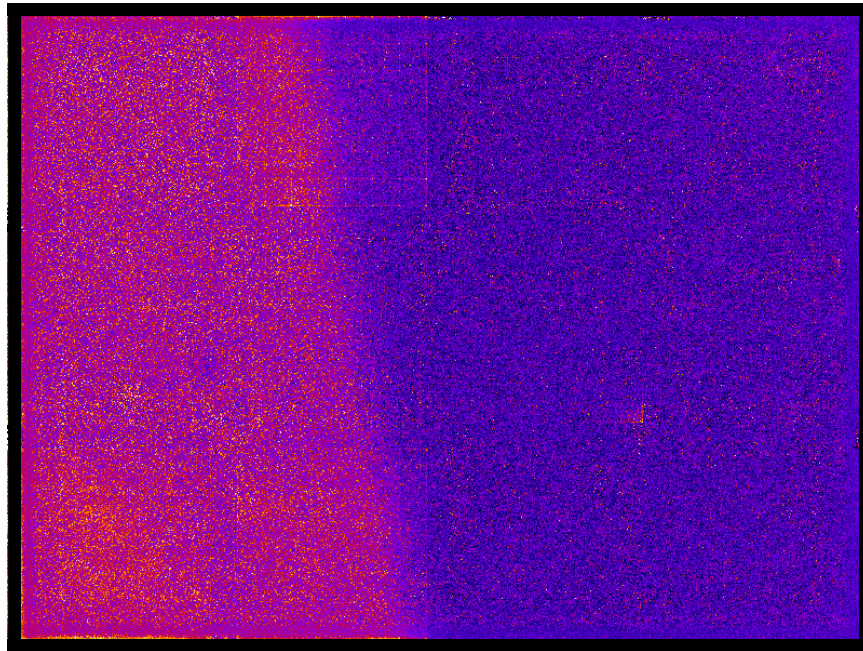


Figure 41: Cf-252 flood field where no SiPMs have to have signals that are above the noise value cutoff.

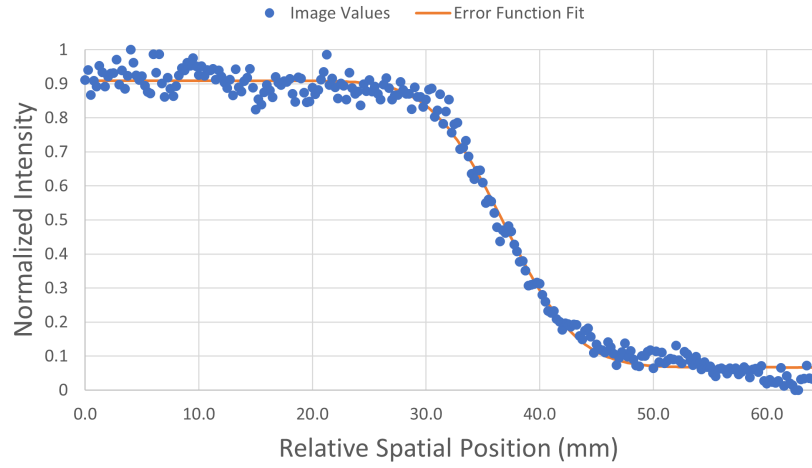


(a) Uncorrected

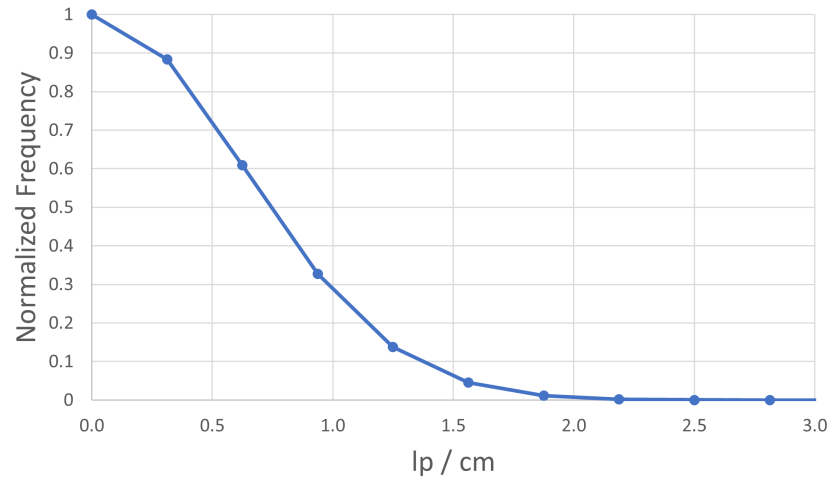


(b) Corrected

Figure 42: Cf-252 edge images where no SiPMs have to have signals that are above the noise value cutoff a) before flood field correction and b) after flood field correction.



(a) Profile



(b) MTF

Figure 43: a) Line profile and b) MTF plot for a Cf-252 edge where no SiPMs have to have signals that are above the noise value cutoff.

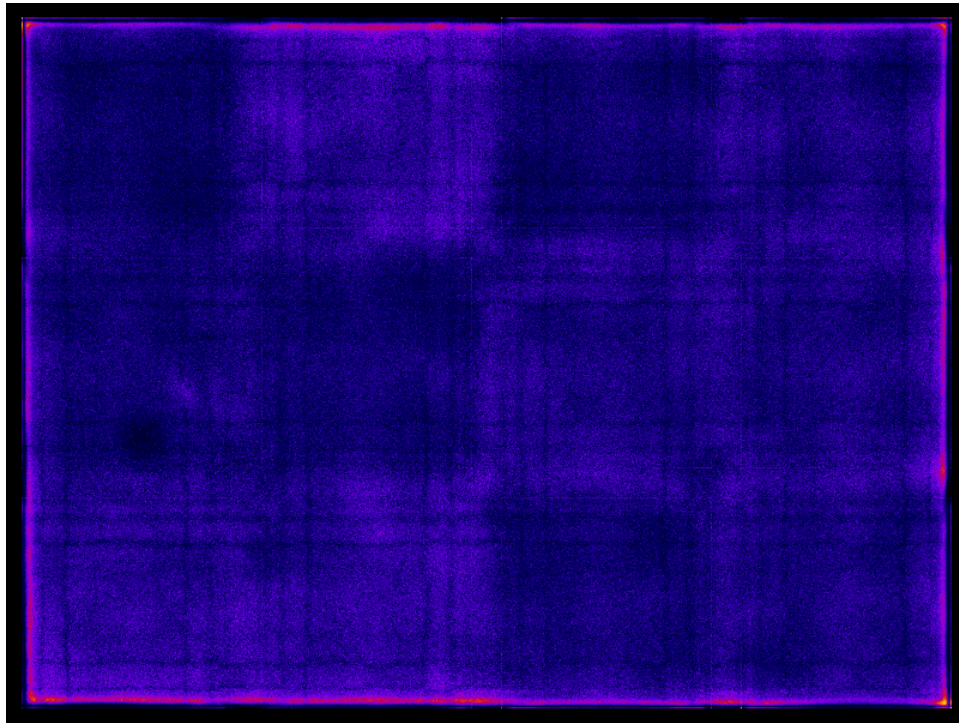
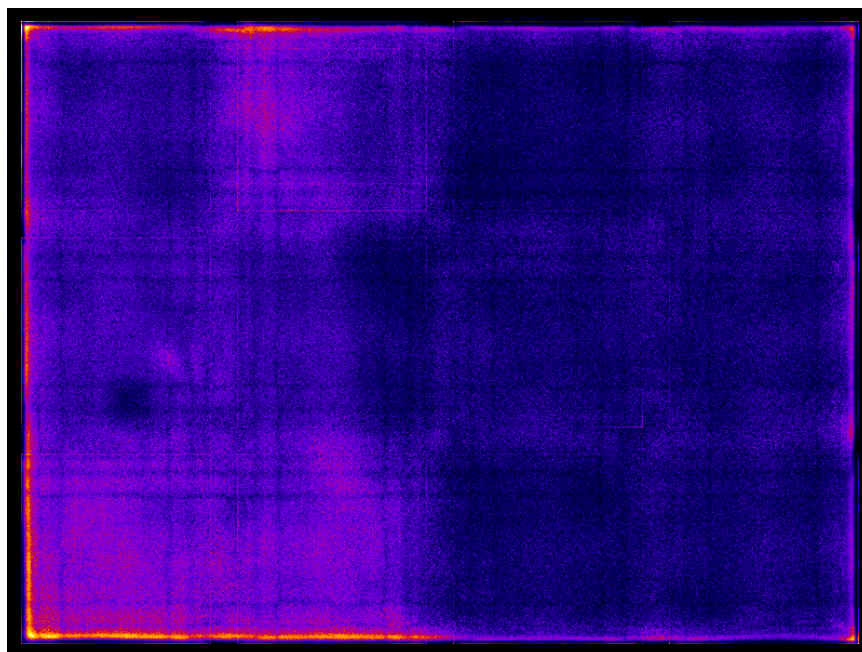
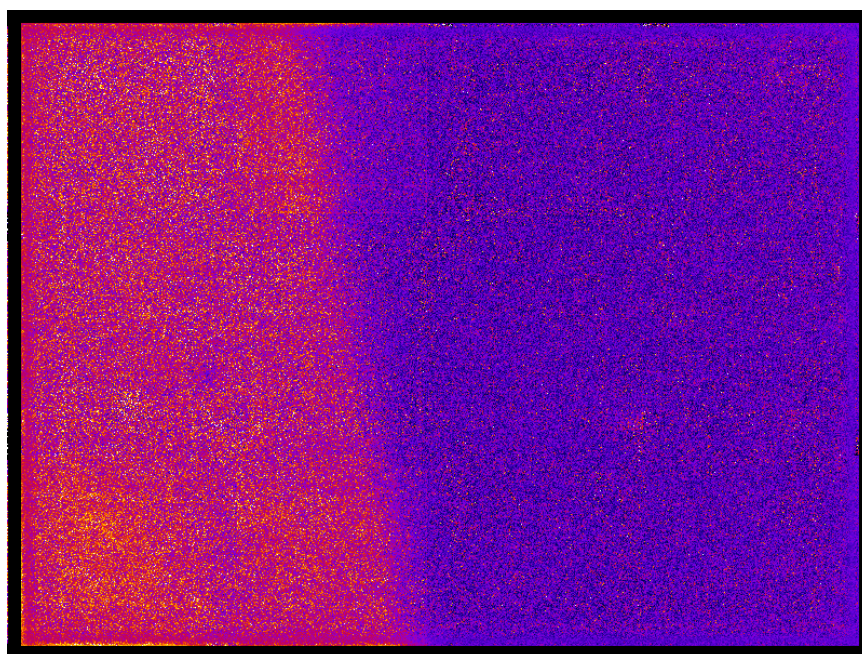


Figure 44: Cf-252 flood field where 4 SiPMs have to have signals that are above the noise value cutoff.

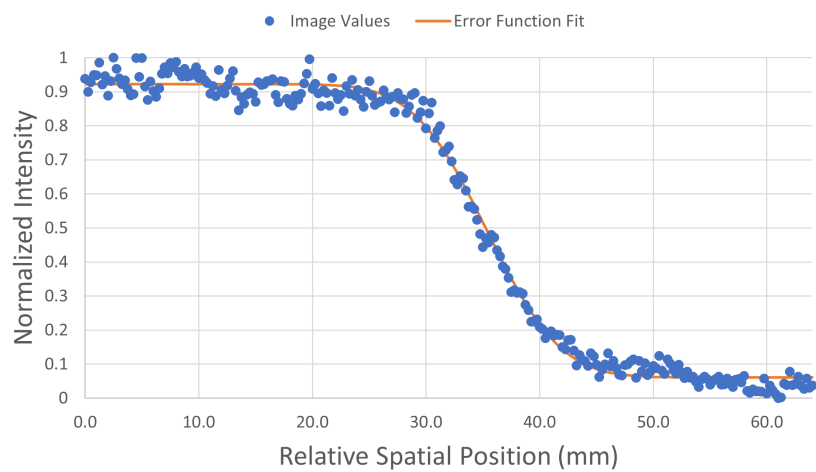


(a) Uncorrected

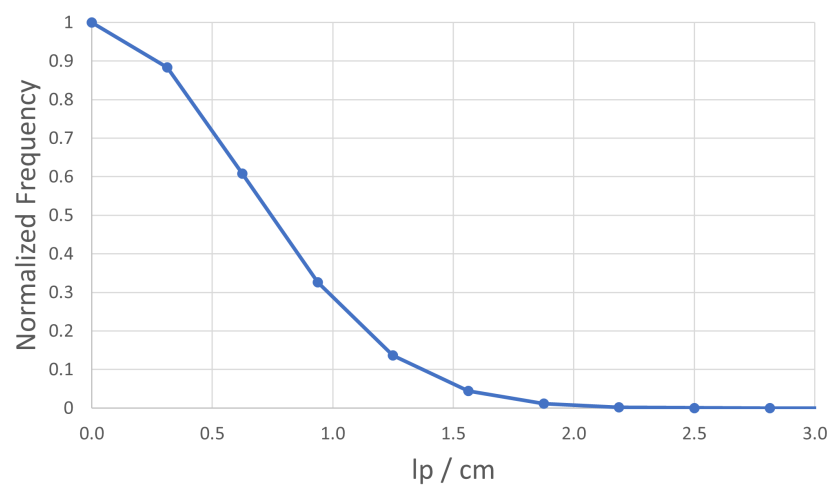


(b) Corrected

Figure 45: Cf-252 edge images where 4 SiPMs have to have signals that are above the noise value cutoff a) before flood field correction and b) after flood field correction.



(a) Profile



(b) MTF

Figure 46: a) Line profile and b) MTF plot for a Cf-252 edge where 4 SiPMs have to have signals that are above the noise value cutoff.

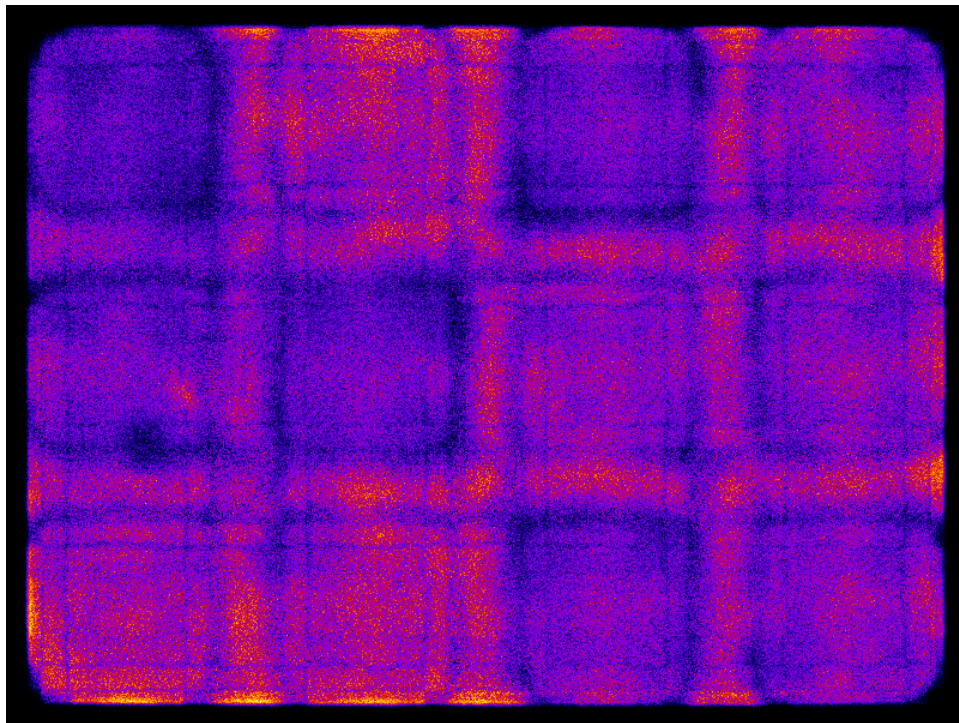
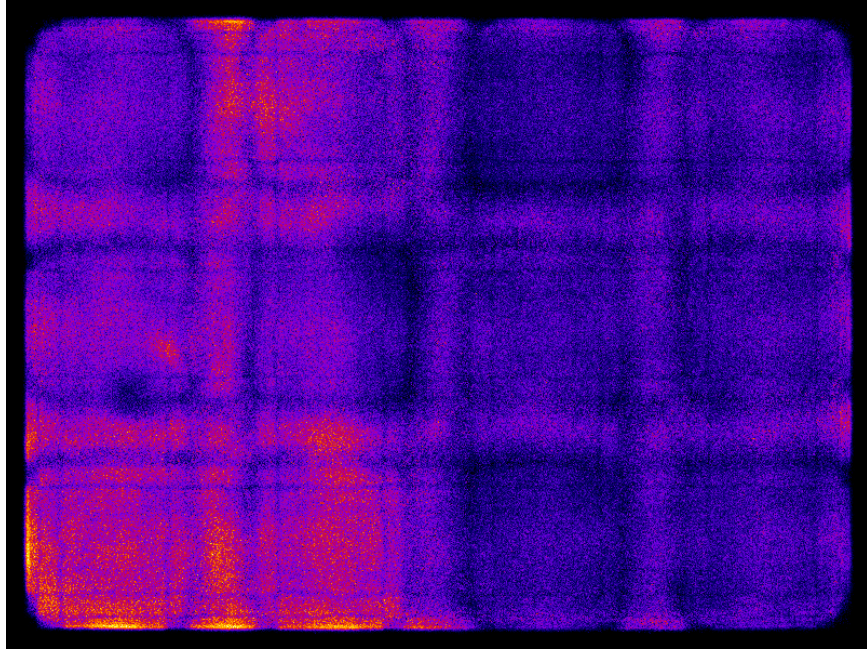
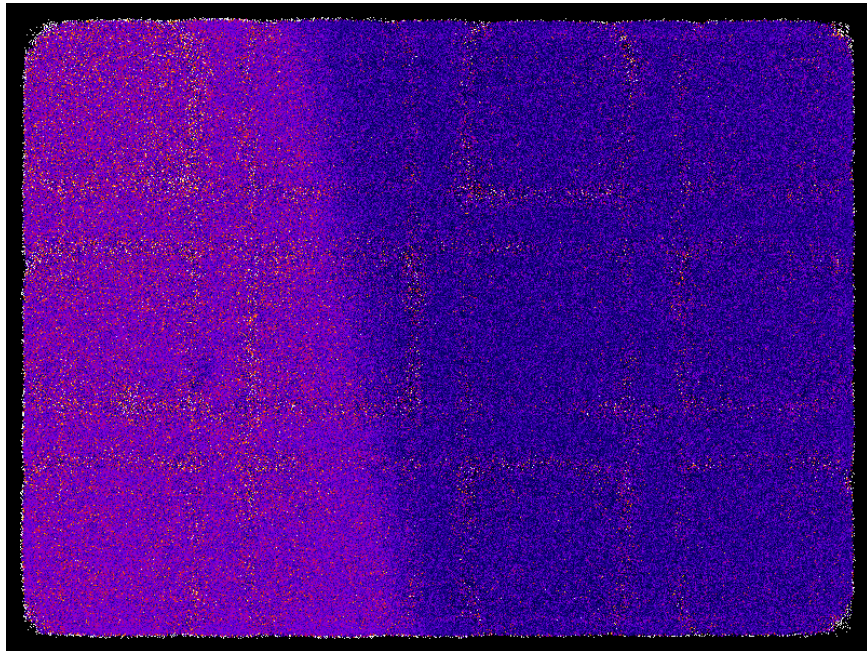


Figure 47: Cf-252 flood field where 4 SiPMs have to have signals that are above the noise value cutoff.

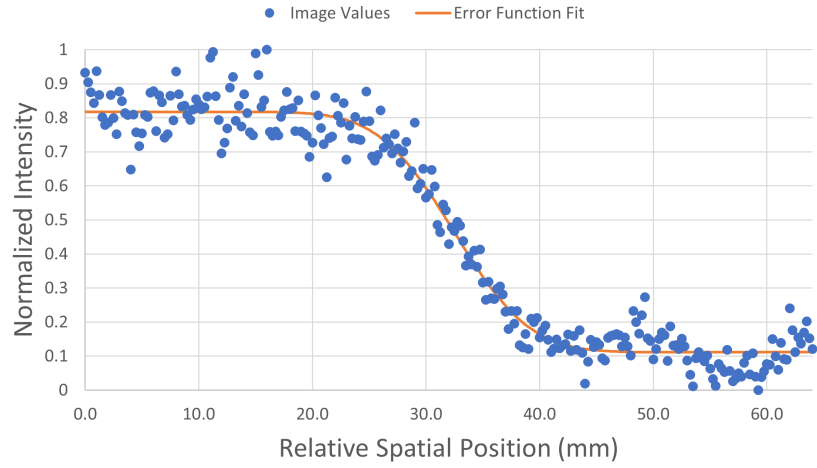


(a) Uncorrected

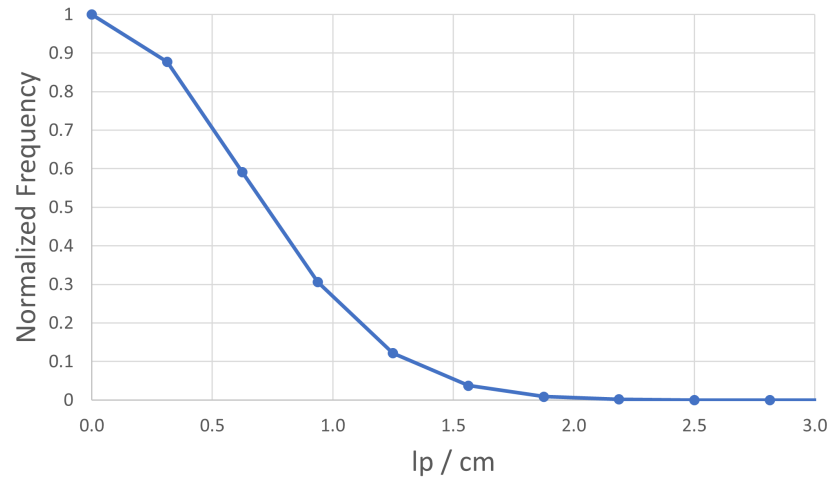


(b) Corrected

Figure 48: Cf-252 edge images where 4 SiPMs have to have signals that are above the noise value cutoff a) before flood field correction and b) after flood field correction.



(a) Profile



(b) MTF

Figure 49: a) Line profile and b) MTF plot for a Cf-252 edge where 4 SiPMs have to have signals that are above the noise value cutoff.

Vita

Christian Xavier Young was born in Allentown, Pennsylvania in 1997. After moving to Wisconsin, he attended Holy Angels Parish School, Aquinas Academy, and Slinger High School, where he graduated from in 2016. After high school, Christian attended Purdue University in West Lafayette, Indiana, where he obtained a Bachelor of Science in Nuclear Engineering in 2020. During his time at Purdue, Christian was active both in the classroom and outside of it. He wrote his first research paper, *A Security Approach for the Example Sodium Fast Reactor*, in 2018 under the direction of Dr. Robert Bean. This paper helped create connections that led to his first internship at the Y-12 National Security Complex in Oak Ridge, Tennessee, where he worked in Global Security and Strategic Partnerships. At Purdue, Christian worked as a Resident Assistant for three years at Shreve Hall, Winifred Parker Hall, and Aspire at Discovery Park. Additionally, he was an active participant at St. Thomas Aquinas Catholic Church and worked as the Social Chair for the American Nuclear Society chapter on campus.

In 2020, Christian began as a PhD student in Nuclear Engineering under Dr. Jason Hayward at the University of Tennessee, Knoxville. Christian continued performing research with Dr. Jeff Preston at the Y-12 National Security Complex, which became an integral part of his thesis work. Christian also interned at Los Alamos National Laboratory after his first year of graduate school, where he worked under the direction of Dr. Kurtis Bartlett and Dr. Karl Smith in ISR-1: Space Science and Applications. During his graduate career, Christian was inducted into Alpha Nu Sigma in 2022, served as the President of the Nuclear Engineering Graduate Student Association for the 2022-2023 school year, and received the Department of Nuclear Engineering Student Service Award in 2023.

Christian completed his doctoral thesis in November 2023. He will be working as a Radiation Detection Engineer at the Y-12 National Security Complex, where he hopes to continue building his portfolio within the defense sector.